

# **DIRECT CHILL AND ELECTROMAGNETIC CASTING OF ALUMINIUM ALLOYS: THERMOMECHANICAL EFFECTS AND SOLIDIFICATION ASPECTS**

THÈSE N° 1509 (1996)

PRÉSENTÉE AU DÉPARTEMENT DES MATÉRIAUX

ÉCOLE POLYTECHNIQUE FÉDÉRALE DE LAUSANNE

POUR L'OBTENTION DU GRADE DE DOCTEUR ÈS SCIENCES TECHNIQUES

PAR

**Jean-Marie DREZET**

Ingénieur, diplômé de l'Ecole Nationale Supérieure de Physique de Grenoble  
de nationalité française

acceptée sur proposition du jury:

Prof. M. Rappaz, directeur de thèse  
Dr M. Bellet, corapporteur  
Prof. J.-A. Manson, corapporteur  
Dr A. Mo, corapporteur  
M. R. von Kaenel, corapporteur

Lausanne, EPFL  
1996



Enfance, mon amour, n'était-ce que cela ? ...

Enfance, mon amour ...

Ce double anneau de l'oeil et l'aisance d'aimer ...

Il fait si calme et puis si tiède, il fait si continuel aussi,

qu'il est étrange d'être là, mêlé des mains à la facilité du jour ...

Éloges

Saint John Perse.

Third Edition : May 2000



# ABSTRACT

The tolerances of semi-continuously cast products of aluminium alloys are very critical if the scalping of the ingot faces is to be minimised before rolling. In the steady state regime of casting, the dimensions of the section of the solidified ingot are lower than those of the mould in the Direct Chill Casting (DCC) or of the inductor in the Electromagnetic Casting (EMC). The contraction of the section, several percents, is larger than the value associated with the thermal contraction of the solid and is also inhomogeneous: the short sides of the ingot contract less than the centre of the rolling faces. In order to study and to understand the mechanisms responsible for such deformation, in-situ measurements and laboratory investigations have been performed whereas a thermomechanical model has been developed. The specific points of this study are as follows:

- measurements of the distortions undergone by the ingot during casting and after complete cooling,
- determination of the thermal boundary conditions corresponding to the primary cooling (contact in between the metal and the mould) and secondary cooling (water jet), using in-situ temperature measurements and inverse modelling,
- measurements of the thermal conductivity of two industrial alloys using inverse modelling and one dimensional casting experiments,
- measurements of the thermomechanical behaviour of two industrial alloys, specifically the elastic modulus by ultrasonic method, the thermal expansion coefficient by dilatometry and the creep behaviour in the solid and mushy state using tensile and indentation tests,
- study of the solidification path of the AA1201 alloy using a finite difference microsegregation model coupled with the Al-Fe-Si phase diagram data; the results have been validated against DTA measurements and extended to situations encountered in the DC/EM casting process,
- computation of the temperature, stress and strain fields in DC and EM-cast ingots with the help of the 2D and 3D thermomechanical finite element code Abaqus; the final ingot cross section for a given mould/inductor design has been calculated,

- comparison of the simulation results with the experiments.

The mechanisms responsible for the main ingot distortions undergone during casting and subsequent cooling, notably the non-uniform contraction of the ingot cross section, have been identified.

Finally, an inverse thermomechanical method for the optimisation of the mould/inductor design is proposed based upon a criterion of maximum flatness of the final ingot. Such a method should allow a reduction in the costs associated with the definition of the mould/inductor designs for new casting conditions. The present work will be extended to more complicated geometries in the Brite-Euram project EMPACT (European Modelling Programme on Aluminium Casting Technology).

## RÉSUMÉ

Les tolérances des produits semi-finis obtenus par coulée semi-continue d'alliages d'aluminium sont très critiques si l'on veut minimiser la rectification ou "scalpage" des faces avant laminage. En régime stationnaire de coulée, les dimensions de la section du lingot solidifié sont inférieures à celle de la section de la lingotière en coulée conventionnelle ou de l'inducteur en coulée électromagnétique. La contraction de la section, plusieurs pour-cents, dépasse nettement la valeur associée à la contraction thermique du solide et de plus est inhomogène, les extrémités du lingot se contractant moins que les milieux des faces. Pour étudier et comprendre les mécanismes responsables, des mesures ont été conduites in-situ et en laboratoire et un modèle thermomécanique a été développé.

Les points majeurs de cette étude sont les suivants:

- mesures des distorsions subies par le lingot à la fois pendant la coulée et après le refroidissement ultérieur du lingot,
- détermination des flux de chaleur des refroidissements primaire (contact métal-lingotière) et secondaire (jet d'eau) lors du régime stationnaire de coulée à l'aide de mesures thermiques in-situ pendant la coulée et d'une méthode inverse,

- mesure de la conductivité thermique de deux alliages industriels à l'aide d'une méthode inverse et d'une coulée unidirectionnelle,
- mesures des propriétés thermomécaniques de deux alliages industriels, plus particulièrement du module d'élasticité par méthode d'ultrasons, du coefficient d'expansion thermique par dilatométrie et du comportement viscoplastique à l'état solide et pâteux à l'aide de tests de fluage et d'indentation,
- étude du chemin de solidification de l'alliage de coulée AA1201 à l'aide d'un modèle en différences finies de microségrégation couplé avec le diagramme de phase Al-Fe-Si, modèle validé par des mesures de DTA et étendu à des situations typiques de la coulée,
- calcul des champs de température, déformation et contrainte dans le lingot pendant la coulée et le refroidissement ultérieur à l'aide du code thermomécanique Abaqus; la section finale d'un lingot est calculée en régime stationnaire pour une segmentation de moule donnée,
- comparaison des résultats de simulation avec les mesures.

Les mécanismes responsables des principales distorsions subies par le lingot lors de la coulée et du refroidissement ultérieur, notamment la contraction non-uniforme de la section en régime stationnaire, ont été identifiés.

Enfin, une méthode inverse d'optimisation de la forme de la lingotière ou de l'inducteur basée sur les calculs thermomécaniques est proposée; elle devrait permettre de réduire les coûts de la procédure de définition des moules pour de nouvelles conditions de coulée. Ce travail de recherche sera repris et étendu à des situations plus complexes dans le cadre du projet Brite-Euram EMPACT (European Modelling Programme on Aluminium Casting Technology).

# ACKNOWLEDGEMENTS

The present work was carried out during 1992-1996 at the Laboratoire de Métallurgie Physique (LMPH) of the Ecole Polytechnique Fédérale de Lausanne (EPFL), Switzerland. This research was funded by the Commission pour l'Encouragement de la Recherche Scientifique, Bern, under grant CERS 2365 and by Alusuisse-Lonza Ltd, Chippis.

I wish to express my sincerest gratitude to Professor Michel Rappaz for his useful guidance, endless encouragement, suggestions and personal interest throughout the course of this work.

Grateful thanks are extended to the members of the thesis committee, Professor H. Hofmann, Dr. A. Mo, Dr. M. Bellet, M. R. Von Kaenel and Professor J.-A. Månson for taking the time to evaluate this manuscript.

I am also very grateful to Professor Wilfried Kurz, head of the LMPH, to all of my colleagues at LMPH and also to the members of the Département des Matériaux (DMX) and its workshop for their kindness and the constant good working atmosphere they have maintained.

I also sincerely thank Dr. Y. Krähenbühl and M. M. Plata for their expertise and guidance of the research project, M. B. Carrupt and C. Moulin for their helpful collaboration during the experimental period at the Alusuisse Company and Prof. G. Eggeler and Dr. P. Vicente for helping with the creep and indentation tests, respectively.

Finally, this work is dedicated to my brother Philippe<sup>1965/1981</sup> in heaven, to my grand-mother, Lucie, and to Marguerite.

Lausanne, April 1996.

Jean-Marie Drezet.



## LIST OF SYMBOLS

$c_0$	nominal composition		%
$c_{eut}$	eutectic composition		wt %
$c_{li}$	liquid composition of element i		wt %
$c_p$	specific heat		$J \cdot kg^{-1} \cdot K^{-1}$
$c_p^e$	equivalent specific heat		$J \cdot kg^{-1} \cdot K^{-1}$
$c_{si}^*$	interfacial solid composition of element i		wt %
$D_i^s$	diffusion coefficient of solute i in the solid phase		$m^2 \cdot s^{-1}$
$D_i^l$	diffusion coefficient of solute i in the liquid phase		$m^2 \cdot s^{-1}$
E	Young's modulus		Pa ( $N \cdot m^{-2}$ )
$f_s$	mass solid fraction		-
$f_{eut}$	eutectic mass fraction		-
h	enthalpy		$J \cdot kg^{-1}$
$I_d$	identity tensor		
$q_i$	solute flux of element i		$wt\% \cdot m^{-2} \cdot s^{-1}$
$k_i$	partition coefficient of element i		-
L	latent heat of fusion		$J \cdot kg^{-1}$
$m_i$	liquidus slope associated with element i		K ou $K/wt.\%$
R	universal gaz constant	(8.316)	$J \cdot mole^{-1} \cdot K^{-1}$
t	time		s
$\delta t, \Delta t$	time increment		s
T	temperature		K, °C
$T_c$	coherency temperature		K, °C
$T_{eut}$	eutectic temperature		K, °C

$T_m$	melting temperature of the pure substance	K, °C
$T_s$	solidus	K, °C
$T_l$	liquidus	K, °C
$\Delta T$	undercooling	K, °C
$w_i$	mass concentration of element i	wt%
$r$	position	m
$r^*$	position of the solid-liquid interface	m
$s$	deviatoric stress tensor ( $= \sigma - \frac{1}{3} \text{tr}(\sigma) \text{Id}$ )	Pa (N·m <sup>-2</sup> )
$Z$	Zener-Hollomon parameter ( $= \dot{\epsilon} \exp(\frac{Q_{\text{def}}}{RT})$ )	s <sup>-1</sup>
$\alpha$	Fourier number ( $= \frac{D_s t_f}{\lambda_2^2}$ )	-
$\alpha$	linear expansion coefficient	K <sup>-1</sup>
$\epsilon$	strain tensor	-
$\epsilon^{\text{el}}$	elastic strain tensor	-
$\epsilon^{\text{th}}$	thermal strain tensor	-
$\epsilon^{\text{vp}}$	viscoplastic strain tensor	-
$\dot{\epsilon}$	strain rate	s <sup>-1</sup>
$\nu$	Poisson's ratio	-
$\kappa$	thermal conductivity	W·m <sup>-1</sup> ·K <sup>-1</sup>
$\lambda_1$	characteristic columnar dendrite spacing	m
$\lambda_2$	characteristic secondary dendrite arm spacing	m
$\Omega$	supersaturation ( $= \frac{c_l^* - c_0}{c_l^* - c_s^*}$ )	-
$\rho$	volumetric mass	kg·m <sup>-3</sup>
$\sigma$	stress tensor	Pa (N·m <sup>-2</sup> )
$\sigma_s, \sigma_{\text{VM}}$	shear stress or Von Mises equivalent stress	Pa (N·m <sup>-2</sup> )

# OVERVIEW

Abstract	1
Résumé	2
Acknowledgements	3
List of symbols	4
Overview	7
<b>1-Introduction</b>	<b>9</b>
1.1 Aluminium alloys and casting techniques	9
1.2 Semi-continuous casting processes	12
1.3 As-cast microstructure and ingot distortions	15
1.4 Motivations, objectives and layout of this work	20
<b>2-Theory and literature survey</b>	<b>25</b>
2.1 Solidification characteristics in DC/EM casting	25
2.2 Mechanical behaviour of metal related to solidification	40
2.3 Continuous casting of aluminium alloys	65
<b>3-Experimental</b>	<b>73</b>
3.1 Measurements on full-size DC/EM castings	73
3.2 Mechanical testing	78
3.3 Laboratory investigation	89
<b>4-Numerical methods</b>	<b>97</b>
4.1 Microsegregation modelling	97
4.2 Inverse temperature modelling	107

4.3 Thermomechanical modelling	112
<b>5-Results and discussion</b>	123
5.1 Experimental results	123
5.2 Modelling results	149
<b>6-Conclusion</b>	175
References	177
Appendix	
I Landau transformation for the solute diffusion	183
II Thermal linear contraction coefficient	185
III High apparent creep activation energies in mushy zone microstructures	187
IV Solidification/remelting in a closed or open system	193
Curriculum vitae	197
Publications	198

# CHAPTER 1

## INTRODUCTION

### 1.1 Aluminium alloys and casting techniques

#### 1.1.1 Aluminium and its alloys

Metals have played an important role in the development of human civilisation. In this development there has not been a metal, apart from steel, as versatile as aluminium, because of its unique intrinsic characteristics [Matu]. In fact, aluminium, the second most plentiful metallic on earth, became an economic competitor in engineering applications as recently as the end of the 19th century.

Owing to its chemical reactivity, aluminium was not extracted as an industrial metal until 1886. In this year, the electrolytic reduction of alumina ( $\text{Al}_2\text{O}_3$ ) dissolved in molten cryolite was independently discovered and developed by Charles Hall in Ohio (USA) and Paul Heroult in France [Peria]. In a relatively short time, aluminium production achieved remarkable growth, due to electrification and later to the airplane industry. In 1921, the annual world production of aluminium reached 200 kilotons, increasing to 1.5 million tons by 1950, and 17.5 million tons by 1988, 3.4 million tons being produced in western Europe. Today aluminium is the second widely used metal after steel and is used in the following applications:

- 25.8%      transportation
- 22.8%      building and construction
- 20.2%      containers and packaging
- 8.6%        electrical engineering
- 6.2%        general engineering
- 16.4%      miscellaneous.

Nowadays, the requirements of the airframe industry for structural materials have changed over the years and the aluminium producers have developed a multitude of new products to meet these needs. Early problems with corrosion threatened the use of aluminium, so researchers developed special

alloys. Requirements for even higher specific strength to save weight were combined with requirements for high ductility to ensure that the structure would deform plastically rather than fracture when accidentally overloaded. For this purpose, the aluminium industry responded with new alloys of the 2xxx and 7xxx series and also Al-Li alloys.

Aluminium and its alloys play also an increasing role in the food packaging and is also an ideal candidate to respond to the weight reduction trend within the automotive industry. As an example, car sheets are of special interest since they allow a reduction of the body weight by up to 50% with similar or even better structural characteristics compared to the conventional steel sheet.

Among the most striking characteristics of aluminium is its versatility. The range of physical and mechanical properties that can be developed, from refined high-purity aluminium to most complex alloys, is remarkable. The properties of aluminium that make this metal and its alloys the most economical and attractive for a wide variety of uses are appearance, light weight, fabricability, physical properties, mechanical properties, and corrosion resistance. As an example, aluminium is often selected for its electrical conductivity, which is nearly twice that of copper on an equivalent weight basis. The thermal conductivity of aluminium alloys, about 50 to 60% that of copper, is advantageous in heat exchangers, evaporators, electrically heated appliances and utensils, and automotive cylinder heads and radiators.

It is convenient to divide aluminium alloys into two major categories: casting compositions and wrought compositions. The designation wrought indicates that certain aluminium alloys are available primarily in the form of worked product, such as sheet, foil, plate, extrusion, tube, forging, rod, bar, and wire. Working operations and thermal treatments transform the cast ingot structure into a wrought structure that may range from fully recrystallised to fibrous. Structure influences strength, corrosion resistance, and various other properties.

A further differentiation for each category is based on the primary mechanism of property development. Many alloys respond to thermal treatment based on phase solubilities. These treatments include solution heat treatment, quenching, and precipitation, or *age hardening*. For either casting or wrought alloys, such alloys are described as heat treatable. A large number of other wrought compositions rely instead on work hardening through mechanical reduction, usually in combination with various annealing procedures for property development. These alloys are referred to as *work hardened*. Some

casting alloys are essentially non-heat treatable and are used only in as-cast or in thermally modified conditions unrelated to solution or precipitation effects.

The Aluminium Association nomenclature for cast and wrought alloy is most widely recognised. For wrought alloys, a four-digit system is used to produce a list of wrought composition families as follows [Hatch]:

- 1xxx controlled unalloyed (pure) compositions (non-heat treatable)
- 2xxx alloys in which copper is the principal alloying element, though other elements, notably magnesium, may be specified (heat treatable)
- 3xxx alloys in which manganese is the principal alloying element (non-heat treatable)
- 4xxx alloys in which silicon is the principal alloying element (non-heat treatable)
- 5xxx alloys in which magnesium is the principal alloying element (non-heat treatable)
- 6xxx alloys in which magnesium and silicon are principal alloying element (heat treatable)
- 7xxx alloys in which zinc is the principal alloying element, but other elements such as copper, magnesium, chromium, and zirconium may be specified (heat treatable)
- 8xxx alloys including tin and some lithium compositions characterising miscellaneous compositions.

### **1.1.2 Casting techniques**

An obvious advantage of aluminium is its comparatively low melting point (660°C when pure), as well as its easy melting and pouring in air without any protective flux covering or inert gas atmosphere, since the oxide surface skin that forms on the molten metal prevents excessive oxidation. The production of aluminium semifabricated products begins with the solidification of a molten alloy in the shape of a casting with the right characteristics for subsequent processing and fabrication. The casting operations, tailored to each product, can be grouped under three main headings:

- **static (or mould) casting** (high pressure die casting, permanent mould casting, sand casting, investment casting, ...) to obtain products (foundry ingots) of near-net final shapes and high mechanical properties,
- **semi-continuous casting** (direct chill and electromagnetic casting) to obtain products, mainly extrusion billets and sheet ingots, of substantial cross-sectional area, of length restricted to several meters (ten at most), used as the starting point in traditional processing and fabrication processes,
- **continuous casting** (thin coiled sheet, strip, twin rolled casting) yielding a rough casting of dimensions fairly close to those of the end-product, thus making it possible to employ downstream processing facilities which are “lighter” and hence cost less than the more traditional processes.

The typical distribution of the primary aluminium production by cast products is given below:

- 52%            sheet ingot
- 27%            extrusion ingot
- 11%            foundry ingot
- 10%            others.

Vertical casting was developed for making slabs with rectangular cross-section for rolling and axisymmetric billets for extrusion. The main advantage of vertical casting is the creation, by suitable positioning of the systems for feeding and cooling the molten metal, of a product having constant structural properties with respect to the longitudinal axis and also the axis of rolling or drawing. The major semi-continuous techniques applied for the production of rolling sheet ingots and extrusion billets are the vertical conventional direct chill (DC) casting and more recently developed, the electromagnetic (EM) casting<sup>1</sup>.

---

<sup>1</sup> Unlike steel, the high thermal conductivity of aluminium alloys makes the molten pool rather shallow, thus preventing the use of a curved continuous casting machine.



## 1.2 Semi-continuous casting processes

### 1.2.1 The direct chill (DC) casting process

A schematic representation of the DC casting process [Emley] is given in figure 1.1 (left side). An open rectangular mould confines the molten metal and distributes the cooling water around the ingot via the water chamber. On start-up, the mould is closed off by a bottom block mounted on a horizontal lowering table (see figure 1.1). Once the process of solidification has begun, the bottom block is lowered, being replaced by the butt of the product being cast. A superheated liquid metal is poured via the nozzle and through a distribution bag into the liquid pool at the top of the bottomless mould. Both forced convection, induced by the incoming jet of liquid metal, and natural convection, generated by the temperature and/or solutal gradients, cause significant fluid motion in the liquid sump. The level of metal is kept constant in the mould by continually adding molten metal. The liquid is subjected to *primary cooling* by conduction of heat through the wall of the water-cooled mould and to *secondary cooling* through direct application of water to the solid shell as it emerges from the mould cavity. After the starting phase, the resulting solid ingot is lowered out of the bottom of the mould at a steady-state casting speed. For a given alloy, the position and shape of the liquidus and solidus isotherms with respect to the mould are dependent on such casting parameters as the superheat in the liquid metal, the method of introducing the metal into the liquid sump, the cooling spray configuration, and the casting speed. The liquid metal superheat, latent heat of fusion, and sensible heat released by the solid as it cools must all be conducted away from the ingot by the mould, the cooling sprays and finally the ambient air.

This process is semi-continuous: once the slab or billet has the desired length, which generally corresponds to the capacity of the furnace and to the depth of the casting pit, the casting is stopped and restarted when the metal and machinery are ready again. Casters have in recent years introduced two main improvements to the vertical semi-continuous casting process with regards to slab or billet quality:

- automation of the casting process, with control exercised over each and every parameter, even during the transient start-up phase. This ensures perfect reproducibility of operations,
- melt level in the mould is a particularly important process parameter since it has direct impact on thickness and structure in the region of contact between the mould and the liquid metal (the skin zone). Techniques have

been developed for melt level measurement which does not depend on physical contact, and for regulation.

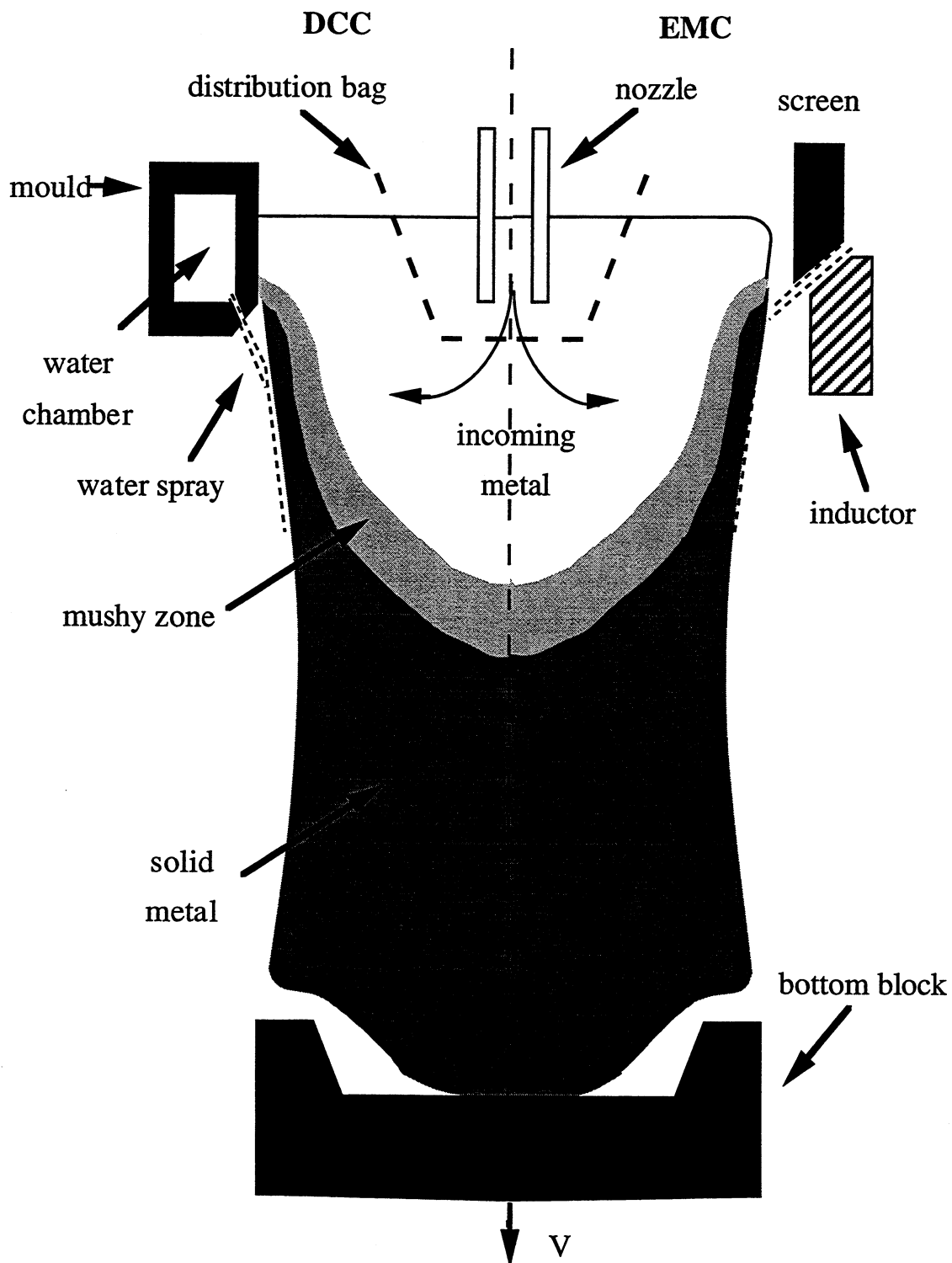


Figure 1.1: sketch (cross section) of the direct-chill (left) and electromagnetic (right) casting processes.

### 1.2.2 The electromagnetic (EM) casting process

Figure 1.1 (right side) is a sketch of electromagnetic casting (Russian type, [Evans]). This process is a radical means of resolving the question of contact

between the metal and the mould in that the latter is replaced by a magnetic field generated by an induction coil which maintains the shape of the melt while it solidifies. This absence of contact allows the surface state to be improved and highly diminishes the cortical zone, to less than 1 mm.

The EM casting technique was developed by the Russian, Z.N. Getselev [Emley], at the end of the sixties. This technique requires a high intensity current, about 6000 A, around the molten metal to confine it. The force capable of supporting the metal results therefore from the combination of the magnetic field created by the passage of the large current in the inductor and the induced electric current generated in the molten metal by the rapid oscillation of the same magnetic field. Whereas the irrotational part of the electromagnetic forces support the liquid metal against gravity at the periphery of the pool, the rotational part causes stirring. Consequently, it diminishes macrosegregation at the edges of the EM cast ingot by distributing more efficiently the alloying elements, and generates self-refinement of the grains by breaking the dendritic arms and forming new nuclei.

In the Russian type technique, an electromagnetic screen is inserted between the ingot and the inductor coil. Firstly, it assures the formation of a regular and linear film of cooling water around the ingot, and secondly, it attenuates the upper part of the magnetic field. Given that the metallostatic pressure in the molten metal decreases with the height, the magnetic force must follow this profile so that the meniscus is as vertical as possible. Otherwise, the force acting on the upper part of the molten metal will be too strong and will flatten the meniscus. It will be then impossible to cast correctly because the molten metal cannot be fed to the edges and corners and excessive leakage will result. The surface of the slab will also be very irregular, rendering it unusable for rolling. Much of the product of EMC is sheet ingot, i.e. of rectangular cross-section, that will subsequently be hot rolled, but there is significant production of rounds.

### **1.3 As-cast microstructure and ingot distortions**

#### **1.3.1 Refining, as-cast microstructure and segregation**

As a general rule, the mechanical properties of an aluminium alloy item are largely dependent on the grain size, which is directly linked to the number of nuclei available during solidification. Since the cooling techniques currently used are limited by the shape of the casting and by the nature and properties of the cast metal, it becomes hard to refine grain sizes by increasing the cooling rate. The solution most widely used is inoculation in the liquid phase. The

inoculants, which are small solid particles, act as preferential heterogeneous nucleation sites. The refiners most widely used by the aluminium industry are composed of Ti and B. The present trend is to limit as far as possible the addition of refiners because they are expensive and remain as foreign particles in the alloy and can give rise to defects during the subsequent transformations required to obtain the finished product. Another possibility to refine the grain size is magnetic stirring.

In DC casting, the solidification of aluminium alloys leads to the formation of columnar grains at the outer part of the ingot, i.e. the part of the ingot which has been in contact with the mould. In EM casting, these columnar grains do not exist due to the absence of mould. Because of this high degree of refining, the as-cast morphology of aluminium alloys at the inner part of the ingot consists in the presence of a large number of equiaxed globular-dendritic grains. The initial destabilisation of the grain surface has been stopped by the growth of the adjacent grains, thus leading to the formation of cauliflower-like crystals. In between these grains, eutectic compounds and intermetallic particles are found.

In the DC and EM casting, diffusion of substitutional impurities in solid aluminium is never complete and thus microsegregation is always present. On the other hand, due to convection, heterogeneities of concentration at the scale of the casting can also occur (macrosegregation). This segregation leads to non-uniform product performance, and can even result in product rejection. For example, the relative differences in concentration of some of the alloying elements in the interior region of the rolling slabs may be up to 20 %, which is considerably higher than the compositional tolerance limits of the aluminium alloys. Macrosegregation at and close to the surface (surface segregation) is a major cause of costly removal of an up to 20 mm thick surface layer before further processing [Mo1].

### **1.3.2 Ingot distortions and possible cracking**

The standard casting process, either DC or EM casting, of aluminium rolling sheet ingots, is generally divided into three distinct phases: the start phase, during which the temperature field, the solidification front, the ingot shape and the liquid metal-air interface (meniscus) change with time (non-stationary phase), the pseudo-stationary phase and the end phase during which liquid pouring is stopped and the ingot cools down. During all these stages, the ingot is subject to many distortions that arise as a consequence of coupled thermal and mechanical effects.

#### *Butt curl and swell*

During the start phase, the ingot experiences higher cooling rate than during the steady state regime. Indeed, at the start of the drop, the ingot butt is chilled both by the bottom block and by the mould. As the block is moved down, the ingot is also cooled down by the lateral water spray (see figure 1.2). This rapid chilling generates excessive thermal stresses which result in the bow of the first section of the ingot. This phenomenon is called "butt curl" [Yu,Droste]. Butt curl is a major problem [Emley] because it reduces the rigid standing of the ingot on the starter block and causes a portion of the ingot to loose thermal contact with the bottom block leading to possible shell remelting inside the mould and break-through of the melt due to a weak cooling of the solidified shell at the bottom [Grün1].

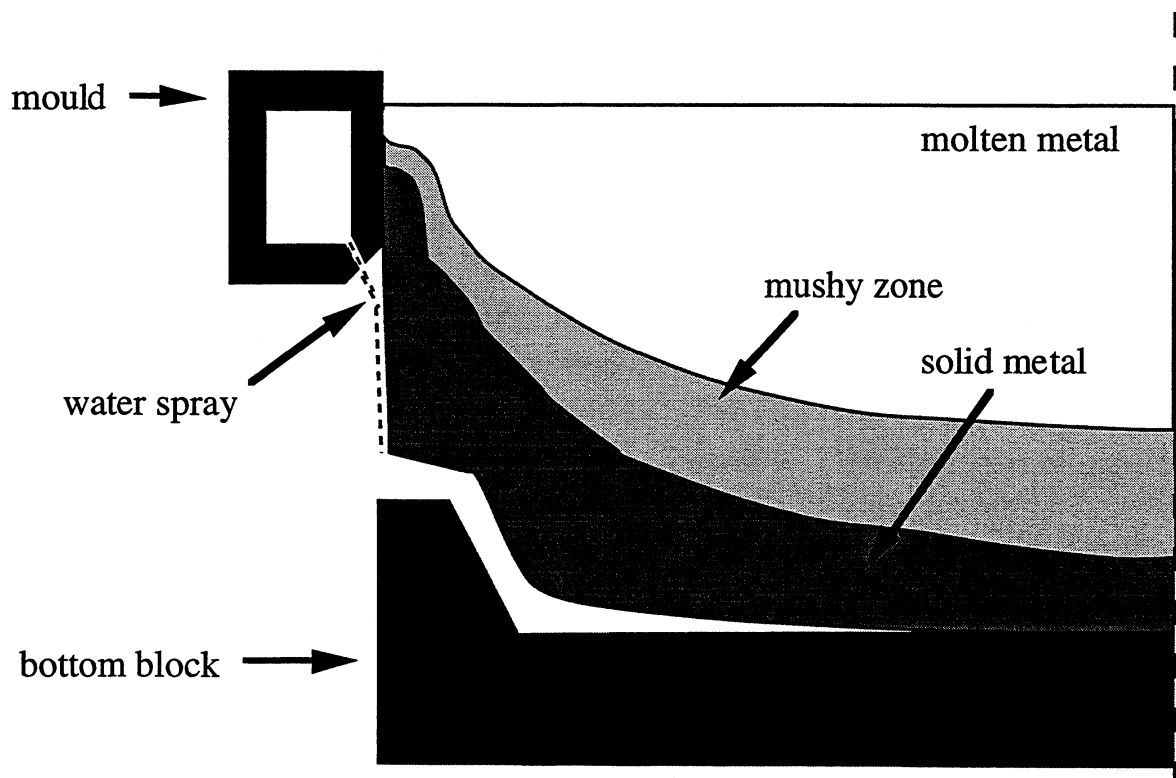


Figure 1.2: schematic representation of the butt-curl phenomenon during the start up phase.

Moreover, water can enter the gap between the starting block and the downside of the ingot: its rapid vaporisation may lead to a "bumping" of the ingot. Eventually, the thermally induced stresses and strains can form cracks and hot tears. Carrupt and Moulin [Carrupt] demonstrated that the decisive criteria in controlling butt curl is not its final value but its rate of evolution. Several solutions like injecting gaz  $CO_2$  into the cooling water system [Droste] or using pulsed water to diminish the cooling during start-up [Alu], were suggested to reduce butt curl. However, the start phase of DC casting of aluminium alloys still remains the most critical period of the process.

"Butt swell" is associated with a thicker section of the butt of the ingot as compared with the rest of the slab. During the start phase, the depth of the liquid pool is much smaller than during the stationary phase as a result of both the reduced casting speed and the partial cooling by the bottom block. Thus, the lateral solidification contraction is also reduced and the slab has nearly the same nominal dimensions as the mould (see figure 1.1). This situation is in fact similar to casting a metal in a permanent mould. On the other hand, once the starting phase is over, the sump deepens and the associated lateral contraction of the slab increases, about 40 mm for a 510 mm wide slab, i.e. about 9% in contraction [Drez1]. Therefore, although it looks as if the foot of the final slab had swollen, it is actually a reduced contraction caused by the thermal conditions during the start phase. This butt swell requires the ingot butt to be sawn before the remainder of the slab can be scalped.

#### *Steady-state inward pull-in of the rolling faces*

After about one meter of casting, a nearly steady-state regime is established for the thermal field. Under pseudo steady-state conditions, the solidified shell contracts inwards, i.e. towards the liquid pool (see figure 1.3, left side). This "pull-in" of the rolling faces is better noticeable after the ingot has cooled down (see figure 1.3, right side). Moreover, this contraction is not uniform throughout the ingot cross-section. If a rectangular mould/inductor is employed, the lateral faces of the resulting ingot are concave ("bone shape") as shown in figure 1.4. To compensate for the larger pull-in measured at the centre of the rolling faces, the sides of the mould are designed with a convex shape, usually with three linear segments [Drez1] (see figure 1.4). At the present time, the mould geometry is designed by a trial-and-error method. Each significant change, such as the alloy being cast, or the size of the ingot, requires considerable experimentation before an appropriate new casting procedure, starting block and mould can be adopted. Consequently, development time and costs are still very high, especially when ingots of large section are to be cast. Further, ingot butts have to be cut and ingot trunks scalped in order to conform to the dimensional tolerances required for the rolling procedure. The scalping operation is an expensive and delicate procedure, especially for large rolling sheet ingot formats, and the removed metal represents up to 10 % of the total ingot weight. In addition, depending on the alloy and ingot format, up to 8 % of the ingots develop cracks, either during casting or during subsequent cooling. Although this metal is re-cast, the additional energy required is a significant cost factor. Moreover the propensity of cracking limits the casting speed and as a consequence the productivity in the aluminium industry. The lack of procedures and practices to prevent distortions and cracking are a major obstacle in casting

the large hard alloys (7xxx serie) slabs with a width and a thickness larger than 1700 mm and 500 mm respectively.

*Ending phase*

At the end of casting, liquid metal is no longer poured and the descent of the bottom block is stopped.

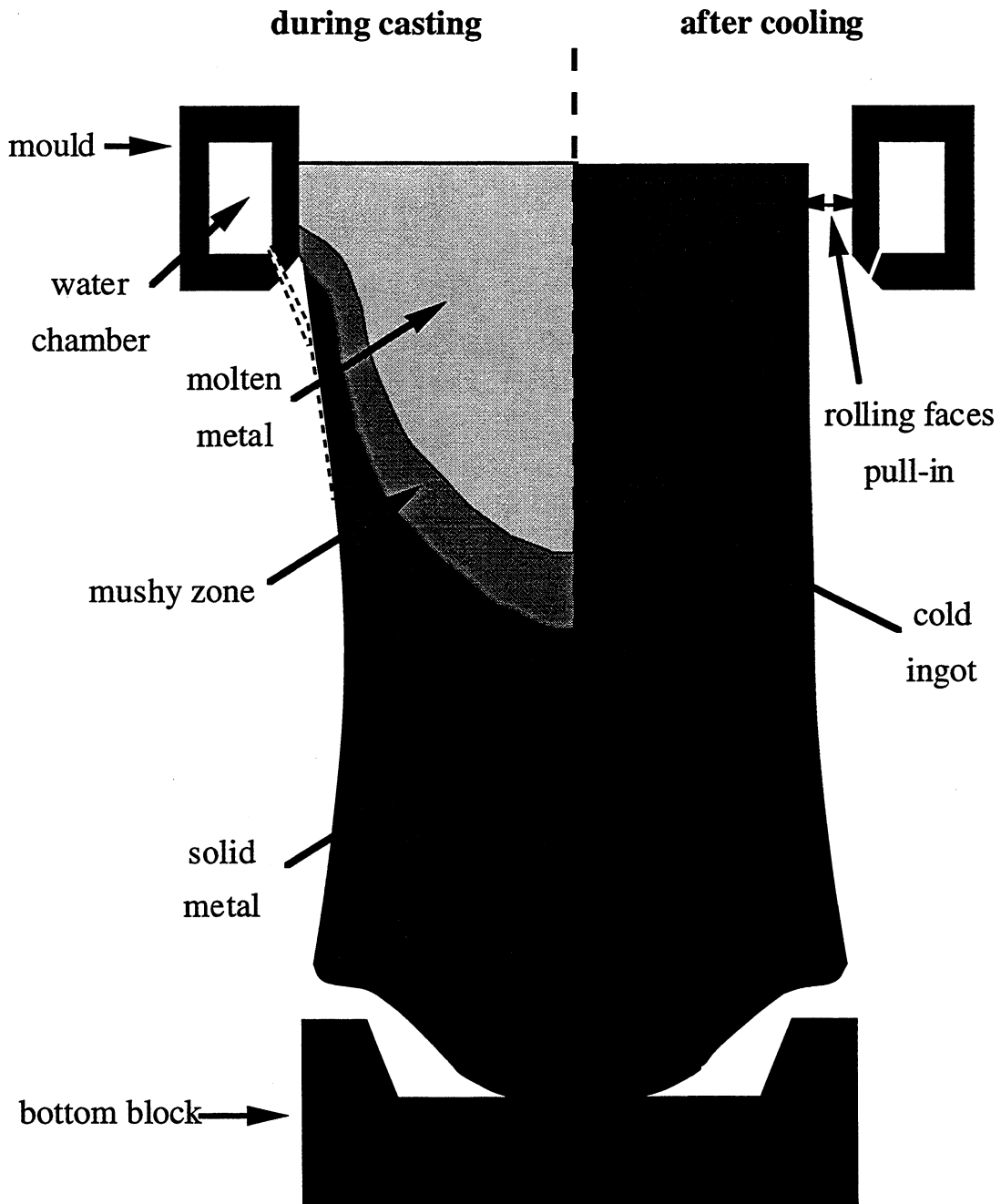


Figure 1.3: rolling faces pull-in during (left) and after (right) solidification.

As a result of this transient temperature evolution, the lateral faces pull-in is also reduced and the metal contraction is localised at the top of the ingot, leading to a large shrink cavity.

## **1.4 Motivations, objectives and layout of this work**

### **1.4.1 Motivations and objectives**

DC/EM casting methods offer the possibility of a wide range of variations in the as-cast microstructure through proper control of the casting conditions. The main limitations occurring in the process are:

- geometrical defects (butt curl and swell, rolling faces pull-in),
- hot tears and cold cracking,
- inhomogeneous distribution of the alloy elements (micro and macrosegregation).

These phenomena have a negative effect on production output, throughput time and cost. A general understanding of the mechanisms involved in the deformation of the metal is therefore of vital importance in reducing the time and cost factors associated with the mould/inductor bow design and optimising the casting process. With the development of powerful numerical methods and computers, mathematical models for the simulation of heat flow and stress generation in a solidifying piece, are a useful tool. Computer simulations are used to replace trial-and-error design procedures because of the reduced costs and time requirements in situations where testing is not feasible. They also provide much physical insight into the deformation process which cannot be observed in real time testing but can be used to help design new casting procedures. However, to make these computer simulations truly useful for the DC/EM casting process, a precise definition of the boundary conditions and of the material properties is required and the results must be first validated against measurements before optimisation of the process can be looked at.

The first objective of the present study has been to develop a thermomechanical model aimed at describing the stress generation in the solidifying ingot. However, due to the many parameters being involved in the DC/EM casting, these simulations heavily rely on experimental measurements. In addition, the thermomechanical properties of the cast alloys must be known up to, or even above the solidus temperature and the thermal boundary conditions associated with the lateral water jet have to be estimated through inverse modelling techniques. Once these values are determined, the results of the simulation must be compared with the experiments and thereafter, new casting procedures can be proposed and investigated. The present work focuses on the geometrical defects of the DC/EM casting with two goals:



- i) understand the basic mechanisms responsible for the non uniform lateral faces pull-in,
- ii) quantify the shape of the final cold ingot through numerical simulation and compare with experiments.

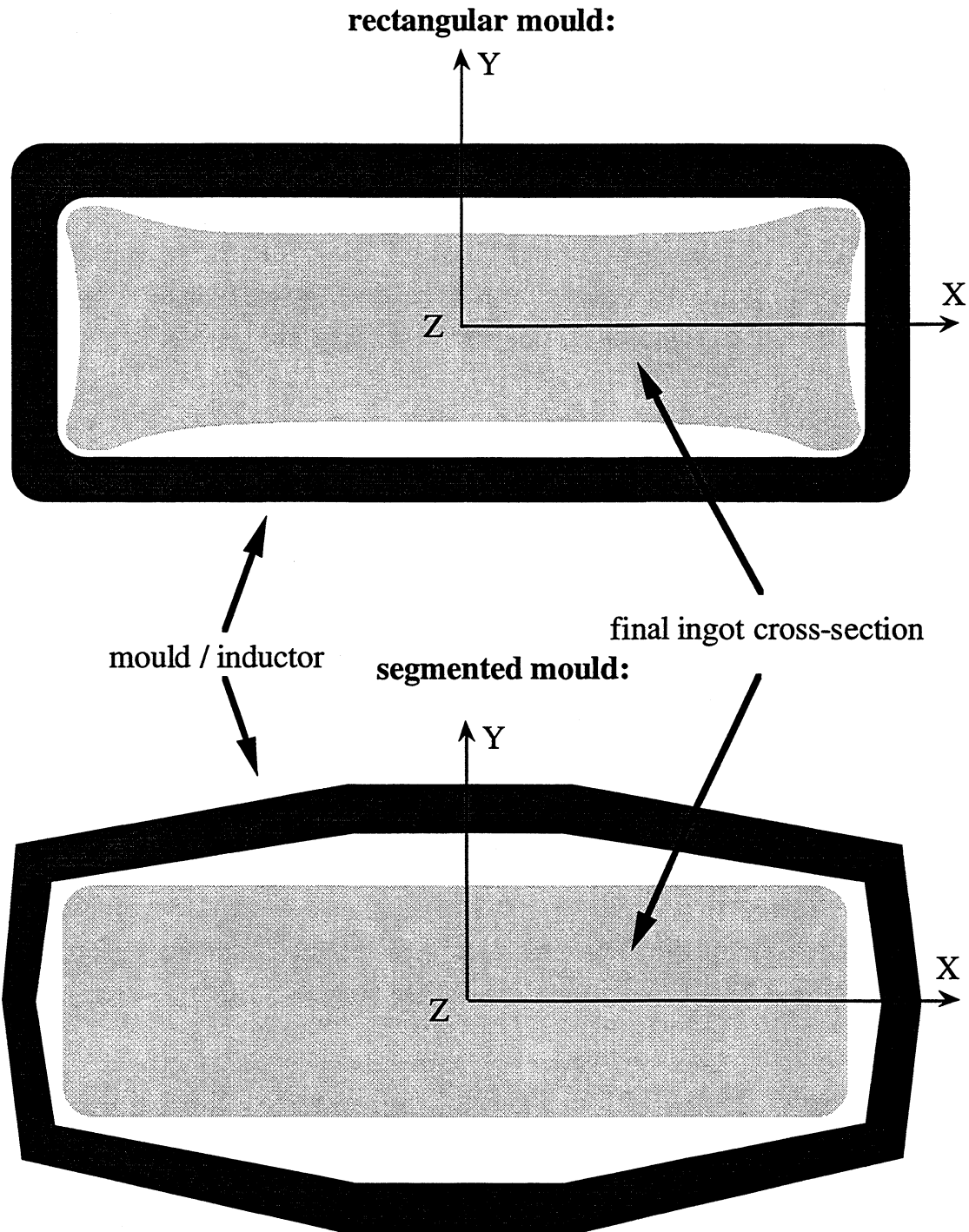


Figure 1.4: non-uniform contraction of the rolling faces and idealised optimisation of the mould shape.

To cope with the detrimental aspect of segregation in casting, the knowledge of the solidification path of the alloy is first required to investigate

the solute heterogeneities at the scale of the microstructure. Most of the microsegregation models do not consider the finite solute diffusion in the solid phase during the solidification whereas this back-diffusion plays a key role in determining the solidification path of the alloy. Moreover, the study of the solidification of industrial alloys demands the use of ternary or higher order equilibrium or non-equilibrium phase diagrams. The second main objective of the present work is to develop a microsegregation model taking into account the diffusion of solute species in the solid and liquid phases. This model is then coupled with phase diagram data so as to deduce the solidification path of industrial alloys.

To achieve these two objectives, existing theories, experimental investigations and numerical methods will be used, as shown in figure 1.5, in order to provide a better understanding of present practice and to suggest future improvements of the DC/EM casting processes. An essential step is the validation of the proposed models against measurements. The following activities have therefore been carried out :

- experimental investigation of the cooling conditions and distortions experienced by the rolling sheet ingot during DC and EM casting and after cooling in an industrial cast house,
- investigation of as-cast morphology and differential thermal analysis of two industrial aluminium alloys,
- determination of the heat extraction provided by the cooling system so as to define relevant thermal boundary conditions for the DC and EM casting processes,
- determination of the thermophysical and thermomechanical properties of two commercial aluminium alloys in the solid and mushy states,
- development and validation of a microsegregation model aimed at predicting the solidification path relevant for globular-dendritic microstructure,
- development and validation of a 2D/3D thermomechanical model,
- investigation of process improvements.

## 1.4.2 Layout of the thesis

The state of the art and the existing theories concerning the plastic behaviour of metals, the solidification microstructures and the thermo-mechanical models aimed at modelling the stress-strain generation in DC and EM casting are presented in chapter 2 (Theory and literature survey). Chapter 3 (Experimental) describes the full scale DC and EM casting experiments achieved at the experimental cast house of the Alusuisse company and other experiments carried out in the laboratory. Chapter 4 (Numerical methods) is devoted to the numerical models used in this work. They treat the solute diffusion, the heat conduction and the stress-strain development, and are either available through commercial packages or have been developed during this work. The results concerning the experimental investigations and the outcomes of the numerical models, as well as a discussion of all these results are presented in Chapter 5 (Results and discussion). The final conclusion sums up the main outcomes of the present work.

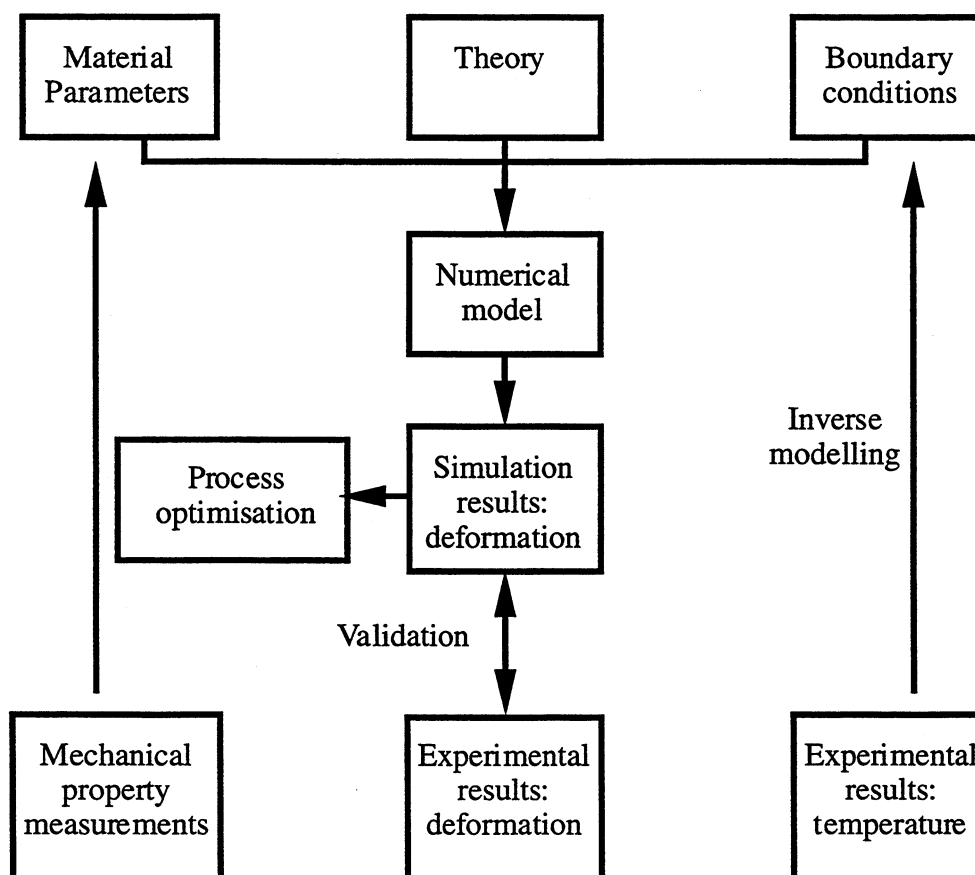


Figure 1.5: general structure of the present work.



## CHAPTER 2

# THEORY AND LITERATURE SURVEY

This chapter reviews the current theories and literature related to the subject of the present work. First, the solidification characteristics in DC/EM castings will be treated. Following is the mechanical behaviour of metals from room temperature to their melting point, with special attention to aluminium and its alloys. Eventually, the experimental investigations and the numerical models aimed at studying the DC/EM casting processes will be reviewed.

### 2.1 Solidification characteristics in DC/EM casting

#### 2.1.1 Solidification characteristics

The concept of solidification comprises the two basic phenomena: nucleation and growth of crystals from the melt [Flem1]. By lowering the temperature of a metal below its equilibrium liquidus temperature, solid becomes the thermodynamically stable form of matter and a transformation from liquid to solid starts. The rate of this process depends primarily on the rate of heat extraction from the system and the driving force for nucleation, as well as growth of crystals, is a function of the degree of undercooling  $\Delta T$  which is created during the solidification process relative to the equilibrium conditions. Nucleation determines the size and morphology of crystals formed from a melt. Many of the final properties of the cast product are determined by conditions under which the primary crystals are nucleated and start to grow.

#### *Structure development in continuous casting*

The freezing range of an alloy is generally represented by a phase diagram. A schematic binary phase diagram is shown in figure 2.1 [Flem1]. The liquidus line represents the temperature at which the liquid alloy begins to solidify, and the freezing process is complete when the solidus temperature is reached, if solidification occurs close to equilibrium conditions, or below the solidus under non-equilibrium conditions. When an alloy of uniform liquid composition  $C_0$  is cooled down, it begins to solidify when its temperature reaches the liquidus temperature  $T_1$ , if nucleation occurs readily. The composition of the solid that forms at  $T_1$  will be different from the composition of the liquid. The ratio of the solid to liquid compositions at a given temperature is called the solute distribution coefficient or partition coefficient  $k$  [Kurz]. In figure 2.1, the liquidus slope  $m$  and the coefficient  $k$  are assumed to be temperature-

independent and  $k$  is lower than unity. In this case, the excess solute rejected by the solid will give rise to a solute-rich liquid layer at the interface. As the alloy is cooled down further, the liquid composition increases. This increase, along with the lowering of temperature, gives rise to solute segregation patterns in the solid if the diffusion of solute in the solid is not very rapid. The build-up of solute in liquid (see figure 2.1) requires diffusion of solute in liquid for further growth. For efficient distribution of the solute in liquid, the interface may change its shape and usually becomes unstable (dendritic growth). Thus the actual solute segregation pattern is dictated by the shape of the interface. In addition to the solute transfer, the interface shape is governed by the more or less effective removal of the latent heat of fusion.

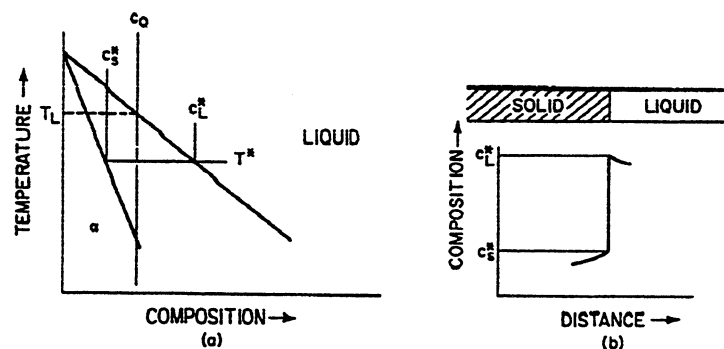


Figure 2.1: solidification of an alloy with equilibrium at the liquid-solid interface, (a) phase diagram, (b) composition profile across the interface [Flem1].

Two distinctly different heat flow conditions exist in continuous casting [Bäck]. In the first case, the temperature gradients in the liquid and the solid are positive such that the latent heat generated at the interface is dissipated through the solid. Such a temperature field gives rise to directional solidification (constrained growth) and results in the columnar zone in a casting, as illustrated in figure 2.2. In the second case, an equiaxed zone exists if the liquid surrounding the solid is undercooled so that a negative temperature gradient is present in the liquid at the interface (unconstrained growth). In this case the latent heat is dissipated through the liquid. Such a thermal condition is generally present at the centre of the cast ingot (see figure 2.2). The principal difference in the two growth modes is that in constrained growth, diffusion of heat and solute atoms from the solid/liquid interface occurs in opposite directions, while the two diffusion processes occur in the same direction in the case of unconstrained growth. However, if nucleation is very effective, “equiaxed” grains can also form in a positive thermal gradient, as shown by Rappaz et al. [Rap3].

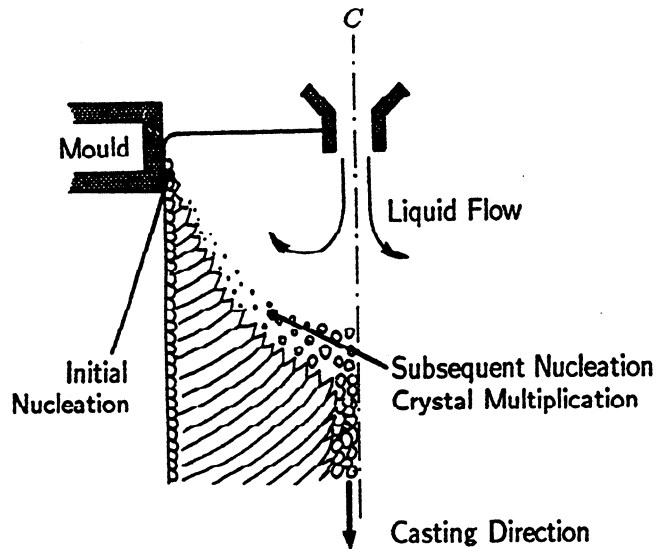


Figure 2.2: origin of crystals in continuous casting [Bäck].

A positive temperature gradient in the liquid at the interface gives rise to a planar solid/liquid interface for pure metals. However, for alloys, the shape of the interface is dictated by the relative magnitude of the interface velocity and the temperature gradients in the solid and liquid at the interface [Flem1,Kurz]. For given temperature gradients and composition, four different interface morphologies can exist depending on the velocity. Below some critical velocity, a planar solid/liquid interface will be present and above this velocity, the planar interface becomes unstable and forms a cellular, a cellular dendritic, or a dendritic interface. For the heat flow condition in which the solid grows in an undercooled melt, a dendritic structure develops both for pure metals and alloys.

### *Growth undercooling*

Crystals grow at a temperature somewhat below that predicted by the equilibrium phase diagram, as represented in figure 2.1. Depending on the rate of heat extraction and on the constitution of the alloy, the morphology of the crystal (columnar, cellular or dendritic) develops in a unique manner. The balance between heat and solute diffusion and the interface stability conditions determine the effective radius of the crystal tip. The actual undercooling of the growing crystal tips,  $\Delta T$ , can be expressed as a sum of the major components [Kurz],  $\Delta T = \Delta T_s + \Delta T_r + \Delta T_k + \Delta T_t$ , where  $\Delta T_s$  is caused by the diffusion layer of solute around the tip,  $\Delta T_r$  expresses the undercooling due to surface energy,  $\Delta T_k$  is the interface kinetic term of atom attachment which is generally small for metals and  $\Delta T_t$  is the thermal undercooling that is zero for constrained growth. In continuous casting of aluminium alloys, the solute build up ahead of growing crystals is the dominant factor determining the growth undercooling.

### *Grain refining and resulting microstructure*

Close control of the cast structure is a major requirement in the production of high-quality aluminium products. In continuous casting, columnar grains are particularly detrimental and must be confined to the skin of the ingot, the thickness of which being the smallest. A fine-grained structure provides a number of technical and economical advantages, including improved and more isotropic mechanical properties, increased casting speed, reduced ingot cracking tendency and better mechanical deformation characteristics. The addition of nucleating agents prevents columnar growth by raising the nucleation temperature so that new crystals may form ahead of the solidification front, as illustrated in figure 2.3 [Bäck]. Al-Ti-B master alloys are extremely effective grain refining agents and are therefore commonly used. Mohanty and coworkers [Moha] studied the mechanisms of grain refinement in aluminium alloys. They showed that, on addition of Al-Ti-B master alloys,  $TiB_2$  particles act as inoculant to form a thin layer of  $Al_3Ti$  on which Al nuclei can grow epitaxially. The cast structure becomes equiaxed almost throughout the casting, with a fine grain size. The density of nucleation sites is so high that for commercial purity alloys, when the spherical solid/liquid interface starts to destabilise, the impingement of solute layers of neighbouring grains occurs at an early stage thus leading to spherical or globular microstructure. Moreover, effective grain refiners prevent the occurrence of twinned crystal growth or “feathery grains” in continuously cast ingots [Bäck].

The surface quality of DC/EM cast aluminium ingots is often reduced by a segregated layer of exudations. Compared to the nominal composition of the alloy, the surface layer is considerably enriched, thus leading to edge cracking during hot rolling of the slabs. This exudated layer is caused by interdendritic melt through the mushy zone driven by the pressure drop due to the air gap formation between the partly solidified shell and the mould [Mo1]. The removal of this surface layer before further processing of the slab leads to considerable costs.



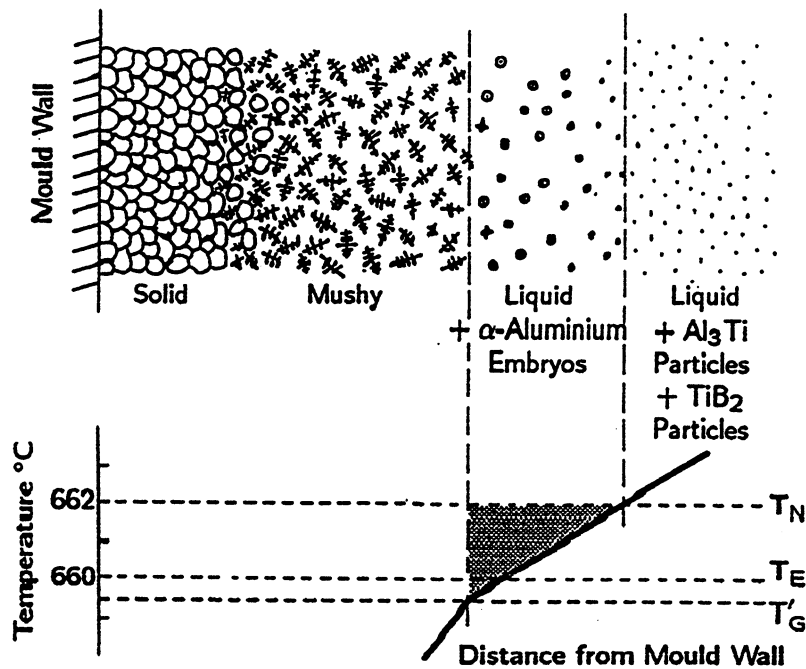


Figure 2.3: representation of solidification and temperature profiles in a DC-casting of commercially pure aluminium, to which an effective grain refiner has been added [Bäck].

### 2.1.2 Microsegregation models

The different solubilities of a solute element in the liquid and solid phases, together with differences in mobility, lead to the spatial concentration variations at the scale of the microstructure known as microsegregation. Variations at the macroscopic level, i.e. at the level of the whole casting, is called macrosegregation, usually induced by fluid and crystals flow. Because these segregations generally deteriorate the physical and chemical properties of materials, they both should be kept to a minimum.

#### *Solidification under equilibrium conditions: the lever rule*

According to the thermodynamic equilibrium phase diagram, solidification of an alloy starts at the liquidus temperature and ends at the solidus or eutectic temperature depending on the solubilities and concentrations of the alloying elements. Under the equilibrium conditions where diffusion in solid and liquid is complete and no undercooling of any kind (no nucleation barrier, no curvature effect, etc) occurs at the interfacial liquid/solid (local equilibrium hypothesis), the compositions of both solid and liquid adjust during cooling in accordance with the phase diagram so that the final solid has the same composition of the original melt. In this case, no microsegregation has developed and the liquid composition  $c_l$  during solidification is given by the so-called lever rule [Flem1]:

$$c_l = \frac{c_0}{[1 - (1-k) f_s]} \quad (2.1)$$

where  $k$  is the constant distribution coefficient and  $c_0$  the nominal composition of the alloy. In case  $c_0$  is greater than the maximum solubility of the solute element in the primary phase, the fraction of eutectic is given by:

$$f_{\text{eut}} = \frac{c_0 - k c_{\text{eut}}}{(1-k) c_{\text{eut}}} \quad (2.2)$$

Generally, for a system containing  $N$  alloying elements at nominal composition  $c_{0i}$  and under the assumption of constant partition coefficients and liquidus slopes, the liquidus surface is defined by:

$$T = T_m + \sum_{i=1}^N m_i c_{li} \quad (2.3)$$

where  $T_m$  is the melting point of the pure metal,  $c_{li}$  the liquid concentration of element  $i$ , and  $m_i$  the corresponding slope of the liquidus. Before reaching a eutectic valley or an invariant point, the temperature and solid fraction are linked by:

$$T = T_m + \sum_{i=1}^N \frac{m_i c_{0i}}{1 - (1-k_i) f_s} \quad (2.4)$$

where  $k_i$  is the constant partition coefficient of element  $i$ . After solidification ( $f_s=1$ ), the solute composition is designated  $c_{0i}$  and no microsegregation occurs. In actuality, however, equilibrium solidification rarely takes place, because the solute diffusion is not so rapid in the solid phase.

### *Scheil's model*

It has long been recognised that during cooling under usual casting conditions, solidification of metallic alloys does not obey the equilibrium lever rule, mainly because of effective solid and liquid diffusion of the present solute atoms. Gulliver [Gul] and Scheil [Scheil] were the first to propose a model to describe solute redistribution under non-equilibrium solidification conditions. Solidification is described inside a closed volume element, which must be large enough to be representative of the mushy zone, but small enough to have a homogeneous temperature. The minimum size is one dendrite in columnar growth and one grain in globular equiaxed growth. The hypotheses of the Scheil's model are the same as for the lever rule, except for solid-state diffusion.

In this model, one assumes that the solute profile in the solid phase is totally “frozen”, i.e. there is no solute diffusion in the solid.

A variation  $df_s$  of the solid fraction leads to a rejection  $(c_{li} - c_{si}^*)$  of solute  $i$  in the liquid, where  $c_{li}$  is the solute content in the liquid and  $c_{si}^*$  the solute content at the interface in the solid. This solute amount has to redistribute in the liquid, which leads to the following mass balance :

$$(c_{li} - c_{si}^*) df_s = (1-f_s) dc_{li} \quad (2.5)$$

Using the local equilibrium hypothesis, one has  $c_{si}^* = k_i c_{li}$ , where  $k_i$  is the partition coefficient for solute  $i$ . This equation may be anatically integrated if the partition coefficient is assumed to be constant. The integration is performed starting at the liquidus temperature, when the liquid is at the nominal composition  $c_{0i}$  and leads to:

$$c_{li} = c_{0i} (1-f_s)^{k_i-1} \quad (2.6)$$

With the help of the equation 2.3, the corresponding temperature can be derived:

$$T = T_m + \sum_{i=1}^N m_i c_{0i} (1-f_s)^{k_i-1} \quad (2.7)$$

In case the liquidus slopes  $m_i$  and the partition coefficients  $k_i$  are temperature or composition dependent, the mass balance given by equation 2.5 can be numerically integrated. Whatever is the nominal composition of the alloy and for partition coefficients less than one, the solute contents of the residual liquid tend to infinity at the end of the solidification and must be physically limited. When the composition reaches an invariant point of the diagram, the model predicts that solidification ends abruptly. In case the system reaches a eutectic point in a binary system, the final amount of eutectic according to the model,  $f_{eut}$ , is given by replacing the liquid composition with the eutectic composition,  $c_{eut}$  in equation 2.6:

$$f_{eut} = \left( \frac{c_{eut}}{c_0} \right)^{\frac{1}{k-1}} \quad (2.8)$$

Lacaze [Lac] pointed out that, when experimental cumulative distribution curves of solute are compared with the calculated Scheil distribution, important discrepancies appear. It is generally observed that the minimum concentration is higher than the expected value of  $k_i c_{0i}$  for  $k_i$  less than one. For higher solid fraction, the experimental curves show a much higher solute content in the solid

than the calculated one, until they cross the Scheil curve. Finally, the actual eutectic fraction is smaller than the predicted one. Some of the improvements made to the Scheil model to account for these discrepancies are described in the following sections.

### *Effect of solid state diffusion on microsegregation*

Brody and Flemings [Bro1] were the first to account for diffusion in the solid during solidification of a binary alloy. In their simple model, they approximated the solute concentration gradient at the solid/liquid interface and derived the following approximate solution by assuming that the local interface is flat (one dimensional or plate-like geometry) and advances with a constant growth rate<sup>1</sup>. For a binary alloy, this gives:

$$c_s^* = kc_0 \left(1 - \frac{f_s}{1 + \alpha k}\right)^{k-1} \quad (2.9)$$

In this equation,  $c_s^*$  is the solute concentration in the solid at the solid/liquid interface and  $\alpha$  is the diffusion Fourier number. This parameter is a measure of the extent of diffusion of solute in the solid and is defined as:

$$\alpha = \frac{D_s t_f}{\lambda_2^2} \quad (2.10)$$

where  $D_s$  is the solute diffusivity in the solid,  $t_f$  the local solidification time and  $\lambda_2$  one-half of the characteristic dendrite arm-spacing. Like the parameter  $k$ ,  $\alpha$  is assumed to be constant during solidification. However, this model overestimates back-diffusion and Clyne and Kurz [Cly] showed that its applicability was limited to  $\alpha k < 1$ . They proposed to replace  $\alpha$  in the analytical expressions of  $c_s^*$  by a heuristic expression  $\gamma$  which depends on  $\alpha$  and varies from 0 to 1 when  $\alpha$  goes from 0 to infinity :

$$\gamma = \alpha [1 - \exp(-1/\alpha)] - 0.5 \exp(-1/2\alpha) \quad (2.11)$$

The important analysis of Clyne and Kurz is that it includes all cases from no diffusion ( $\gamma = 0$ ) to complete diffusion ( $\gamma = 0.5$ ) in the solid thus giving the Scheil and lever rule equation, respectively. One key problem of the above approach is the choice of the characteristic dimension  $\lambda_2$  to be used in calculations, because predictions are very sensitive through the parameter  $\alpha$ . Very recently, Kobayashi [Kob] derived an analytical solution for the one

---

<sup>1</sup> The equations were also derived assuming a parabolic growth, see [Bro1].

dimensional solidification problem assuming parabolic growth. With an infinite serie of confluent hypergeometric functions, Kobayashi obtained a solution to the diffusion equation. However, in order to obtain a calculated result for the cases when  $k < 0.3$  and  $\alpha < 1$ , one has to evaluate as many as 11000 terms in the infinite serie.

### *Effect of solute build-up in the liquid*

Very few analytical expressions were derived to take into account the finite solute diffusivity of alloying elements in the liquid phase, because diffusion in the liquid is much faster than in the solid at the scale of  $\lambda_2$ . Nevertheless, the evaluation of the solute build-up in front of the solidification front is necessary in order to estimate the tip undercooling. As pointed out by Giovanola and Kurz [Giov], this is a rather difficult task because the description of the overlapping diffusion fields in the liquid and of the development of dendrite arms is extremely complicated. However, the stationary solute diffusion field around a parabolic dendrite tip has been calculated by Ivantsov [Ivan,Kurz]. Assuming a paraboloid of revolution to approximate the real dendrite tip shape, the supersaturation  $\Omega$ , which expresses the solute build-up in the liquid in front of the interface, is given as a function of the solutal Péclet number  $P_c$ :

$$\Omega = \frac{c_l^* - c_0}{c_l^* - c_s^*} = P_c \cdot \exp(P_c) \cdot E_1(P_c)$$

$$\text{with } P_c = \frac{VR}{2D_l} \quad (2.12)$$

where  $R$  is the dendrite tip radius,  $V$  the growth rate,  $D_l$  the liquid diffusivity and  $E_1$  the exponential integral function<sup>1</sup>. Equation 2.12 does not give the operating point of the dendrite tip since, for a given supersaturation or Péclet number, the solution is a function of the product  $RV$ . The marginal stability criterion [Kurz] allows to determine the dendrite tip radius  $R$  and therefore the growth rate  $V$  of the dendrite. Giovanola and Kurz [Giov] have also derived a relation for segregation during rapid solidification, arguing that in this case, the assumption of complete diffusion in the liquid is no longer valid, especially near the dendrite or cell tip. Neglecting solid state diffusion, they proposed a model in which the solid fraction is assumed to be a second order polynomial of  $c_s^*$

---

<sup>1</sup>  $E_1(x) = \int_x^\infty \frac{\exp(-z)}{z} dz$

from the tip to a solid fraction  $f_x$ . The solid concentration at the dendrite or cell tip is a function of the supersaturation  $\Omega$  and is given by equation 2.12. For solid fractions larger than  $f_x$ , the segregation is described by the Scheil's model (equation 2.6).

### *Numerical models*

Numerical simulation of solidification may be helpful to improve the description of the solidification process, e.g. the undercooling of the dendrite tip, to predict solute distribution in the solid and liquid phases and to account for variations of the partition coefficient and of the diffusivity. Different geometry and characteristic lengths were adopted to model the microsegregation during solidification of alloys. In the case of well-developed dendritic microstructures, some authors, [Bro1,Kir], chose a size of the volume element based on the average secondary arm spacing. For alloys with less developed dendritic columnar structure, the size of the volume element to be considered is closed to the primary spacing. Matsumiya et al. [Matsu] assumed that columnar dendrites form with a regular hexagonal arrangement of their centres. Microsegregation in a binary alloy solidified in the form of deep cells, assumed to be cylindrical, was predicted by Dean et al. [Dean] using a finite difference model which takes into account solid state diffusion and flow of liquid between cells driven by solidification shrinkage. The authors found that intercellular fluid flow exerts a small, but discernible, influence on micro-segregation and cell shape. All of these numerical models assumed no undercooling, and particularly no tip undercooling, and equilibrium at the interface, with the partition coefficient given by the phase diagram. Except for the model of Matsumiya [Matsu] which calculates diffusion in the liquid phase, it was assumed in all cases that the liquid phase is chemically homogeneous.

Different numerical techniques were used to deal with the problem of solid and/or liquid state diffusion in an expanding domain: Ganesan and Poirier [Gan] proposed an implicit Crank-Nicholson method and most of the numerical work concerning microsegregation was performed using a finite difference technique. Bohner [Bohn] and Matsumiya et al. [Matsu] solved the diffusion equations in a similar fashion: the interface is moved in discrete jumps from one node to the next in a fixed mesh and the time increment required for that jump is calculated from solute diffusion and heat transfer parameters. This technique is known as the "jumping nodes technique". Halder et al. [Halder] and Roosz and Exner [Roosz] took into account in their one dimensional numerical model the effect of dendrite arm coarsening on the solute diffusion, thus considering the time-dependence of  $\lambda_2$  (typically,  $\lambda_2 \approx t^{0.33}$ ). They studied the solidification path of a

large number of compositions in the aluminium-rich corner of the Al-Cu-Mg system and represented the microstructural constituents (primary crystals, binary eutectic mixture and ternary eutectic) in so-called “restricted-equilibrium phase and microstructure diagrams”. To preserve solute balance when dendrite arm coarsening is taken into account, Kirkwood [Kir] proposed a modified version of the Brody-Flemings model where liquid of nominal composition,  $c_0$ , is added to compensate for size change of the volume element, thus diluting the liquid but maintaining the average composition. Another possibility is to add some extra liquid at the composition of the existing liquid, but this procedure will not conserve the solute content [Flem1].

Element distribution and microstructural features in dendritically solidified binary and ternary alloys were addressed by Rettenmayr [Ret]. This author developed an implicit finite difference model to compute the solute diffusion in the solid and liquid phases and pointed out that the strong dependence of the partition coefficient with temperature and other element concentrations necessitates an accurate description of phase equilibria.

Thévoz et al. [Thé1] and Rappaz et al. [Rap1] proposed a numerical model of solute diffusion at the scale of a grain for equiaxed solidification of dendritic alloys. These authors assumed complete solute mixing within the interdendritic liquid, no back-diffusion in the solid, spherical diffusion around the grain, and dendrite tip kinetics of an isolated dendrite, as shown in figure 2.4. Using an explicit time-stepping scheme, the authors solved the coupled equations at the scale of a dendritic grain whose final size is given by a nucleation law. This microscopic model served as a basis for a general micro-macroscopic numerical code aimed at modelling the solidification of alloys and named 3-MOS [Thé2]. In their overview of solute diffusion models, Thévoz and Rappaz [Thé3] presented a common approach to model the growth of a single equiaxed grain in different microstructures, fully dendritic, globulitic and nodular cast iron. The corresponding schematics of the solute profiles are shown in figure 2.5. Recalescence during solidification of aluminium alloys and final grain sizes could be obtained with such models.

Finally, an exhaustive review of the solute segregation models has been made by Battle [Batt]. It was noticed by many authors that discrepancy between computed solute distribution and experimental results could be due to a bad knowledge of the effect of temperature and composition on the solute diffusion and partition coefficient. A coupling with the calculated phase diagram seems to be a prerequisite to a correct modelling of microsegregation. The problem of the complex geometry of the solid-liquid interface can also be raised. Eventually,

the solute distribution in globular equiaxed grains, as produced in EM/DC casting, has not been investigated.

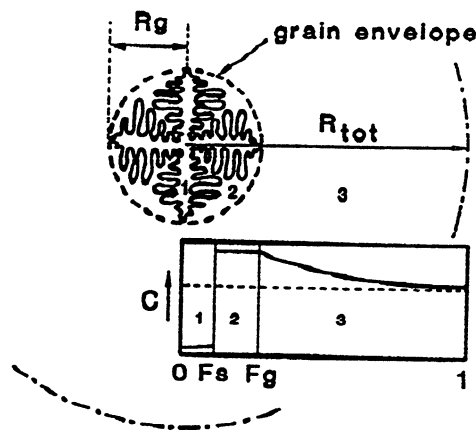


Figure 2.4: schematic representation of the diffusion model of Thévoz and Rappaz for equiaxed dendritic solidification, region 1: solid phase; region 2: interdendritic liquid and region 3: free liquid around the grain envelope [Thé1].

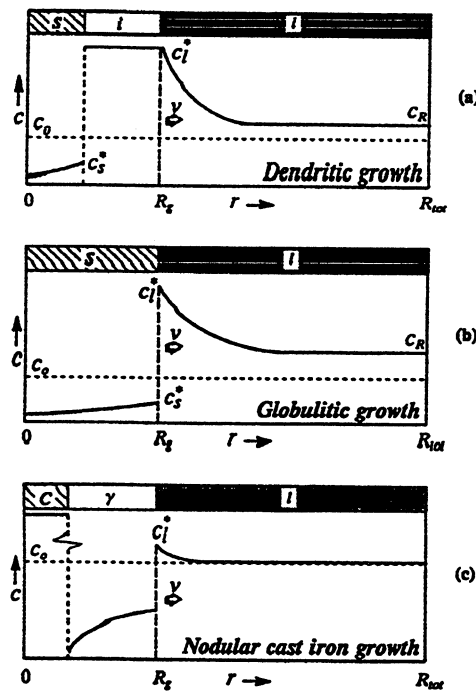


Figure 2.5: schematics of the solute profiles associated with dendritic (a), globulitic (b) and nodular cast iron (c) structures [Thé3].

### 2.1.3 Solidification paths in multi-components alloys

Since iron and silicon are common impurities in commercial purity aluminium (1xxx series, i.e grades of alloys containing up to 1% impurities or minor additional elements), the phase equilibria in the Al-rich corner of the Al-Fe-Si system has been intensively investigated by many authors and a



compilation of all this work was recently published by Petzow and Effenberg [Petzow]. Figure 2.6 shows the equilibrium liquidus surface of the aluminium-rich corner of the Al-Fe-Si system. The domain for primary precipitation of the aluminium solid solution phase  $\alpha$ -Al is limited by those of the compounds  $\text{Al}_3\text{Fe}$ ,  $\alpha$ -AlFeSi or  $\tau_5$  ( $\text{Al}_{7.4}\text{Fe}_2\text{Si}$ ),  $\beta$ -AlFeSi or  $\tau_6$  ( $\text{Al}_9\text{Fe}_2\text{Si}_2$ ), and Si. The iron content is kept low in order to obtain good corrosion resistance and to avoid the formation of large brittle  $\text{Al}_3\text{Fe}$  particles. The intersection of the  $\alpha$ -Al domain with the domain of one of this compound defines a line which corresponds to a monovariant reaction between the liquid, the  $\alpha$ -Al phase and the corresponding compound. The nature of these monovariant lines is eutectic in the present system. The intersection of three monovariant lines gives birth to two peritectic reactions (points  $U_{10}$  and  $U_{11}$  in figure 2.6):



and one ternary eutectic reaction (point  $E_1$  in figure 2.6):



The solid solubility of Si in aluminium is relatively large, its maximum being 1.65 wt.% at  $577^\circ\text{C}$ . On the other hand, the solubility of iron in aluminium is very small, less than 0.05 wt.%. In this ternary system, the liquidus surface is nearly a plane, i.e. the liquidus slopes can be considered as constant. Furthermore, the partition coefficients do not greatly depend on composition.

The solidification kinetics during a monovariant reaction can be predicted using an appropriate extension of the Scheil's model [Flem1]. The zero diffusion in the solid state prevent any peritectic reactions and when the solidification path, i.e. the alteration in the liquid composition as the alloy solidifies, strikes the line of twofold saturation, the binary eutectic  $\alpha$ -Al +  $\text{Al}_3\text{Fe}$  forms and grows as the liquid composition moves along the monovariant line  $e_{11}$ - $U_{10}$  (see figure 2.6) to the first peritectic temperature  $632^\circ\text{C}$ . At this temperature, just as the analogous binary case, the phase  $\text{Al}_3\text{Fe}$  stops forming and in place the phase  $\tau_5$  forms until the peritectic point  $U_{11}$  is reached. Thus the binary eutectic  $\alpha$ -Al +  $\tau_5$  forms between  $632^\circ\text{C}$  and  $613^\circ\text{C}$  and the binary eutectic  $\alpha$ -Al +  $\tau_6$  forms between  $613^\circ\text{C}$  and the ternary eutectic temperature  $573^\circ\text{C}$ . At  $573^\circ\text{C}$ , the remaining liquid solidifies as a ternary eutectic. On the other hand, in order to determine correctly the position on the liquidus surface corresponding to complete solidification, back diffusion behind the solidification front still has to be considered, otherwise residual liquid will always reach a point on a monovariant line or at the ternary eutectic point. For that purpose, the

knowledge of the change with composition of the partition coefficients, of the diffusion coefficients and of the liquidus surface are necessary prerequisites to make calculations and this information can be provided by softwares for thermodynamic calculations coupled with appropriate databanks. Thermo-Calc [The] is one example.

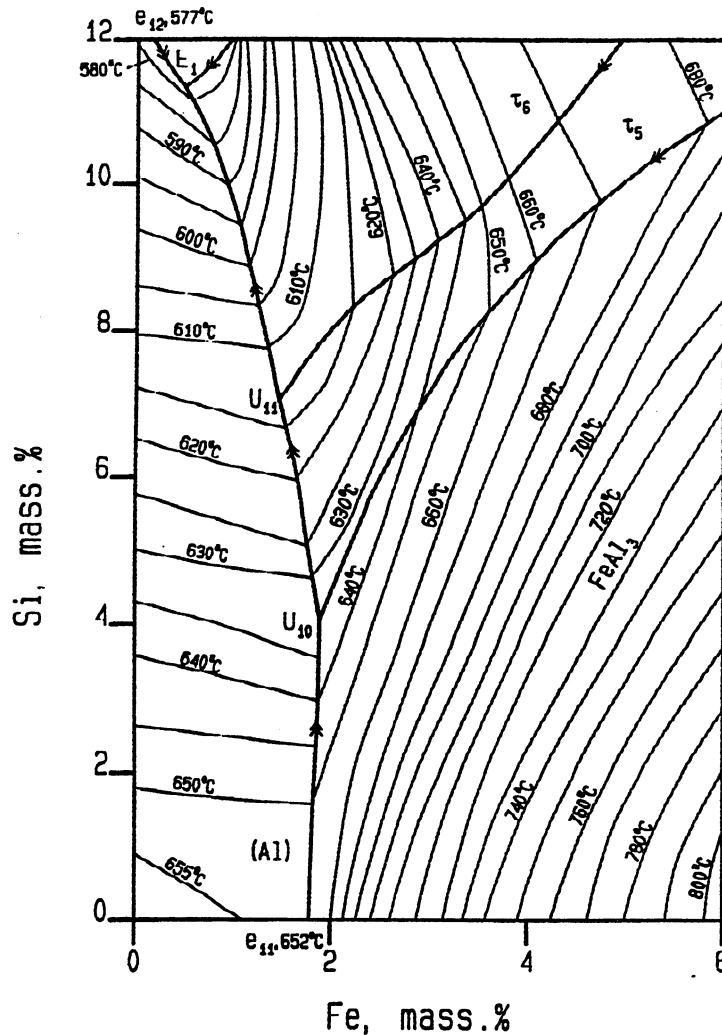


Figure 2.6: liquidus surface of the Al-rich corner of the Al-Fe-Si equilibrium phase diagram [Petzow].

Langsrud [Lan1] clearly demonstrated that the equilibrium phase diagram as shown in figure 2.6 fails to predict the variation in the phase distribution that is observed across a DC-cast rolling slab due to high and different cooling rates, from 0.5-1°C/sec in the centre of the slab to approximately 5-10°C/sec at the surface of the ingot. The metastable Al<sub>6</sub>Fe, Al<sub>x</sub>Fe, and Al<sub>m</sub>Fe phases are observed at high cooling rates [Bäck], thus indicating the need of a “metastable phase diagram” in which the phase fields of these compounds appear. According to Langsrud, the solidification rate influences the nucleation and growth kinetics of solid phases, thereby causing a shift of phase boundaries and peritectic/eutectic points towards lower Si-concentrations and higher Fe-

concentrations. These observations were accounted for by assuming a cooling-rate-dependent displacement of phase boundaries and triple points as indicated in figure 2.7.

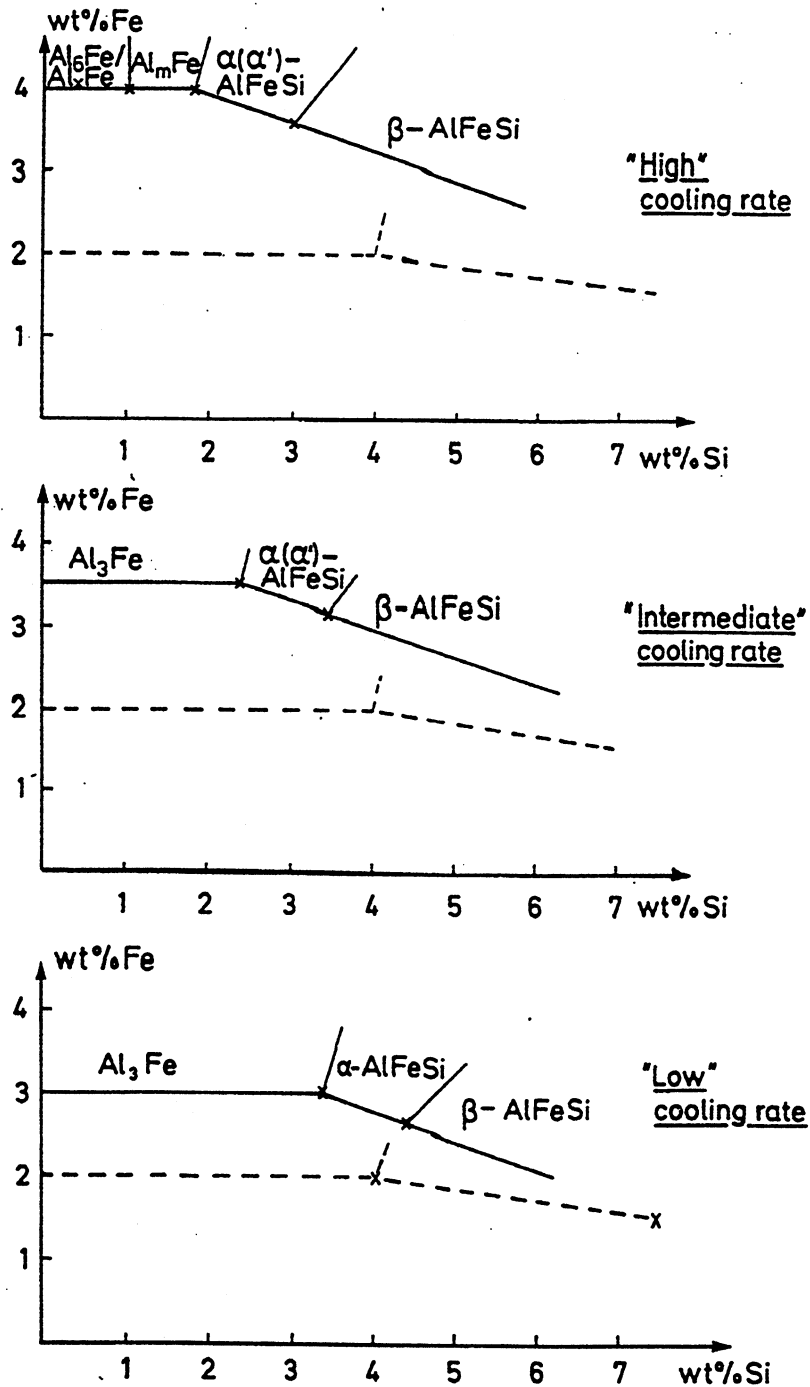


Figure 2.7: metastable Al-Fe-Si liquidus surfaces as suggested by Langsrud [Lan1]. The stable liquidus surface is represented with dotted lines.

Including these metastable phase diagrams in the software Thermo-Calc and assuming that peritectic reactions are completely suppressed due to the high cooling rates encountered in DC-casting, i.e. that the phases observed in the materials are always precipitated from the liquid, Langsrud et al [Lan2]

developed a model, named Alstruc, for the calculation of as-cast microstructures in DC-cast 1xxx, 3xxx, and 6xxx-series alloys. They calculated the phase distribution using the Clyne and Kurz model [Cly] and compared their results with observed phase distribution in DC-cast ingots. Tromborg et al [Tro] applied the same methodology to study the solidification path of 3xxx-series alloys with the more complicated rate-dependent Al-Fe-Si-Mn-Mg quinary phase diagram. These authors compared the calculated amount of elements in solid solution with measurements of electrical resistivity using the fact that this quantity increases linearly with the solute contents in the aluminium solid solution.

## **2.2 Mechanical behaviour of metal related to solidification**

When solidifying, aluminium alloys contract as do most metal [Camp]. There are three quite different contractions to be dealt with, as illustrated in figure 2.8. As the temperature reduces, the first contraction to be experienced is that in the liquid state, leading possibly to natural convection. Afterwards comes the contraction on solidification which is due to the rearrangement of the atoms in a regular close-packed (face-centred-cubic for aluminium) crystalline array. The solidification shrinkage is estimated to be around 7 % for pure aluminium [Camp,Mond,Hatch]. The possible insufficient metal feeding to compensate for this contraction often leads to shrinkage porosity and/or hot tearing [Dahle]. The final metal contraction takes place in the solid state and gives rise to deformation, residual stresses and even cracking. Thermomechanical effects are crucial as soon as the metal has reached the point at which it develops its solid-like character. For the optimisation of DC/EM casting using mathematical models, adequate knowledge is needed about the mechanical behaviour of the cast metal, in particular for the viscoplastic behaviour at high temperature. In this section, we will concentrate on the mechanical behaviour of aluminium and its alloys from the temperature at which they acquire a solid-like character down to room temperature.

Any deformation can be considered as the sum of a reversible and an irreversible strain. The reversible strain is the sum of the deformation due to temperature changes and of the elastic strain. This reversible deformation disappears if the temperature or the stress return to its initial conditions. On the contrary, the irreversible deformation, i.e. the plastic or creep strain, remains after the stress has been removed. This plastic deformation of metals is produced by the movement of dislocations in the solid. After a brief description of the existing theories concerning the plastic flow of metals and particularly of aluminium and its alloys, empirical and constitutive models aimed at relating stress to temperature, strain, strain-rate and sometimes internal variables, will be

reviewed. Eventually, the present knowledge of the mechanical behaviour of aluminium alloys in their solidification range will be presented.

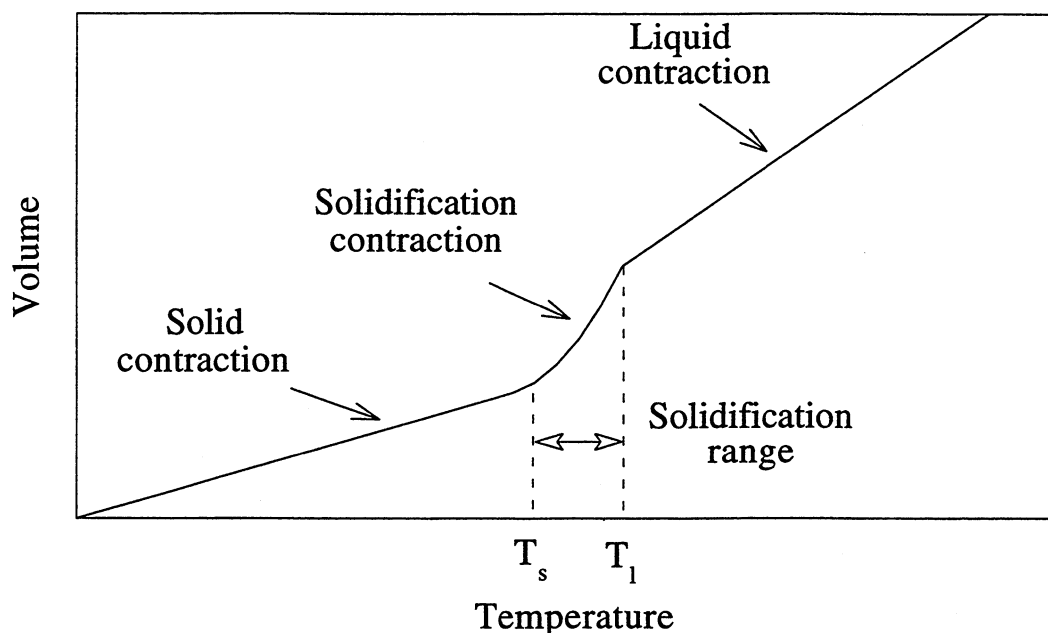


Figure 2.8: schematic illustration of the three shrinkage regimes: in the liquid, during freezing, and in the solid, [Camp].

### 2.2.1 Reversible deformations

The thermal strain is a consequence of a volume change with temperature. As the variation of volume with temperature is not linear [Hatch], the proportionality factor, i.e. the coefficient of thermal expansion is not constant. For this reason, either the mean or the differential coefficient of thermal expansion can be used in the calculations. Using the mean coefficient, the general equation for the thermal strain tensor,  $\epsilon_{ij}^{th}$ , at temperature  $T$  is:

$$\epsilon_{ij}^{th} = \alpha_m(T) (T - T_0) \delta_{ij} \quad (2.16)$$

where  $T_0$  is the reference temperature and  $\alpha_m(T)$  the mean coefficient of expansion between  $T_0$  and  $T$ ,  $\delta_{ij}$  is the Kronecker symbol.  $T_0$  is the temperature at which the thermal strain is supposed to be zero. Using the differential coefficient of expansion  $\alpha_d(T)$ , the thermal strain is given by:

$$\epsilon_{ij}^{th} = \int_{T_0}^T \alpha_d(\theta) \delta_{ij} d\theta \quad (2.17)$$

According to the one-dimensional Hooke's law, the elastic strain is proportional to the stress, and the proportionality factor is the Young modulus,  $E(T)$ . The elastic strain in one dimension is given by:

$$\varepsilon^{el} = \frac{\sigma}{E(T)} \quad (2.18)$$

In three dimensions, the Hooke's law relates the elastic strain to the stress for isotropic materials as follows [Tim]:

$$\varepsilon_{ij}^{el} = \frac{1+\nu}{E} \sigma_{ij} - \frac{\nu}{E} \sigma_{kk} \delta_{ij} \quad (2.19)$$

where  $\nu$  is the Poisson's ratio and  $\sigma_{kk}$  is the trace of the stress tensor (implicit summation is made on repeated indices). A distinction should be made between the dynamic and the static moduli of elasticity. The dynamic modulus is determined on the base of damping measurements and the static modulus with tensile tests. Both moduli are close to each other. However, the measurement of the static modulus in the tensile test is difficult because a proportionality between stress and strain can only be observed at very low stresses. In fact, already at these low stresses, time-dependent deformation processes, as for example inelastic creep, can happen, especially at high temperatures.

### 2.2.2 Plastic deformation and deformation-mechanism maps

Plastic flow is caused by the shearing, or deviatoric part  $\sigma_s$  of the stress field  $\sigma$ .  $\sigma_s$  is also known as the Von Mises equivalent stress. In terms of the principal stresses  $\sigma_1$ ,  $\sigma_2$  and  $\sigma_3$  [Bellet]:

$$\sigma_s = \sqrt{\frac{1}{2} [(\sigma_1 - \sigma_2)^2 + (\sigma_2 - \sigma_3)^2 + (\sigma_3 - \sigma_1)^2]} \quad (2.20)$$

or in terms of the deviatoric stress tensor  $s$ :

$$\sigma_s = \sqrt{\frac{3}{2} (s_{ij} s_{ij})} \quad (2.21)$$

$$\text{where } s_{ij} = \sigma_{ij} - \frac{1}{3} \sigma_{kk} \delta_{ij} \quad (2.22)$$

is the deviatoric part of the stress tensor. This shear stress exerts forces on the defects present in the solid, such as dislocations, vacancies, solute atoms, causing them to move. The shear strain rate,  $\dot{\varepsilon}$ , reflects the density of these

defects and the velocity at which they move. In terms of the principal plastic strain rates  $\dot{\epsilon}_1$ ,  $\dot{\epsilon}_2$  and  $\dot{\epsilon}_3$ , the shear strain rate is :

$$\dot{\epsilon} = \frac{1}{3} \sqrt{2 [(\dot{\epsilon}_1 - \dot{\epsilon}_2)^2 + (\dot{\epsilon}_2 - \dot{\epsilon}_3)^2 + (\dot{\epsilon}_3 - \dot{\epsilon}_1)^2]} \quad (2.23)$$

or in terms of the strain rate tensor  $\dot{\epsilon}_{ij}$  :

$$\dot{\epsilon} = \sqrt{\frac{2}{3} \dot{\epsilon}_{ij} \dot{\epsilon}_{ij}} \quad (2.24).$$

For simple tension,  $\sigma_s$  and  $\dot{\epsilon}$  are related to the tensile stress  $\sigma_1$  (applied tensile stress) and strain-rate  $\dot{\epsilon}_1$  (axial strain rate) by:

$$\sigma_s = \sigma_1 \text{ and } \dot{\epsilon} = \dot{\epsilon}_1 \quad (2.25)$$

since  $\dot{\epsilon}_2 = \dot{\epsilon}_3 = -0.5 \dot{\epsilon}_1$ , where Poisson's ratio is taken as 0.5 because the strains are plastic (constant volume). Equations 2.20 to 2.25 are used to generalize the results obtained by uniaxial tension to more complex three dimensional stress state. The three main creep deformation mechanisms, dislocation glide, dislocation creep and diffusion creep, are detailed hereafter.

### Low-temperature plasticity: dislocation glide

Dislocation glide involves the movement of dislocations along slip planes. This motion is almost always obstacle-limited as illustrated in figure 2.9 and the interaction of potentially mobile dislocations with other dislocations, with solute or precipitates, with grain boundaries, and with the periodic friction of the lattice itself, determines the rate of flow. The moving dislocations overcome these barriers by thermal activation. Orowan [Oro] demonstrated that a density  $\rho_m$  of mobile dislocations, moving through a field of obstacles with an average velocity  $v$  determined almost entirely by their waiting time at obstacles, produced a strain-rate given by:

$$\dot{\epsilon} = \rho_m b v \quad (2.26)$$

where  $b$  is the magnitude of the Burgers' vector of the dislocation. Using this equation, Frost and Ashby [Frost] derived the following rate-equation for discrete-obstacle controlled plasticity:

$$\dot{\epsilon} = \dot{\epsilon}_0 \exp\left(-\frac{\Delta F}{k T} \left(1 - \frac{\sigma_s}{\tau_s}\right)\right) \quad \text{with } \dot{\epsilon}_0 = \beta v \left(\frac{\sigma_s}{\mu(T)}\right)^2 \quad (2.27)$$

where  $\Delta F$  is the total free energy required to overcome the obstacle without aid from external stress and  $\mu(T)$  the shear modulus.  $\tau_s$  is a material parameter which reduces the activation energy to zero, forcing the dislocation through the obstacle with no help from thermal energy. Depending on the strength of the obstacles, the activation energy  $\Delta F$  varies from  $0.2\mu b^3$  to  $2\mu b^3$ , with a mean value of  $0.5 \mu b^3$ , i.e.  $206 \text{ kJ/mole}^1$ , and the athermal stress  $\tau_s$  reflects the strength, density and arrangement of the obstacles.

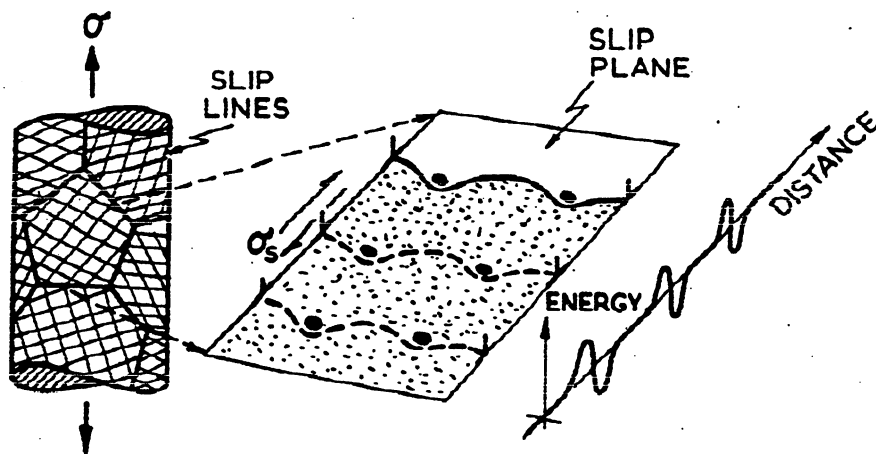


Figure 2.9: low-temperature plasticity limited by discrete obstacles, from Frost and Ashby [Frost].

For heavily deformed solid solutions, solution strengthening is masked by forest hardening (multiplication of dislocations associated with work hardening). A dispersion of strong particles of a second phase blocks the motion of the dislocations. A gliding dislocation can move only by bowing between and bypassing strong and stable particles, giving a contribution to the flow strength which scales as the reciprocal of the particle spacing, and which has a very large activation energy (Orowan mechanism). On the other hand, a precipitate, when finely dispersed, can be cut by moving dislocations.

### High-temperature plasticity: dislocation creep

Dislocation creep occurs by dislocation glide aided by vacancy diffusion. At high temperatures, dislocations acquire a new degree of freedom: they can climb as well as glide [Diet]. If a gliding dislocation is held up by discrete obstacles, a little climb may release it, allowing it to glide to the next set of obstacles where the process is repeated (see figure 2.10). Since dislocation climb

<sup>1</sup> This energy is  $N_A \cdot \Delta F$  where  $N_A$  is the Avogadro number.



requires diffusion of vacancies or interstitials, the rate controlling step is atomic diffusion. Above  $0.3 T_m$  ( $\approx 0^\circ\text{C}$  for pure aluminium) and about  $0.4 T_m$  ( $\approx 100^\circ\text{C}$ ) for its alloys, these materials exhibit a strong rate-dependent plasticity or creep, much stronger than that of the mechanisms described in the previous section. In this high-temperature regime, the strain-rate is expressed as follows:

$$\dot{\epsilon} \propto \left(\frac{\sigma_s}{\mu(T)}\right)^n \quad (2.28)$$

where  $n$  is the stress exponent. This regime is therefore called power-law creep. Weertman [Weer] and more recently Gittus [Git] proposed a model based upon the diffusion-aided movement of dislocations in a three-dimensional network (substructure) and derived a value of 3 for the stress exponent (so-called steady-state natural creep law). However, creep measurements with a range of metals show that the stress exponent,  $n$ , varies from 3 to 8, with a value of 5 most commonly found. The steady-state creep rate is often well described by a power-law relation:

$$\dot{\epsilon} = A \frac{D_v \mu(T) b}{k T} \left(\frac{\sigma_s}{\mu(T)}\right)^n \quad (2.29)$$

where  $A$  and  $n$  are material constants,  $D_v$  is the bulk or lattice diffusion coefficient.

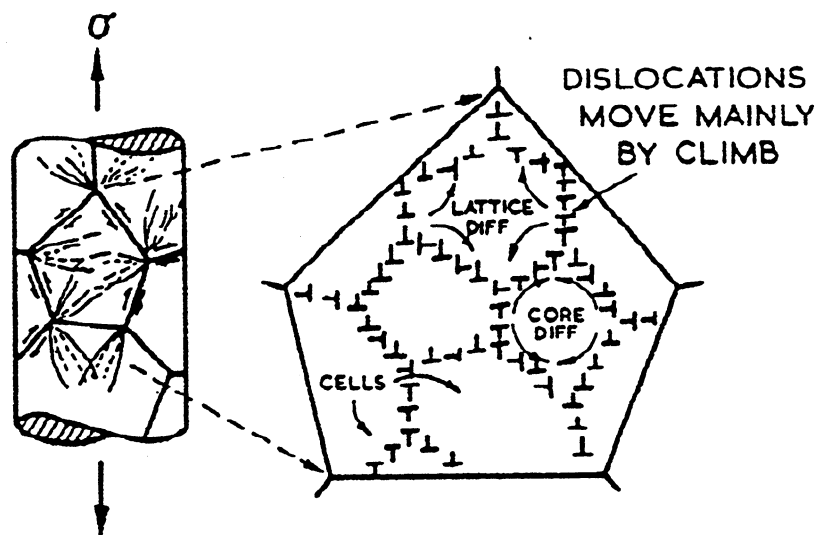


Figure 2.10: power-law creep involving cell-formation by climb, [Frost].

To explain the increase in the stress exponent and the drop in the creep activation energy at lower temperatures, it is necessary to assume that the transport of matter via dislocation core diffusion contributes significantly to the overall diffusive transport of matter as illustrated in figure 2.10. This is taken

into account by replacing the diffusion coefficient in equation 2.29 by the effective diffusion coefficient:

$$D_{\text{eff}} = D_v f_v + D_c f_c \quad (2.30)$$

where  $D_c$  is the core diffusion coefficient, and  $f_v$  and  $f_c$  are the fractions of atom sites associated with each type of diffusion.  $f_v$  is essentially unity whereas the value of  $f_c$  is proportional to the dislocation density. At high temperatures, lattice diffusion is dominant (high-temperature creep) whereas at lower temperatures or higher stresses, core diffusion becomes dominant (low-temperature creep). At low stresses, below  $5 \cdot 10^{-6} \mu(T)$ , a linear dependence ( $n=1$ ) is observed [Harp]; this is known as Harper-Dorn creep. On the other hand, at stresses above  $10^{-3} \mu(T)$ , the simple power-law breaks down, i.e. the measured strain rates are higher than those predicted by equation 2.29. This is due to a transition from climb-controlled to glide-controlled flow. In the Arrhenius rate law, as present in the diffusion coefficient, it is supposed that the thermal fluctuations assist dislocations to overcome the activation barrier, whereas in plastic deformation the applied stress acts together with thermal fluctuations in overcoming the barrier as illustrated in figure 2.11.

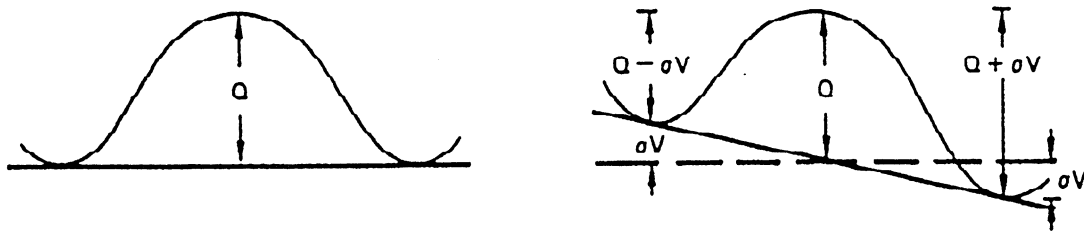


Figure 2.11: schematic illustration of an activation barrier for slip and the effect of applied stress on skewing the barrier, [Diet].

The rate of overcoming this barrier is proportional to  $e^{-Q/RT}$ . In the presence of stress, the rate of moving dislocations from left to right is proportional to  $e^{-(Q-\sigma v)/RT}$  and from right to left  $e^{-(Q+\sigma v)/RT}$  ( $v$  is an activation volume) thus resulting in the steady-state hyperbolic sine equation which relates stress, temperature and strain-rate under hot-working conditions, as proposed by Garafalo [Gar1]:

$$\dot{\epsilon} = A_1 [\sinh(\alpha \sigma_s)]^n \exp\left(\frac{-Q}{RT}\right) \quad (2.31)$$

where  $1/\alpha$  is the threshold stress  $\sigma_0$  deduced from the measurements. At low stresses,  $\alpha \sigma_s < 0.8$ , this law reduces to a simple power law, while at larger stresses,  $\alpha \sigma_s > 1.2$ , it becomes an exponential law.

Jonas et al. [Jon] gathered experimental data from extrusion tests, compression tests, torsion tests and creep tests for pure aluminium and temperatures varying from 200°C to 600°C, and plotted the results with  $\dot{\epsilon} / A_1 e^{-Q/RT}$  and  $\sinh(\alpha\sigma_s)$  on the axes as shown in figure 2.12 thus showing the good correlation with equation 2.31, giving a straight line with slope n.

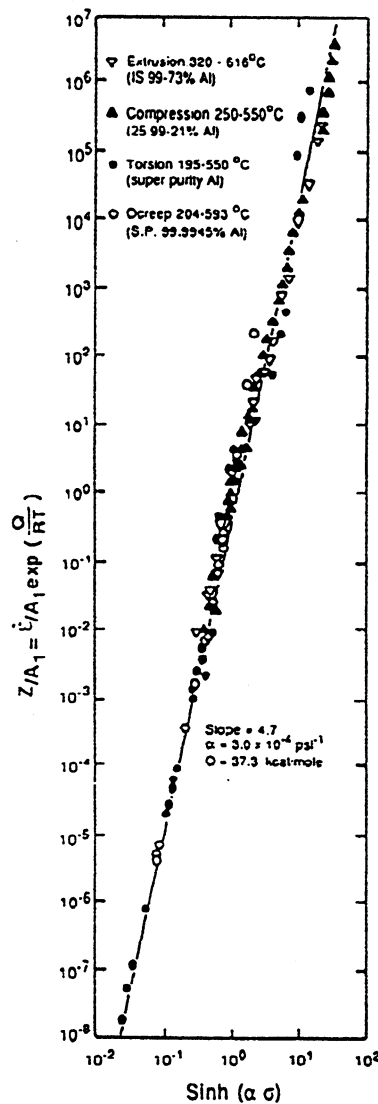


Figure 2.12: experimental results of several workers on aluminium showing the validity of the hyperbolic sine relationship, from Jonas [Jon].

The apparent activation energy  $Q$  in the power-law breakdown regime often gives values which exceeds that of self-diffusion and indicates sometimes that the recovery process differs from that of climb-controlled creep.

Solute atoms are obstacles to dislocation motion and result in solute hardening. They interact with stationary and moving dislocations introducing a friction stress for glide-controlled creep and a solute-drag which retards climb-controlled creep (solute atoms are attracted to the dislocations, large ones in

open regions (tension) and smaller ones in zones in compression, and form a cloud of solute atoms around the dislocations which is dragged along with them). The stress dependence of creep in solid solutions falls into two classes: those with the exponent  $n$  of equation 2.29 varying between 4 and 7 like in Al-Zn alloys [Lang] and those with  $n$  around 3 like in Al-Mg alloys [Lang]. On the other hand, a dispersion of strong particles of a second phase blocks dislocation glide and climb and helps to stabilise a dislocation substructure (cells). The stress exponent  $n$  is found to be high, typically 7 or more; and the activation energy is larger than that of self-diffusion. Most precipitates, when fine, are not stable at creep temperatures, but when coarse, they behave like a dispersion [Lang].

### Diffusion creep

Diffusion creep becomes the controlling mechanism at high temperatures and relatively low stresses,  $\sigma/\mu(T) < 10^{-4}$ . Nabarro [Nab] and Herring [Her] demonstrated that the creep process was controlled by stress-directed atomic diffusion: stress changes the chemical potential of the atoms on the surfaces of the grains in a polycrystal in such a way that there is a flow of vacancies from grain boundaries experiencing tensile stresses to those which have compressive stresses. At the same time, there is a corresponding flow of atoms in the opposite direction, thus leading to the elongation of the grain as schematically represented by Frost and Ashby [Frost] in figure 2.13. The Nabarro-Herring creep equation is:

$$\dot{\epsilon} = \frac{14 \sigma_s b^3}{k T d^2} D_v \quad (2.32)$$

where  $d$  is the grain size and  $D_v$  the lattice diffusion coefficient. At lower temperatures ( $T < 500^\circ\text{C}$ ), grain-boundary diffusion predominates and Coble [Diet] derived the following relation:

$$\dot{\epsilon} = \frac{50 \sigma_s b^4}{k T d^3} D_{gb} \quad (2.33)$$

where  $D_{gb}$  is the boundary diffusion coefficient.

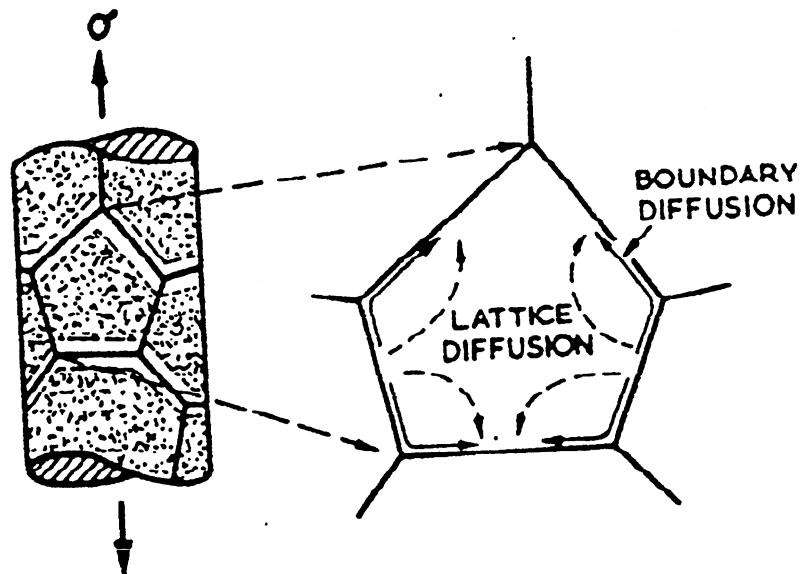


Figure 2.13: diffusional flow by diffusional transport through and round the grains, [Frost].

Solid solution influences diffusional flow by changing the diffusion coefficient and can also impose a drag on boundary dislocations slowing the rate of creep. On the other hand, a dispersion of a second phase influences the way in which a grain boundary acts as a sink and source of vacancies, introducing a large interface-reaction barrier to diffusion and a threshold stress below which creep stops.

The effects of the presence of stable precipitates in the aluminium matrix on the creep behaviour was studied by Barrett et al. [Barr]. These authors investigated the newtonian creep of Al and Al-Fe0.5wt% at high temperatures and low stresses. They compared their results with the prediction of the Nabarro-Herring theory (equation 2.32 and 2.33) and showed that although the stress dependence (newtonian creep) and temperature dependence (activation energy close to that of self diffusion) are in good agreement with the theory, the observed absolute creep rates are 1500 times faster than the predictions, as reported in figure 2.14. They also observed the formation of subgrains during creep and the reduction of the creep rate by a factor of 100 at the same temperature and stress in the presence of precipitates of  $\text{Al}_3\text{Fe}$ , in spite of the fact that the grain size of the alloy is smaller by a factor of 30. Barrett et al. determined the creep activation energy of the Al-Fe0.5wt% alloy and found a value, 640 kJ/mole at  $630^\circ\text{C}$ , which is several times higher than that for self diffusion of Al (142 kJ/mole). They concluded that newtonian creep in this case is controlled by a dislocation process rather than by diffusional flow and

proposed a simple theory based on the climb controlled generation of dislocations from a fixed density of sources.

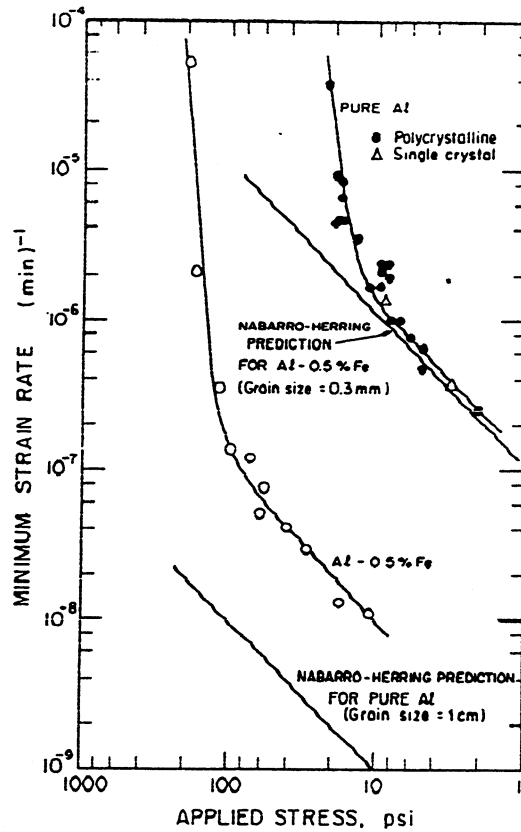


Figure 2.14: comparison of creep data for pure Al and Al-Fe0.5wt% with the predictions of the Nabarro-Herring theory, [Barr].

### Deformation-mechanisms map

The rate equations presented above describe the mechanical behaviour at steady-state ignoring the effects of work-hardening and of transient creep. Frost and Ashby [Frost] summarised information about the range of dominance of each mechanism of plasticity and the rates of flow they produce in a stress-temperature space. Frequently, more than one creep mechanism will operate at the same time. If several mechanisms are operating in parallel, i.e. independently of each other, then the steady-state creep rate is given by the sum of the creep rate of each mechanism. In this case, the fastest mechanism will dominate the creep behaviour. If the mechanisms are operating in series, i.e., they operate in sequence, then the slowest mechanism will control the creep behaviour.

The deformation-mechanism map for pure aluminium with a grain diameter of 10  $\mu$  is shown on figure 2.15. The axes of the diagram are the normalised stress  $\sigma_s/\mu(T)$  and temperature  $T/T_m$  where  $T_m = 933\text{K}$  ( $660^\circ\text{C}$ ) is the melting temperature. The diagram is divided into fields which show the regions of stress

and temperature over which each of the steady-state deformation mechanism is dominant. The boundaries of these fields are obtained by equating the appropriate rate-equations and solving for stress as a function of temperature. They represent combination of stress and temperature where the respective strain-rates for the two deformation mechanisms are equal. Contours of iso-strain rate can be calculated from the constitutive equations and plotted on the map. The upper bound of the diagram is the stress to produce slip in a perfect dislocation free crystal.

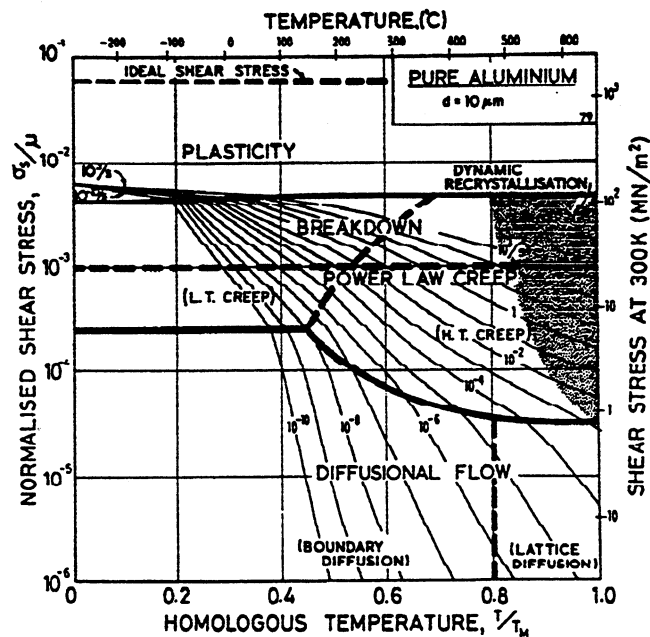


Figure 2.15: deformation mechanism map of pure aluminium, from Frost and Ashby [Frost].

### 2.2.3 Mechanical testing and empirical models

With the help of mechanical tests, the behaviour of aluminium and its alloys has also been described by empirical or semi-empirical relations, i.e. equations with a more or less physical basis, but which give a good fit to experimental data [Bellet]. The tests in which the resistance of a material against plastic deformation is measured are usually carried out at constant temperature and at either constant strain-rate or stress, both kinds of tests being just different and complementary ways of investigating the kinetic law. Depending on the type of test, the empirical relation defines either the flow stress,  $\sigma$ , or the strain-rate,  $\dot{\epsilon}$ , as a function of the other variables. Such types of empirical relations have been extensively used in the low and high-temperature regions because they are easily tractable in a numerical model and they have long been the only ones available.

In the constant extension rate test (CERT) [Hosf], the strain increases in proportion to time. Often, the test is done at constant cross head speed of the testing machine. The force necessary to deform the specimen is measured and converted into the true stress. At low temperatures ( $T < 300^\circ\text{C}$ ), assuming that the flow stress is not strongly dependent on  $\dot{\epsilon}$  and that it can be fitted by empirical relations which exclude this parameter, the most commonly used relation is the Holloman's power-curve relation [Diet]:

$$\sigma = K(T) \epsilon^{n(T)} \quad (2.34)$$

where  $n(T)$  is the strain-hardening exponent and  $K(T)$  the strength coefficient. The perfectly plastic solid is described by  $n = 0$ . The strain-hardening exponent  $n$  for pure aluminium falls from 0.7 at 40K to about 0.1 at 650K [Hosf]. The objection with equation 2.24 is that the stress increases indefinitely with the strain although a plateau or steady-state is usually reached. To overcome this problem, Voce [Voce] proposed the following relation:

$$\sigma = \sigma_0 + (\sigma_s - \sigma_0) [1 - \exp(-\epsilon/\epsilon_c)]^m \quad (2.35)$$

where  $\sigma_0$  is the initial yield strength,  $\sigma_s$  the steady-state stress and  $\epsilon_c$  and  $m$  two parameters characterising the strain-hardening. In the original Voce equation,  $m$  was set to 1, but simple work-hardening and recovery theory leads to  $m = 0.5$  and for practical purposes, Sellars [Sell1] considered  $m$  as an adjustable parameter to give the best fit to the curvature between  $\sigma_0$  and  $\sigma_s$ . Figure 2.16 illustrates the Holloman and Voce relations. In fcc metals, the strain hardening exponent decreases with increasing temperature. This results in the stress-strain flattening out with increasing temperature and the tensile strength being more temperature-dependent than the yield strength.

Polakovic et al. [Pola] studied the shape of aluminium stress-strain curve as a function of deformation rate, temperature and material purity. They demonstrated that when aluminium is not pure (Al 99.5%), the stress-strain curves, irrespectively of temperature and strain-rate, get shifted with respect to Al 99.99% by 25% towards higher stress values. They also have shown that multiplying the strain rate by 6 provokes a shift of the stress-strain curve by 60% towards higher stress values. The influence of strain-rate on the shape of the stress-strain curve at room temperature was measured by Wire et al. [Wire] for the 1xxx-series (Al 99%) alloys and is shown in figure 2.17. Wire et al. fitted the experimental stress-strain curves to the following relation:

$$\sigma = \sigma_0 (\epsilon_0 + \epsilon)^n \quad (2.36)$$



where the three parameters  $\sigma_0$ ,  $\epsilon_0$ , and  $n$  depend on temperature and strain-rate.

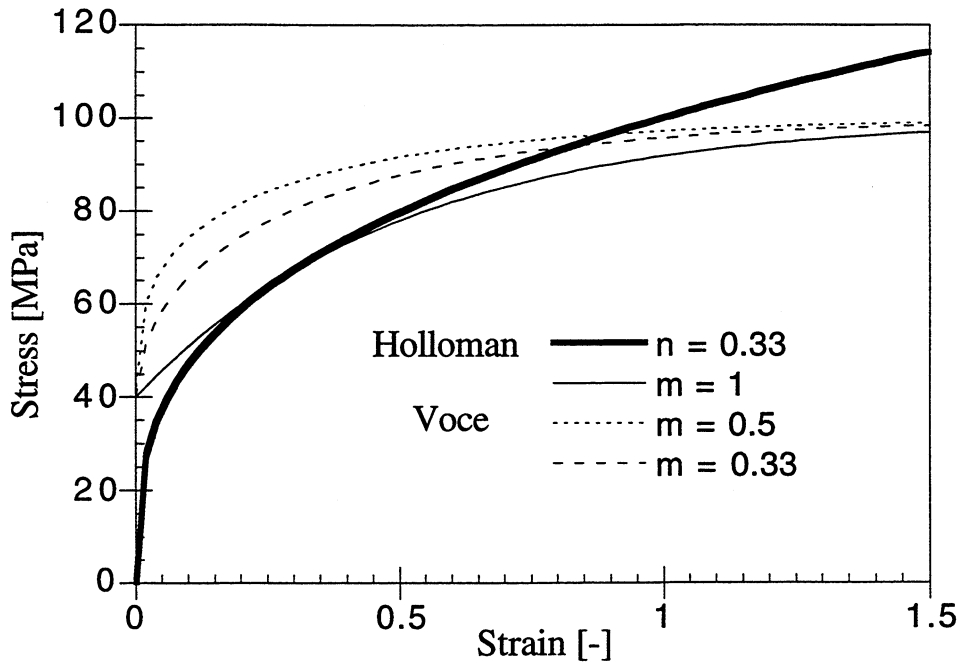


Figure 2.16: illustration of the Holloman and Voce relations ( $\sigma_0 = 40$  MPa and  $\sigma_s = 100$  MPa).

Sellars [Sell1] carried out compression tests of initially recrystallised AA3003 (Al-Mg1wt%) alloy: typical stress-strain curves are reported in figure 2.18. As a result of the combined effects of work-hardening and dynamic recovery, the flow stress rises at a decreasing rate until a steady-state is reached. The level of the curve is sensitive to both the strain rate  $\dot{\epsilon}$  and temperature  $T$ , because recovery is a thermally activated process and so give more effective softening at low  $\dot{\epsilon}$  and/or high temperatures. For alloys in which there is no precipitation or transformation reaction in the temperature range of interest, the effect of  $\dot{\epsilon}$  and  $T$  on stress and microstructure can be combined in terms of the Zener-Hollomon parameter [Zen]  $Z$  defined as:

$$Z = \dot{\epsilon} \exp\left(\frac{Q_{\text{def}}}{RT}\right) \quad (2.37)$$

where  $Q_{\text{def}}$  is the activation energy for deformation, of the order of the energy for self diffusion for hot working conditions. Sellars [Sell1] represented accurately the tensile stress-strain curves by the use of the Voce relation (equation 2.35) in which the parameters are all functions of  $Z$ .

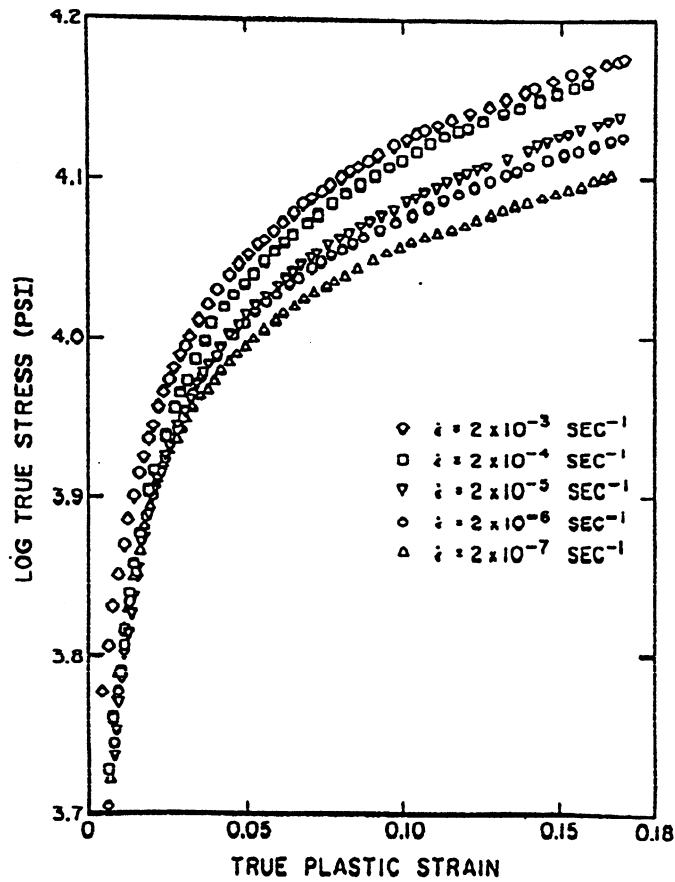


Figure 2.17: influence of the strain-rate on stress-strain curves of AA1100 alloy at room temperature, [Wire].

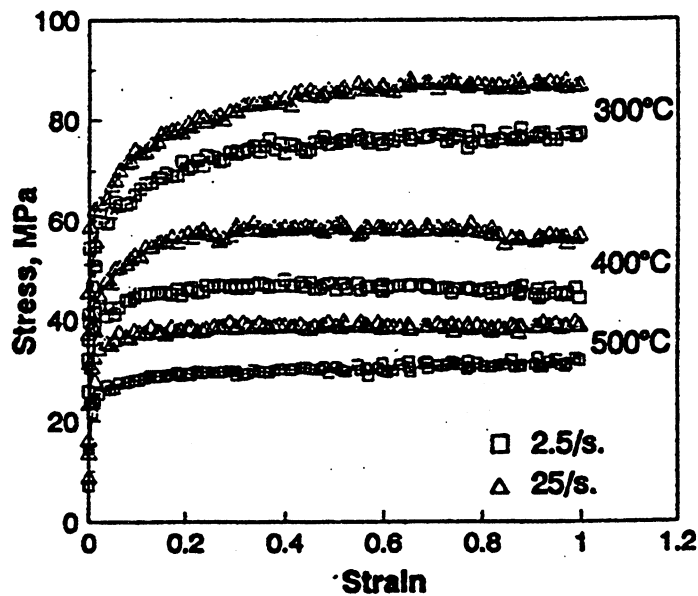


Figure 2.18: influence of the strain-rate on stress-strain curves of AA3003 alloy at 300°C, 400°C and 500°C, [Sell1].

At temperatures higher than 300°C, the mechanical behaviour of aluminium alloys is strongly dependent on the strain-rate and this quantity is often treated as the independent variable:

$$\dot{\epsilon} = \dot{\epsilon}(\sigma, \epsilon, T) \quad (2.38).$$

To obtain the creep curve of a metal, a constant load or stress is applied to a tensile specimen maintained at constant temperature, and the strain (extension) of the specimen is recorded as a function of time. Figure 2.19 illustrates a typical creep curve [Diet]. Following an initial rapid elongation of the specimen,  $\epsilon_0$ , the creep rate decreases with time, then reaches essentially a steady-state in which the creep rate changes little with time, and finally the creep rate increases rapidly with time until fracture occurs. Thus it is natural to discuss the creep curve in terms of its three stages. The first stage of creep, known as primary creep, represents a region of decreasing creep rate. Primary creep is a period of predominantly transient creep in which the creep of the material increases by virtue of its own deformation. The second stage of creep, known as secondary or steady-state creep, is a period of nearly constant creep rate which results from a balance between the competing processes of strain-hardening (generation of dislocations) and recovery (annihilation of dislocations).

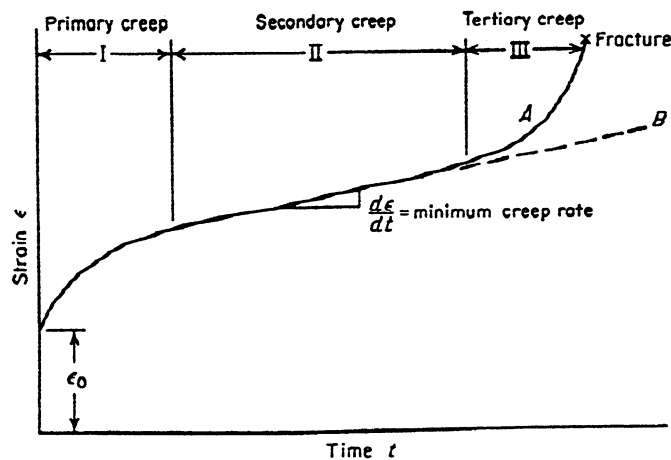


Figure 2.19: typical creep curve showing the three steps of creep at constant load (A) or constant stress (B), [Diet].

The average value of the creep rate during secondary creep is called the minimum creep rate. Third stage or tertiary creep mainly occurs when there is an effective reduction in cross-sectional area either because of necking and/or internal void formation. The minimum creep rate for a given temperature and stress is the most important parameter derived from a creep curve. The relative extension of the primary stage decreases with temperature for aluminium alloys.

Andrade [And] considered that the constant-stress creep curve represents the superposition of two separate creep processes which occur after the sudden strain which results from applying the load. As illustrated in figure 2.20, the first component of the creep curve is a transient creep with a creep rate decreasing with time. Added to this is a constant-rate viscous creep component. In order to represent the creep curve, Garafalo [Gar2] proposed the following relation :

$$\varepsilon = \varepsilon_0 + \varepsilon_t (1 - e^{-rt}) + \dot{\varepsilon}_s t \quad (2.39)$$

where  $\varepsilon_0$  is the instantaneous strain in loading,  $\varepsilon_t$  and  $r$  are two parameters describing the transient creep and  $\dot{\varepsilon}_s$  is the steady-state creep rate.

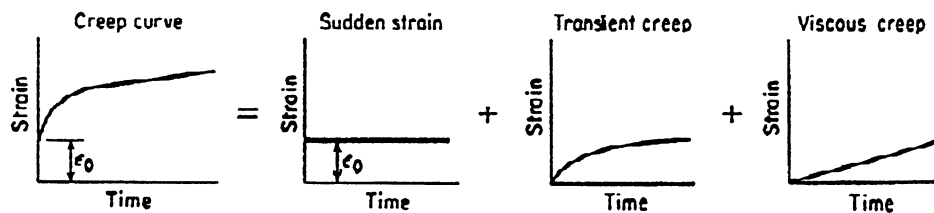


Figure 2.20: Andrade's analysis of the competing processes which determine the creep curve, [Diet].

Aside creep tests, many investigators [Sell2, Wong, Shep] used other mechanical tests, such as torsion, extrusion or compression, to study the behaviour of aluminium alloys at high temperatures. When the deformation domain is restricted to almost steady-state conditions at high temperatures (above  $0.5 T_m$ ) and low strain-rates ( $\dot{\varepsilon} < 0.01 \text{ s}^{-1}$ ), the flow stress can be expressed as a function of the external variables alone, i.e.  $T$  and  $\dot{\varepsilon}$ . Furthermore, the influence of temperature and strain-rate can often be collapsed into a single variable by the use of the Zener-Hollomon parameter (see equation 2.37). Many such models exist in the literature e.g. the power-law creep and sinh laws. In these models, the influence of microstructure is not explicitly accounted for. It is assumed that the microstructure attains steady-state instantaneously with the external variables. Consequently, in such models the state equation implicitly includes the microstructural effects and the flow stress is a function of the Zener-Hollomon parameter alone. Although these models are not accurate in deformation domains in which the transients to steady-state significantly impact the deformation behaviour, they were very often used, particularly to describe the power-law breakdown. The most widely used relation between  $\sigma$  and  $Z$  is the phenomenological Garafalo relation [Gar1]:

$$Z = A \left[ \sinh \left( \frac{\sigma}{\sigma_0} \right) \right]^n \quad (2.40)$$

where  $A$ ,  $\sigma_0$ , and  $n$  are material parameters. As pointed out in section 2.2.2, this relation reproduces the power law creep at stresses lower than  $0.8 \sigma_0$  and the exponential law at stresses higher than  $1.2 \sigma_0$ . Table 2.1 sums up the work of different investigators on aluminium and its alloys. The values of the different parameters present in relation 2.40, the activation energy, the constant  $A$ , the threshold stress  $\sigma_0$  and the exponent  $n$ , are reported together with the exact composition of the investigated alloy and some relevant information. Most of the investigated alloys being in an annealed state, the creep activation energy remains close to that of self diffusion. In the hot working range, 5xxx series alloys exhibit large values of  $Q$ ,  $\sigma_0$  and  $n$ . Nevertheless, no data exist for aluminium alloys in the as-cast state.

Composition	Conditions	A [s <sup>-1</sup> ]	Q [kJ/mol]	$\sigma_0$ [MPa]	n [-]
Al.	high purity [Wong]	1.4 10 <sup>12</sup>	156.	22.66	4.7
Al. (1xxx series)	commercial purity [Wong]	2.35 10 <sup>10</sup>	156.	22.66	4.7
Al-Fe0.17wt%- Si0.06wt%	recrystallised [Sam]	8.55 10 <sup>12</sup>	177.2	31.02	4.75
Al-Fe0.7wt%- Si0.05wt%	extruded and homogenized [Shep]	38.0 10 <sup>10</sup>	156.7	27.	3.84
Al-Mg2.5wt% (AA5052)	hot working [Well]	1.46 10 <sup>12</sup>	196.	50.	7.11
Al-Mg4.5wt% (AA5182)	hot working [Well]	2.64 10 <sup>11</sup>	196.	50.	5.78

Table 2.1: parameters of the sinh law for different aluminium alloys.

In order not to neglect the strain hardening of the material, the deformation resistance-strain curves of aluminium and its alloys at intermediate temperatures have been fitted to the Ludwick relation [Diet] in which strain and strain-rate effects are considered to be multiplicable:

$$\sigma = F(T) \varepsilon^{n(T)} \dot{\varepsilon}^{m(T)} \quad (2.41)$$

where  $F(T)$  is a temperature-dependent function and  $m(T)$  is the strain-rate sensitivity.

Motomura et al. [Moto] studied the resistance deformation of annealed 1xxx, 3xxx and 5xxx series alloys over the temperature range 300-500°C and for strain-rate varying from 1 to 12 s<sup>-1</sup>. They considered  $n$  and  $m$  constant in this temperature range and described the temperature-dependence of  $F(T)$  not through the classical Arrhenius form but through its developed form:

$$F(T) = a + b/T + c/T^2 \quad (2.42)$$

Magnin et al. [Mag] measured the mechanical behaviour of an Al-Cu 4.5wt% with the help of a Gleeble machine. Strain-rates were in the range 10<sup>-3</sup>-10<sup>-2</sup> s<sup>-1</sup> and special heat treatment was first established so as to reproduce the as-cast microstructure of this heat-treatable alloy. The results of the tensile tests were fitted to a modified version of the Ludwick relation:

$$\sigma = F(T) (\varepsilon + \varepsilon_0)^{n(T)} (\dot{\varepsilon} + \dot{\varepsilon}_0)^{m(T)} \quad (2.43)$$

where  $\varepsilon_0$  and  $\dot{\varepsilon}_0$  are two parameters describing previous deformation. Magnin et al. used an optimisation procedure similar to that described by Kozłowski [Koz] to find the optimal rheological parameters.

Nedreberg [Ned] studied and proposed a continuous description of the mechanical properties of the heat-treatable Al-Mg-Si alloy AA6063 in its whole casting range, i.e. from its solidus temperature down to room temperature. One of the main problems with the tensile tests was to obtain a microstructure in the test specimen approximately equivalent to that during casting, i.e. without any precipitation of the Mg<sub>2</sub>Si phase. The author adopted the following solution: in experiments at temperatures higher than 300°C, the temperature is first elevated to approximately 550°C and then lowered as fast as possible to the experimental value so as to obtain a nearly as-cast microstructure. In experiments at temperatures lower than 300°C, the temperature was increased from room temperature as fast as possible to the experimental temperature. Fjaer and Mo [Fja1] used these results in a FEM model so as to study the thermal stresses in DC casting of aluminium billets. The mechanical behaviour of the AA6063 alloy was described by the modified Ludwick relation (equation 2.43) in which  $\varepsilon_0$  was set to 0.001 and  $\varepsilon$  was considered to be the accumulated plastic strain below 427°C assuming that above this temperature strain-hardening is negligible.  $\dot{\varepsilon}_0$  was also set to 0 and  $F(T)$ ,  $n(T)$  and  $m(T)$  were expressed using hyperbolic tangent and polynomial functions [Fja1].

## 2.2.4 Constitutive models for elastic-viscoplastic materials

Bodner et al. [Bod] and Anand et al. [Ana] proposed an elastic-viscoplastic representation that is suitable for large deformations, temperature range and general straining. The basis of the formulation is the separation of the total deformation rate into elastic and inelastic, geometrically irreversible, components that are functions of state variables:

$$\dot{\epsilon} = \dot{\epsilon}_{el} + \dot{\epsilon}_{in} \quad (2.45)$$

This theory, therefore, does not require a yield criterion. Recently, constitutive equation systems were developed to describe the behaviour of metals from their melting temperature down to room temperature [Mill]. The goal of these internal variable models is to describe accurately the current microstructure and changes in properties resulting from previous loading history. Phenomenologically, the constitutive model can be described as follows: a kinetic law, which refers to the kinetics of flow at a fixed structure, describes the flow strength at a particular strain-rate and temperature and for a given microstructure. It can be written in functional form as:

$$\sigma = F(\dot{\epsilon}, T, s_i) \quad (2.46)$$

where  $s_i$  ( $i=1,2,\dots$ ) are called structure or internal variables. In the course of deformation, the structure parameters, such as for example the dislocation density, change because of such effects as strain hardening and recovery. These changes are described by a set of structure-evolution laws of the form:

$$\frac{ds_i}{dt} = G_i(\dot{\epsilon}, T, s_j) \quad (2.47).$$

Generally, the first step in developing constitutive models is to identify the minimum number of state variables that are necessary over the domain of interest ( $T, \dot{\epsilon}, \epsilon$ ). More or less complex and physically-based systems were developed in order to study the stress and strain generation through process modelling.

Rosselet [Ross] developed a constitutive equation system for the description of the viscoplastic behaviour of typical materials (austenitic and martensitic steel, superalloy and stellite) used in laser cladding processes including phase transformation and structural changes in the materials. Due to the complexity of the mechanical behaviour of these materials and of the straining experienced during the process, a rather large number of internal

variables was necessary, thus limiting this model to computations of residual stresses produced by the laser cladding process in a one dimensional geometry.

Concerning aluminium and its alloys, many constitutive models were proposed. Sample and Lalli [Sam1] and Lalli and De Ardo [Lall] developed a viscoplastic constitutive model with one internal state variable, called hardness, for commercially pure aluminium to make predictions of hardness distribution after a hot working operation. This model was evaluated for extruded or fully recrystallised aluminium rods, for temperatures greater than 200°C and strain-rates between 0.01 and 10 s<sup>-1</sup>. Smelser and Richmond [Smel] implemented this constitutive model in the finite element code Abaqus in order to compute the air gap formation during the solidification of a cylindrical casting and concluded that inelastic constitutive models are required for accurate predictions of stresses and consequently strains in solidifying materials.

Brown et al. [Brow] proposed an internal variable constitutive model for hot working of metals aimed at representing large deformations of metals at high temperatures. They employed a single scalar as an internal variable to represent the isotropic resistance to plastic flow offered by the internal state of the material. This internal variable was denoted by  $s$  and called deformation resistance. Brown et al. made the assumption that the state variable entered the flow equation as a ratio with the equivalent tensile stress:

$$\dot{\epsilon} = \dot{\epsilon} \left( \frac{\sigma_s}{s}, T \right) \quad (2.48)$$

The evolution equation for the internal variable  $s$  was assumed to be of the form:

$$\dot{s} = h(\sigma_s, s, T) \dot{\epsilon} - \dot{r}(s, T) \quad (2.49)$$

where  $h(\sigma_s, s, T)$  is a function describing dynamic processes, that is strain-hardening and dynamic recovery, while static recovery is accommodated through the function  $\dot{r}(s, T)$ . Brown et al. performed specific experiments so as to determine the specification functions and derived the parameters for a commercial purity aluminium. The following functional form of the flow equation was selected to accommodate both the power law and exponential dependence of the strain-rate on the stress at constant structure:

$$\dot{\epsilon} = A \exp \left( \frac{-Q}{RT} \right) \left( \sinh \xi \frac{\sigma_s}{s} \right)^{1/m} \quad (2.50)$$



where  $A$  is a pre-exponential factor,  $Q$  the activation energy,  $m$  the strain-rate sensitivity and  $\xi$  a material parameter. Figure 2.21 illustrates the correlation of the constitutive model with isothermal compression tests at constant strain-rate and different temperatures. The deformation resistance,  $s$ , increases from a temperature-dependent initial value to a constant value corresponding to the steady-state regime ( $\dot{s} = 0$ ). From this point, the flow stress is given by the sinh equation. This model is also able to reproduce strain softening.

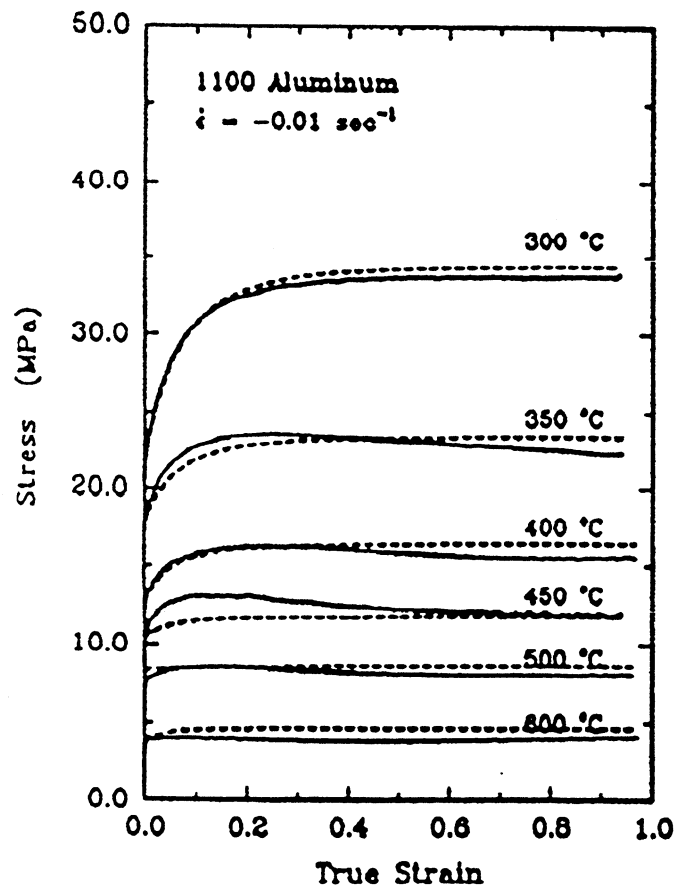


Figure 2.21: ability of the constitutive model to reproduce isothermal compression tests (solid lines), [Brow].

Mo and Holm [Mo2] discussed the use of constitutive equations with internal variables in mathematical calculations of the thermally-induced strains and stresses in DC casting of aluminium alloy billets. They used the so-called MATMOD (materials model) equations originally developed by Miller [Mill] to compute the thermally-induced stress at two locations in the billet. The selected version for high-purity aluminium contains two internal variables representing kinematic and isotropic strain-hardening and recovery, called respectively  $R$  and  $D$ . The one-dimensional version of MATMOD equation that relates viscoplastic strain-rate  $\dot{\epsilon}$  to stress  $\sigma$ , temperature  $T$ , and the internal variables together with the two evolution equations for  $R$  and  $D$  are described in [Mo2, eq. 1-3]. The

authors compared the calculated stress generated during casting using the internal variables model with stresses predicted by the traditional description of representative stress-strain curves. According to Mo and Holm, a serious shortcoming in using classical description of rate-sensitive plastic materials is that the accumulated effective plastic strain is regarded as a state variable and that kinematic hardening and recovery are neglected.

Eventually, Sample et al. [Sam2] derived a two internal state variables model predicting flow stress and microhardness of commercial purity aluminium assuming additive decomposition of the flow curve into steady-state flow and hardening components. The authors were interested in large strain behaviour covering a temperature range spanning from room temperature to near the melting point and strain rates typically encountered during fabrication processes ( $0.01-10 \text{ s}^{-1}$ ). Their model is able to predict the flow behaviour adequately for arbitrary thermomechanical histories. It also has the potential of directly predicting the room temperature mechanical properties such as the yield stress.

### **2.2.5 Behaviour in the semi-solid state**

In the mushy zone, i.e. when the solid fraction is in between 0 and 1, with solidified grains in a surrounding residual liquid, the material has little resistance to shear stresses. Even at a late stage in the solidification, the resistance is quite small. This stage and the magnitude of mechanical properties vary for the various alloys depending on how the residual liquid tends to distribute in between the grains. When liquid globules are present at the grain boundaries, the strength is maintained by intergranular cohesion, since most of the grain boundaries are fully solidified. The mechanical behaviour will depend mainly on the fraction of liquid and on the solidification microstructure, globular or dendritic.

One of the major characteristics of aluminium alloy related to solidification processes is the coherency temperature, i.e. the temperature at which a continuous dendritic or globular network offers a mechanical resistance to deformation [Clax,Dahle]. At this point, the alloy behaves less as a liquid and begins behaving as a solid and the solidification process must accommodate the corresponding transition of properties such as elasticity, shear strength or thermal conductivity and thermal contraction. Claxton [Clax] measured the coherency temperature of several commercial aluminium alloys by considering that the continuity of the network of adjacent dendrites bridged and welded in a liquid matrix could be evidenced by a sharp change in the amount of torque

required to rotate a disk in this continuous skeleton. He used a viscometer which measured the torque required to rotate a graphite disk in a slowly cooled melt. Since coherency depends not only upon physical bridging of the dendrites but also upon the shear strength of the resulting skeleton, it is difficult to specify a single value of torque at which coherency is complete; Claxton chose a torque of 2 in.-lbf (226 Nmm) and the measured coherency temperatures are reported in Table 2.2 together with the liquidus temperature and the solid fraction at coherency for various alloys. Highly dendritic structures lead to a solid fraction at coherency which is lower than for globular structure. The more skeletal the structure, the lower the solid fraction at coherency.

Alloy	Liquidus temperature [°C]	Coherency temperature [°C]	Solid fraction at coherency [%]
AA1100	658	657	44
AA3003	657	656	32
AA3004	651	649	27
AA5182	637	630	43

Table 2.2: coherency temperatures of selected alloys [Clax].

Arnberg et al. [Arnb] proposed a similar way of measuring the dendritic coherency: they used a plate which is slowly rotated in the melt during controlled solidification and the torque and temperature are measured. The coherency point is deduced from the derivative of the torque/temperature curve. In the light of their measurements, Arnberg et al. concluded that an increase in the amount of alloying elements will cause dendrites to become coherent earlier, i.e. at lower solid fraction. They also showed that grain refinement delays the dendritic coherency, while an increase of cooling rate will cause an earlier dendritic coherency point.

Although the mechanical behaviour of semi-solid alloys is of great importance for the modelling of thermomechanical stresses and hot tearing during casting, it is usually poorly known. Nevertheless, some interesting experiments have been designed by Ackerman and Kurz [Ack]. They recorded the force necessary to separate at a given rate two cylinders after they acquired a concentric layer of solidified metal over their entire surface. The tensile stress was therefore applied in a direction which was perpendicular to the growth axis of the columnar crystals. Ackerman and Kurz measured a strain-rate sensitivity

of 0.34 for the Al-0.5wt.% Mg alloy at temperatures around 650°C. In order to study the hot tearing, Wisniewski and Brody [Wisn] investigated the mechanical behaviour in tension of partially solidified Al-Cu alloys as a function of liquid fraction, microstructure and strain-rate and Decultieux et al. [Decul] performed hot-tearing tests derived from casting industry practice and based on a bar tensile condition due to the mould restraint.

The most relevant approach in investigating the mechanical behaviour of alloys in their solidification range was undertaken by Vicente [Vicen, Brans] who designed a rheological test which consisted in indenting at constant temperature and constant speed a solidifying alloy by a needle. The measured resistance was then interpreted in terms of a viscoplastic law using a finite element code (“computer-assisted rheology”) and assuming that the semi-solid behaviour of the metal can be described by a viscoplastic Norton-Hoff law:

$$\dot{\epsilon} = K \left( \frac{\sigma}{\sigma_0} \right)^n \quad (2.51),$$

where  $K$ ,  $\sigma_0$  and  $n$  are temperature dependent parameters. These parameters were fitted by comparing the result of a FEM code with the measured force-displacement curve. Figure 2.22 shows the increase in the strain-rate sensitivity ( $m = 1/n$ ) of the Zn-8wt.%Sn alloy from the solid to the semi-solid ranges.

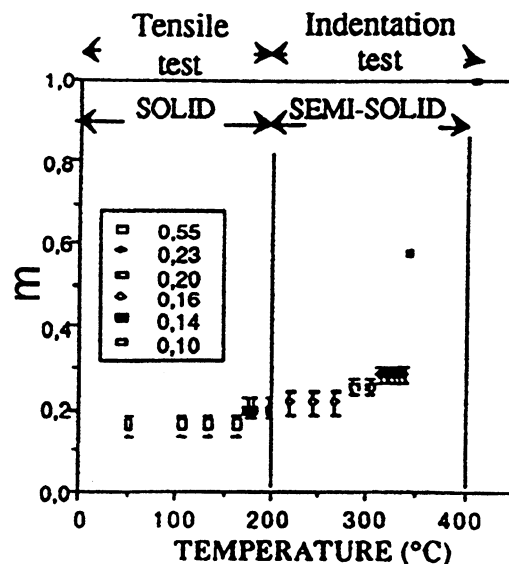


Figure 2.22: increase in the strain-rate sensitivity of a Zn-Sn8wt% in the solid and semi-solid temperature ranges as measured by tensile and indentation tests, [Vicen].

Experimental details and main outcomes of the current test are described in section 4 since this test was retained in this study to investigate the two

industrial aluminium alloys AA1201 and AA3104 at temperatures higher than the solidus.

Over the last few years, new metal forming processes in the semi-solid state have been developed [Flem2]: these processes are made possible because of the particular thixotropic properties of alloys when they are vigorously agitated during the early stage of solidification. The fluid-like character of the as-produced slurry is the result of the non-dendritic structure of the primary phase and it is retained after the alloy has been fully solidified and reheated beyond the solidus without agitation [Secon]. This kind of structure can be therefore deformed under very low stresses without any important segregation of the liquid phase. Recently, Nguyen et al. [Nguy] proposed an isothermal constitutive model for semi-solid alloys based on the concepts of continuous media and theory of mixtures.

## **2.3 Continuous casting of aluminium alloys**

### **2.3.1 Experimental investigations**

The number of articles dealing with the deformation of ingots during semi-continuous casting of aluminium alloys is rather limited. The deformation associated with the starting phase, namely the butt curl and butt swell (see section 1.3.2), has been studied by Spear and Hu [Spea, Hu]. These authors have found that these two distortions can be controlled by a reduction of the heat extracted through the bottom block. Instead of using pulsed water cooling during the start-up phase of the casting process, they suggested to inject carbon dioxide under high pressure into the ingot cooling water upstream of the mould and to cover the bottom block with an insulating pad. Droste and Schneider [Droste] have studied the effects of the casting velocity and of the cooling water volume on the butt curl and swell of DC-cast aluminium ingots. They showed that the butt curl increased with the casting speed and that very low water volumes and high casting velocities can promote film boiling mechanisms, thus leading to retarded cooling and strongly decreased butt curl. According to Lawrence [Law], butt swell could be eliminated if a flexible mould was used. Recently, Carrupt and Moulin [Carrupt] investigated the effect of the block design on the butt curl formation for both DCC and EMC technologies. They concluded that butt curl is not sensitive to bottom block design when using a reduced cooling technique like carbon dioxide injection or pulsed water.

The deformation of the ingot cross-section during the steady state regime of semi-continuous DC-casting and the mould design required to produce flat sheet ingots have been studied by Weaver [Wea1,Wea2]. This author considered an

incremental layer of metal AB in the longitudinal short transverse cross-section of the ingot as shown in figure 2.23 (right side): as solidification proceeds, this layer passes through the isotherms depicted in figure 2.23 (left side), cools and contracts to become A'B' and then A''B''. Weaver pointed out that to keep points B, B' and B'' on the centre line for symmetry reasons, point A must move towards the ingot centre as it takes the positions A' and A''. Further, this author carried out a large number of casting trials using the alloy AA1050 and changing the size and the casting speed. He showed that the ingot contraction is proportional to  $T^2 V$ , where T is the desired thickness of the ingot and V the casting speed.

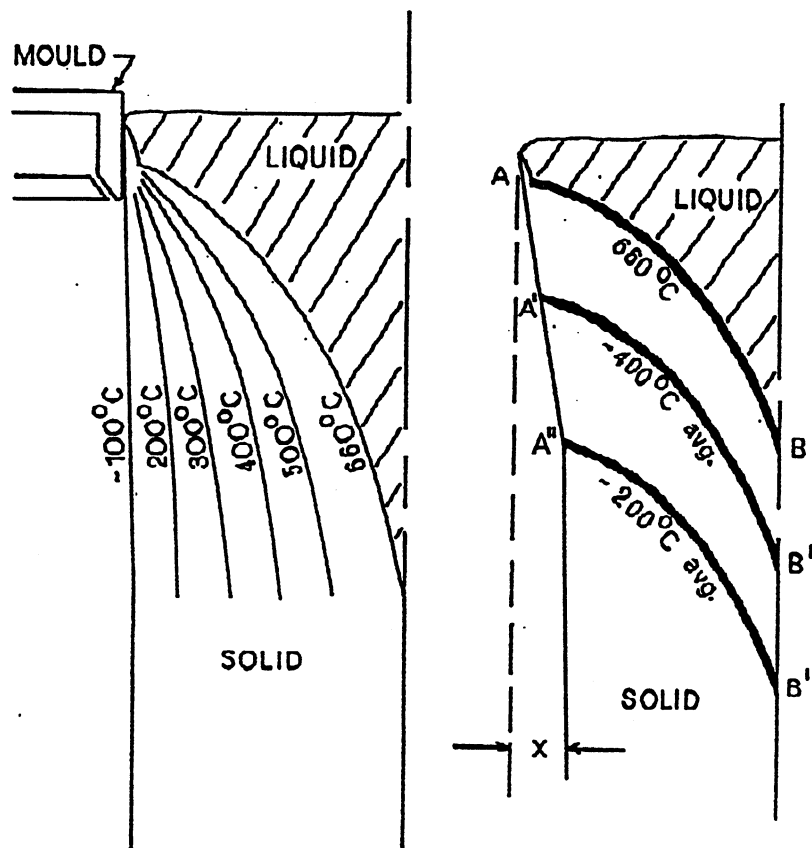


Figure 2.23: central ingot profile showing isotherms (left) and schematic representation of ingot rolling face pull-in mechanism (right), [Wea1].

Assuming that the heat extraction is radial (i.e., parabolic shape of the isotherms in the metal under the liquid pool), Weaver also showed that the sump depth is also proportional to  $T^2 V$ . Then, without giving a physically-based interpretation of this deformation, he proposed a semi-empirical model based on casting trials to predict the cross-section changes of DC-cast ingots. In order to produce “flat” ingots, he proposed the following relationship:

$$MO(x) = K_1 \cdot T + K_2(x) \cdot T^2 \cdot V \quad (2.52),$$

giving MO, the mould opening, as a function of  $x$ , the distance to the short sides of the ingot (see figure 1.4). The two alloy-dependent constants,  $K_1$  and  $K_2$ , were determined from the experiments.  $K_1$  corresponds to a uniform thermal contraction and  $K_2$  is a pull-in function which depends on the distance to the short sides of the ingots. Weaver also showed that the mould design required to produce flat ingots changed from a two-straight lines shape, to an almost sinusoidal shape and eventually to a three-straight lines shape when the aspect ratio of the ingot (width over thickness ratio) was increased [Wea2].

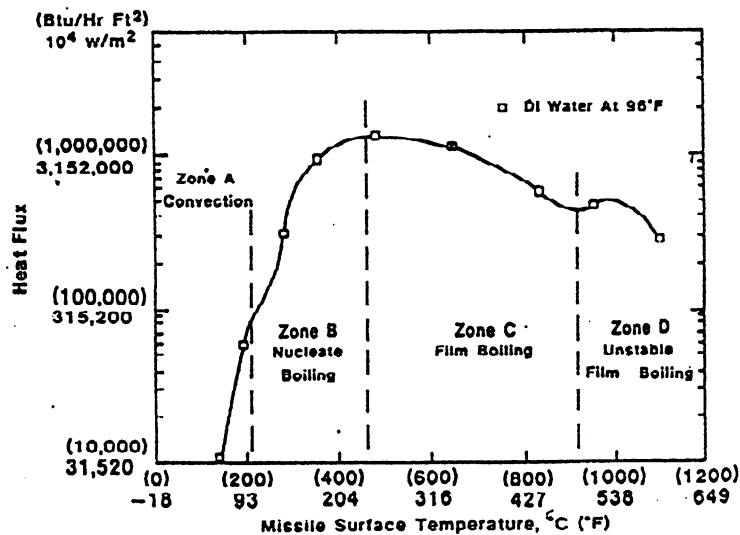


Figure 2.24: typical heat fluxes under different boiling mechanisms [Hu].

Since the air gap formation between the solidifying metal and the mould is directly linked to the pull-in of the rolling faces of the ingot, the heat transfer mechanisms between metal and mould and the formation of an air gap were also studied intensively, in particular by Ho and Pehlke [Ho] and by Nishida et al [Nish]. However, the air gap formation during the semi-continuous casting of aluminium alloys has not been investigated experimentally. DC casting of aluminium has been the subject of considerable development in recent years, mostly as a result of an improved understanding of the heat flow involved. Yu [Yu] studied the heat transfer mechanisms when quenching a preheated missile in water and showed that in the case of DC casting, the ingot cooling rate highly depends on the mode of boiling of the cooling water. Four mechanisms [Incro, chap.10] were distinguished depending on the missile temperature: unstable film boiling, film boiling, nucleate boiling and convection. These mechanisms are illustrated in figure 2.24.

### 2.3.2 Analytical models

The internal constraints which appear in castings were investigated by Weiner and Boley [Wein] in a theoretical study of a simple slab casting. These authors assumed elastic-perfectly plastic behaviour of the solid in which the yield point of the solid is zero at the melting point and increases as the casting cooled down. Considering a slab under the Neumann temperature distribution and constrained against bending but otherwise free of tractions, they found that plastic flow of the solid occurs at the very beginning of solidification. The elastic-plastic regimes and stress<sup>1</sup> history of a given particle during uni-directional casting are illustrated in figure 2.25.

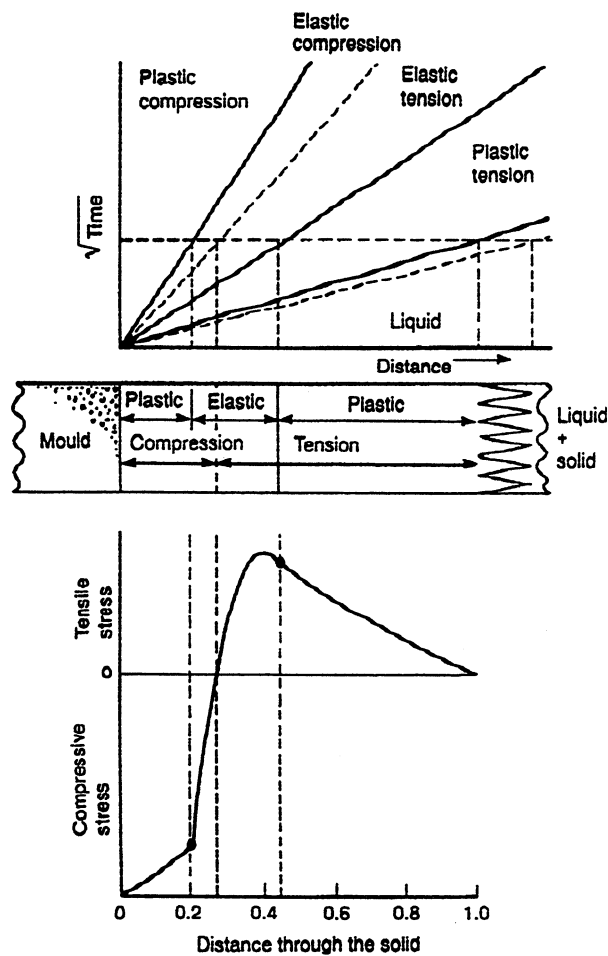


Figure 2.25: elastic and plastic regimes in a simple slab casting as found by Weiner and Boley [Wein].

On freezing, a given particle of metal is subject to tension, and since the yield stress is initially zero, its behaviour is at first plastic. As it cools down, the

<sup>1</sup> The authors calculated the stress normal to the solidification direction.



tensile stress on it increases and remains equal to the yield stress corresponding to its temperature until such time as the rate of increase of stress upon it is less than the rate of increase of its yield stress. It then starts to behave elastically. Soon after, unloading begins, the stress on the particle decreasing rapidly, becoming compressive, and finally reaching the yield stress in the opposite direction. Its behaviour remains plastic thereafter. To sum up the findings of Weiner and Boley, three deformation regimes are present in a solidifying material: a plastic zone in tension at the solidification front, since the strength of the solid is low; a central region where the stresses are in the elastic range; and a zone at the surface of the casting where there is plastic flow in compression (see figure 2.25).

The model by Weiner and Boley did not take into account any time-dependent flow or creep effects, which are certainly not negligible at temperatures near the melting temperature. Dour et al. [Dour] proposed an interesting semi-analytical approach for the calculation of the stresses induced by temperature inhomogeneities in continuously cast billets. These authors displayed the time evolution of temperature, stress and strain-rate in an Ashby type diagram (see section 2.2.2) using, as a visco-plastic law, the sum of all the mechanisms indexed by Frost and Ashby [Frost]. They made clear that purely plastic laws are irrelevant in such calculations and showed that diffusional flow at high temperature and power-law creep and later on power-law breakdown are the main active mechanisms in the thermally-induced plastic flow.

### 2.3.3 Numerical models

With the development of powerful numerical methods and computers, mathematical models for the simulation of fluid flow [Grün1, Grün2], heat flow and stress generation in a solidifying piece, are being used increasingly in order to understand better, to optimise and to design casting processes [Rich1, Zab, Thom1, Kat1].

Numerical methods became very useful to determine all the thermal boundary conditions associated with the casting configuration, especially the heat extraction along the faces of the ingot. Weckman and Niessen [Weck] studied the steady-state thermal field associated with the DC casting of AA6063 billets, using a finite element method. They derived the effective heat transfer coefficient as a function of the vertical position on the outside surface of the ingot using existing theories of forced convection, nucleate boiling heat transfer and film cooling and found good agreement with experimental data. Bakken and Bergström [Bak] proposed a method for the determination of surface heat

transfer to the cooling water and mould based on in-situ temperature measurements, the so-called "harp method". The heat flux was deduced from the measurements with the help of a polynomial collocation method but practical experimental error sources remained important.

Thermomechanical modelling of continuously cast ingots started first in the steel industry. Special attention was paid to the thermal stresses generation in the early stage of solidification and to the associated air gap formation [Rich2, Kris] as well as to the bulging of the strand induced by the ferrostatic head pressure [Gril]. Due to the much lower thermal conductivity of steel compared to aluminium and the associated deep liquid pool, the thermo-mechanical state of a strand can be computed under the assumption of two-dimensional generalised plane strain: this "slice method" consists in following a metal cross-section as it passes through the mould and then into the region where the surface is cooled by water sprays. Thomas et al. [Thom1, Thom2] developed a finite element model to predict first the thermal history and then the associated stress generation in a steel ingot using an elasto-viscoplastic constitutive relationship.

In DC/EM casting, the coupling between thermal and mechanical effects is particularly strong during the start phase: high thermal gradients induce thermal stresses which deform the ingot and these deformations modify in counter part the heat extracted through the starting block or the mould. The start phase of DC casting of aluminium slabs has been studied by Hannart et al. [Hann]. These authors computed in three dimensions the thermal stresses with special emphasis on the induced strains, which play a major role in the initiation of cracks and butt curl formation. Fjaer and Jensen [Fja2] recently studied the influence of the starter block shape on the butt deformation of sheet ingots whereas Jensen and Schneider [Jen] investigated experimentally and numerically the effect of various casting parameters on the crack tendency. Using an inverse heat transfer model, Wiskel and Cockcroft [Wiskel] investigated the surface crack formation during the start-up phase of the DC casting of the 5182 alloy. On the other hand, butt curl is particularly critical during the start-up phase of electromagnetic (EM) casting because the meniscus can be destabilized in the magnetic field leading to a premature cessation of the casting process [Kräh]. Mariaux et al. [Mar] developed a two dimensional numerical model which coupled thermal aspects with mechanical effects and computed butt curl during the EM-casting start phase.

Different degrees of sophistication in treating the plastic deformation of the metal and different numerical methods were used to compute the stress generation during semi-continuous casting. Moriceau [Mori] and Janin [Jan]

used a temperature-dependent elasto-plastic model to simulate the stress generation and to study the hot cracking tendency inside DC-cast round billets. Mathew and Brody [Math] introduced steady-state creep deformations into their analysis of the thermal stresses and Heinlein et al. [Hein] proposed a boundary element method to study transient temperature fields and associated stress fields in static solidifying bodies. Brody et al. [Bro2] emphasised the need of accurate mechanical properties of partially solidified alloys in order to predict correctly hot tearing of round aluminium ingots. The most comprehensive modelling work concerning thermomechanical effects during DC casting of aluminium billets has been carried out by Fjaer and Mo [Fja1]. These authors developed the finite element model Alspen in which the thermally-induced strains and stresses that develop during the casting process were calculated taking into account viscoplasticity but they did not address the computation of the rolling faces pull-in in three dimensions.

### **Conclusion**

It is surprising that in the previous studies of DC or EM casting, the non-uniform distortions of the ingot cross-section in the steady-state regime has not been investigated, whereas attention has been focussed on butt curl. Moreover, very few studies addressed the calculation of the solidification path of an alloy freezing in an equiaxed globular structure. This review will serve as a basis in defining a microsegregation and a thermo-mechanical model, with particular attention in determining the model input data.



## CHAPTER 3

# EXPERIMENTAL

Full-size DC and EM castings have been carried out in the experimental cast house of the Alusuisse company for several purposes:

- i) temperatures have been measured for the determination of the heat extraction along the rolling faces by inverse modelling,
- ii) as-cast samples have been obtained in this way for further laboratory investigations (mechanical testing, 1D castings, DTA and metallography),
- iii) the ingot contraction has been measured in situ and after complete cooling in order to validate the predictions of the thermomechanical 2D and 3D models.

These measurements are explained in section 3.1. On the other hand, thermomechanical calculations require a good knowledge of the properties (expansion coefficient, Young's modulus, viscoplastic parameters) up to the high temperatures. For that purpose, several experiments detailed in section 3.2 have been performed. Finally, the thermal conductivity, the solidification path and the final microstructure of the alloys have been determined, as reported in section 3.3.

### 3.1 Measurements on full-size DC/EM castings

#### 3.1.1 Alloys and casting conditions

Four non heat-treatable aluminium alloys were cast with the compositions given in Table 3.1. The grain refiner was the titanium boron aluminium alloy, Al-Ti5wt%-B2wt%. These four aluminium alloys are typical of the three main series of aluminium wrought alloys, AA1000, AA3000 and AA5000 series (see section 1.1). This first serie includes superpurity aluminium (higher than 99.99%) and the various grades of commercial purity aluminium containing up to 1% impurities or minor additional elements.

In the 3000 serie, the intermetallic compound that is in equilibrium with the solid solution has a composition closely corresponding to the composition of  $Al_6Mn$ . The binary Al-Mn alloys containing up to 1.25 wt.% Mn are commercially employed as non-heat-treatable alloys designated as AA3003. The

commercially more widely used alloy which has a further addition of about 1.2 wt.% Mg (3104), is particularly used in cans for the beverage industry.

Alloy/Element	Fe	Si	Mg	Mn
<b>1201</b>	0.41	0.14	0.012	0.018
<b>3104</b>	0.46	0.22	1.14	1.04
<b>5754</b>	0.24	0.18	2.75	0.27
<b>5182</b>	0.27	0.16	4.28	0.28

Table 3.1: Composition (wt%) of the four aluminium alloys investigated in the present study.

The Al-Mg binary system is the basis for a widely used class of non-heat-treatable aluminium 5000 series alloys containing from 0.8 to slightly more than 5 wt.% Mg.

Aluminium alloys of the 1000, 3000 and 5000 series are used in packaging through three main categories [Matu]: flexible packaging (use of flexible materials such as foil or sheet to form a container), beverage cans and closures for bottles. The beverage can industry is now the largest market in aluminium sheet. Due to the need for thinner walls for lower weight, the quality requirements of alloys used for cans, such as 3104 and 5182, are becoming more stringent, which demands a close control of the alloy processing right from the casting operation.

#### *Casting conditions*

The DCC and EMC trials were carried out at the experimental cast house of Alusuisse with a fully automated casting machine including a control of the metal level in the mould. The nominal ingot cross section was 1860 x 510 mm for the DCC trials and 1800 x 500 mm for the EMC trials; the cast height was typically 3 to 4 m. The casting parameters such as the water cooling flow rate and the metal distribution bags were kept constant for every combination of alloy and casting speed. A standard shape of the bottom block and pulsed water cooling techniques during the starting phase were employed for all the experiments. In the steady state regime of the DC casting, a low level of metal in the mould was reached (65 mm from the top of the mould).

The mould was not optimised specifically for these trial experiments. Its lateral side was made out of three straight lines as shown in figure 3.1. The contraction of the ingots cast with this mould was usually too large and non-uniform to fulfil the flatness requirements of an industrial production. Nevertheless, this mould allowed to carefully measure the contraction of the ingot. The inductor used for the EMC trials was designed to produce 500 mm thickness sheet ingots. The liquid metal was maintained all around the ingot at a constant distance of about 6 mm from a magnetic screen with the help of an electromagnetic field produced by a current of 6 kA and 2500 Hz circulating inside the inductor. The inductor and screen were also made out of three straight lines along the rolling faces of the ingot.

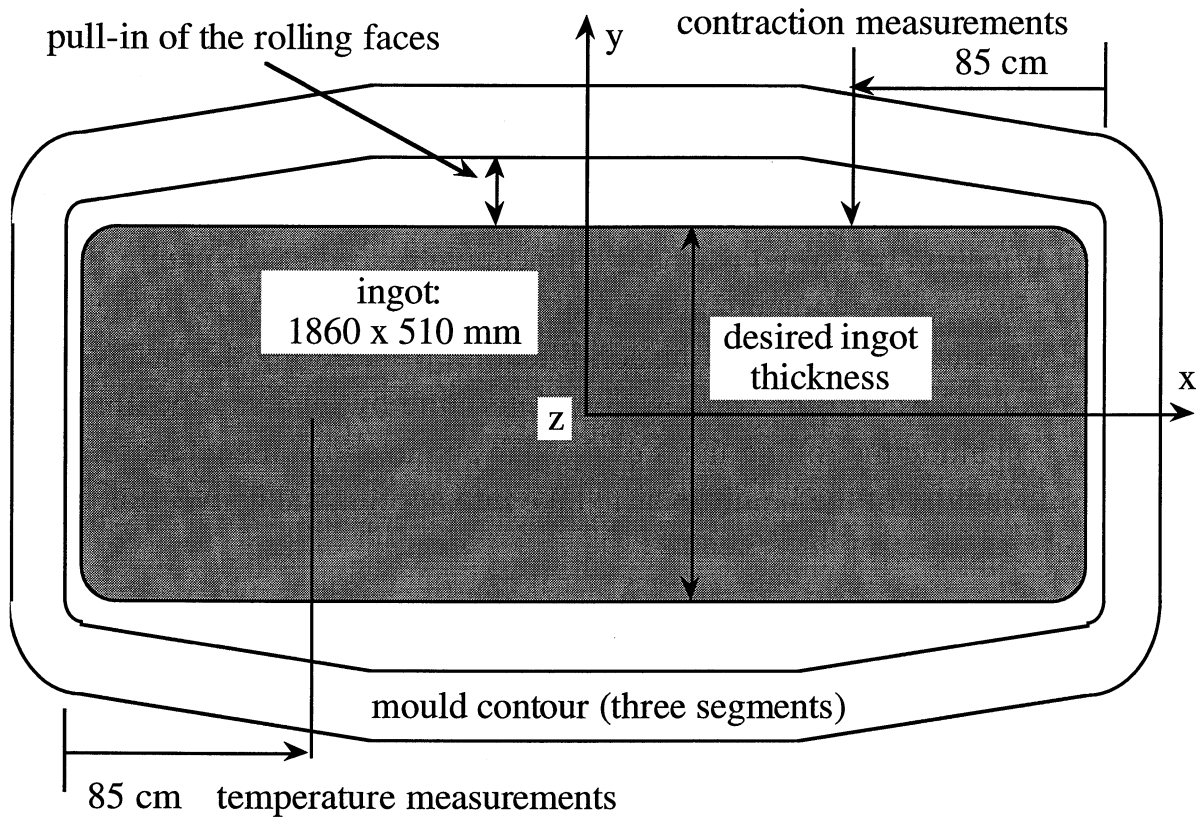


Figure 3.1: schematic top view of the mould shape and position of the experimental set-ups.

### 3.1.2 Deformation and temperature measurements

#### *Deformation measurement after cooling*

After complete solidification and cooling of the ingot in the pit, it was reintroduced through the mould/inductor and the lateral contraction of the ingot was measured every ten centimetres around the slab and at different heights: in

the butt zone, at mid-height (at least 2 meters from the butt in order to ensure nearly steady-state conditions) and in the upper part (head) of the casting.

#### *Sump depth and cooling curves measurements*

Figure 3.2 shows the experimental set-up used to determine the sump depth. This measurement was made at 85 cm from the short side of the casting (see figure 3.1). A set of five thermocouples attached to the end of stainless steel rods was introduced into the metal during casting after a steady-state regime was reached. The last rod was submerged along the centre line of the ingot and the first one was near to the lateral surface. In order to make sure that the five rods “disappeared” at the constant withdrawal speed in the liquid pool, they were pulled downwards by two non-instrumented guiding rods, previously introduced into the metal. During their descent, the rods were guided through a specially designed rail (see figure 3.2). The type K thermocouples (Chromel-Alumel) were linked to a data-logger and the five temperatures were recorded every 0.1 second. This method allowed the sump depth to be calculated by considering the end of solidification measured by the thermocouple placed at the centre line of the casting. Such measurements also gave the temperature profile in the solid part of the ingot and the shape of the solidification front during the steady-state casting regime. These results were used to determine by inverse modelling the heat extraction along the rolling faces of the slab and to adjust the increase in the thermal conductivity of the liquid so as to take into account the convection in the liquid pool.

#### *In-situ measurement of the air gap*

Figure 3.3 shows the experimental set-up used to measure the gap distance between the metal and the mould/inductor during the steady-state of the process. This set-up was located 85 cm from the other short side of the ingot (see figure 3.1). A quartz rod carrying two thermocouples was introduced into the liquid pool. The rod was free to move downwards through a guiding cylinder and at the same time, it was also free to move along the stand by translation of the cylinder on two guiding rails. The quartz rod first dropped into the liquid under its own weight and its extremity was then “swallowed” by the mushy zone. From that instant, the quartz rod moved downwards at the casting speed of the ingot. When the solidifying metal shell pulled away from the mould surface, the rod followed and its lateral and vertical displacements were recorded by two sensors. The two thermocouples inserted into the quartz rod measured the temperatures at two locations near to the ingot surface (see figure 3.3).



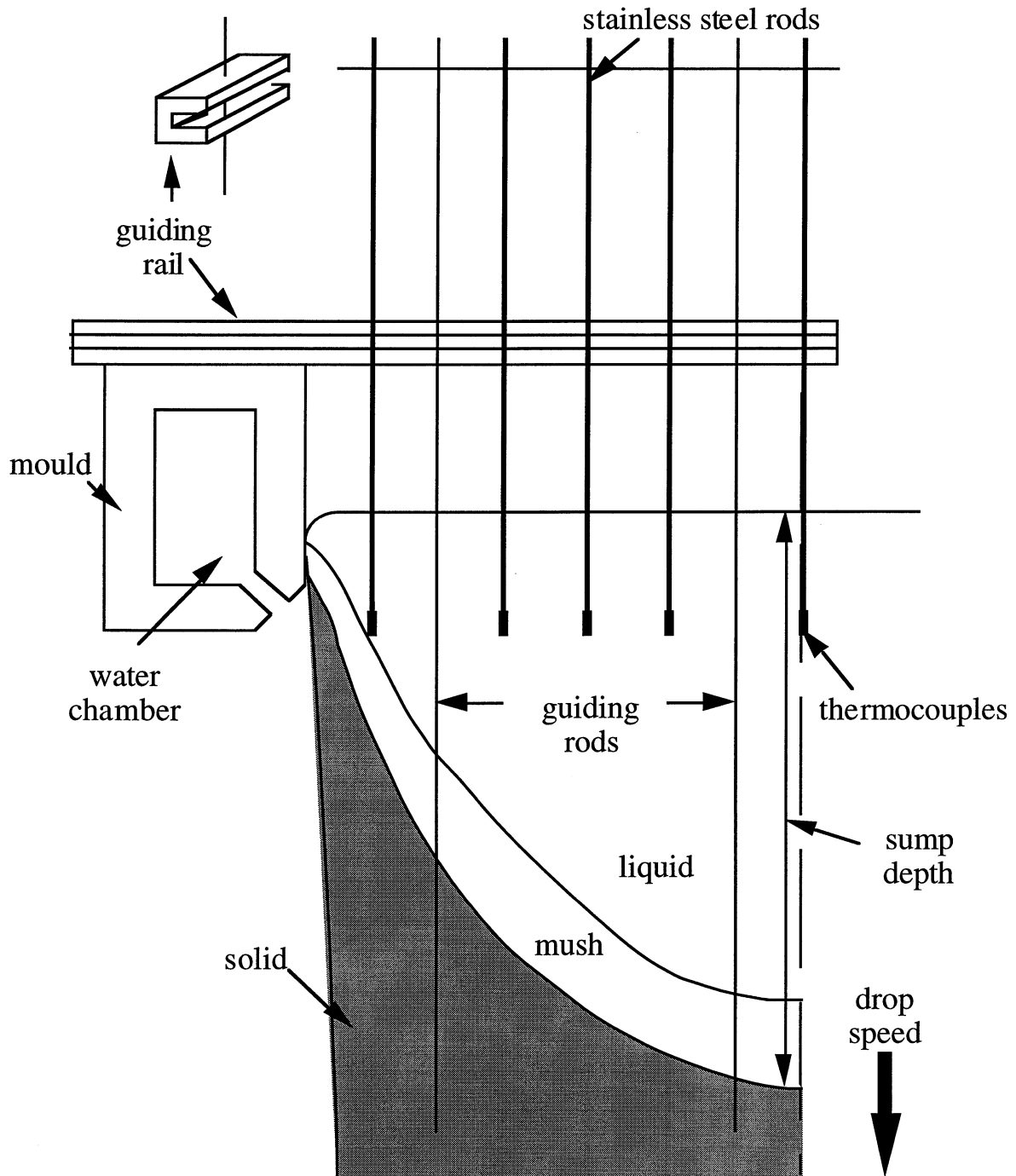


Figure 3.2: experimental set-up for the measurement of the temperature profile and sump depth.

These data permitted to assess more precisely the shape of the mushy zone near the mould wall. In order to test the accuracy of this simple set-up, the contraction measured at the exit of the mould/inductor was compared with the value given by a displacement sensor, which was attached to the bottom of the mould/inductor. It is to be noted that the two thermocouples wires were not soldered together since they were directly immersed into the molten aluminium. Thus, the time of entrance of the rod into the liquid pool could be determined accurately from the time of electrical contact.

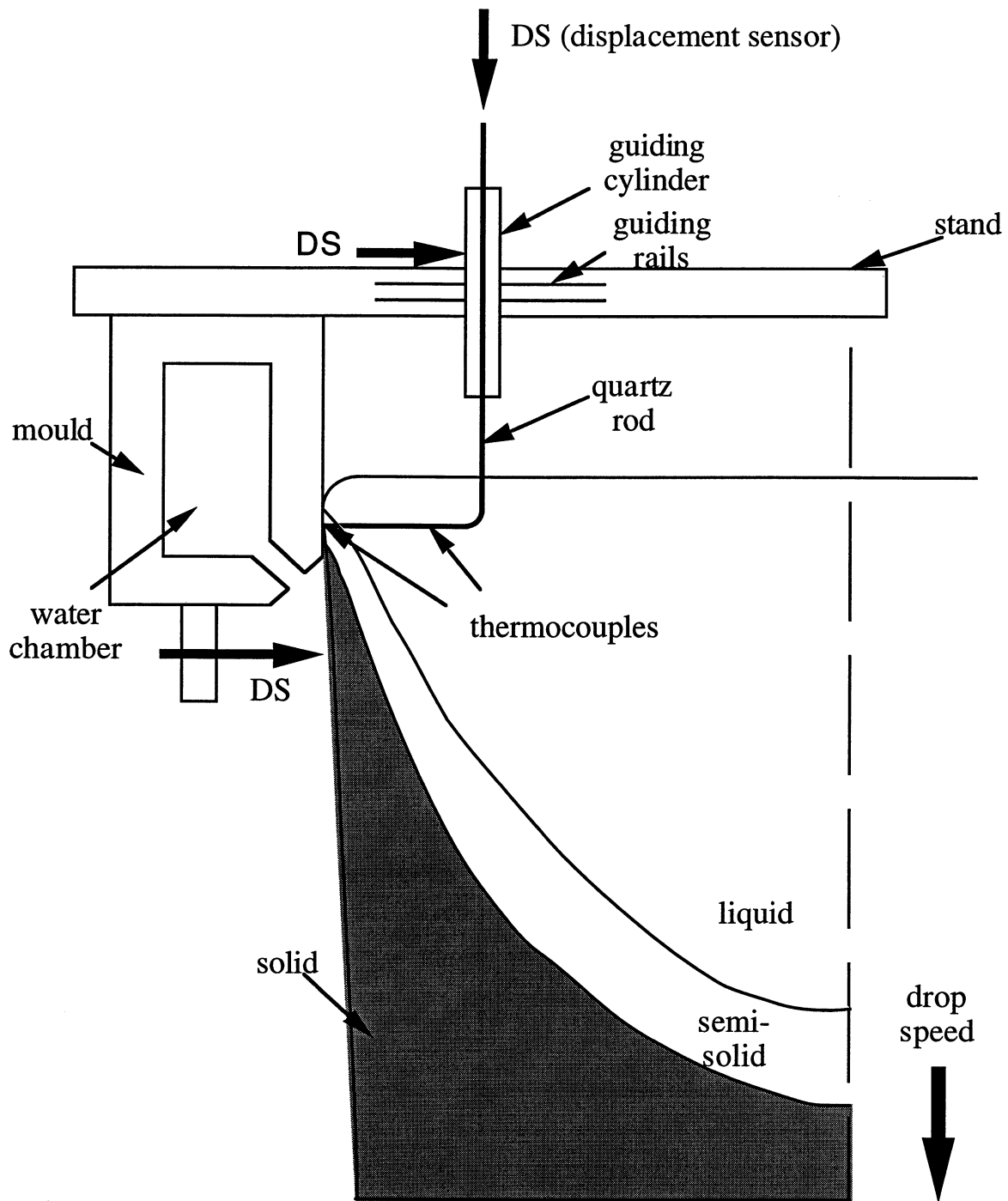


Figure 3.3: experimental set-up for the in-situ measurement of the casting displacement inside the mould/inductor.

The results concerning these in-situ measurements during DC/EM casting are given in chapter 5.

## 3.2 Mechanical testing

### 3.2.1 Dilatometry

The measurement of the thermal expansion coefficient of the alloys 1201 and 3104 was performed in air atmosphere using the high temperature

dilatometer SETARAM (DHT 2050K) at the Laboratory of Ceramics (LC/EPFL). The principle of the dilatometer is described in figure 3.4. The sample, a cylinder (diameter 10 mm, height 15 mm) of aluminium, is placed inside a vacuum chamber.

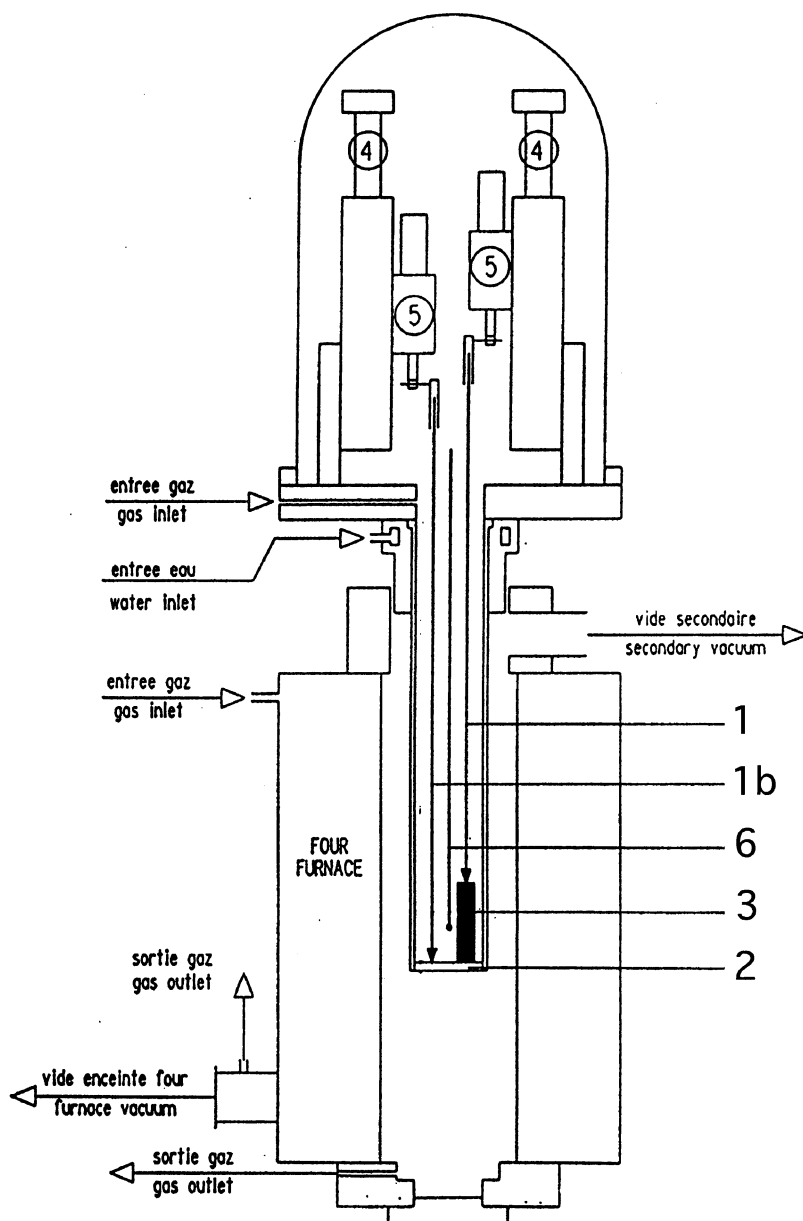


Figure 3.4: schematic diagram of the dilatometer, (1) and (1b) sensors, (2) stand, (3) sample, (4) optical displacement sensor, (5) force sensor and (6) thermocouple.

One sensor (measurement) monitors the movement of the top surface of the sample whereas another sensor (reference) detects the stand, a piece of alumina, on which lies the sample. The movement of each sensor is measured by an optic displacement sensor. The force applied on the sensors is monitored by two force sensors and limited to a given value. A thermocouple measures the temperature near the sample. The high temperature dilatometer gives reliable results only for

temperatures higher than 200°C. For the present measurements, the sample temperature was increased at a constant rate, 10°C/min, up to the coherency temperature of the alloy. The relative displacement of both sensors was automatically interpreted as the differential linear thermal expansion of the sample at a given temperature.

The results obtained for pure aluminium (Al 99.999%) and the alloys 1201 and 3104 are shown in section 5.

### **3.2.2 Measurement of the Young modulus using ultrasonics**

The measurement of the Young modulus from room to near melting temperatures was performed using an ultrasonic sound method developed at the Ecole Nationale Supérieure des Céramiques Industrielles (ENSIC-Limoges-France). In the seventies, Lynnworth [Lynn] and Papadakis [Papa] showed the ability of such a method to measure the elastic constants of solids at high temperatures. The backgrounds of the pulse-echo method are fully detailed in the thesis by Cuttard [Cutt] and a brief description is given hereafter.

The measurements described here were carried out with the system illustrated in figure 3.5, consisting of a pulse generator (Panatherm 5010), a two-channel oscilloscope with camera, and a magnetostrictive transducer attached to an ultrasonic transmission line (wave guide or lead-in wire), which in turn is attached to the specimen. A transmission line between the specimen and the transducer is required because the first one is placed in a furnace whereas the second one must be kept below its Curie temperature (around 300°C) so as to preserve its magnetostrictive properties. The thermal and mechanical coupling in between the different parts forming the wave guide and the specimen, is achieved by the use of greases or refractory cements. Tungsten wire is used for the part of the ultrasonic transmission line that is connected to the magnetostrictive transducer whereas alumina is used for the part connected to the specimen. The specimen and a portion of the lead-in wire are placed within an electric heating system (Eurotherm) in air. A Pt-Pt 10wt% Rh thermocouple monitors the temperature of the tested sample which is heated at a constant rate of 1°C/min. The magnetostrictive transducer is a ferromagnetic bar (Remendur or PTZ ceramic), which must be polarised by a permanent magnet as shown in figure 3.5.

Under a pulse of current, the magnetic field generated inside the coil induces the production of an ultrasonic vibration by the ferromagnetic bar owing to its magnetostrictive properties. The generated ultrasonic pulse travels to the specimen and echoes from the ends of the specimen. The resulting echoes are

sensed by the transducer and displayed on the oscilloscope as indicated in figure 3.5. Each interface between the different parts of the wave guide leads to reflection and partial transmission of the ultrasonic wave. By modifying the sections and lengths of these parts, the acoustic impedance of the transmission line can be adjusted so that the attenuation of the echoes is estimated to the point of being unusable, and the superposition of echoes avoided. The ultrasonic system uses broad-band pulses of centre frequency around 100 kHz. As-cast samples of 1201 and 3104 aluminium alloys were machined so as to obtain cylinders, 5 mm in diameter and 8 cm in length.

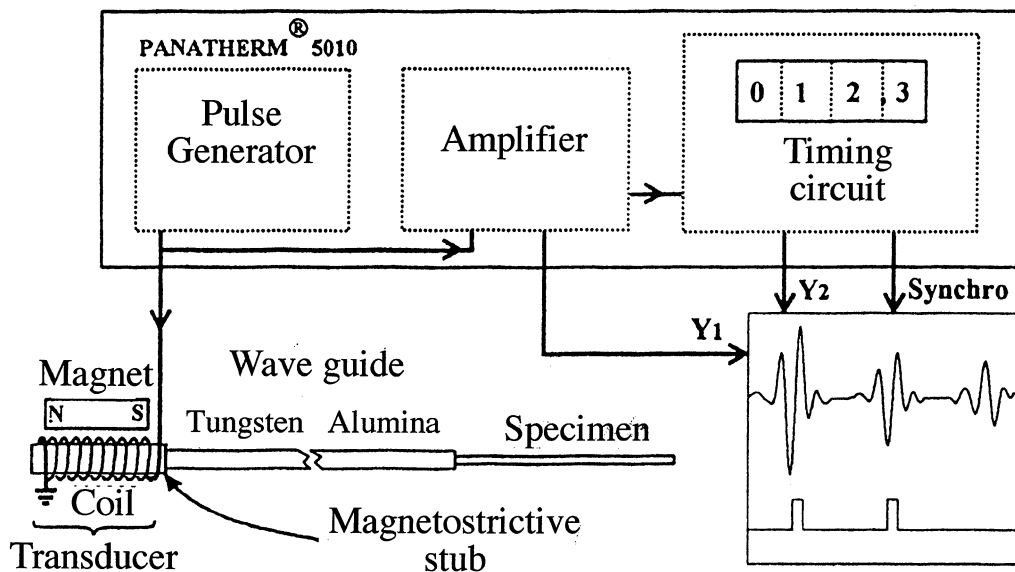


Figure 3.5: Electronic and ultrasonic system used for measuring travel time and echo amplitudes. Instrument has facility for selecting half-cycles within echoes and measuring time between centres of selected half cycles.

The pulse generator measures the travel time between pairs of echoes selected by the observer by means of “selector monitor” adjustments on the instrument [Papa]: the first echo comes from the reflection on the entrance surface of the specimen, the second one from the end. The travel time,  $t$ , is the mean value of 50 measurements. For a specimen of length  $L$ , the velocity,  $v$ , of an ultrasonic wave inside the specimen is given by:

$$v = \frac{2L}{t} \quad (3.1).$$

Provided the diameter of the specimen (5 mm) is small compared to the wavelength<sup>1</sup> (about 5 cm) [Lynn], the velocity  $v$  is related to the Young's modulus  $E$  and the density  $\rho$  of the specimen by:

$$E = \rho v^2 \quad (3.2).$$

In this calculations, the density has been given the constant value of 2650 kg/m<sup>3</sup> but the length of the specimen has been corrected for thermal expansion using the linear thermal expansion coefficient as found in Hatch (cf. appendix II). The time interval between any pairs of echoes is read within  $\pm 0.05 \mu\text{s}$ , thus leading to errors in modulus evaluation less than 0.5 percent. The results of the temperature-dependence of the Young's modulus of the 1201 and 3104 alloys are given in chapter 5.

### 3.2.3 Tensile creep tests

Tensile creep tests were carried out by applying a given tensile load to the sample held at a fixed temperature, using the high resolution creep machine Mayes (TC.30) at the Mechanical Metallurgy Laboratory (LMM/EPFL). A schematic of the equipment used to apply a constant load to a specimen maintained at high temperature is shown in figure 3.6. The lever-loading ratio is 1:15 and the specimen is located within the uniform hot zone of a three zone temperature-controlled furnace. To ensure that the load is applied axially to the specimen, universal couplings and crossed-knife edge connections are incorporated into the loading system. They act as "links in a chain", avoiding bending stresses in the specimen under load. During loading, the capstan is adjusted until the loading lever is horizontal. A load cell (30kN) measures continuously the load applied to the specimen. A uniform temperature zone (maximum difference lower than 4°C) is obtained in the middle of the furnace.

Creep strain measurement required machining annular ridges near the ends of the specimen gauge length, as depicted in figure 3.7. Two extensometers, with heads having grooves exactly fitting over the specimen ridges, were attached to the test piece. Under the tensile load, the bottom pull rod does not move but the top pull rod moves vertically upwards as the specimen extends by creep deformation. The extensometer arms extend out of the furnace so that changes in gauge length can be monitored continually by measuring the relative movement of arms attached to the top and bottom of the specimen, as shown in

---

<sup>1</sup> This wavelength is also large compared to the characteristic size of the heterogeneities present in the specimen, notably the grain size (100  $\mu\text{m}$  for as-cast samples).

figure 3.7. Two inductive linear displacement transducers, T1 and T2 in figure 3.7, monitor the specimen elongation. If the system is well aligned, each transducer records the same specimen extension: this is used to check the alignment of the loading system. The precision when measuring the extension of the specimen is close to 0.05% at an elongation of 10 mm.

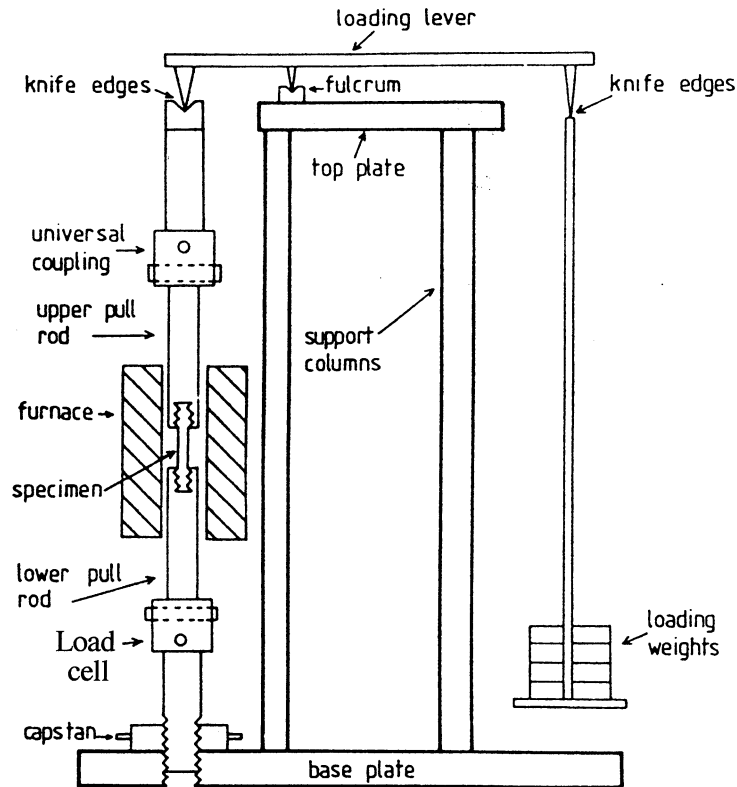


Figure 3.6: schematic illustration of the lever-loading creep machine.

From as-cast alloys, standard creep specimens with a 40 mm gauge length and a 14 mm diameter were machined [Drez2].

While the applied load remains constant throughout the creep test, the true stress on the specimen increases as the specimen extends and the cross-sectional area decreases. Considering a specimen of original length  $l_0$  and cross-sectional area  $A_0$  creeping under a constant force  $F$ , the length becomes  $l$  and the cross-sectional area becomes  $A$  after a time  $t$ . Assuming constant specimen volume, the true stress,  $\sigma$ , can be calculated:

$$\sigma = \frac{F}{A} = \frac{F}{A_0} \cdot \frac{l}{l_0} = \frac{F}{A_0} \cdot \exp \epsilon \quad (3.3),$$

the true strain  $\epsilon$  being defined as:

$$\epsilon = \ln \left( \frac{l}{l_0} \right) \quad (3.4).$$

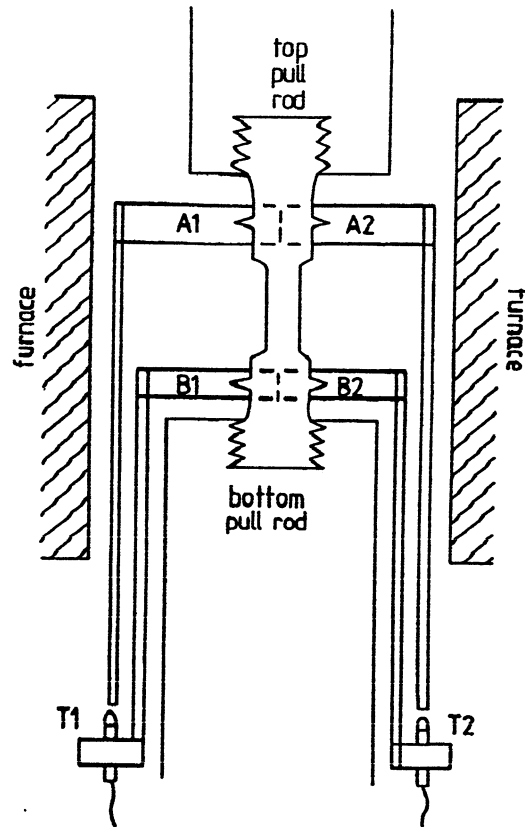


Figure 3.7: schematic diagram showing the extensometer fitting onto annular ridges on the test piece. A1 and A2 are the extensometer heads at the top and B1 and B2 at the bottom. T1 and T2 are two transducers monitoring the relative movement of the extensometers.

The creep testing machine used for the present investigation is linked with a data acquisition system (HP216 and Macintosh). A reading is performed every 15 sec. The stored quantities are :

- $t$ , current time
- $T_1$  and  $T_2$ , the temperatures measured on the specimen
- $\epsilon_1$  and  $\epsilon_2$ , the elongation recorded by the two extensometers
- $F$ , the load applied on the test piece.

Using the mean value of  $\epsilon_1$  and  $\epsilon_2$ , the true stress and the creep rate,  $\dot{\epsilon}$ , are automatically calculated and stored. A typical creep curve is shown in figure 3.8. The deformation is reported on the left axis and the creep rate on the right axis using a logarithmic scale. Such curves allow a precise determination of the minimum creep rate for a given alloy, temperature and load.



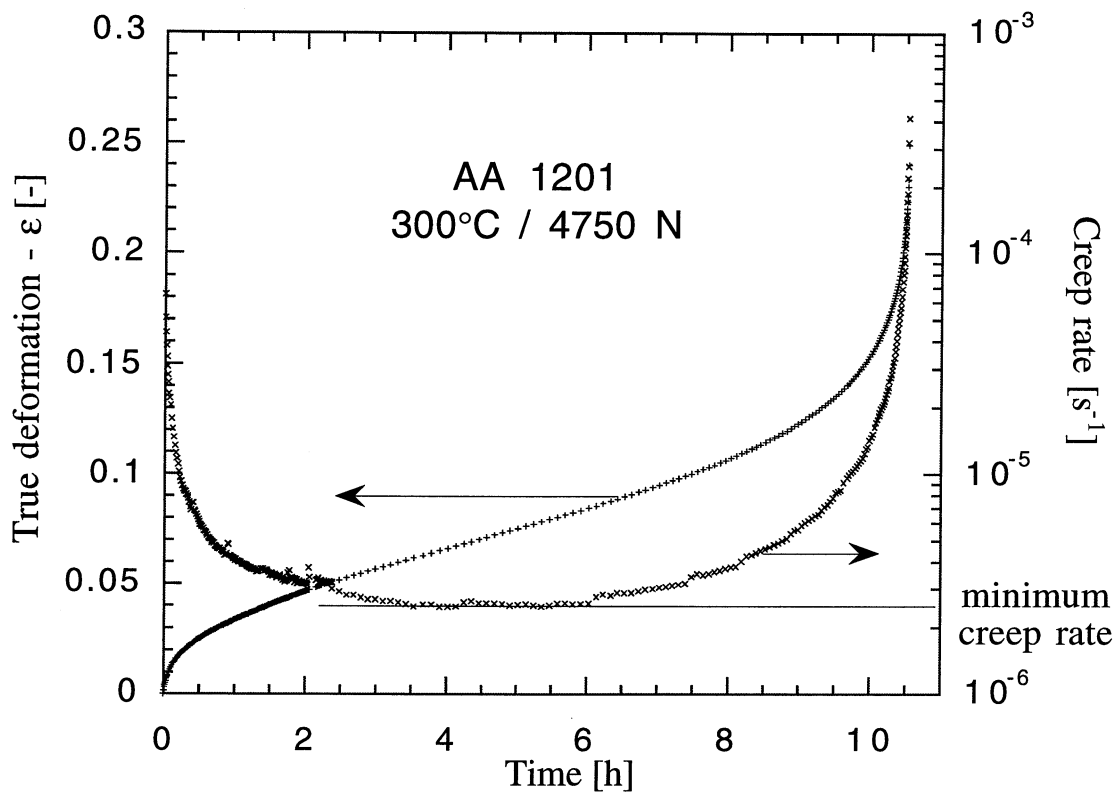


Figure 3.8: typical creep curve and determination of the minimum creep rate.

Creep tests were performed with the alloys 1201 and 3104 at temperatures ranging from 300 °C to 645°C and at stresses between 0.25 and 30 MPa (see chapter 5)

### 3.2.4 Indentation tests

Although the mechanical behaviour of semi-solid alloys is of great importance for the modelling of thermomechanical stresses and hot tearing during casting, it is usually poorly known. In the present case, the mechanical behaviour of the 1201 and 3104 alloys in the semi-solid state was investigated in compression using the simple indentation test capable of reproducing the typical strain rates encountered in solidification processes ( $10^{-4}$  -  $10^{-1}$  s $^{-1}$ ) [Dour] and developed at the Cemef (Ecole des Mines de Paris / Sophia Antipolis). The idea is to associate a simple test geometry with a numerical FEM analysis of the obtained flow. This kind of approach was named Computer Assisted Rheology [Brans, Vicen]. It can also be thought as an “inverse mechanical modelling”.

A heated metal crucible was used to melt and control the temperature of the alloy (volume: about one litre). The temperature was kept constant and uniform as far as possible throughout the ingot: this was not easy to achieve since the latent heat release of the alloy perturbs the temperature control. An as-cast sample was first heated to a given temperature in the solidification range and

then indented by a 6 mm diameter needle that was pushed at a constant rate into the metal. The description of the apparatus is given in figure 3.9. A thermocouple (type K) placed at the extremity of the needle, allowed a close control of the temperature. A load cell (50 N, 500 N and 5000 N) recorded the resistance to deformation of the metal.

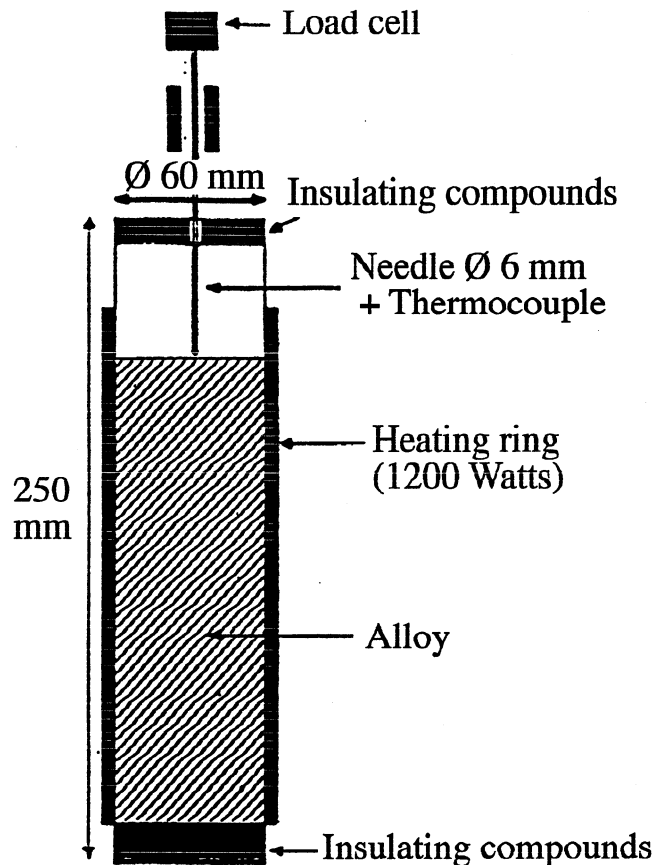


Figure 3.9: experimental set-up for the indentation test.

The basic assumption is that the semi-solid behaviour of the metal can be described by a viscoplastic Norton-Hoff law:

$$\sigma = K(T) \cdot \dot{\epsilon}^m \quad (3.5),$$

where  $K(T)$  is the temperature-dependent consistency and  $m$  the strain rate exponent for the stress. The viscoplastic Norton-Hoff law is incorporated in the FEM software code FORGE2, originally developed at Cemef for forging [Bellet] and integrating an automatic remeshing facility. Figure 3.10 shows the details of the enmeshment of the metal under the needle (axisymmetric situation). FORGE2 was used to predict theoretical force versus needle displacement curves with various values of  $m$ . Such calculated curves are shown in figure 3.11 with a consistency of  $1 \text{ MPa s}^m$ . After a transient hardening stage,

the force presents a linear regime with a low slope increase due to friction on the needle sides. Note that  $m = 1$  corresponds to a Newtonian flow. Above a certain temperature, the force-displacement curves of the needle present many fluctuations and their shape are totally different from the simulation result. Below this temperature, the experimental curve is fairly smooth (see figure 3.12) and agrees with the numerical result. This temperature is considered to be the coherency temperature of the alloy (see section 2.2.5).

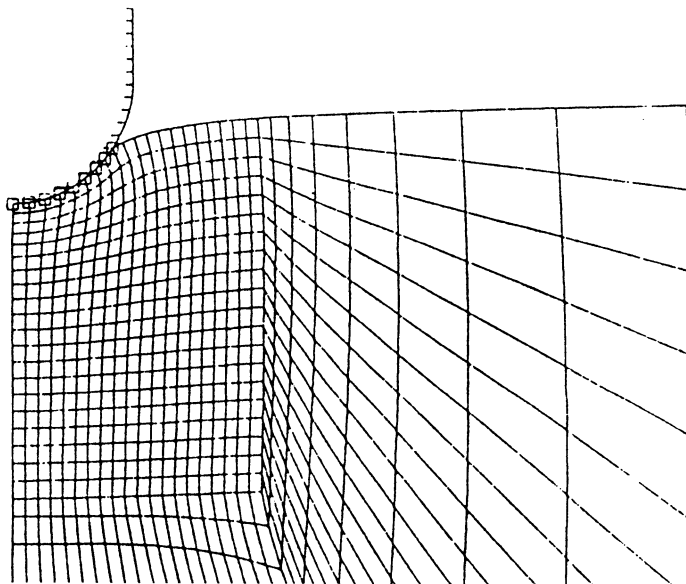


Figure 3.10: detail of the enmeshment under the needle used by FORGE2 to compute the force-needle displacement curves.

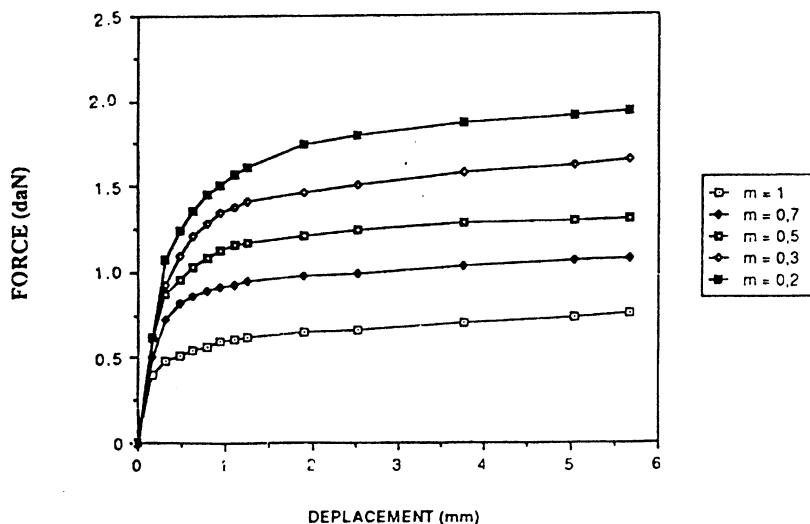


Figure 3.11: computed force-needle displacement curves for different values of  $m$  ( $K = 1 \text{ MPa s}^m$  and  $V = 0.02 \text{ m/sec}$ ).

Experimental curves obtained for the 1201 alloy at  $635^\circ\text{C}$ , i.e.  $5^\circ\text{C}$  above the solidus temperature, are presented in figure 3.12 for three different

indentation speeds. The force at the curve slope change,  $F$ , is determined, for each needle speed, as the intersection of the initial hardening regime and the linear regime as shown in figure 3.12 (alloy 1201 at 635°C).

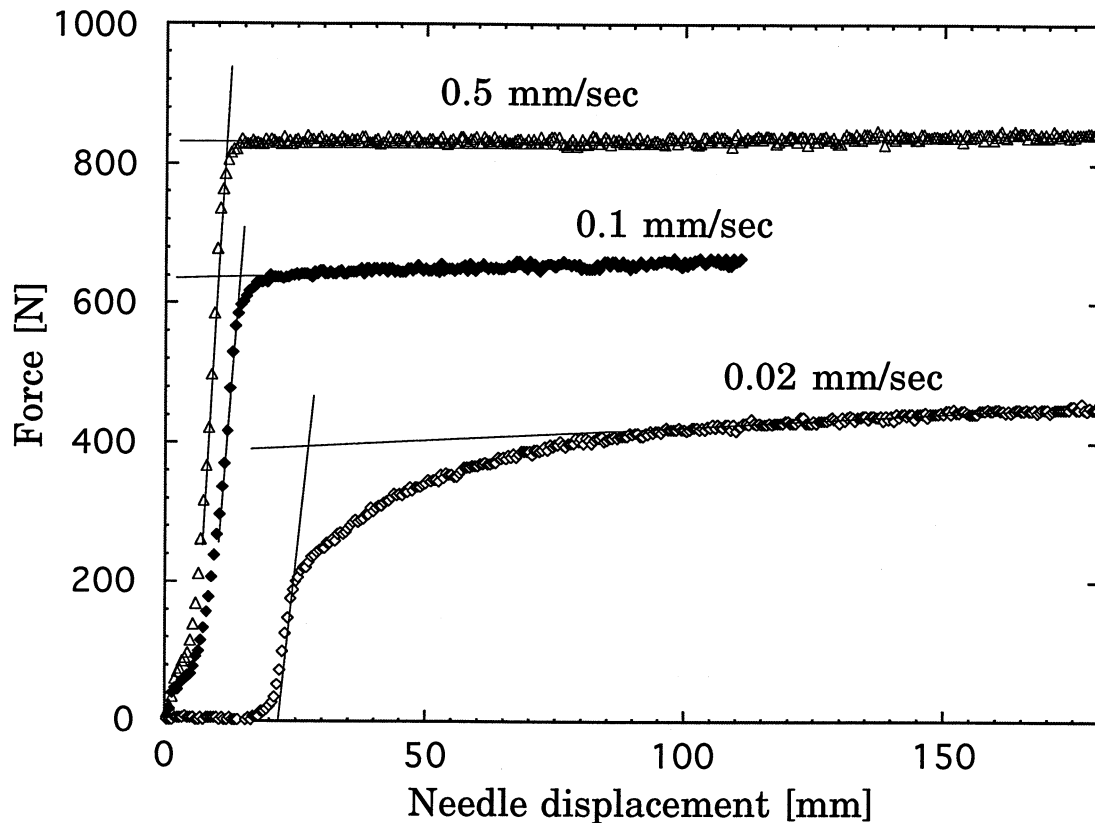


Figure 3.12: experimental force-needle displacement curve measured at 635°C for the alloy 1201 and determination of the strength at the slope change.

Assuming that the needle speed,  $V$ , is proportional to  $\dot{\epsilon}$ , the strength  $F$  is therefore proportional to  $V^m$  (equation 3.5). Hence, the strain-rate sensitivity exponent,  $m$ , is taken as the mean slope of the curve  $\ln F - \ln V$ , as shown in figure 3.13. Knowing the values of  $m$  at each temperature, it is then possible to obtain the consistency,  $K(T)$ , by adjusting the experimental curves with the numerical ones (see figures 3.11 and 3.12). The results concerning the determination of the coherency temperature, the consistency and the strain-rate sensitivity exponent for the alloy 1201 and 3104 are given in paragraph 5.1.

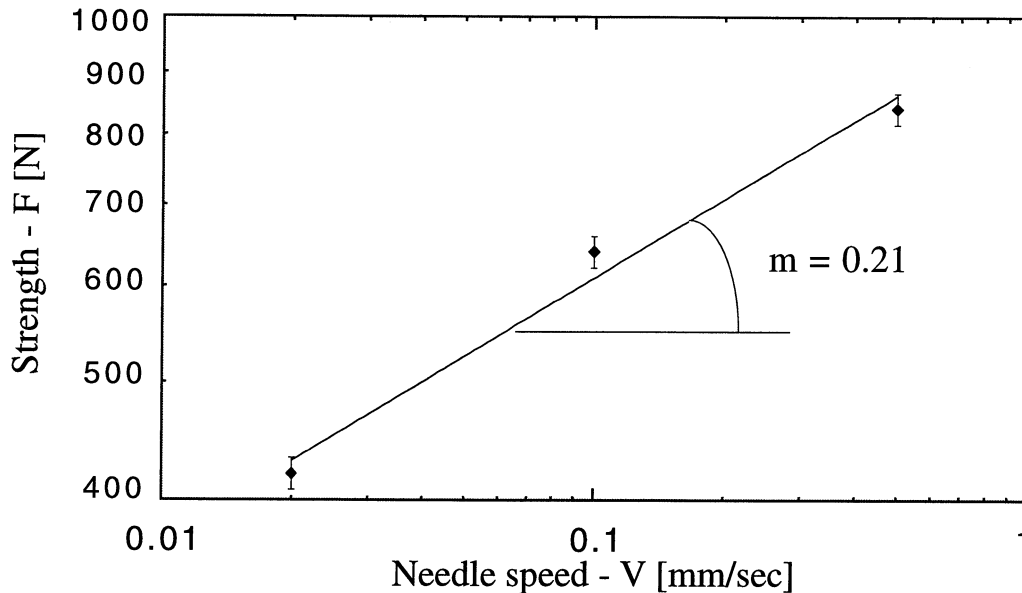


Figure 3.13: strength as a function of the needle speed and determination of the strain-rate sensitivity exponent,  $m$  (1201 at 635°C).

### 3.3 Laboratory investigations

As-cast samples directly cut and machined from DC-cast slabs were used for further laboratory investigations: instrumented 1D castings for thermal conductivity estimation, differential thermal analysis and metallography.

#### 3.3.1 Unidirectional laboratory casting

Cylindrical castings, 70 mm in diameter and about 15 cm in length, of 1201 and 3104 aluminium alloys were solidified in the laboratory under one-dimensional heat flow conditions using the experimental set-up described by Ampuero et al [Ampu] and schematically presented in figure 3.14. This set-up has the advantage to prevent any convection associated with pouring effect since the ceramic mould and the metal are first preheated together in a furnace. The casting procedure is as follows:

- the as-cast alloy is melted in a crucible using an electric furnace (Solo),
- the instrumented ceramic mould is preheated at 750°C in another furnace (about 2 hours),
- the liquid alloy is cast in the preheated ceramic mould<sup>1</sup> surrounded by the furnace,

<sup>1</sup> A lid is added on the top of the mould so as to reduce heat losses.

- the system is left for about one hour until a uniform temperature (about 720°C) is reached. The furnace is then removed and a water-cooled copper chill is applied to the bottom surface of the mould; at the same time, the data acquisition is started.

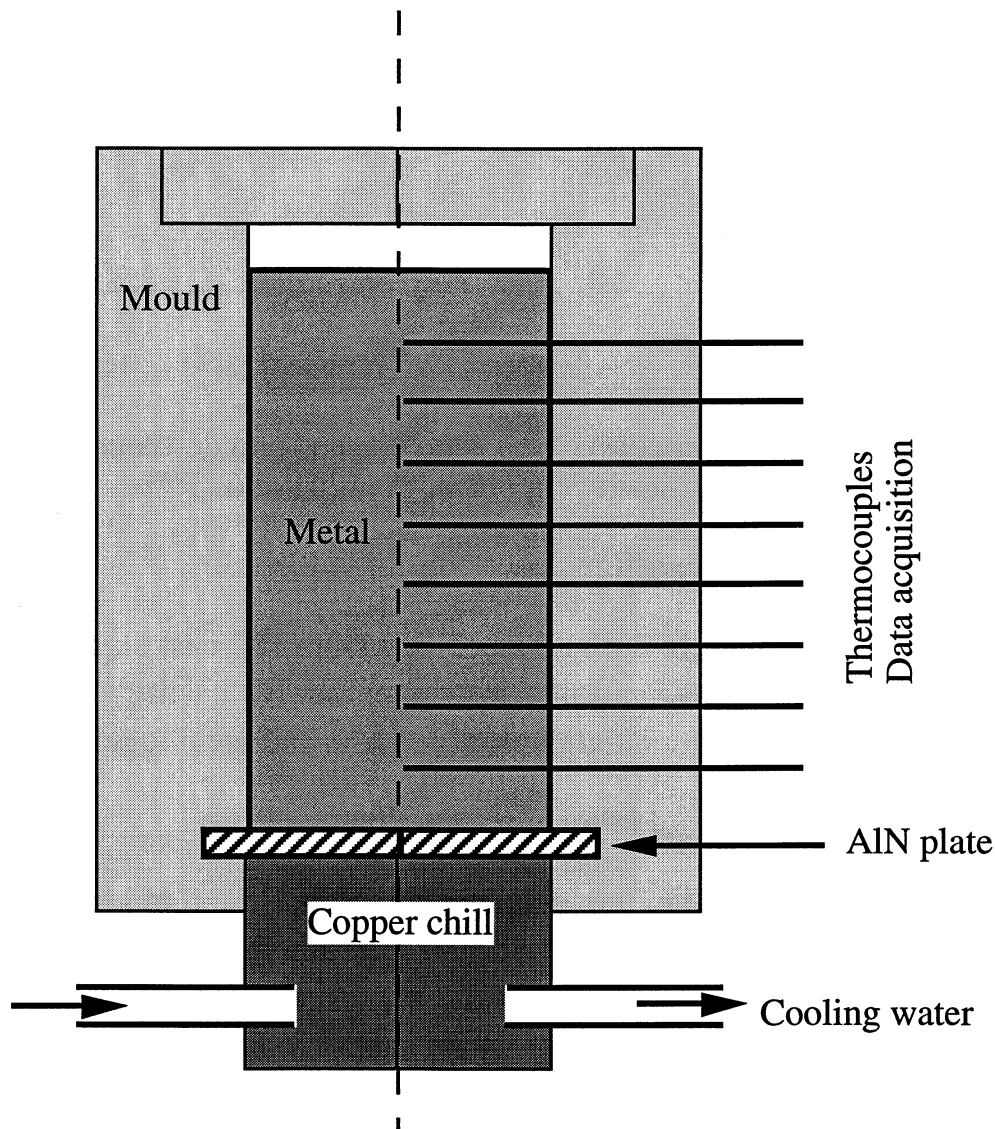


Figure 3.14: experimental set-up used for the 1D castings.

The ceramic mould is made out of different pieces of a very low thermal conductivity (about 0.1 W/mK) and high temperature resistant material (Promat™) and the copper chill probe has the same diameter as the cast cylinders. The bottom surface of the mould is made out of a thin aluminium-nitride (AlN) plate having a high thermal conductivity (around 150 W/mK) and a good thermal shock resistance. It is previously covered by a thin layer of alumina so as to prevent the metal from sticking on it. Hence, a nearly unidirectional heat flow situation is obtained inside the casting.

Eight Pt/PtRh10% (type S, 0.2 mm diameter wires) thermocouples in two-hole alumina capillary tubes, 1.2 mm in diameter, were then placed at various heights in the ceramic mould (10, 20, 40, 60, 80, 100, 120 and 140 mm from the bottom surface) in such a way that the welded beads were along the axis of symmetry of the mould, as shown in figure 3.14. The data acquisition of the temperatures recorded in the casting was carried out using a high precision Hewlet Packard (HP3457A) voltmeter and an acquisition unit linked to an HP310 microcomputer.

The recorded thermal histories were used to determine by an inverse calculation the temperature-dependent thermal conductivity of the two industrial alloys 1201 and 3104 (see sections 4.2 and 5.2), the first thermocouple located near the chill serving as one boundary condition (imposed temperature).

### **3.3.2 Differential thermal analysis**

Differential thermal analysis (DTA) was carried out so as to validate the microsegregation model presented in section 4.1. DTA consists in heating or cooling a small sample at a constant rate together with a reference specimen (see figure 3.15). The temperature difference between them, or more precisely the voltage difference induced by the Seebeck effect, is measured as a function of time. When the sample is going through a phase change, latent heat is liberated or consumed and the sample temperature lags behind the furnace or reference temperature.

The METTLER TA apparatus was used for the DTA measurements of two industrial alloys, 1201 and 3104. Two alumina crucibles, 6 mm in diameter and 4 mm in height, were used: the first one served as the reference and the sample was placed in the second one. The sample weighted about 150 mg and Argon atmosphere was used.

The DTA apparatus was first calibrated using Al 99.999% and performing runs at different heating or cooling rates. The peak on-set temperature was determined from the intersection of the base line with the tangent to the signal as shown in figure 3.16. The peak on-set at melting shifts towards higher temperatures with faster heating rates as reported in figure 3.17. Extrapolating peak on-set temperatures to a zero heating rate leads to a temperature of 655.8°C, 4.5°C lower than the melting temperature of pure aluminium which is 660.3°C [Mond]. The thermocouple correction was therefore set to 4.5°C and all curves have been shifted by this quantity.

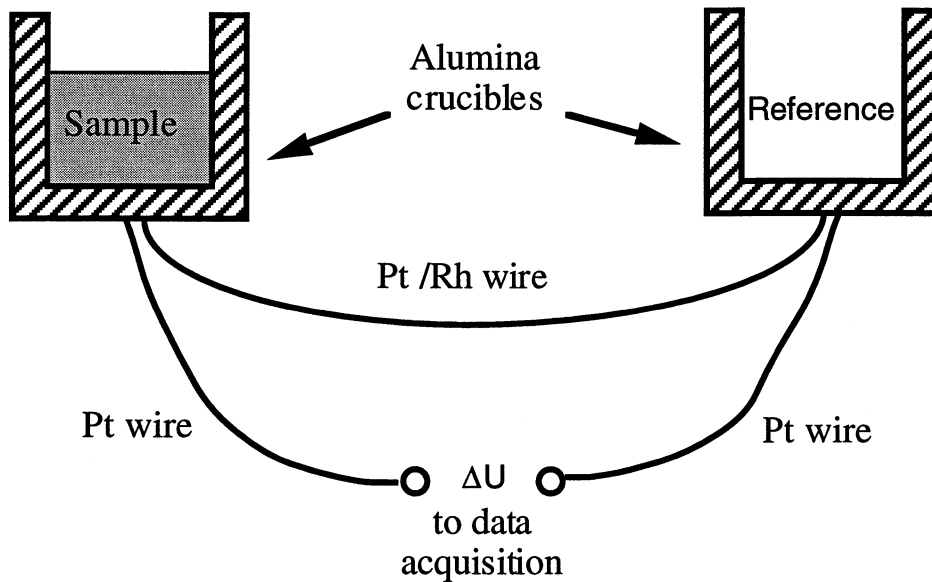


Figure 3.15 : schematic representation of the DTA apparatus and principle.

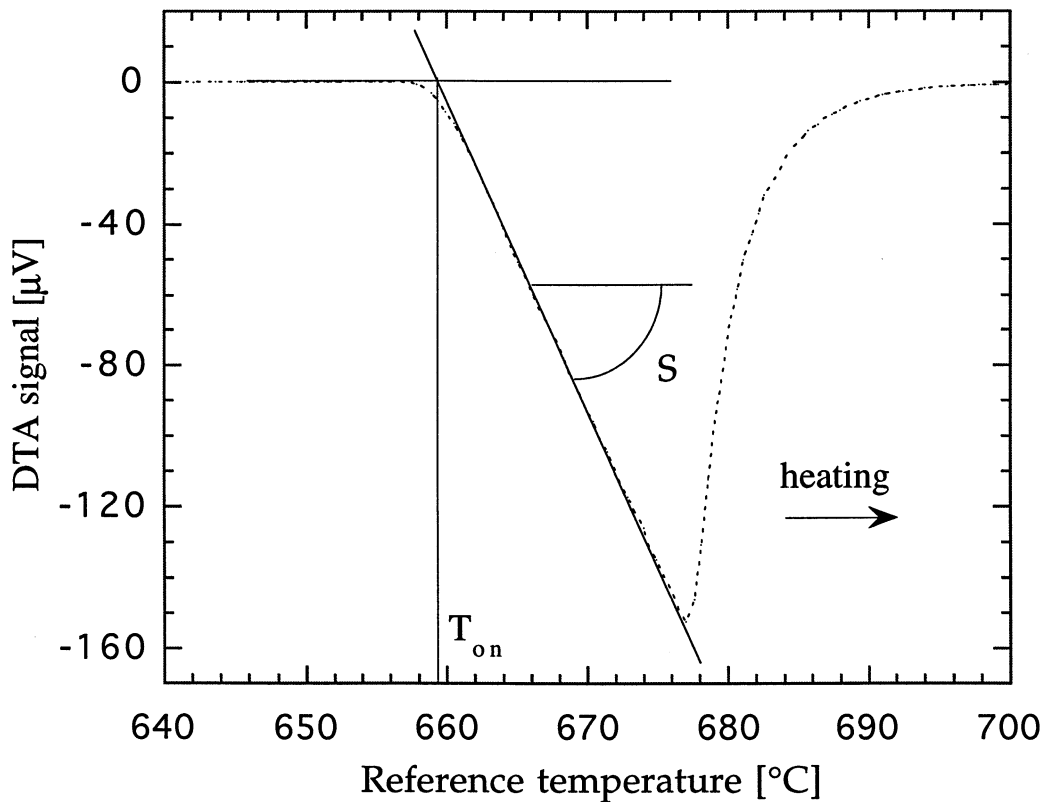


Figure 3.16: determination of the peak on-set temperature,  $T_{\text{on}}$ , and of the sensitivity factor  $S$  when calibrating the apparatus with pure aluminium (the heating rate is + 10K/min).

The base line, due to the difference in specific heat between the sample and the reference, has to be subtracted from the raw DTA curve. The base line under the peak is assumed to follow a cubic spline function which links regression lines on both extremities of the peak (see figure 3.18).



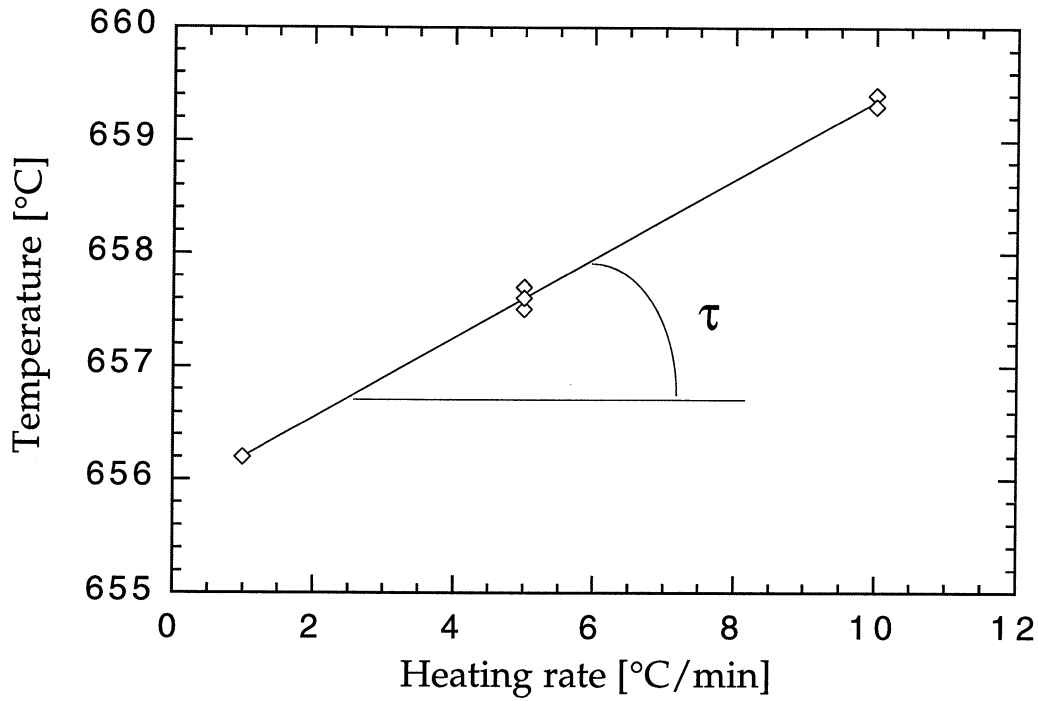


Figure 3.17: Peak on-set temperatures as a function of the heating rate and determination of the time lag,  $\tau_{\text{lag}}$ , for pure aluminium.

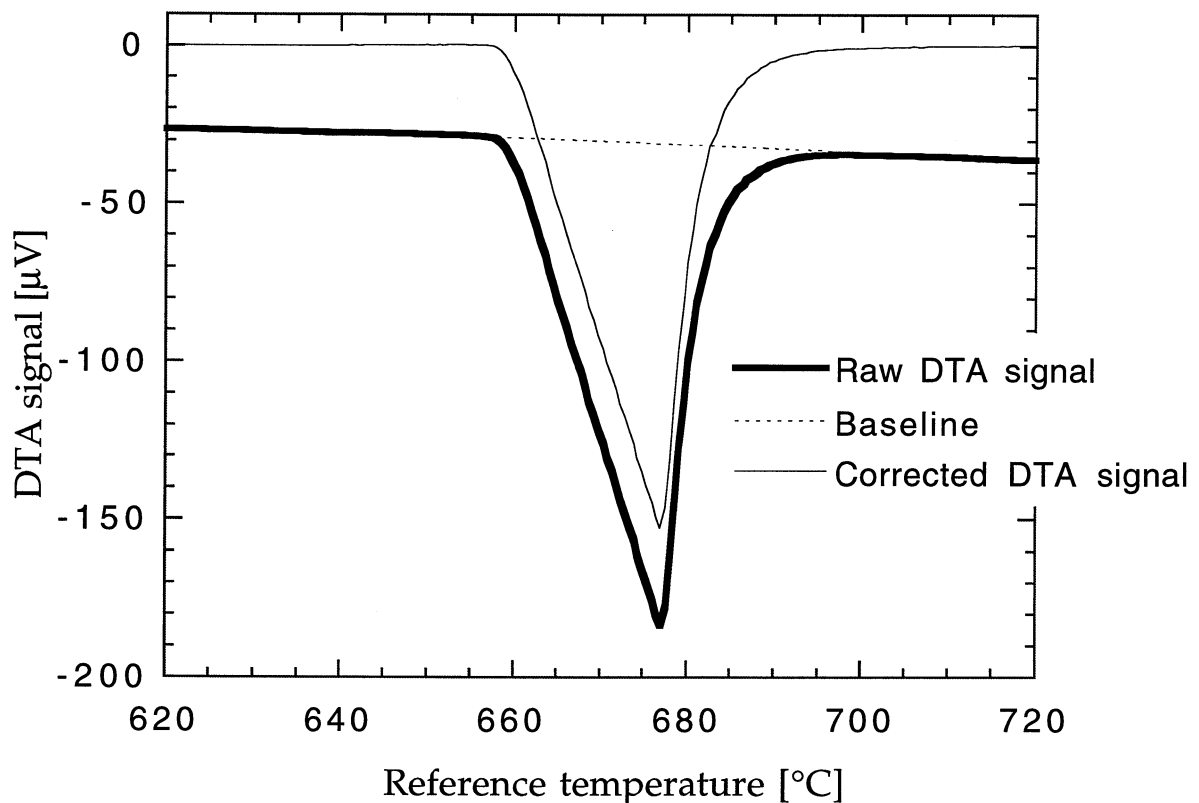


Figure 3.18: base line on a raw DTA curve (pure aluminium).

Taking into account the thermal inertia of the system and the sensitivity of the apparatus, the sample temperature,  $T_s$ , is given by [Magn]:

$$T_s = T_r - \tau_{lag} \cdot \dot{T} + \frac{\Delta U}{S} \quad (3.6)$$

where  $T_r$  is the reference temperature,  $\dot{T}$  the heating or cooling rate,  $\Delta U$  the base line corrected DTA signal and  $\tau_{lag}$  the time lag. The sensitivity factor,  $S$ , is determined as the maximum slope of the melting peak of pure aluminium as shown in figure 3.16, and was found to be  $S = 8.5 \mu\text{V}/^\circ\text{C}$ . The time lag,  $\tau_{lag}$ , corresponds to the slope of the linear regression of the on-set peak temperature as a function of the heating rate curve. Its value was found to be  $\tau_{lag} = 0.35 \text{ min}$  (see figure 3.17).

Applying equation 3.6, the sample temperature can be represented as a function of time. During melting of a pure substance, this temperature remains constant. Note that when cooling the sample, equation 3.6 is still valid:  $\dot{T}$  becomes negative and  $\Delta U$  positive.

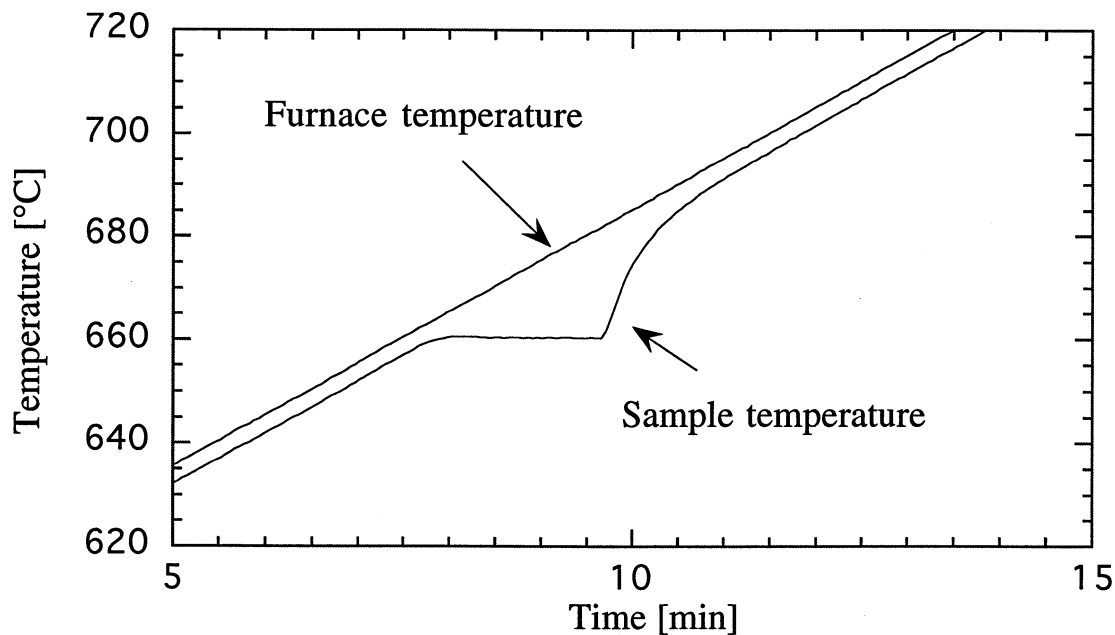


Figure 3.19: Furnace and sample temperatures as a function of time (pure aluminium, +10K/min).

When testing an alloy, the solid fraction curve can be calculated from the DTA curve, assuming that the surface under the peak is proportional to the solid fraction of the alloy at the considered time and corresponding sample temperature (see equation 3.6), i.e.:

$$f_s(T) = \frac{A_T}{A_{tot}} \quad (3.7)$$

where  $A_T$  is the surface at the temperature  $T$  and  $A_{tot}$  the total surface under the peak. This procedure can be performed when cooling or heating the sample: it is schematically presented in figure 3.20.

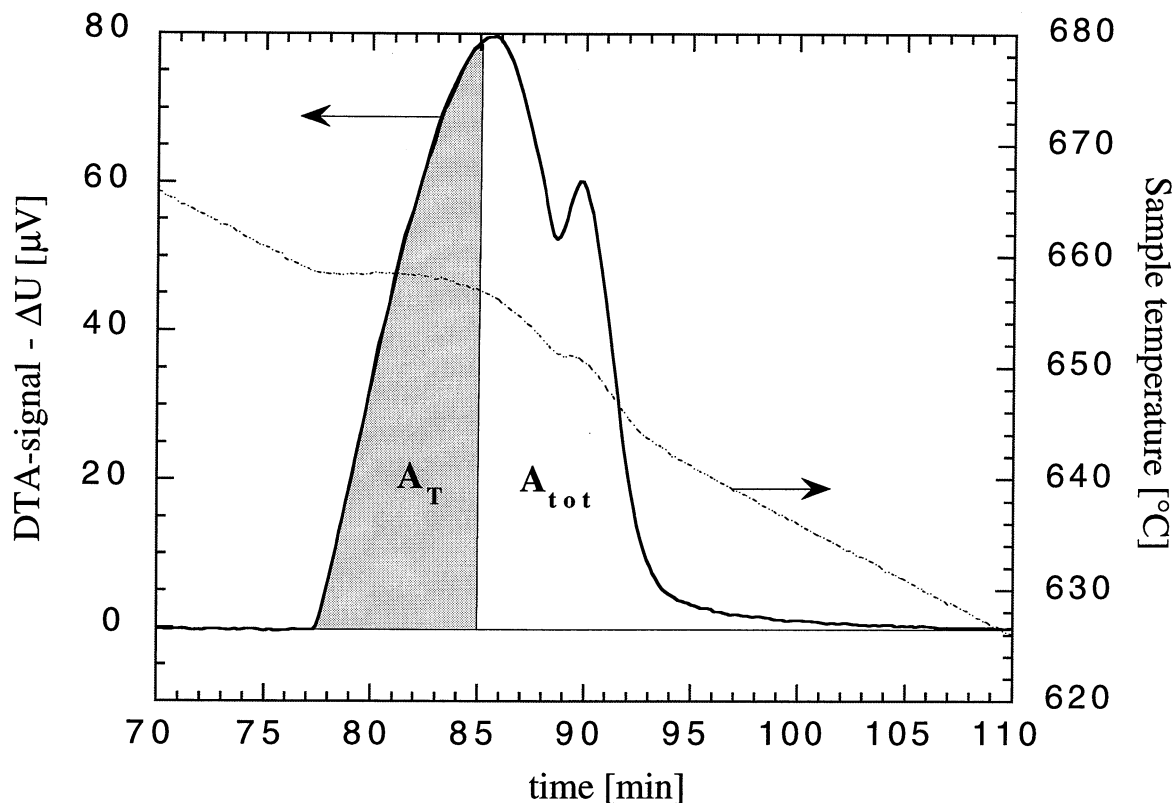


Figure 3.20: Calculation of the solid fraction from a DTA curve (1201, -1K/min).

### 3.3.3 Metallography

Micrography of as-cast materials were conducted for grain inspection, notably for the evaluation of the mean diameter of globular equiaxed grains. After polishing the samples with 16  $\mu\text{m}$  and 1  $\mu\text{m}$  diamond paste and alcohol, they were etched with borofluoric acid ( $\text{HBF}_4$ , 5% in water) as an electrolyte with an inox cathode<sup>1</sup> using a voltage of 35 V during approximately 60 seconds (epitaxial Barker oxidation).

Grain sizes have been determined using simple intercept measurements on the plane of polish [Meta]. The mean intercept length,  $L$ , gives a good idea of the mean grain diameters. To calculate  $L$ , a test circle was laid down several times to give the total test-line length,  $L_t$ , on a micrograph viewed at a magnification  $M$ .  $L$  is therefore given by [Meta]:

<sup>1</sup> The sample plays the role of the anode.

$$L = \frac{L_t}{PM} \quad (3.8)$$

where P is the total number of grain-boundary intersections with the test circle. For equiaxed grains that do not vary much in size, the circle is applied to the micrograph until about 36 intersections are obtained.

## NUMERICAL METHODS

The interest in numerical methods has grown considerably with the advent of powerful computers and sophisticated algorithms. In the present work, numerical methods were intensively used. A finite difference method (FDM) was developed to compute the solute diffusion in the solid and liquid phases (microsegregation) during the growth of a globular grain; this model is presented and validated against the classical lever-rule and Scheil's models in the first section of this chapter. Inverse modelling based on the maximum a posteriori (MAP) algorithm and implemented in the heat flow code 3-MOS [Thé3], has been used to determine the stationary heat flux leaving the ingot surface during the DC casting process; this was completed using temperature measurements inside the slab. Moreover, inverse modelling permitted the determination of the temperature-dependent thermal conductivity of two industrial alloys using temperature measurements of well-defined laboratory castings. The inverse modelling method is presented in section 4.2. Eventually, a model aimed at calculating the thermal stresses and strains during DC/EM casting processes is exposed in section 4.4. The computations were conducted using the general thermomechanical code Abaqus [Abaq].

### 4.1 Microsegregation modelling

In this section, a model for the computation of microsegregation during solidification of metallic alloys using the finite difference method is presented. The problems of back-diffusion in the primary solid phase, of solute diffusion in the liquid phase, of eutectic precipitation at the end of solidification, and of possible remelting during air-gap formation in DC casting are being addressed for an open system, i.e., for a small volume element whose overall solute content is not necessarily constant. This type of calculation is necessary if macrosegregation at the scale of the whole ingot is to be described [Comb]. It has been included in this work as a start-up phase of a Brite-Euram program which includes both thermomechanical and micro/macro-segregation aspects. Assuming uniform temperature in the small volume element, the variations of enthalpy and of total solute content are assumed to be known functions of time resulting from the average continuity equations solved at the scale of the whole casting. The present model allows to calculate the local solidification path (i.e., cooling curve, volume fraction of solid, and concentration profiles in the solid and liquid phases). It is based upon a numerical solution of the diffusion

equations using two coordinates transformations. The number of solute species is not limited and the model is validated against the lever rule and Scheil's models assuming only two solute elements for the sake of simplicity.

#### 4.1.1 Microstructure morphologies

The geometry of the computation domain is a simplification of real microstructure geometries encountered in castings. It is described in figure 4.1 and is characterised by the parameter *igeo*. A plate-like morphology is described by a one-dimensional geometry (*igeo* = 1). On the other hand, secondary arms of well-developed dendrites ( $r_0 = \frac{\lambda_2}{2}$ ) or primary trunks of columnar cells ( $r_0 = \frac{\lambda_1}{2}$ ) are approximated by a cylindrical geometry (*igeo* = 2). Eventually, globulitic microstructures typical of heavily inoculated aluminium alloys is approximated by a spherical geometry (*igeo* = 3). Assuming constant and equal liquid and solid densities, the size of the domain element,  $r_0$ , over which the diffusion calculation is performed, is constant.

#### 4.1.2 The equations

Knowing at a given time  $t$ , the enthalpy  $h(t)$  and the average local solute concentration  $\bar{w}_i(t)$  of element  $i$  in the considered volume, the present model calculates the new temperature,  $T^{t+\Delta t}$ , the mass fraction of solid,  $f_s^{t+\Delta t}$ , solute concentration profile in the liquid and solid phases  $w_i(r)^{t+\Delta t}$ , for each element  $i$ .  $r$  is the space variable, varying in between 0 and  $r_0$ . Assuming constant thermophysical properties, the specific enthalpy is related to the solid mass fraction and the temperature by:

$$h = c_p T + L(1 - f_s) \quad (4.1)$$

where  $c_p$  and  $L$  are the specific heat capacity and latent heat of fusion, respectively. The solid mass fraction is defined as a function of the geometric parameter *igeo* as follows:

$$f_s = \left[ \frac{r^*}{r_0} \right]^{igeo} \quad (4.2)$$

where  $r^*$  is the position of the solid-liquid interface (\* refers to interfacial solid-liquid quantities). When derivating equation 4.2, one obtains:

$$\dot{f}_s = \frac{df_s}{dt} = \frac{igeo \cdot v}{r_0} \cdot \left[ \frac{r^*}{r_0} \right]^{igeo-1} \quad (4.3)$$

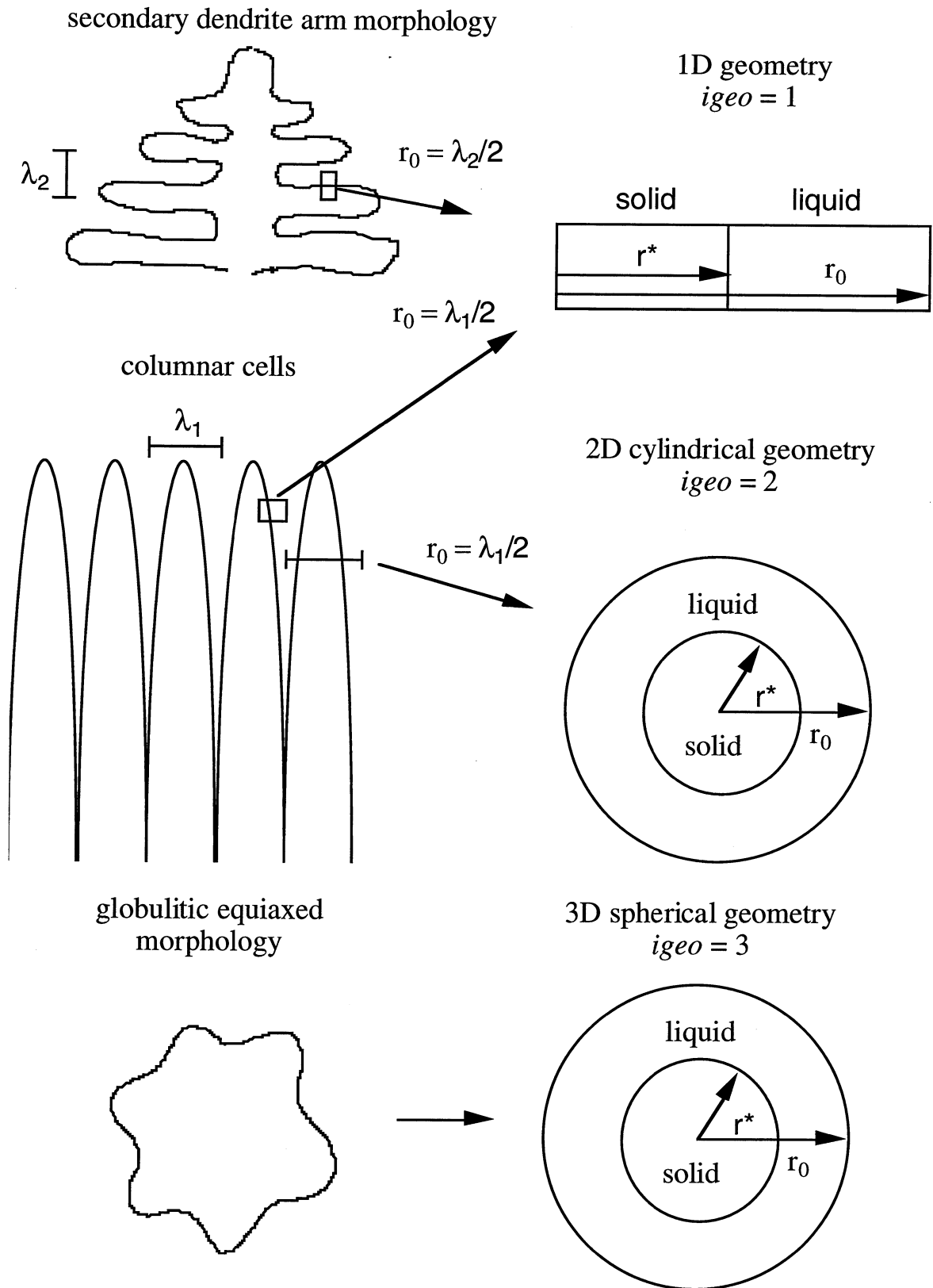


Figure 4.1: the three geometries considered in the microsegregation model and the associated value of the parameter  $igeo$ .

where  $v = \frac{dr^*}{dt}$  is the solid-liquid interface velocity. Neglecting undercooling of any kind and assuming<sup>1</sup> constant liquidus slopes  $m_i$ , and partition coefficients,  $k_i$ , the uniform temperature  $T$  of the volume element equals the liquidus temperature given by:

$$T = T^m + \sum_i m_i w_i^* \quad (4.4)$$

where  $T^m$  is the melting temperature of the pure metal,  $i$  the index of the solute element and  $w_i^*$  the interfacial liquid concentration of solute element  $i$ . Local thermodynamic equilibrium at the solid-liquid interface is imposed:

$$w_{is}^* = k_i w_i^* , \forall i \quad (4.5)$$

$w_{is}^*$  being the interfacial solid concentration of element  $i$ . Solute profiles are determined by the Second Fick's law in the solid phase:

$$\text{div} [D_i^s(T) \overrightarrow{\text{grad}} w_i] = \frac{\partial w_i}{\partial t} \quad \text{for } r \in [0, r^*(t)] \text{ and } \forall i \quad (4.6)$$

and in the liquid phase:

$$\text{div} [D_i^l(T) \overrightarrow{\text{grad}} w_i] = \frac{\partial w_i}{\partial t} \quad \text{for } r \in [r^*(t), r_0] \text{ and } \forall i \quad (4.7)$$

where  $D_i^s(T)$  and  $D_i^l(T)$  are the temperature-dependent solid and liquid diffusivities of element  $i$ , respectively. Using the Laplace operator,  $\Delta$ , and assuming that  $D_i^s$  is not concentration dependent, equation 4.6 can be expressed as a function of the parameter *igeo*:

$$\text{div} [D_i^s(T) \overrightarrow{\text{grad}} w_i] = D_i^s(T) \cdot \Delta w_i = D_i^s(T) \left[ \frac{\partial^2 w_i}{\partial r^2} + \frac{\text{igeo} - 1}{r} \frac{\partial w_i}{\partial r} \right] = \frac{\partial w_i}{\partial t} \quad (4.8)$$

for  $r \in [0, r^*(t)]$  and  $\forall i$

Equation 4.7 is transformed in the same way. The velocity of the solid-liquid interface,  $v$ , is given by the solute flux conservation:

$$v = \frac{dr^*}{dt} = \frac{D_i^s G_i^s - D_i^l G_i^l}{w_i^* - w_{is}^*} , \forall i \quad (4.9)$$

---

<sup>1</sup> These assumptions will be released when coupling the present model with the equilibrium phase diagram calculated by Thermo-Calc (cf. chapter 5).



where  $G_i^s$  and  $G_i^l$  are the interfacial solute solid and liquid gradients of element  $i$ , respectively, as schematically represented in figure 4.2.

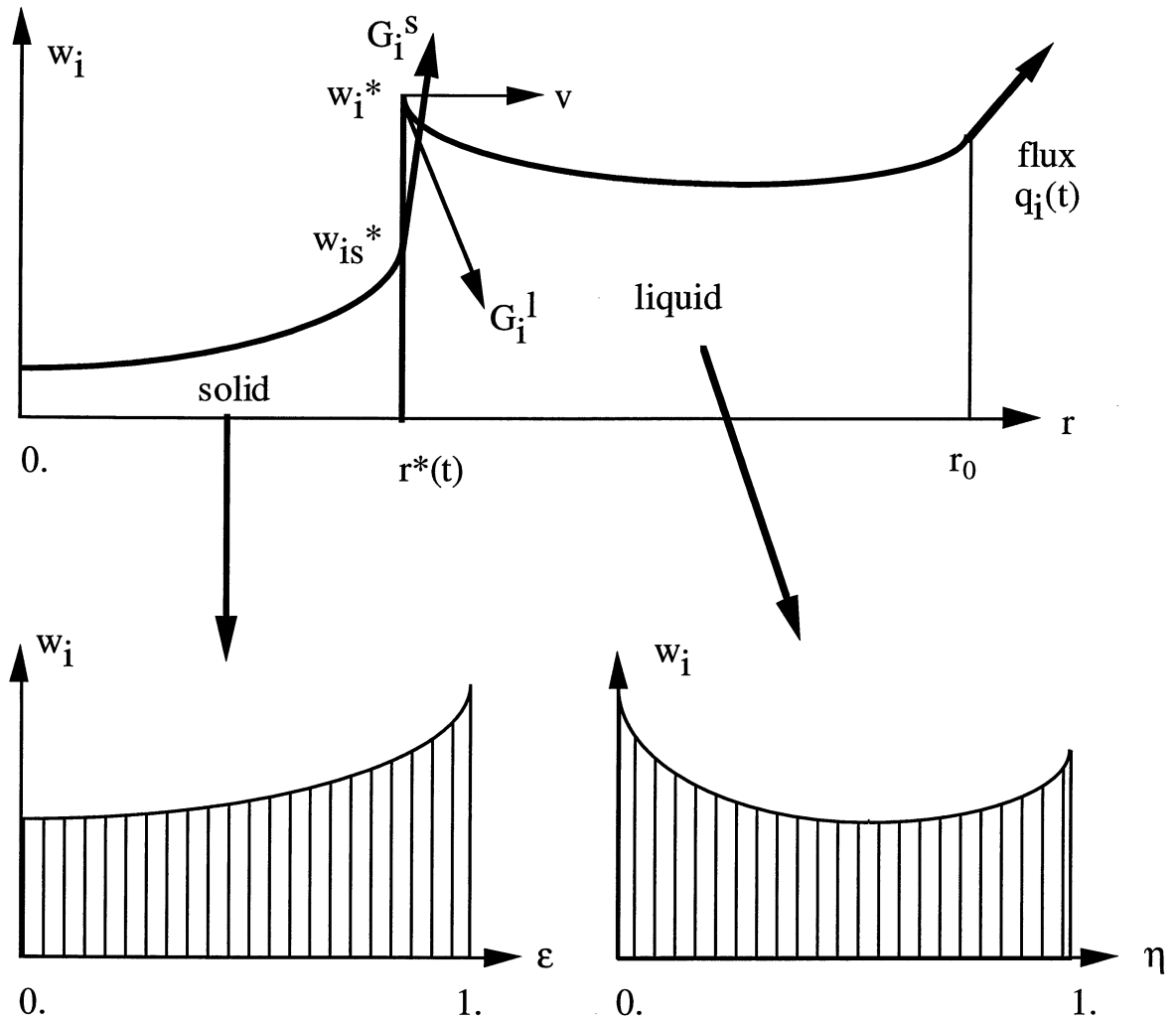


Figure 4.2: the computation domain together with the boundary conditions and the two Landau transformations.

The following boundary conditions are applied:

$$\frac{\partial w_i}{\partial r} = 0 \quad (1) \quad \text{for } r = 0 \quad \text{and } \forall i \quad (4.10)$$

$$\text{and } D_i^l \frac{\partial w_i}{\partial r} = q_i(t) = \frac{r_0}{i g e o} \cdot \frac{d \bar{w}_i}{d t} \quad \text{for } r = r_0 \quad \text{and } \forall i \quad (4.11)$$

---

<sup>1</sup> for symmetry reasons.

where  $q_i(t)$  is the time-dependent solute flux entering the domain by macrosegregation which is proportional to the time-derivative of  $\bar{w}_i(t)$ <sup>1</sup>. A close system corresponds to  $q_i(t) = 0$  for each value of  $i$  and the total solute content of element  $i$  remains constant and equal to its nominal value ( $\bar{w}_i = w_i^0$ ). For an open system,  $\bar{w}_i(t)$  is a known function that could be calculated for example from a coupled macrosegregation calculation [Comb]. To start the calculation, a small initial volume fraction (0.1%) is considered at the liquidus temperature. The initial solute concentrations in both phases, are given by the lever-rule (cf. section 2.1.2).

### 4.1.3 Solution algorithm

The present model solves the equations of diffusion in the solid and liquid phases with the help of two coordinates transformations (or Landau transformations [Land,Crank]), which map the solid domain  $[0, r^*(t)]$  and the liquid domain  $[r^*(t), r_0]$  onto the fixed  $[0, 1]$  interval as shown in figure 4.2. The details of this transformation are given in Appendix I. For each solute element and for a given time increment,  $\Delta t$ , and solid-liquid interface velocity,  $v$ , the microsegregation module solves the diffusion equations in both phases using a fully implicit Finite Difference scheme (FDM). This gives as a result the new concentration profiles and the new interfacial solute gradients.

The computation of the solidification path in a ternary system ( $i=1,2$ ) is completed with a fixed time increment  $\Delta t$ . During the primary phase solidification, the solid-liquid interface velocity,  $v$ , is guessed thus providing the new volume fraction of solid,  $f_s^{t+\Delta t}$ , and the new temperature,  $T^{t+\Delta t}$ , through the use of equations 4.1 to 4.3. On the other hand, the microsegregation module allows the computation of the new liquid interfacial concentration of each element, thus readily providing the new liquidus temperature (equation 4.4). This process is iterated until the temperature deduced from the new interfacial concentrations matches that obtained from the heat balance, i.e. the difference becomes lower than a given tolerance ( $10^{-6}$  °C). To limit the number of iterations, the first guessed interface velocity is taken from the previous solute profiles (equation 4.9). Once, a monovariant eutectic line is reached, the diffusion calculations are stopped and the remaining liquid fraction is assumed to correspond to the eutectic fraction. In the results section (chapter 5), the

---


$$1 \bar{w}_i(t) = \frac{ig_{eo}}{r_0^{ig_{eo}}} \int_0^{r_0} w_i(r) r^{ig_{eo}-1} dr$$

thermodynamic data of the alloy ( $k_i$  and  $m_i$ ) will be deduced from the results given by Thermo-Calc.

#### 4.1.4 Validation of the model and influence of the geometry

The present microsegregation model has been validated using the numerical integration of the lever rule and Scheil's equations for a ternary system (see section 2.1.2). The material parameters of the ternary system used for the present validation are typical of an aluminium alloy and are given in table 4.1. Note that this system is closed owing to the fact that  $\bar{w}_1$  and  $\bar{w}_2$  are both constant. A spherical geometry ( $igeo = 3$ ) is considered here and the enthalpy slope is constant and equal to  $-3.10^3 \text{ JKg}^{-1}\text{s}^{-1}$ , thus leading to a solidification time of about 200 sec.

heat capacity	$c_p$	$1080 \text{ JKg}^{-1}\text{K}^{-1}$
latent heat of fusion	L	$388. 10^3 \text{ JKg}^{-1}$
volume dimension	$r_0$	$100. 10^{-6} \text{ m}$
melting temperature	$T^m$	933 K
solute content (element 1)	$\bar{w}_1$	0.05 -
solute content (element 2)	$\bar{w}_2$	0.05 -
liquidus slope (element 1)	$m_1$	-600 K
partition coefficient (element 1)	$k_1$	0.25 -
liquidus slope (element 2)	$m_2$	-600 K
partition coefficient (element 2)	$k_2$	0.1 -
eutectic temperature	$T_{eut}$	600 K
liquid solute diffusivity (lever rule)	$D^l$	$10^{-6} \text{ m}^2\text{s}^{-1}$
solid solute diffusivity (Scheil's model)	$D^s$	$10^{-14} \text{ m}^2\text{s}^{-1}$

Table 4.1: material parameters used for the validation of the microsegregation model.

To solve the diffusion equations, the microsegregation module used 50 nodes in the solid and 50 nodes in the liquid phase, equally spaced. A sensitivity

analysis revealed that a liquid diffusivity of  $10^{-6} \text{ m}^2\text{s}^{-1}$  leads to a complete solute mixing at the scale of the domain, the Fourier number being in this case  $2 \cdot 10^4$  (see equation 2.10), whereas a solid diffusivity of  $10^{-14} \text{ m}^2\text{s}^{-1}$  prevents any diffusion in the solid phase (Fourier number of  $2 \cdot 10^{-4}$ ). Three cases were studied for the validation:

- i) all solute diffusivities equal to  $10^{-6} \text{ m}^2\text{s}^{-1}$  (lever rule approximation),
- ii) liquid diffusivities are  $10^{-6} \text{ m}^2\text{s}^{-1}$ , whereas solid diffusivities are equal to  $10^{-14} \text{ m}^2\text{s}^{-1}$  (Scheil's approximation),
- iii) element 1 follows the lever-rule approximation and element 2 the Scheil's approximation (lever + Scheil).

These three cases can be numerically integrated using the equations derived in section 2.1.2. Figure 4.3 shows the calculated  $f_s$ -T curve compared with the numerical solution for the three cases. The agreement is very good and the relative error in the total solute content is always lower than 0.5%.

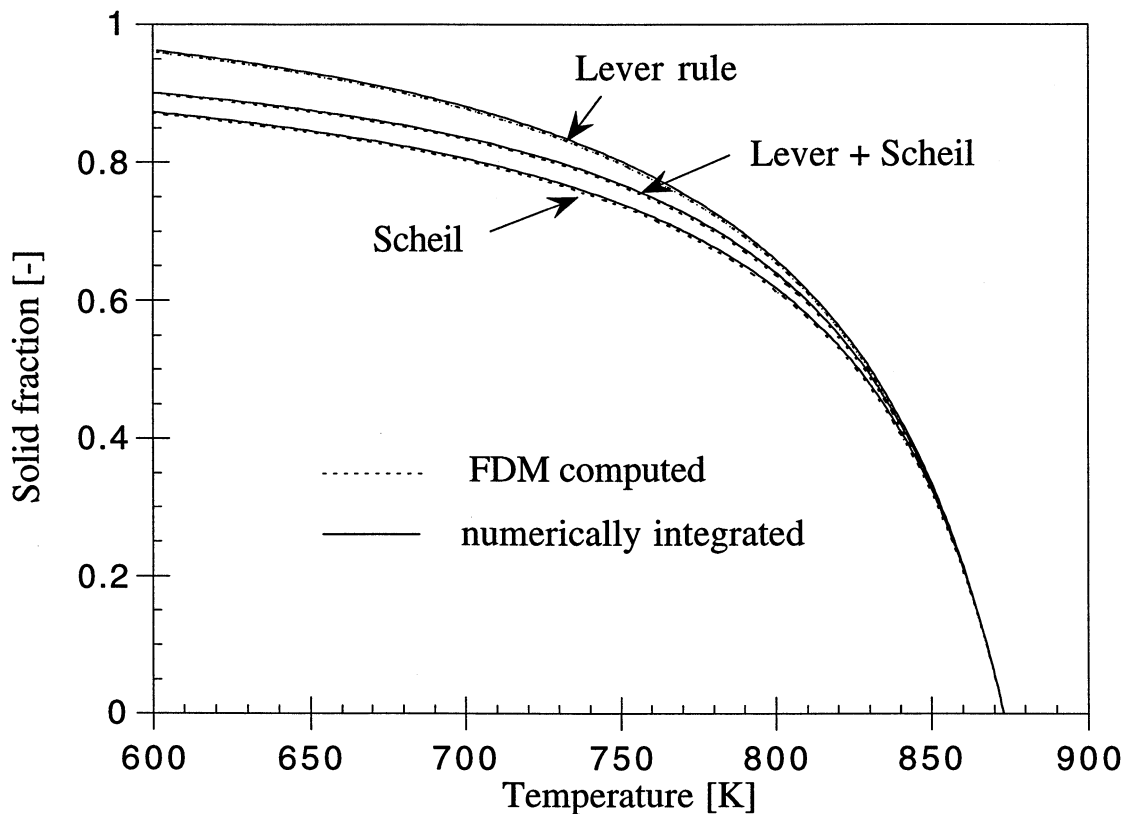


Figure 4.3: validation of the microsegregation model using numerical integration of the lever and Scheil's equations.

Figure 4.4 shows the concentration profiles at different times during the solidification for the case (iii): please note the frozen solute profile of element 2,

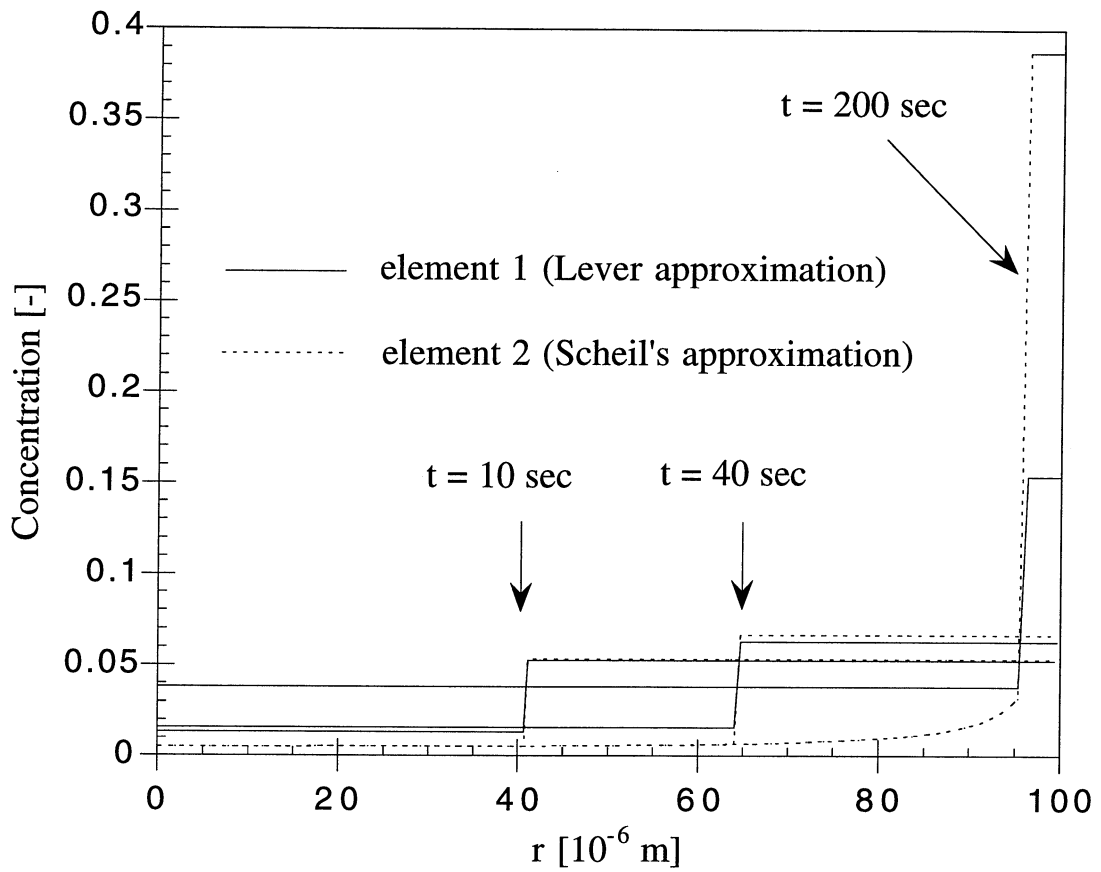


Figure 4.4: computed concentration profiles for case (iii) at different times.

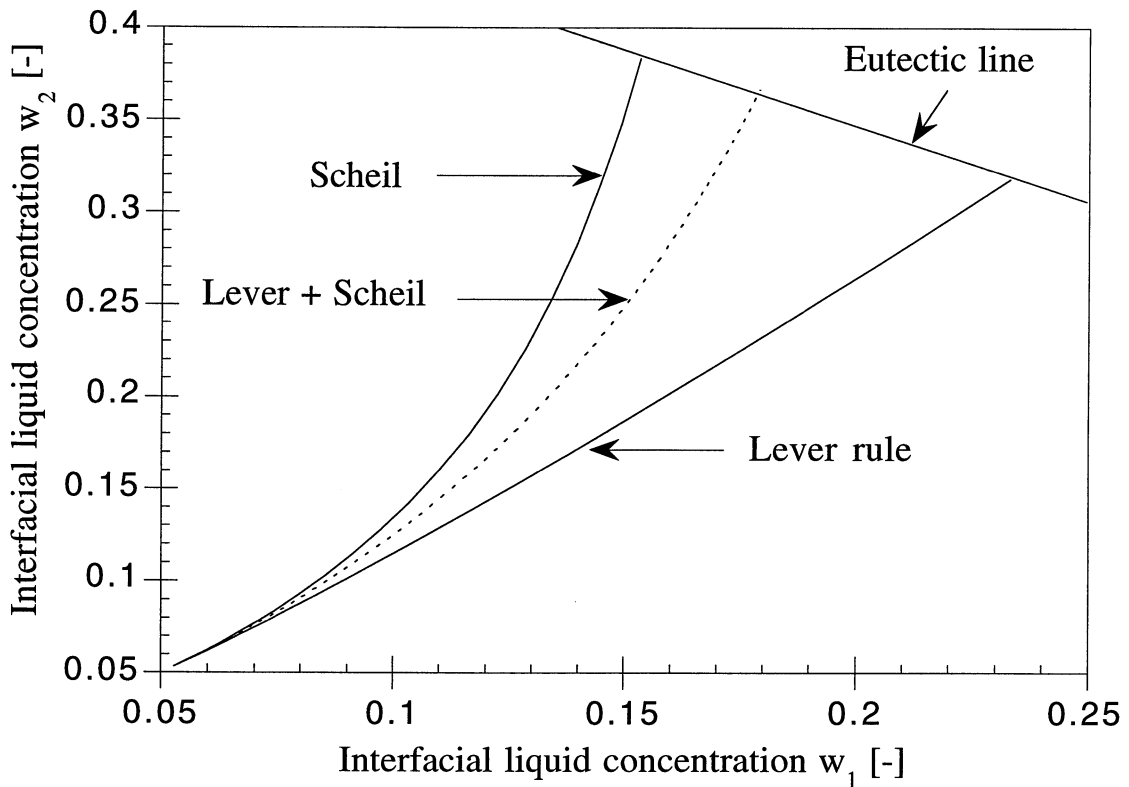


Figure 4.5: computed solidification paths for the three cases.

typical of the Scheil's approximation. The calculated solidification paths, i.e. the position of the interfacial liquid concentrations ( $w_1^*, w_2^*$ ), are plotted in figure 4.5 for the three cases. The eutectic line is also represented. Due to the low partition coefficient of element 2, the paths are bent towards high solute 2 contents, with respect to the lever rule.

Finally, figure 4.6 shows the influence of the geometry on the solidification paths. The  $f_s$ - $T$  curves have been computed using different values of the geometric parameter  $igeo$  and are compared with the curves resulting from the lever-rule and Scheil's models. For this case, the solid and liquid diffusivities of both solute elements were set to more realistic values,  $9 \cdot 10^{-12} \text{ m}^2\text{s}^{-1}$  and  $9 \cdot 10^{-9} \text{ m}^2\text{s}^{-1}$ , respectively.

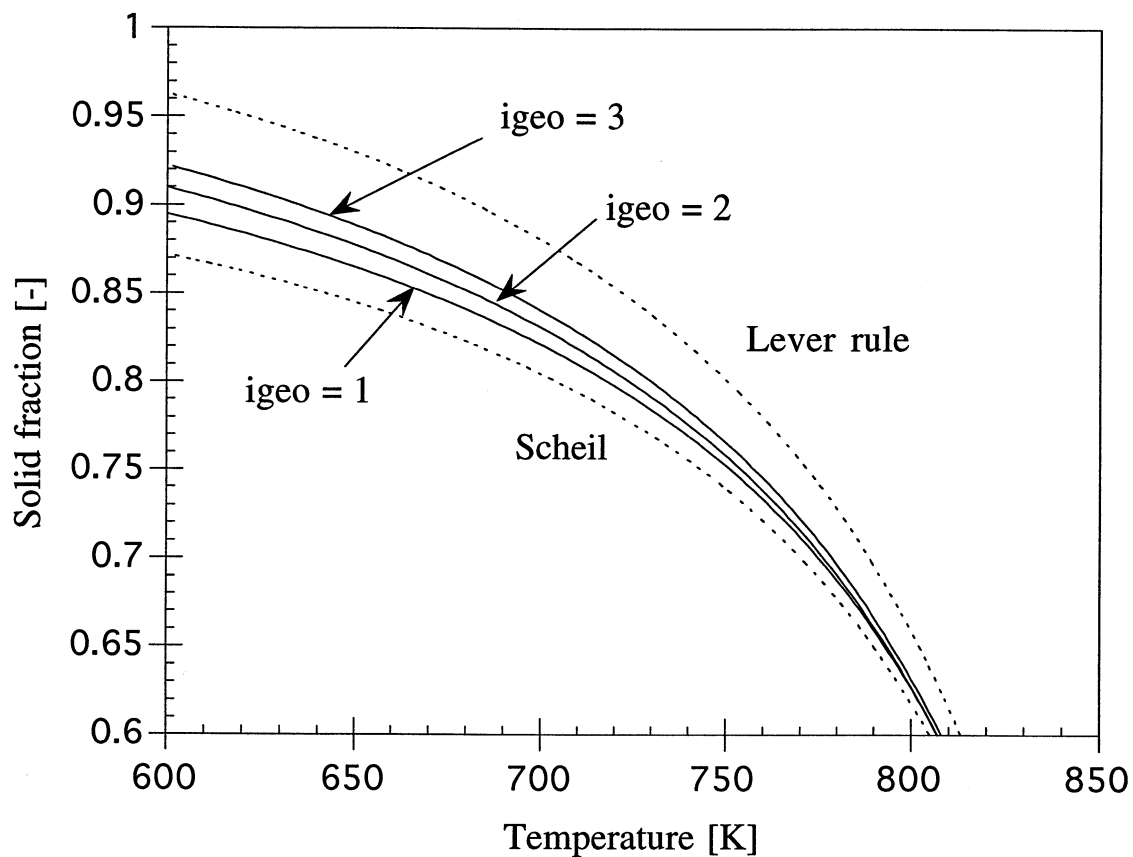


Figure 4.6: influence of the morphology on the solidification path.

As could be expected, diffusion from the solid-liquid interface is favoured when going from a plate-like ( $igeo = 1$ ) to a spherical geometry ( $igeo = 3$ ). Accordingly, the solidification path moves closer to the lever-rule limit as the parameter  $igeo$  increases.

## 4.2 Inverse temperature modelling

As will be shown in the results section (chapter 5), deformation of the DC/EM cast ingots is mainly due to thermomechanical effects. Therefore, a detailed knowledge of the temperature distribution in the ingot is required.

Solving a direct heat conduction problem consists in finding the temperature field in a domain with conditions prescribed at an initial time and at the boundaries of the domain. On the other hand, the goal of an inverse problem is to determine the boundary conditions and/or the initial conditions and/or some thermophysical properties of the material with the help of interior temperature measurements. To cope with the lack of thermophysical properties and/or boundary conditions, inverse modelling constitutes an interesting solution which was used in the present work to determine the temperature-dependence of the thermal conductivity of two industrial aluminium alloys and the stationary thermal boundary conditions along the rolling faces of the ingot during the DC casting process.

### 4.2.1 Direct and inverse heat conduction problems

The direct heat conduction problem in solidification is non-linear since it involves the latent heat release during the freezing of the alloy and the temperature-dependent properties; it can be solved using numerical methods. The 3-MOS (Micro-Macroscopic Modelling of Solidification) software code that has been developed at the LMPH [Thé3] was used to compute the thermal field in the steady-state regime of casting. This code is based upon a finite element method (FEM) and upon an enthalpic formulation of the heat conduction problem: the enthalpy at a given position,  $h$ , is calculated and then using the  $T(h)$  relationship, the corresponding temperature is determined. Further details concerning the assembling of the finite elements and the time integration can be found in [Thé3].

Using temperature measurements made under well-defined conditions, a direct code, such as 3-MOS, can be used to deduce boundary conditions or thermophysical data. This is the so-called *inverse methods*. For heat flow problems, these methods are based upon a minimisation of the errors between calculated and measured temperatures at given locations and times, the calculated values being obtained from a numerical solution of the heat flow equation, i.e. from a *direct* finite element calculation. The minimisation can be based upon a standard least-squares technique, or it can be modified using a *Maximum A Posteriori* (MAP) algorithm as suggested by Milano and Scarpa [Rap2]. This technique has been implemented into the finite element code 3-

MOS. A brief description of the theoretical background and of the numerical implementation in 3-MOS is given here; further details can be found in [Rap2].

#### 4.2.2 Theoretical aspects of the inverse method

Let assume that temperatures,  $T_{ij}^m$ , have been measured by a set of thermocouples placed at well defined positions,  $r_j$  ( $j = 1, N_m$ ) in a solidifying ingot and/or mould parts. The measurements have been made for a series of  $N_t$  times  $t_i$  ( $i = 1, N_t$ ). These measured temperatures are used to deduce a set of  $N$  parameters  $\vec{\beta} = \{\beta_1, \beta_2, \dots, \beta_N\}$  via a minimisation of the function [Rap2] :

$$S(\vec{\beta}) = \sum_{i=1}^{N_t} \sum_{j=1}^{N_m} \frac{1}{\sigma_T^2} \left[ T_{ij}^m - T_{ij}^c(\vec{\beta}) \right]^2 + \sum_{k=1}^N \frac{1}{\sigma_k^2} \left[ \beta_k - \beta_k^0 \right]^2 \quad (4.12)$$

where  $T_{ij}^c(\vec{\beta})$  are the calculated temperatures at time  $t_i$  and position  $r_j$ . The standard deviation,  $\sigma_T$ , is a typical error associated with the temperature measurements whereas  $\sigma_k$  is a typical interval within which each of the parameter  $\beta_k$  is allowed to vary around an a priori (i.e. guessed) parameter,  $\beta_k^0$ . The MAP algorithm resumes to the standard least-squares method when the  $\sigma_k$ 's are set to infinity. On the other hand, a parameter  $\beta_k$  will be fixed to the guessed value  $\beta_k^0$  if the corresponding deviation,  $\sigma_k$ , is made very small. The parameters to be adjusted,  $\beta_k$ , can be tabulated values or coefficients of a polynomial development of thermophysical properties or of time- or temperature-dependent boundary conditions. An iterative procedure is used to find the solution  $\vec{\beta}$  minimising  $S(\vec{\beta})$ . The method is then as follows:

1. give an initial guess of the parameters  $\beta_k^0$ , and set the values at iteration  $v = 0$  to these values<sup>1</sup>
2. calculate the temperatures  $T_{ij}^c(\vec{\beta}^v)$  with the direct FEM technique
3. deriving equation 4.12 with respect to each  $\beta_k$  gives  $N$  equations in which the temperatures  $T_{ij}^c(\vec{\beta}^v)$  appear together with the sensitivity coefficient  $X_{ijl}$  :

$$X_{ijl} = \frac{\partial T_{ij}^c(\vec{\beta}^v)}{\partial \beta_l} \quad (4.13)$$

---

<sup>1</sup>  $\beta_k^v = 0 = \beta_k^0$



4. the sensitivity coefficients can be calculated numerically by the following approximation:

$$X_{ijl} \cong \frac{T_{ij}^c(\overrightarrow{\beta^{v+1}}) - T_{ij}^c(\overrightarrow{\beta^v})}{\delta\beta_l} \quad (4.14)$$

where  $\delta\beta_l$  is an a priori variation of the component  $l$  of the vector  $\overrightarrow{\beta^v}$ ,

5. linearizing the calculated temperatures at the next iteration:

$$T_{ij}^c(\overrightarrow{\beta^{v+1}}) = T_{ij}^c(\overrightarrow{\beta^v + \Delta\beta}) \cong T_{ij}^c(\overrightarrow{\beta^v}) + \sum_{k=1}^N X_{ijk} \cdot \Delta\beta_k \quad (4.15)$$

allows then to obtain the increments of the coefficients,  $\Delta\beta_k$ . If these increments are smaller than a certain tolerance, then the solution  $\overrightarrow{\beta}$  has been found. If not, then replace  $\overrightarrow{\beta^v}$  by  $\overrightarrow{\beta^{v+1}}$  and go back to point 2.

Please note that, within each iteration,  $(N+1)$  direct problems are solved with the direct code, which might be CPU-intensive especially if the problem is 3-dimensional and the number of parameters  $N$  is large. In two dimensions, this problem is less critical and the MAP algorithm has been implemented as a main program calling the direct FEM heat-flow code 3-MOS considered as a subroutine.

### 4.2.3 Applications of the inverse method

The first application of this inverse modelling method was the estimation of the temperature dependence of the thermal conductivity of two industrial aluminium alloys. In this case, the unknown  $\overrightarrow{\beta}$  is the vector  $\{\kappa_1, \kappa_2, \dots, \kappa_N\}$ , where the  $\kappa_k$ 's are the values of the thermal conductivity of the medium at some tabulated temperatures,  $T_k$ . The values of  $\kappa$  in each interval,  $[T_k, T_{k+1}]$ , are linearly interpolated as illustrated in figure 4.7. For this application, small cylindrical castings of aluminium alloys were solidified under one-dimensional heat flow conditions using the experimental set-up described in section 3.3 [Ampu]. This set-up has the advantage to prevent any convection associated with pouring effect since the ceramic mould and the metal are first preheated together in a furnace. Once a uniform temperature is reached, the furnace is removed and an instrumented water-cooled copper chill is applied to the bottom surface of the mould. The latter is made out of a thin aluminium-nitride plate having a high thermal conductivity. Eight thermocouples were placed at various heights of the aluminium ingots (10, 20, 40, 60, 80, 100, 120 and 140 mm from

the chill). The first thermocouple near the chill was taken as a boundary condition (imposed temperature) to determine by an inverse calculation the temperature-dependent thermal conductivity of the two industrial aluminium alloys using the seven remaining cooling curves. The computation domain is shown in figure 4.7.

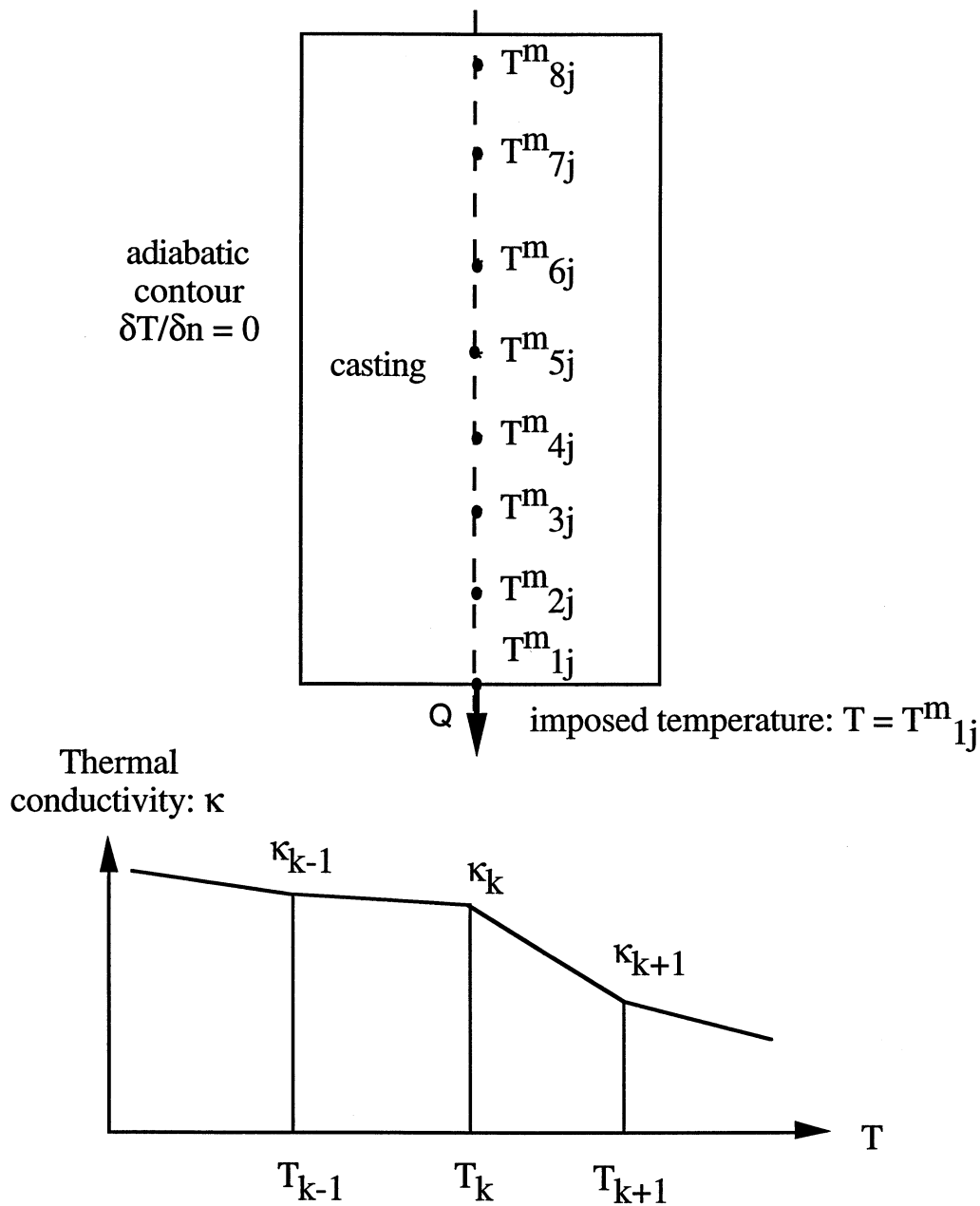


Figure 4.7: computation model with boundary conditions and tabulated values of the thermal conductivity. The positions of the thermocouples inside the casting are also represented.

An adiabatic boundary condition was set at the lateral and upper surfaces of the ingot, since the ceramic mould was made of a very low thermal diffusivity

material (Promat™). The calculated thermal conductivities are reported in section 5.2.

The second application of the inverse method was the determination of the steady-state heat extraction along the rolling faces of the ingot during DC casting. A stationary height-dependent heat flux was estimated along the vertical boundary of the casting. So  $\vec{\beta}$  is the vector  $\{q_1, q_2, \dots, q_N\}$ , where the  $q_k$ 's are heat fluxes for a set of given vertical positions,  $z_k$ , the values of the heat flux in each interval  $[z_k, z_{k+1}]$  being linearly interpolated (see figure 4.8). In order to determine these coefficients, cooling curves were measured at the mid-plane of a DC-cast ingot in the steady-state regime of casting (see section 3.1). The thermocouples being moved with two long rods already trapped by the solid part of the ingot, they were translated downwards at the casting speed.

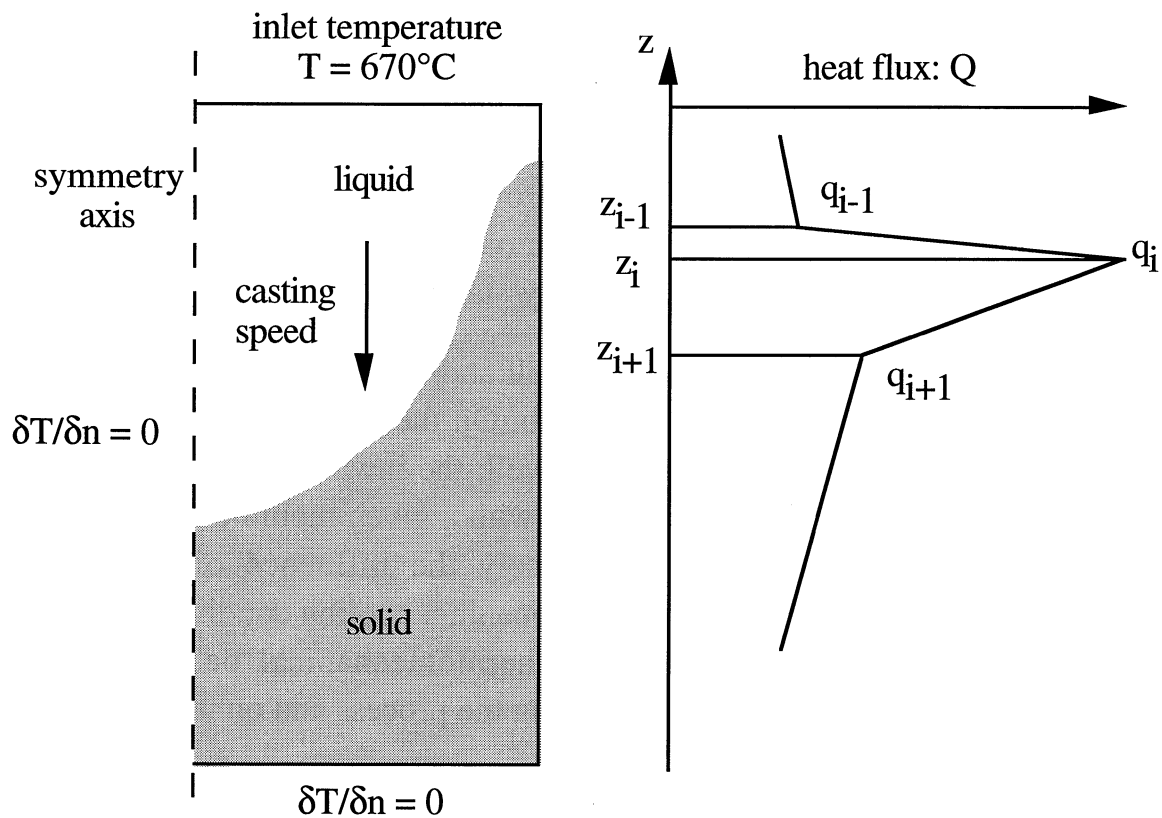


Figure 4.8: computation domain with the boundary conditions for the determination of the stationary heat flux along the rolling faces of a DC-cast ingot.

These cooling curves were then converted into temperature profiles along the height of the ingot (stationary conditions) and then used to deduce by inverse modelling the height-dependent heat flow extracted along the lateral surface of the slab by the mould (primary cooling) and by the water jet (secondary

cooling). This was possible because the software 3-MOS can account for an advection term, the casting speed in the present case. Moreover, the sum in equation 4.12 is performed on the indice  $j$  alone, owing to the fact that a stationary thermal field is searched. For this application, the computation time was increased by the fact that for each direct FEM calculation a steady-state regime had to be reached. To limit this problem, the perturbation calculations were restarted from the steady-state temperature profile obtained at the former iteration. Experimental details of the measurements are given in section 3.1 and the computed heat fluxes are reported in section 5.2.

### **4.3 Thermomechanical modelling**

Two-dimensional (2D) and three-dimensional (3D) models based upon the software Abaqus [Abaq] have been developed for the computation of the thermomechanical state of the solidifying strand during DC and EM-casting and subsequent cooling to room temperature of the ingot in the pit. Based upon a finite element formulation, the models determine the temperature distribution, the stresses and the associated deformation in the metal. The thermal stresses are partially relieved by viscoplastic mechanisms and accordingly the final ingot distortion is expected to be larger than that of a purely elastic metal. Transient thermomechanical computations are carried out on a variable domain from the start phase of casting up to the pseudo steady-state regime.

The 2D model can predict the butt swell and the inward rolling faces pull-in in the mid-plane of symmetry of the slab. On the other hand, the 3D model allows to compute the butt curl, the butt swell, the inward rolling faces pull-in and the final ingot cross-section associated with a given mould design. The aim of these two models is to assess precisely the influence of the process parameters (casting speed, mould/inductor opening, cooling conditions, etc.) and of the alloy composition on the ingot thermomechanical behaviour, with particular emphasis on its deformation during the process and on its final shape.

#### **4.3.1 The 2D model**

Since three-dimensional transient computations are very intensive, the present investigation was limited in a first step to two dimensions. The computation domain includes the liquid metal, the mushy zone and the solid part. The coordinate system is fixed with respect to the slab. The bottom block is assumed to have a constant shape. The domain of calculation is increasing over time as new liquid metal is fed to the system. This extending domain is modelled by the addition of successive layers of a predefined enmeshment.

### Computation domain

Figure 4.9 shows the computation domain used for the study of the contraction of the rolling faces. This domain corresponds to one of the plane of symmetry of the slab (plane (yz)). Since this mid-plane section is perpendicular to the rolling faces and the width to thickness ratio of the slab is large (about 4), the heat flow is assumed to be two-dimensional and mechanical aspects are reduced to a plane-deformation problem.

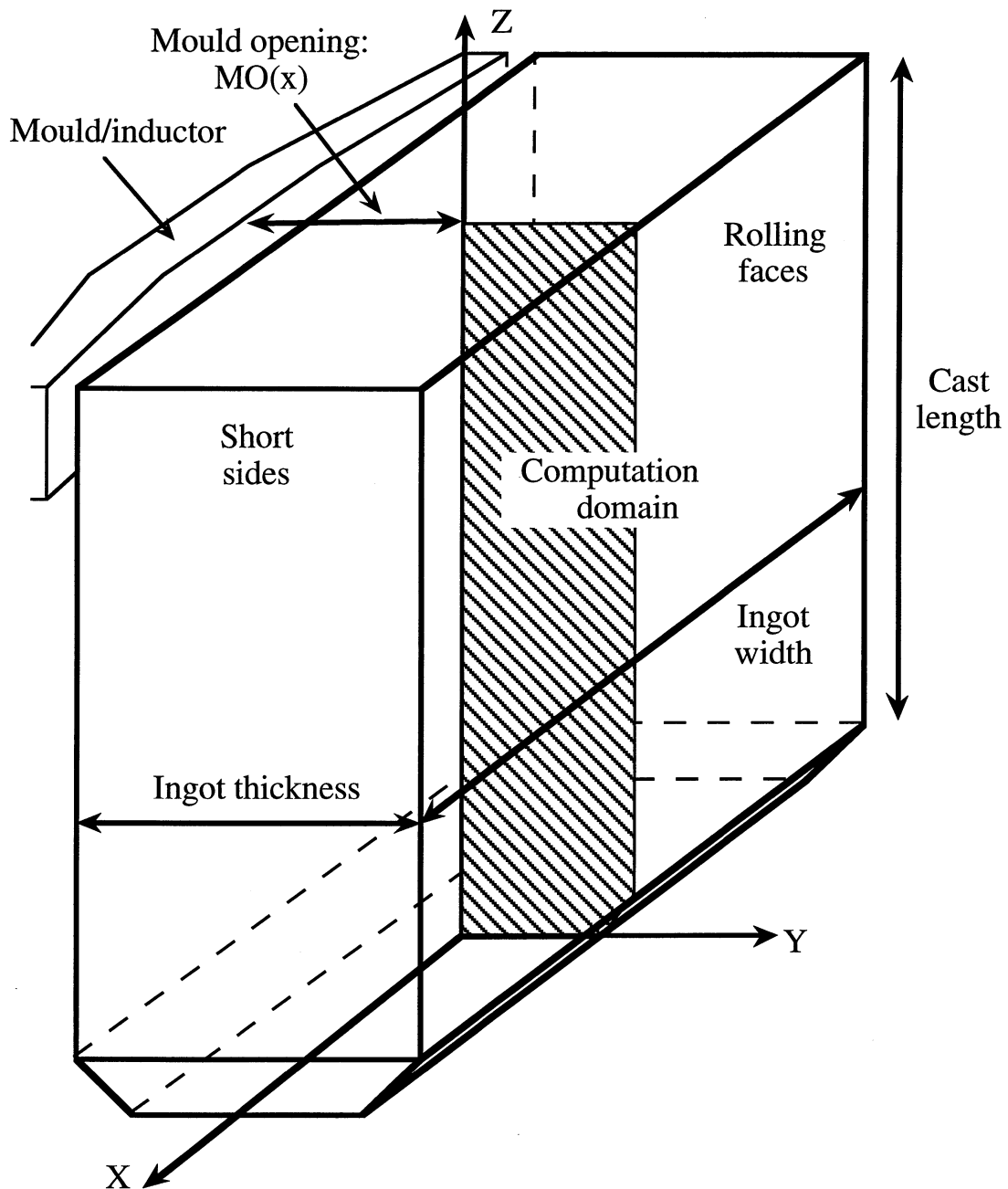


Figure 4.9: the 2D computation domain.

### *Thermal aspects*

Leaving aside convection in the molten pool, the thermal evolution within the slab is predicted by solving the heat conduction equation:

$$\rho C_p^e \frac{\partial T}{\partial t} - \text{div} (\kappa \cdot \overrightarrow{\text{grad } T}) = 0 \quad (4.16),$$

where  $\kappa$  is the thermal conductivity,  $\rho$  is the density and  $T$  is the temperature field.  $C_p^e$  is the equivalent specific heat which accounts for the latent heat released during solidification. The aluminium alloys investigated in this study contain only small amounts of impurities or alloying elements. Therefore, their specific heat,  $C_p$  and latent heat,  $L$ , are close to the values characterising pure aluminium. The values which have been used in the numerical simulations that follow are taken from Pehlke [Pehl] and are given in Table 4.2 ( $T_L$  and  $T_S$  are the liquidus and solidus temperatures of the alloy, respectively). The latent heat was set to  $9.5 \cdot 10^8 \text{ J/m}^3$  [Pehl]. Even though most of the latent heat is released near the liquidus for such an alloy, the volume fraction of solid,  $f_s$ , has been assumed to be linear between these two temperatures for a faster convergence of the computations. In the mushy zone, the specific heat has been averaged over the solid and liquid phases. Thus the equivalent specific heat was given by:

$$\rho C_p^e = \rho C_p^s f_s + \rho C_p^l (1 - f_s) + \frac{L}{T_L - T_S} [u(T_L - T) - u(T_S - T)] \quad (4.17),$$

where  $u$  is the Heaviside function<sup>1</sup> (the indices  $s$  and  $l$  refer to the solid and liquid, respectively).

Contrary to the specific heat, the thermal conductivity of aluminium alloys is highly dependent on the alloying elements or impurities, even at low concentration. Thus, special attention has been paid to the exact knowledge of the temperature-dependent thermal conductivity. The calculated thermal conductivities using inverse modelling (see section 4.2) were used here.

Despite the low thermal conductivity of liquid aluminium (80-90 W/mK), the value of the thermal conductivity in this phase was increased to a larger value in the numerical computations (300 W/mK) so as to account for liquid convection in the sump. This value was determined by calculating the steady

---

<sup>1</sup>  $u$  is defined as follows:  $u(x) = 1$  if  $x \geq 0$  and  $u(x) = 0$  if  $x < 0$

state sump depth in the plane of symmetry ( $yz$ ) (see figure 4.10) and by comparing the result with the measured value (see section 3.1).

T (°C)	$C_p$ (kJ/kg.K)	T (°C)	$C_p$ (kJ/kg.K)
27	0.905	427	1.090
127	0.950	527	1.135
227	0.998	$T_S$	1.181
327	1.043	$T_L$	1.086

Table 4.2: specific heat as a function of temperature as used in the computations.

The thermal problem is solved in a two-dimensional domain which corresponds to the solidifying strand. The boundary conditions that are applied to DCC, are summarised in figure 4.10 and detailed hereafter:

- S1 is adiabatic for symmetry reason;
- S2 is the ingot-bottom block interface. The thermal flux through this interface is assumed to obey a Cauchy-type law. The sink temperature which is in this case the mean bottom block surface temperature was set to 100°C whereas the heat transfer coefficient,  $h$ , was chosen to be a decreasing function of the vertical displacement of the ingot so that the computed 3D results (see section 4.3.2) give a butt curl during the starting phase which is close to the experimental result.
- S3 is the lateral surface of the ingot where the cooling is represented by the heat flux as determined using inverse modelling (see section 4.2). At the top of the mould where the alloy is in direct contact with the mould (DCC), the prescribed heat flux is set to a given value until the ingot temperature is lower than the coherency temperature of the alloy corresponding to the temperature at which an air gap forms (see chapter 5); this primary cooling is absent for EMC. After the air gap has formed in DCC, the surface of the ingot is assumed to be almost adiabatic until the point of impact of the water cooling. The remaining part of S3 corresponds to the secondary cooling zone (water jet). The calculated height-dependent heat flow on the lateral surface of the slab is converted into a heat transfer coefficient depending on the position and a constant water temperature of 10°C.

- S4 is the upper moving boundary of the domain. The incoming flow of liquid metal is modelled by the activation of successive layers of the enmeshment. The temperature of the new volume element is set to that of the incoming metal, 670°C. The rate at which new layers are introduced corresponds to the casting speed and the lateral cooling conditions are translated along the external faces of the slab according to the casting speed as well.

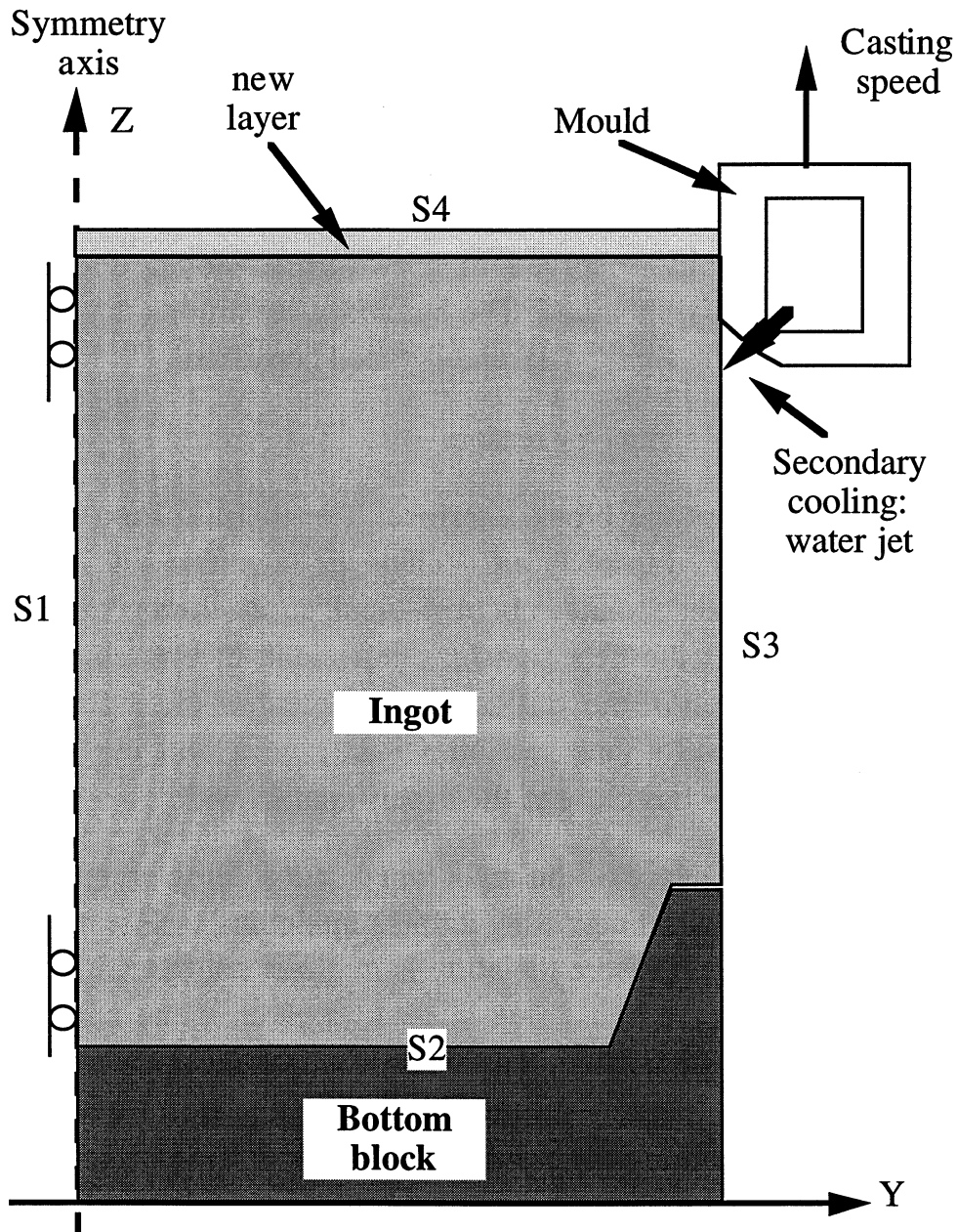


Figure 4.10: schematic representation of the calculation domain with its boundaries.



### *Mechanical aspects*

A two dimensional Cartesian model with planar deformation, i.e.  $\delta\epsilon_{XX} = \delta\epsilon_{XY} = \delta\epsilon_{XZ} = 0$ , has been used. So as to give some rigidity to the system, the central part of S2 is mechanically fixed, whereas the remaining part is free. The points located on the boundaries S3 and S4 are free to move, whereas those on S1 are free to slide along the z-axis.

The density of the metal is supposed to be constant ( $\rho = 2650 \text{ kg/m}^3$ ). The liquid metal is assumed to be incompressible and fluid motion is neglected (except for the increased thermal conductivity introduced for the liquid phase). The liquid is modelled as a medium with a low elastic modulus. Above its coherency temperature,  $T_c$ , the alloy is treated like a liquid and below  $T_c$ , it is treated like a solid (the coherency temperature is the temperature at which the dendrites form a coherent network that develops some strength, thus resulting in a behaviour close to that of a solid; above this temperature, the grains are free to move and the solid-liquid mixture is treated rather like a liquid, see section 2.2.5). The contribution of the metal shrinkage during solidification is neglected owing to the constant liquid feeding within the mushy zone [Drez1]. The alloy is allowed to contract as soon as it reaches its coherency temperature. The determination of  $T_c$  is detailed in section 3.2.

Under the assumption of instantaneous equilibrium, the variation of the internal stress tensor,  $\delta\sigma$ , during a time interval,  $\delta t$ , is obtained in terms of the external force field variation,  $\delta f$  (in this case gravity), by solving the following incremental equation:

$$\text{div } \delta\sigma + \delta f = 0 \quad (4.18).$$

The incremental deformation tensor  $\delta\varepsilon$  is assumed to be a superposition of elastic, thermal and viscoplastic components  $\delta\varepsilon^e$ ,  $\delta\varepsilon^{\text{th}}$  and  $\delta\varepsilon^{\text{VP}}$  :

$$\delta\varepsilon = \delta\varepsilon^e + \delta\varepsilon^{\text{th}} + \delta\varepsilon^{\text{VP}} \quad (4.19).$$

The elastic deformations are related to the internal stresses by Hooke's law:

$$\delta\sigma = [D] \cdot \delta\varepsilon^e \quad (4.20),$$

where  $[D]$  is the stiffness matrix defined in terms of the Young and Poisson moduli,  $E$  and  $\nu$ . The thermal deformations are related to the local temperature variation,  $\delta T$ , through the equation:

$$\delta\varepsilon_{ij}^{\text{th}} = \alpha \cdot \delta T \cdot \delta_{ij} \quad (4.21),$$

where  $\alpha$  is the linear expansion coefficient and  $\delta_{ij}$  is the Kronecker symbol. The temperature dependence of the Young modulus,  $E$ , and Poisson's ratio,  $\nu$ , and of the dilatation coefficient,  $\alpha$ , is taken into account and the values of these parameters are assumed to be equal to that of pure aluminium [Mond,Hatch]. The differential temperature-dependent coefficient of linear thermal expansion as found in Hatch [Hatch] was transformed into a mean coefficient taking the coherency temperature of the alloy as the reference temperature. This procedure is detailed in appendix II. The Young modulus rapidly decreases from its value of 40 GPa at  $T_c$  to a very low value, 0.1 GPa, above the coherency temperature. These values are listed in Table 4.3 whereas the Poisson modulus,  $\nu$ , is assumed to be constant and equal to 0.37.

T (°C)	E [GPa]	T (°C)	E [GPa]
25	68.2	$T_c$	40
200	60.6	$T_c + 1^\circ\text{C}$	0.1
400	51.8	$T_L$	0.1
$T_S$	41.8	$T_{\text{inlet}}$	0.1

Table 4.3: Young modulus as a function of the temperature as used for the computations.

In addition to the elastic and thermal strains, the present model accounts for the time- and temperature-dependent creep flow behaviour of aluminium. The strains generated by creep being physically indistinguishable from those resulting from quasi time-independent plastic flow, particularly at elevated temperatures, the plastic and creep deformations are treated in an unified manner via a "plastic-creep" strain rate. At high temperature, the primary creep is neglected and the viscoplastic incremental deformation of the solid is assumed to be given by :

$$\delta \underline{\epsilon}^{vp} = 3/2 \cdot (\dot{\epsilon}_{vp} \cdot \delta t) \cdot \frac{s}{\sigma_{vm}} \quad (4.22),$$

where  $\sigma_{vm}$  is the equivalent Von Mises stress,  $s$  the deviatoric stress tensor and  $\dot{\epsilon}_{vp}$  is the isotropic viscoplastic strain rate of the material. The minimum creep rates measured at different temperatures and loads (see section 3.2) were fitted using the Garafalo law [Gar1]:

$$\dot{\epsilon}_{vp} = A \left( \sinh \left( \frac{\sigma_{vm}}{\sigma_0} \right) \right)^n \exp \left( -Q/RT \right) \quad (4.23),$$

where  $A$ ,  $\sigma_0$ , and  $n$  are some alloy-dependent constants,  $Q$  represents the apparent creep activation energy,  $R$  and  $T$  are the universal gas constant and temperature respectively. The basic assumption concerning the semi-solid behaviour of the metal is that it can be described by a viscoplastic Norton-Hoff law:

$$\dot{\epsilon}_{vp} = k(T) \cdot \left( \frac{\sigma_{vm}}{\sigma_0} \right)^n \quad (4.24),$$

where  $k$ ,  $\sigma_0$  and  $n$  are temperature-dependent parameters. These parameters were measured using indentation tests (see section 3.2).

### *Numerical procedure*

The finite element program ABAQUS has been employed to perform the numerical computations. It allows the user to specify complex viscoplastic behaviour of materials and flexible boundary conditions through user-subroutines [Abaq]. Successive layers of elements can be added to simulate the evolution of the casting shape. The fully coupled heat transfer/stress analysis is performed using 4 nodes quadrilateral elements, bilinear in displacement and temperature. The non-linearities introduced by the material properties (creep and latent heat) and by the contact are treated by a Newton-Raphson iterative scheme: at each time step, iterations with an updating of the material characteristics, are made until both thermal and mechanical equilibrium are reached within the tolerances set by the user. The viscoplastic behaviour of the metal was treated using a creep analysis (creep option) in which plastic deformation may occur under any non-zero stress meaning that there is no yield function (see equations 4.23 and 4.24). The time step was controlled by two accuracy parameters: the maximum temperature change to be allowed in any increment at any node of the model (2°C) and the maximum allowable difference in the creep strain increment (0.01%) calculated from the creep strain rates based on conditions at the beginning and end of the increment. An implicit integration scheme was used and the typical time step was of the order of 0.5 sec. The computation time was about 24 hours on a HP-735 workstation for a domain including 2000 nodes and for modelling about 1.5 hour of casting.

### **4.3.2 The 3D model**

The 3D model is an extension of the 2D model and is therefore very similar except for the points detailed hereafter. The computation domain as viewed from

the ingot centre in figure 4.11, represents one quarter of the slab since the two planes (xz) and (yz) are planes of symmetry. The bottom block and the mould are not part of the model and are thus assumed to have a constant shape.

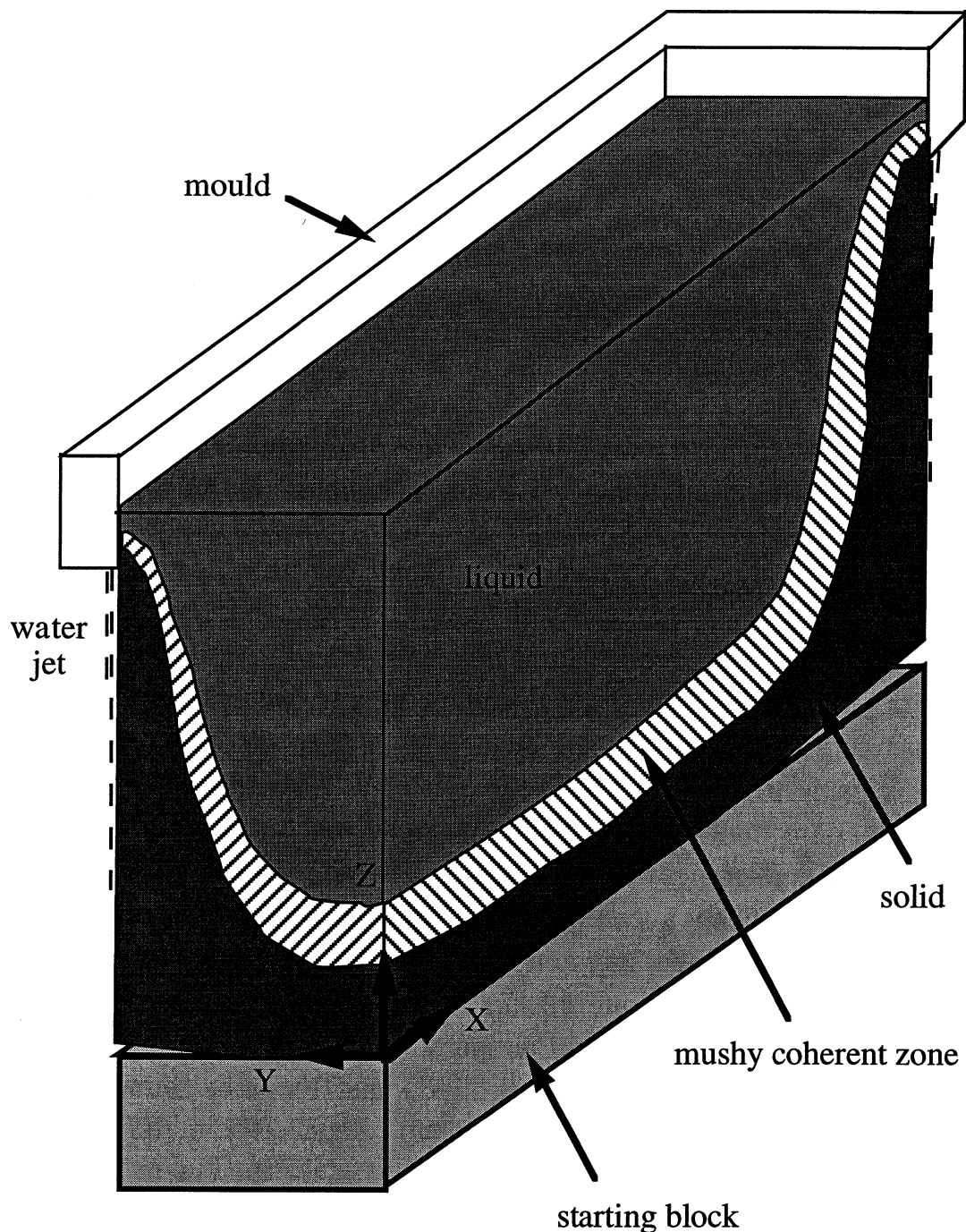


Figure 4.11: schematic view of the DC casting process. This part corresponds to the computation domain of the slab (one fourth for symmetry reason).

Except for the origin of the ingot (see figure 4.11) which is fixed so as to give enough rigidity to the system, the points located on the two planes of

symmetry (xz) and (yz) are free to slide in their respective planes. From a thermal point of view, these two planes are adiabatic for symmetry reasons.

The finite element mesh is made of layers, 2 cm in thickness; each layer fits the exact design of the mould as shown in figure 4.12 which represents a top view of the initial ingot shape.

The fully coupled simultaneous heat transfer and stress analysis was performed by Abaqus using 8 nodes brick elements with trilinear displacement and temperature interpolations. To improve the convergence of the plasticity algorithm and therefore reduce the computation time, the viscoplastic behaviour of the metal was treated using a rate-dependent plasticity analysis (rate-dependent option). In this case, the rate of plastic flow, defined by the strain rate, depends on the amount by which the stress exceeds a yield value. Provided the plasticity algorithm has converged, the time integration was controlled by one accuracy parameter: the maximum temperature change to be allowed in any increment at any node of the model ( $2^{\circ}\text{C}$ ). An implicit integration scheme was used but the typical time step remained of the order of 0.2 sec, thus leading to considerable computation times.

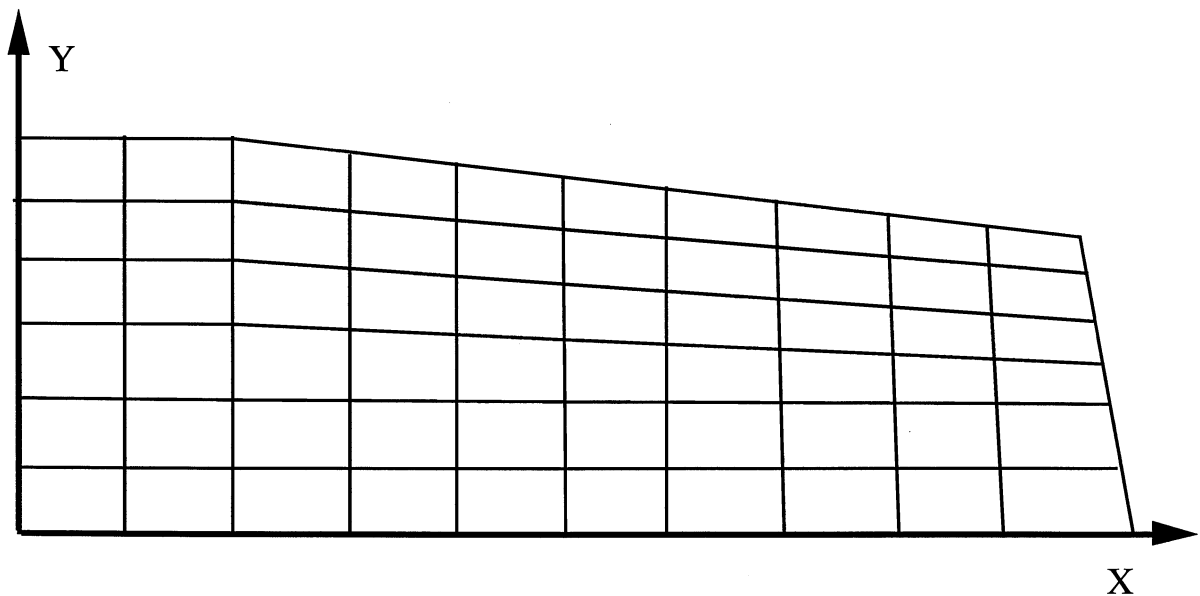


Figure 4.12: finite element enmeshment of a layer of the casting, as viewed from the top (nominal ingot format: 1860 x 510 mm).



## RESULTS AND DISCUSSION

In this chapter, the experimental and modelling results are presented and discussed. Whenever possible, numerical results are compared together with the measurements. Possible future developments are also suggested. First, the experimental results obtained using the procedures described in chapter 3 will be presented. Then, the computation results provided by the numerical models presented in chapter 4 will be used to emphasise the main outcome of the present work.

### 5.1 Experimental results

#### 5.1.1 Measurements on full-size DC/EM castings

The measurements on full-size DC/EM castings performed at the experimental cast house of the Alusuisse company are presented in this section. They will be helpful to understand better the main mechanisms responsible for the ingot distortions and will also serve as a basis for the validation of the thermomechanical computations of the ingot deformations.

##### *Temperature profile and sump depth*

Figure 5.1 shows the cooling curves recorded during the DC casting of the 1201 ingot cast at 80 mm/min. These measurements were performed after the steady state regime of casting was reached, i.e. after a cast length of at least one meter. The position of the thermocouples from the lateral surface of the ingot is indicated on the figure. Using the withdrawal speed of the ingot, the time scale on the horizontal axis has been converted into the distance from the top surface of the liquid metal. Similarly, figure 5.2 shows the cooling curves recorded during the DC casting of the 3104 ingot cast at 50 mm/min. From these measurements, it is apparent that the liquid pool is approximately uniform in temperature (about 665°C), due to strong convection and low superheat. The temperature at each thermocouple location starts to decrease significantly as soon as the metal begins to solidify. Figure 5.3 shows the steady-state temperature profile within the 1201 ingot during DC casting and the sump depth as determined from the five temperature histories of figure 5.1. The values of the liquidus and solidus temperatures of the alloys 1201, 3104, 5754 and 5182, were determined by Gabathuler [Gaba] by means of thermoanalysis (for conditions close to those of the DC casting).

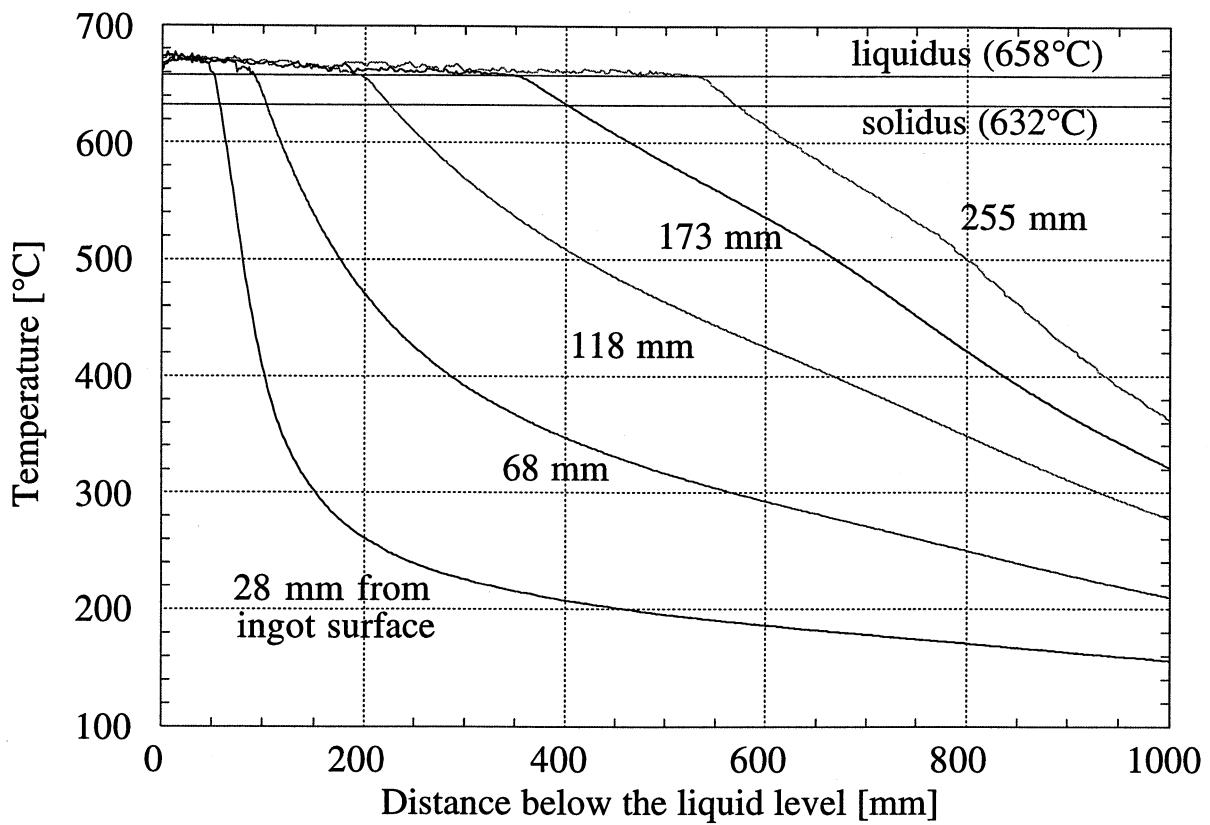


Figure 5.1: measured temperatures during the DC casting of the 1201 alloy cast at 80 mm/min (format: 1860 x 510 mm).

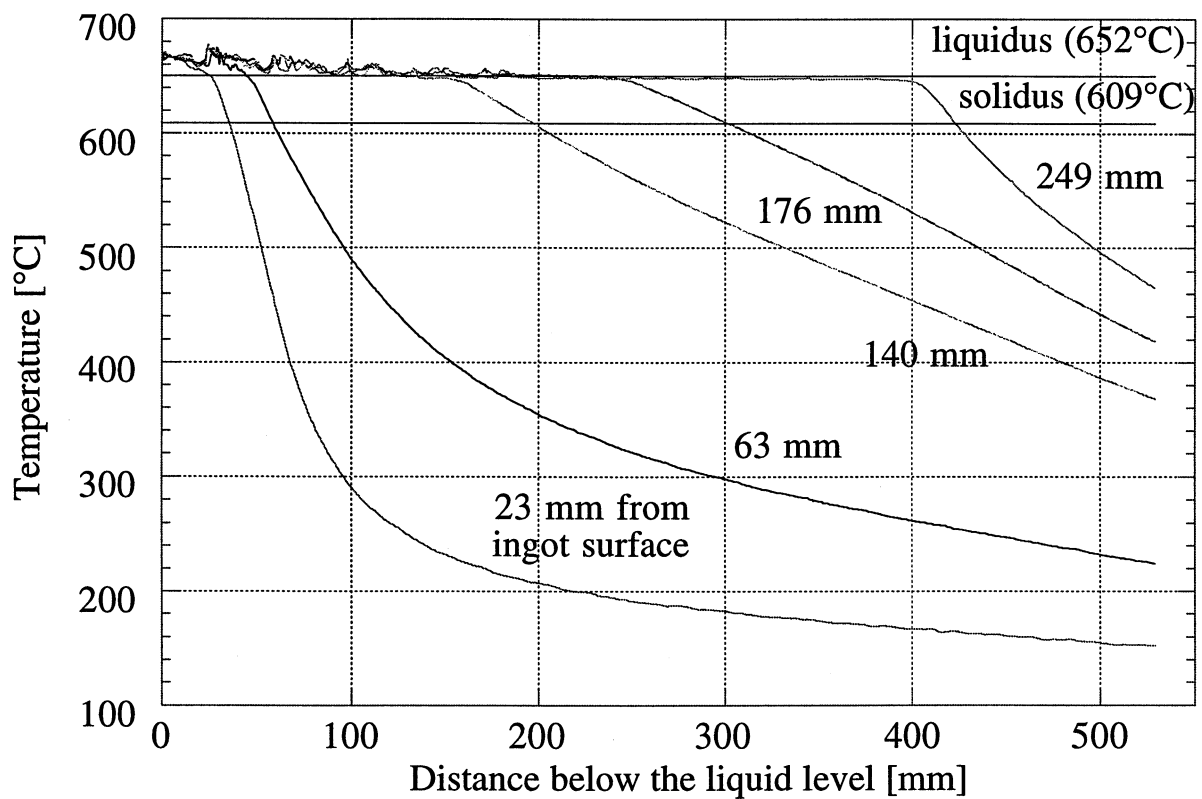


Figure 5.2: measured temperatures during the DC casting of the 3104 alloy cast at 50 mm/min (format: 1860 x 510 mm).



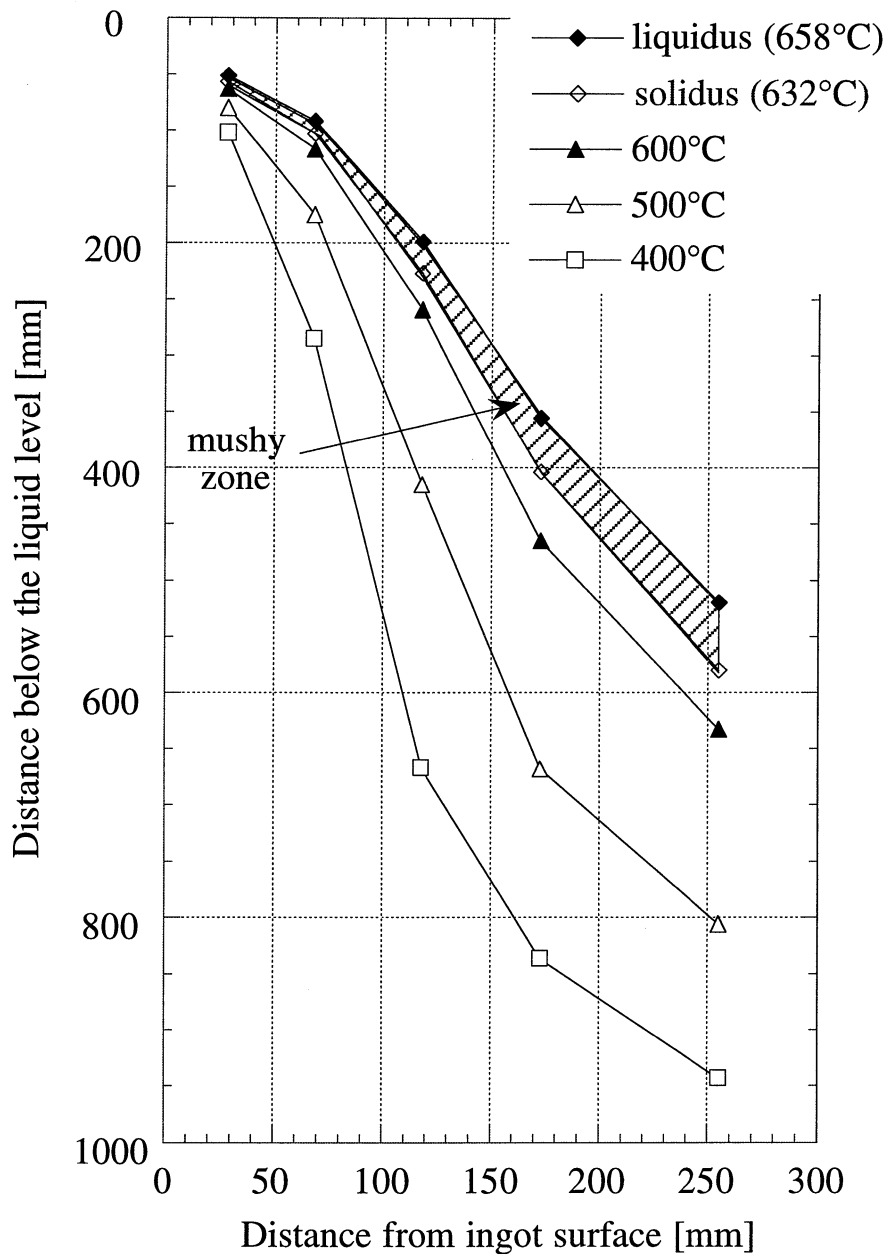


Figure 5.3: temperature profile of the 1201 alloy ingot during the DC casting process as deduced from figure 5.1.

For the alloy 1201, these values are 658°C and 632°C, respectively. They were used to evaluate the sump depth. The deep sump depth shown in figure 5.3 (580 mm) is due to the high casting speed used for this particular ingot, lower casting speeds resulting in shallower sumps as reported in Table 5.1. The same procedure was applied to the DC casting of the ingot 3104: the steady-state temperature profile is shown in figure 5.4. The sump depth for this alloy decreases to about 430 mm owing to the lower casting speed used (50 mm/min); this value is close to the 425 mm sump depth measured for the 1201 alloy at the same casting speed (see table 5.1).

Casting speed [mm/min]	50.	60.	80.
Sump depth [mm]	425.	480.	580.

Table 5.1: sump depth as a function of the casting speed (alloy 1201, format 1860 x 510 mm).

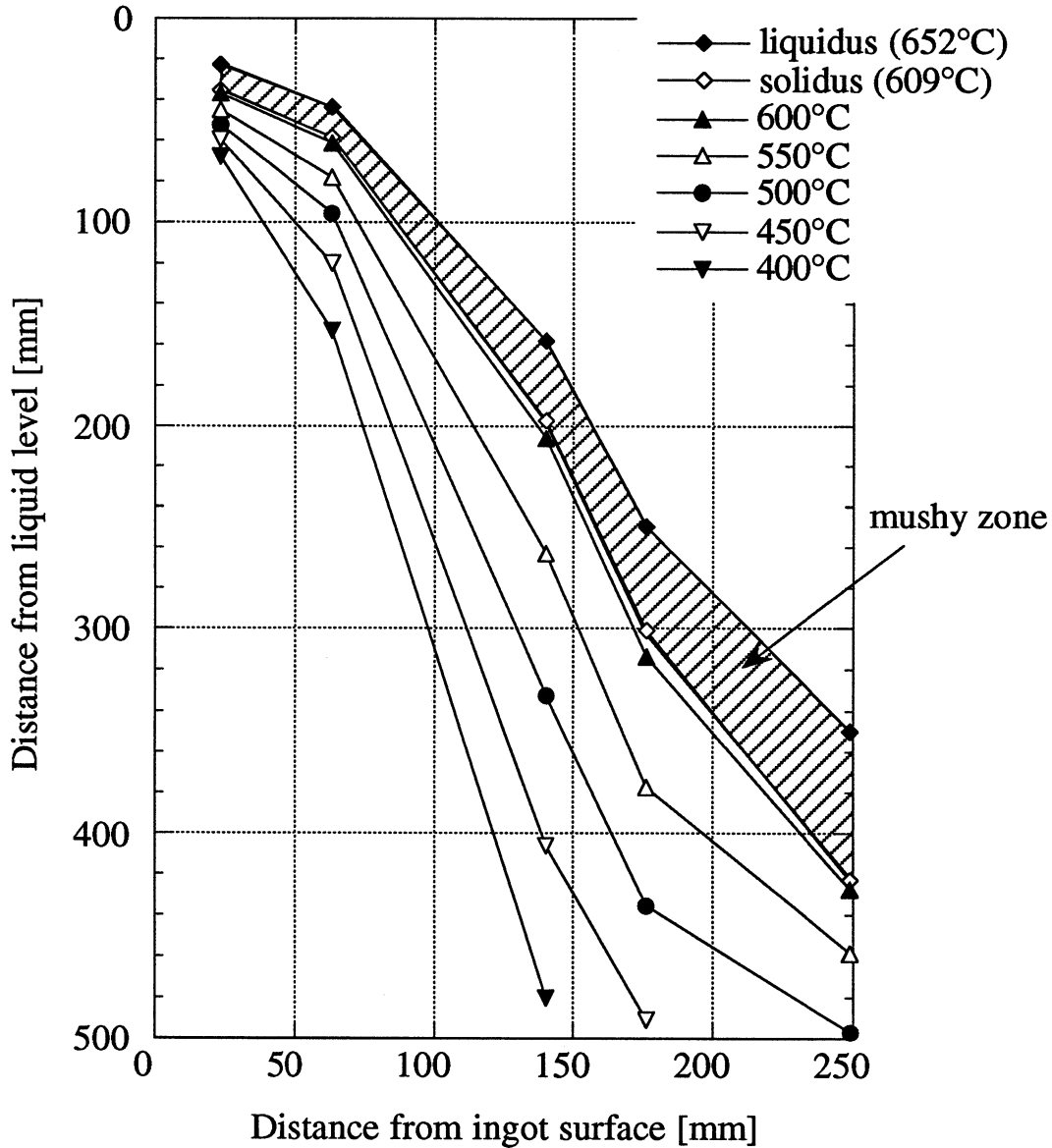


Figure 5.4: temperature profile of the 3104 alloy ingot during the DC casting process as deduced from figure 5.2.

#### *Contraction of the solidifying shell*

The recorded temperatures and contraction of the solidifying shell in the mould using a quartz rod (see section 3.1) are shown in figure 5.5 for the alloy 5754 DC-cast at 60 mm/min. These data are again represented as a function of the distance below the top liquid surface, as measured by the vertical

displacement sensor (see figure 3.3). They have been measured after a steady-state regime of casting had been reached. These temperatures were recorded at the surface and at 50 mm from the ingot surface.

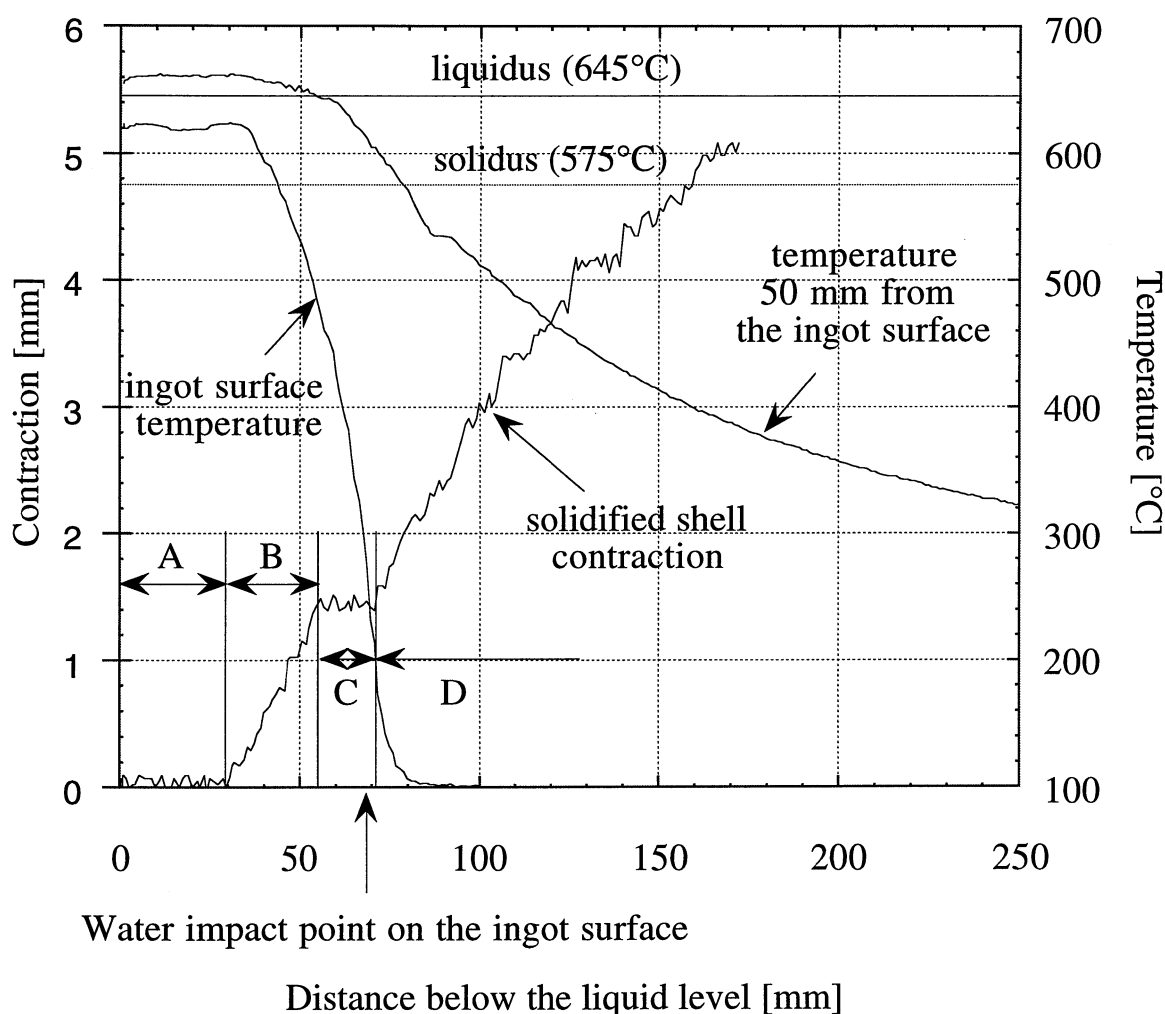


Figure 5.5: measured pull-in and temperatures inside the mould of the 5754 alloy during DC casting (casting speed: 60 mm/min).

As can be seen, the initial height where the metal and the mould are in good thermal contact is about 30 mm (zone A in figure 5.5). Then, an air gap forms over a distance of 25 mm (zone B) and remains at a constant clearance of 1.5 mm for the next 20 mm (zone C). After this short plateau, the metal pulls away from the mould at a nearly constant rate (zone D). The displacement of the ingot measured by the moving quartz rod was checked at the exit of the mould with the value recorded by the displacement sensor which was attached below the mould (see figure 3.3). The two measurements were in fairly good agreement (typically within 10% error). Moreover, the surface temperature at the exit of the mould is too low to allow surface remelting and possible exudation. The point of impact of the cooling water on the lateral side of the ingot is shown in figure 5.5.

It almost coincides with the end of the constant air gap zone. The surface temperature of the ingot just below the cooling water spray is about 200°C. As can be seen in figure 5.5, the surface temperature of the ingot during the contact period A is already below the liquidus of the alloy whereas, at 50 mm from the surface of the metal, the metal is still totally liquid. Although the temperature measured at the surface of the ingot might be slightly biased by an incomplete wetting of the thermocouple, it increases slightly (about 10°C) at the onset of the air gap formation (beginning of zone B in figure 5.5) when the heat extraction is decreased. At the temperature of 620°C measured at the surface of the 5754 alloy ingot when it pulls away from the mould, the volume fraction of solid is estimated to be about 70% according to Gabathuler [Gaba]. Clearly, the metal contraction in the mould occurs when the surface of the alloy is still in the semi-solid state. However, this contraction does not exceed 1 or 2 mm before the water jet is applied.

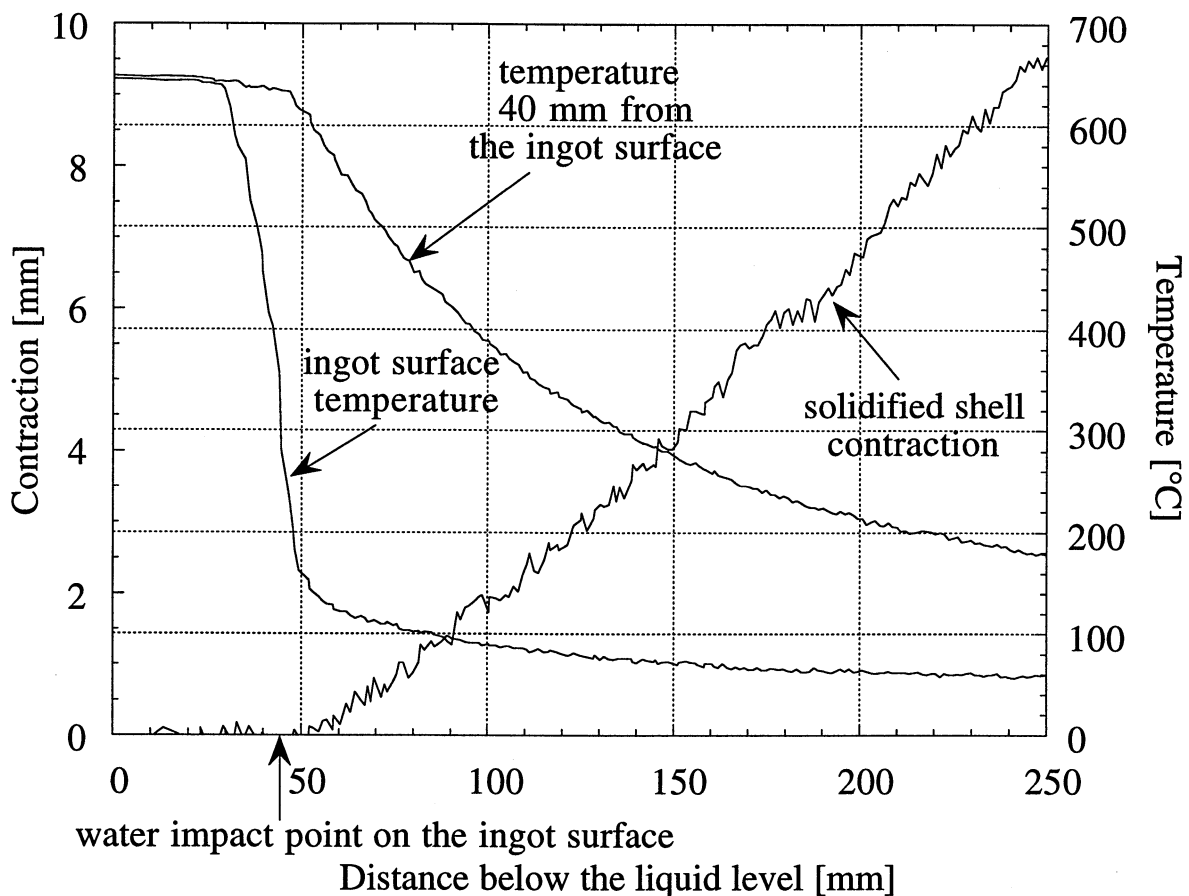


Figure 5.6: measured pull-in and temperatures inside the inductor of the 5182 alloy during EM casting (casting speed: 66 mm/min).

Similarly, figure 5.6 shows the recorded temperatures and displacement of the solidifying shell during the steady-state EM casting regime of the alloy 5182 cast at 66 mm/min. The displacement plateau observed in DC casting (zone C in

figure 5.5) is no longer present and the contraction of the shell just below the point of impact of the cooling water occurs at nearly constant rate. At 250 mm below the top liquid surface, the rolling face pull-in is almost 10 mm. The two temperatures within the EM-cast ingot were recorded at the lateral surface and at 40 mm from the surface. The surface temperature at the point of impact of the water cooling is about 200 °C as was already the case for the DC-casting process. Above this point, the temperature within the liquid near the surface is much more uniform than in DC casting due to firstly, the absence of a direct contact with a mould and secondly, the strong convection induced by the electromagnetic field [Kräh].

### *Contraction of the cold ingot*

The three measured cross-section profiles shown in figure 5.7 have been obtained for the 3104 ingot DC-cast at 70 mm/min. These profiles have been measured after complete cooling at three different heights of the ingot and the interior mould shape is also represented for comparison. Instead of producing flat rolling sheet ingots, the design of the present mould lead to W-type shape ingot cross sections. After a transient stage of about one meter, the cross section shape remains nearly constant: this corresponds to a nearly stationary thermomechanical stage. Near the top of the ingot (head), the section change of the ingot becomes less pronounced as is the case of the start-up stage. Figure 5.7 clearly shows that the rolling faces pull-in is important : about 25 mm for the half ingot thickness at the centre of the ingot in the steady-state casting regime. The contraction of the ingot near the two short sides remains nearly constant during the entire casting process and is much smaller (about 6 mm). The horizontal line at 255 mm indicates the desired half thickness of a perfectly flat ingot. This value, which is somehow arbitrary, is fixed to a value close to the final thickness of the short sides.

The global ingot contraction is defined as  $\log(T/MO)$  where T is the ingot thickness after complete cooling to room temperature and MO is the corresponding mould opening. It is shown with the opposite sign in figure 5.8. In the steady-state regime of the casting, the metal contraction is about 9.5 % in the central part of the rolling faces but only about 2.5 % near the short sides. The required contraction to produce a perfect flat ingot of 510 mm thickness with this mould geometry is also shown for comparison. The contraction near the short sides is slightly less than the desired value, thus leading to a thickness which is slightly larger than expected. At the opposite, the ingot contracts too much in the centre when a stationary regime is obtained. In order to understand better the mechanisms responsible for the contraction of the ingot during semi-

continuous DC casting process, the contraction in the steady-state regime of the process was measured for various casting conditions and alloy compositions.

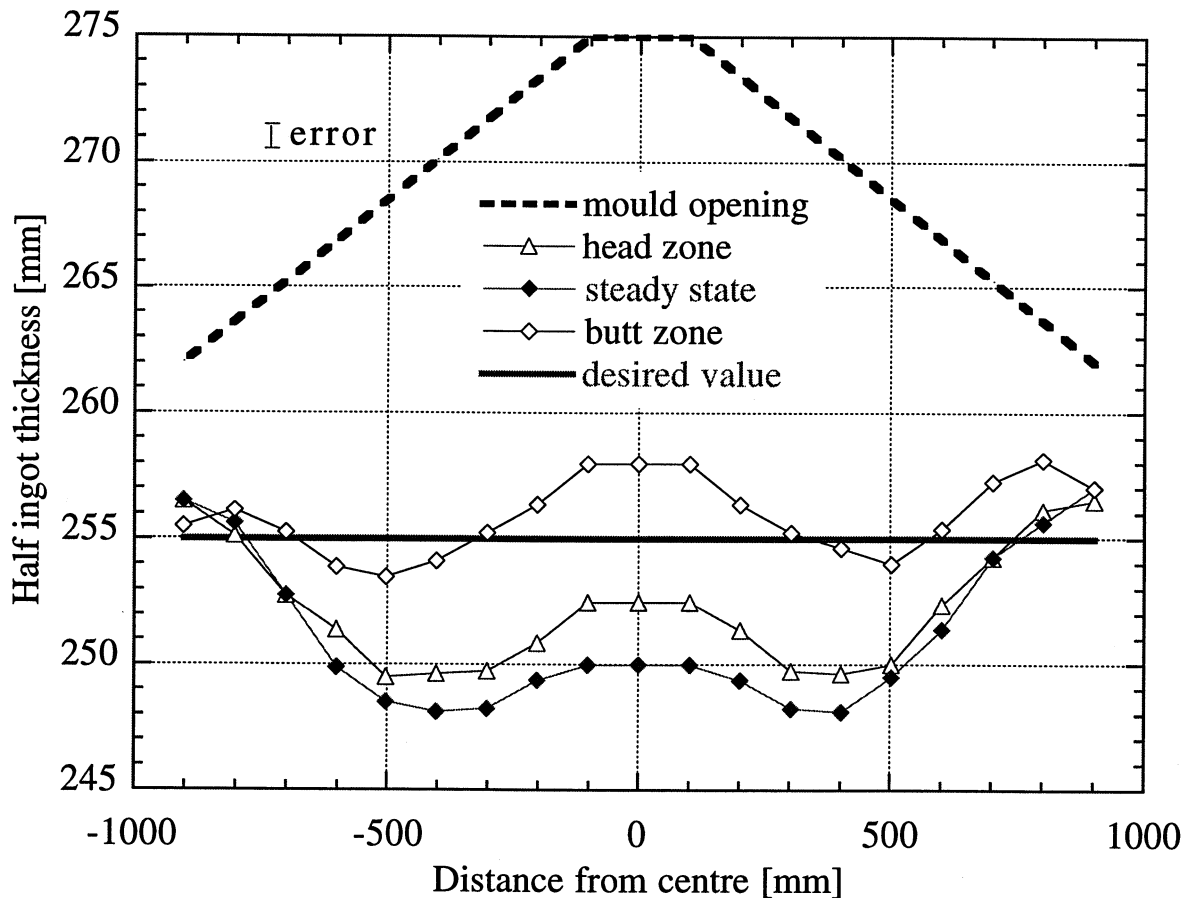


Figure 5.7: contraction of the 3104 DC-cast ingot in the starting zone (butt zone), stationary and end zone (head zone) phases and geometry of the mould (casting speed: 70 mm/min, nominal size: 1860 x 510 mm).

The influence of the casting speed on the contraction of the ingot in the stationary regime of casting for the alloys 1201 and 3104 is shown in figure 5.9 and 5.10, respectively. For both alloys, it is apparent that the pull-in of the rolling faces centre increases with the withdrawal speed whereas the ends of these faces are almost unaffected by the casting speed. The influence of the alloy composition and grain refinement on the steady-state profile of the lateral faces is shown in figure 5.11, for a casting speed of 60 mm/min. The three alloys were grain refined just before casting with 50 ppm of Al-Ti5wt%-B2wt% ; the case of the non-grain refined alloy 1201 is also shown in this figure. As can be seen, the ingot contraction is not affected much by the microstructure. For the same casting conditions, the alloy 5754 exhibits the largest rolling face pull-in at the centre of the lateral faces, the alloys 3104 and 1201 showing decreasing contractions. As for the influence of the casting speed, the alloy composition does not appear to affect the level of contraction near the short sides of the ingot.

The measurement of the EM-cast ingot cross-section is shown in figure 5.12 for the alloy 3104 cast at 65 mm/min. The profile of the electromagnetic screen and the estimated position of the liquid meniscus are also plotted. The shape of the liquid free surface is simply given by subtracting the estimated gap (about 6 mm) from the position of the magnetic screen and neglecting the radius of curvature at the ingot corners [Kräh]. The maximum pull-in in the steady-state regime appears again at the centre of the rolling faces and is about 17 mm, which represents a contraction of 7% with respect to the estimated free liquid lateral surface. Near the short sides of the ingot, the contraction, 11 mm, seems to be larger than in DC casting. However, due to the radius of curvature of the liquid meniscus at the ingot corners, the effective contraction with respect to the free liquid surface is only about 7 mm. This value is close to that measured for the DC cast ingot shown in figure 5.7.

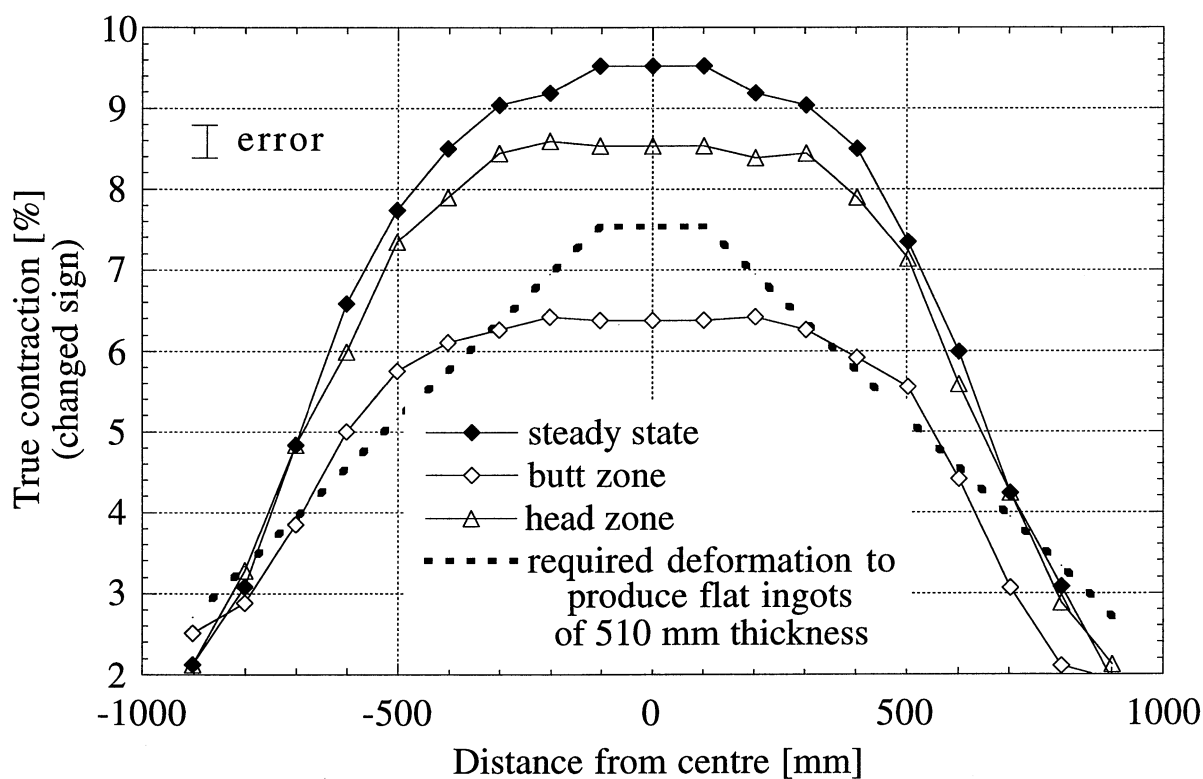


Figure 5.8: true contraction (with opposite sign) of the 3104 ingot cast at 70 mm/min as deduced from figure 5.7.

### Discussion

Weaver [Wea1,Wea2] has explained the ingot deformation occurring during semi-continuous casting in terms of the extension of the liquid pool and of the shape of the solid shell. His model is based on the hypothesis that the heat extraction is uniform and horizontal. As seen in figure 5.3 and 5.4, this is clearly not the case. Moreover, the model of Weaver requires numerous casting trials

for the estimation of the alloy-dependent constants  $K_1$  and  $K_2$  (equation 2.52). The present experimental investigation, in particular the in-situ measurements of the temperature field and of the surface pull-in of the rolling faces, allows to assess more clearly the main mechanisms leading to the non-uniform contraction of the ingot during DC/EM casting.

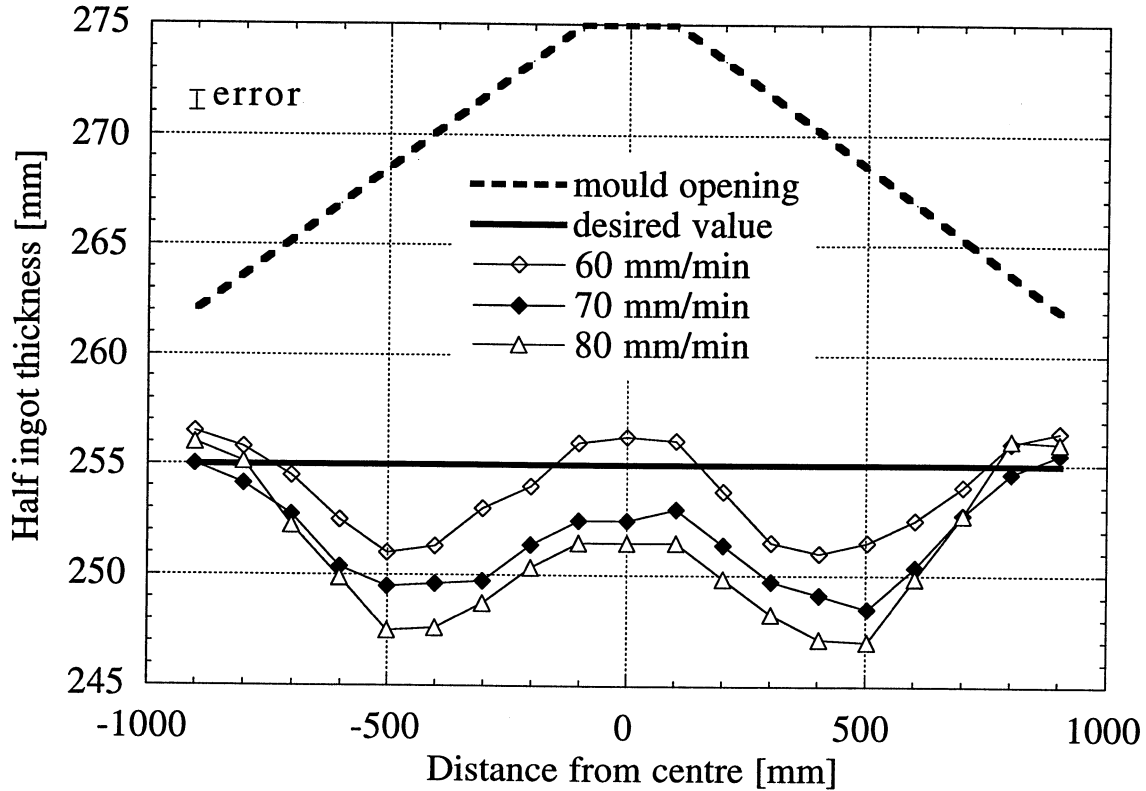


Figure 5.9: influence of the casting speed on the ingot contraction for the alloy 1201 in the steady state regime.

During solidification of a metal, there are essentially two contributions to the ingot contraction, the first one being associated with the phase change (about 6.5% in volume for aluminium [Mond]) and the second contribution arising from the solid state thermal contraction during subsequent cooling (about 1.5%). During the liquid-to-solid phase transformation, there is a constant liquid feeding within the mushy zone to compensate for the density variation. For an aluminium-4.5 wt pct copper alloy, it has been shown that the associated pressure drop within the liquid is not more than one tenth of the atmospheric pressure when no microporosity forms [Ampu]. For alloys having an even larger solidification interval (e.g., Al-Mg), feeding is more difficult and as a result, microporosity may develop more easily. Micrographs of the as-cast ingots revealed almost no microporosity (see figure 5.23). In any case, the pressure drop of the liquid within the mushy zone induced by the density change between



the liquid and solid phases is certainly too low to explain the section change of the cast ingots<sup>1</sup>. Considering figure 5.5, for example, it is seen that the initial pull-in (up to the plateau labelled “C”) only represents 1.5 mm, i.e. 0.6 % in contraction. At the end of this plateau (i.e., 70 mm below the top liquid surface), the surface is totally solid and the solidus line is already 30 to 40 mm in the interior of the ingot (see figure 5.3 and 5.4). Thus, the solid skin of the ingot is already well developed and cannot be deformed by the pressure drop of the liquid within the mushy zone.

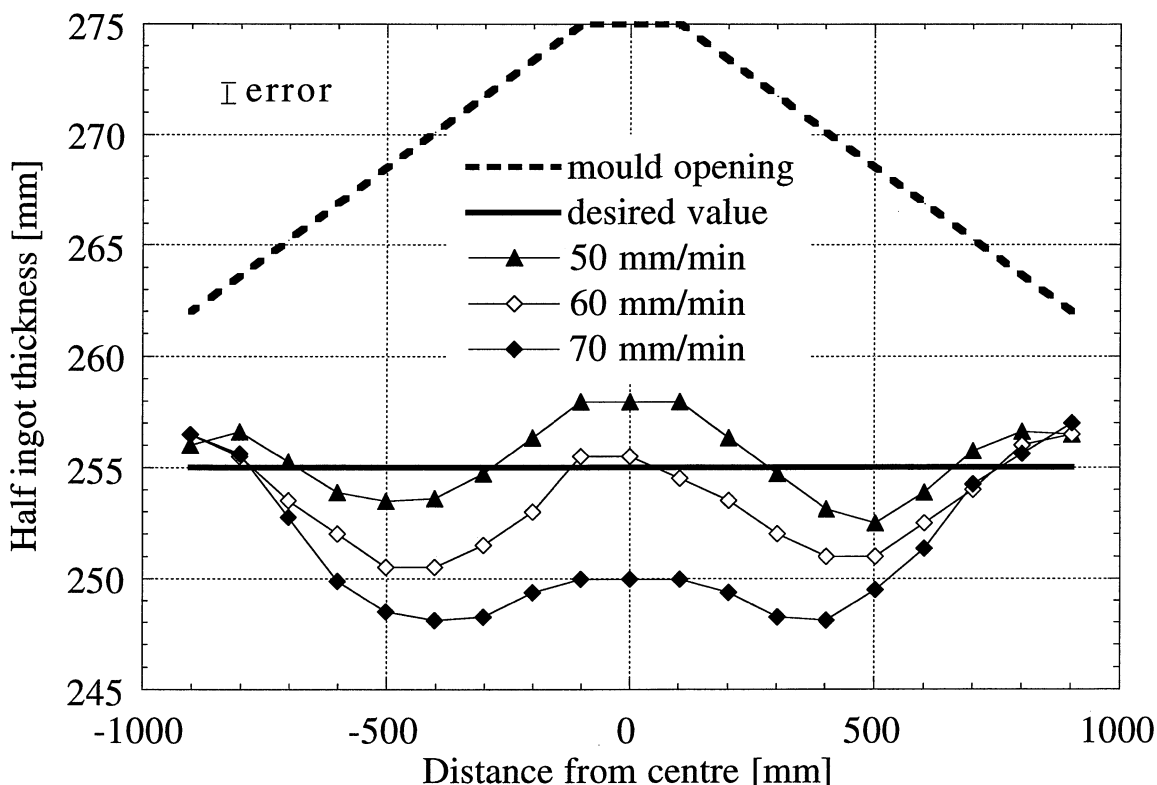


Figure 5.10: influence of the casting speed on the ingot contraction for the alloy 3104 in the steady state regime.

The 9.5% pull-in measured at the ingot centre during DC casting or the 7% pull-in measured during EM casting after complete cooling is therefore a consequence of the deformation of the solid ingot. Although thermal contraction is only 1.5% for a uniform temperature specimen, the *cumulated deformation* and associated *bending* during continuous casting can explain the large pull-in of the rolling faces. Such a mechanism, which is supported by the transient

<sup>1</sup> In case of incomplete liquid feeding, the maximum solid deformation associated with the shrinkage in the mushy zone would be lower than the maximum level of microporosity which could be expected in such alloys (about 1% in volume fraction or 0.3% linear contraction).

deformation state near the bottom of the ingot (see figure 5.7), will be presented in section 5.2.3 in the light of the numerical results. Nevertheless, the main features of this mechanism can be addressed now.

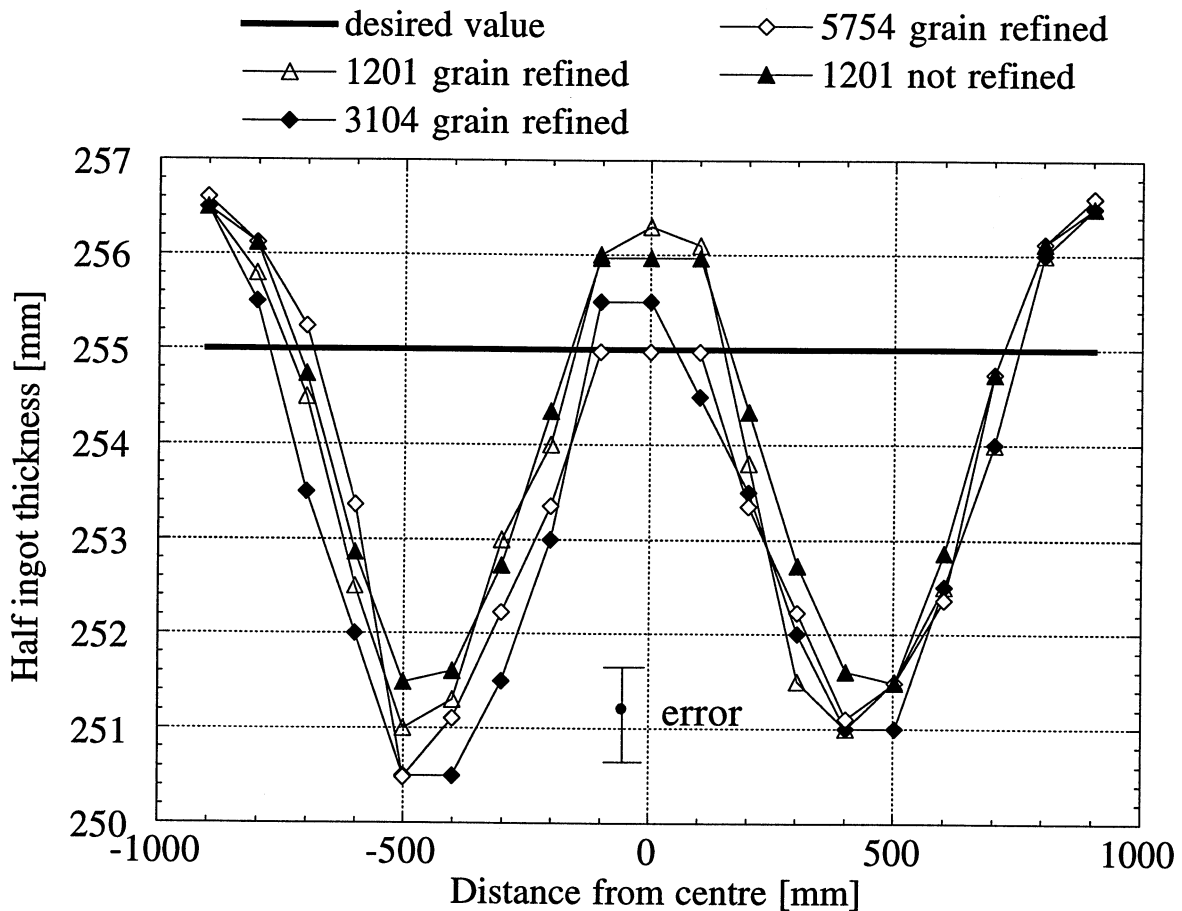


Figure 5.11: influence of the alloy composition and inoculation conditions on the ingot contraction during the DC casting process (casting speed: 60 mm/min).

During cooling, the metal experiences a high non-uniform thermal gradient (see figure 5.3 and 5.4) which gives rise to differential thermal contraction and high stresses that can be partially relieved by creep. During DC casting, the alloy undergoes two different coolings, the first one when it is in direct contact with the mould and the second one under the cooling water spray. This leads to the appearance of a thin solid shell in between the two cooling zones and nearly parallel to the mould. This thin shell contracts under the high local thermal gradient (figure 5.5), the metalostatic pressure being too small to withstand the displacement of the solidified shell. On the contrary, during EM casting, the metal experiences only one cooling, the water spray, and the deformation is continuous (figure 5.6). However, at about 100 mm below the top liquid surface, the contraction is about the same in both processes (2.5 mm or 1 % contraction). At this height, the solid skin is already well developed and extends beyond the second thermocouple attached to the quartz rod, i.e., the surface skin is at least

40 to 50 mm thick in both DC and EM castings. Such a skin continues to thicken and deform during further cooling of the casting.

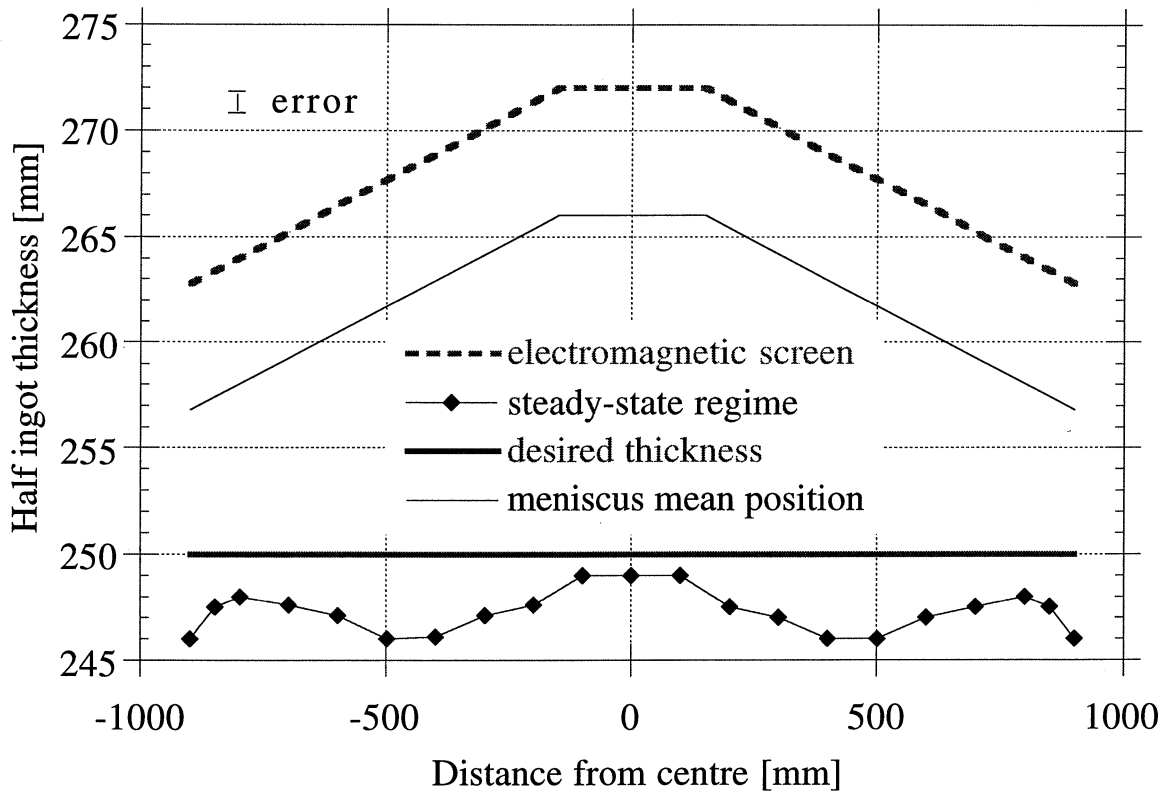


Figure 5.12: steady-state contraction of the 3104 alloy EM-cast at 65 mm/min, geometry of the inductor and estimated position of the meniscus (nominal size: 1800 x 500 mm).

As shown by the experiments, the contraction of the edges in the  $y$ -direction of the casting (figure 3.1) is much smaller (about 2.5%) and almost unaffected by the cast length (figure 5.7), by the casting speed (figures 5.9 and 5.10) and by the alloy composition (figure 5.11). Near the short sides of the ingot, the sump may have about the same shape as along the rolling faces (see figure 5.3 and 5.4) but it is now turned 90 deg. with respect to the situation in the plane ( $yz$ ). Accordingly, the pull-in of the short sides along the  $y$ -direction (see figure 3.1) is prevented by the solid shell and corresponds only to the thermal contraction of the alloy (pull-in of 7 mm, i.e. 2.5 %). In other words, the pull-in of the short sides of the ingots is close to the contraction of an ingot that is continuously cast at very low speed, i.e., close to the thermal shrinkage seen in a mould-cast ingot cooled from the bottom.

The non-uniform deformation of the ingot in between the short sides and the centre of the rolling faces is therefore qualitatively understood but a quantitative analysis would have to account for 3-dimensional and viscoplastic effects. However, the use of three straight segments is over simplistic if truly flat

ingots are to be produced. Such design can diminish indeed the variation of the ingot thickness around an average value (i.e., can decrease the concavity of the final bone-shape ingot), but it clearly undercorrects the pull-in along the inclined segments (see figure 5.7 for example).

The calculation of the pull-in of the rolling faces and the resulting ingot cross section requires a precise knowledge of the boundary conditions and of the thermomechanical properties of the alloy. Furthermore, it must be performed for an evolutive and three dimensional domain so as to obtain steady state conditions and to simulate the edge reinforcement along the short sides. It will be presented in sections 5.2.2 and 5.2.3 of this chapter.

### **5.1.2 Mechanical properties**

The knowledge of the mechanical properties of the two aluminium alloys, 1201 and 3104, considered in the present study, was a prerequisite to the numerical modelling (see chapter 4) as input data. The results concerning the measurements of the thermal expansion coefficient, of the Young's modulus and of the viscoplastic behaviour of the alloy in the solid and mushy states, are presented and discussed in this section.

#### *Thermal expansion*

The distortions undergone by the metal during casting and subsequent cooling is mainly the result of thermal contraction from the solidus temperature (or coherency point) down to room temperature. Therefore, it is necessary to know exactly the temperature dependence of the thermal linear expansion coefficient that will be transformed for the computations as a mean thermal contraction coefficient taking as a reference temperature the coherency temperature of the alloy (see appendix II). The thermal expansion coefficient can also vary as a function of the solute content of the alloy. That is why the measurements of this coefficient was undertaken. At temperatures near the solidus, the alloy can start melting and the reference is modified (see section 3.2.1). Therefore, only the results obtained under an increasing temperature ramp were retained.

The results of the measurements of the true thermal linear expansion coefficient are shown in figure 5.13 for the alloys 1201 and 3104. For comparison, the values taken from Hatch [Hatch] are also represented. It is clear from figure 5.13 that the impurities or alloying elements in the alloys 1201 and 3104 have no measurable influence on the thermal expansion coefficient. In the

thermomechanical models, the coefficients determined at different temperatures by Hatch will be used.

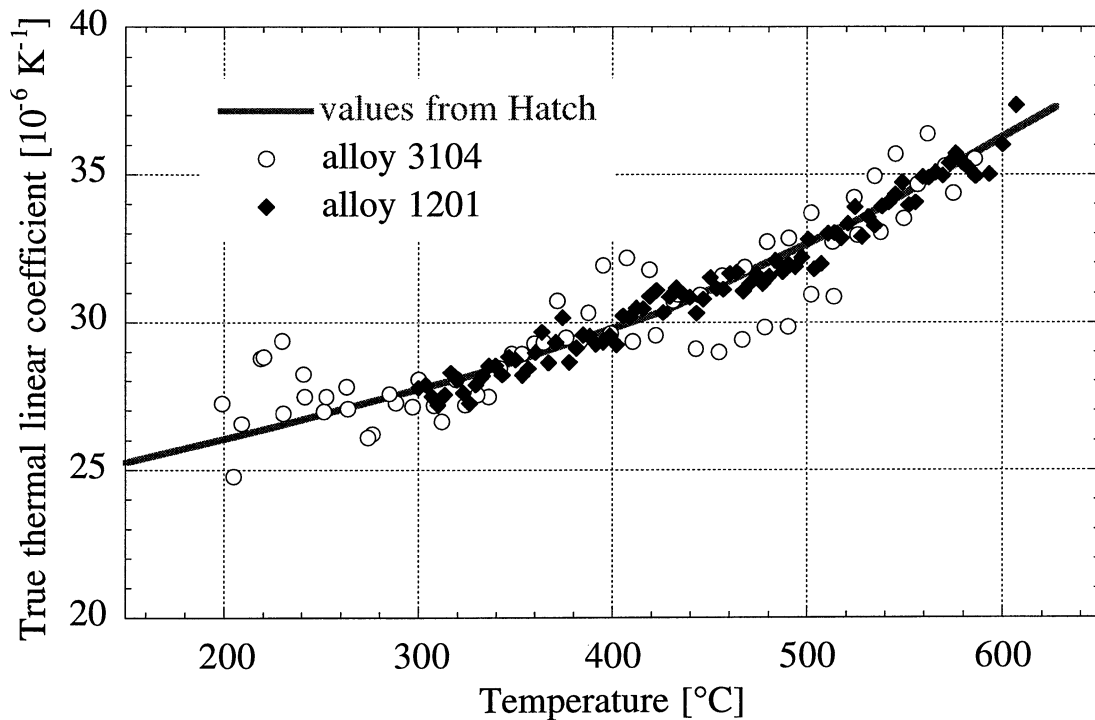


Figure 5.13: true thermal linear expansion coefficient measured for the alloys 1201 and 3104, together with the values from Hatch.

### *Young's modulus*

The measurement of the Young's modulus using ultra-sonics is described in section 3.2.2. The results are presented here. Figure 5.14 shows the measured Young's modulus as a function of the temperature for both alloys 1201 and 3104. The values for pure aluminium from Mondolfo [Mond] are also represented. Once again, the impurities or alloying elements have no significant influence on the Young's modulus and the values from Mondolfo will be used for the thermomechanical computations. Note that when the temperature approaches the solidus temperature of the alloy 3104, 609°C, the Young's modulus rapidly falls down. Unfortunately, the ultra-sonics method used for these measurements did not allow to obtain reliable values of the Young's modulus in the solidification interval of the alloy because of a large attenuation of the signal due to bad transmission through the interface between the sample and the wave guide.

### Viscoplastic behaviour in the solid state

The viscoplastic behaviour of the alloys 1201 and 3104 in the solid state was investigated using tensile creep tests, as described in section 3.2.3. The results of these measurements are reported in this section.

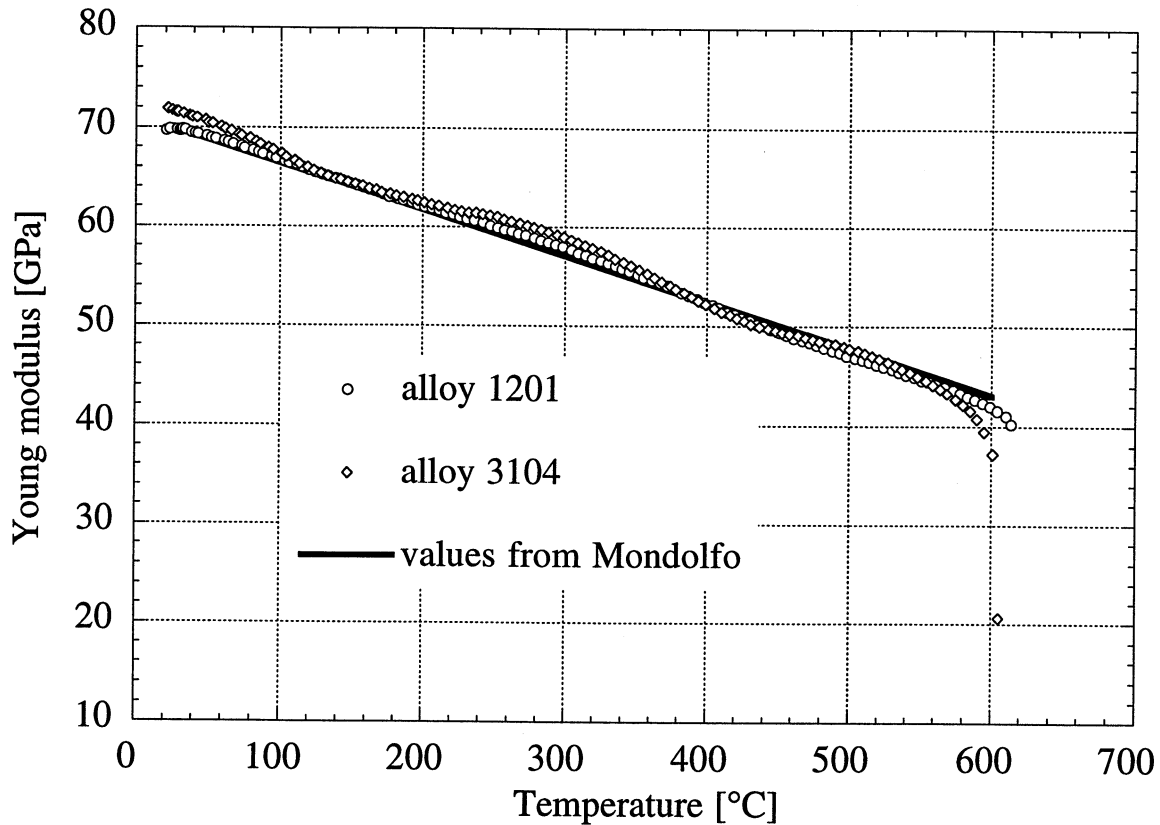


Figure 5.14: Young's modulus measured for the alloys 1201 and 3104, together with the values from Mondolfo.

Figure 5.15 shows the measured minimum creep rate for the alloy 1201 as a function of the stress on a logarithmic scale for temperatures varying from 300°C to 640°C. At a given temperature, the points are almost aligned, which means that the creep rate is given by:

$$\dot{\epsilon}_{\min} = k(T) \cdot \sigma^{n(T)} \quad (5.1)$$

The value of the stress exponent,  $n$ , decreases with temperature, as indicated in figure 5.15. For the thermomechanical computations, the measured minimum creep rates at different temperatures and loads were fitted using the Garafalo law [Gar1]:

$$\dot{\epsilon}_{\min} = A \cdot \left( \sinh \left( \frac{\sigma}{\sigma_0} \right) \right)^n \exp \left( -Q/RT \right) \quad (5.2)$$

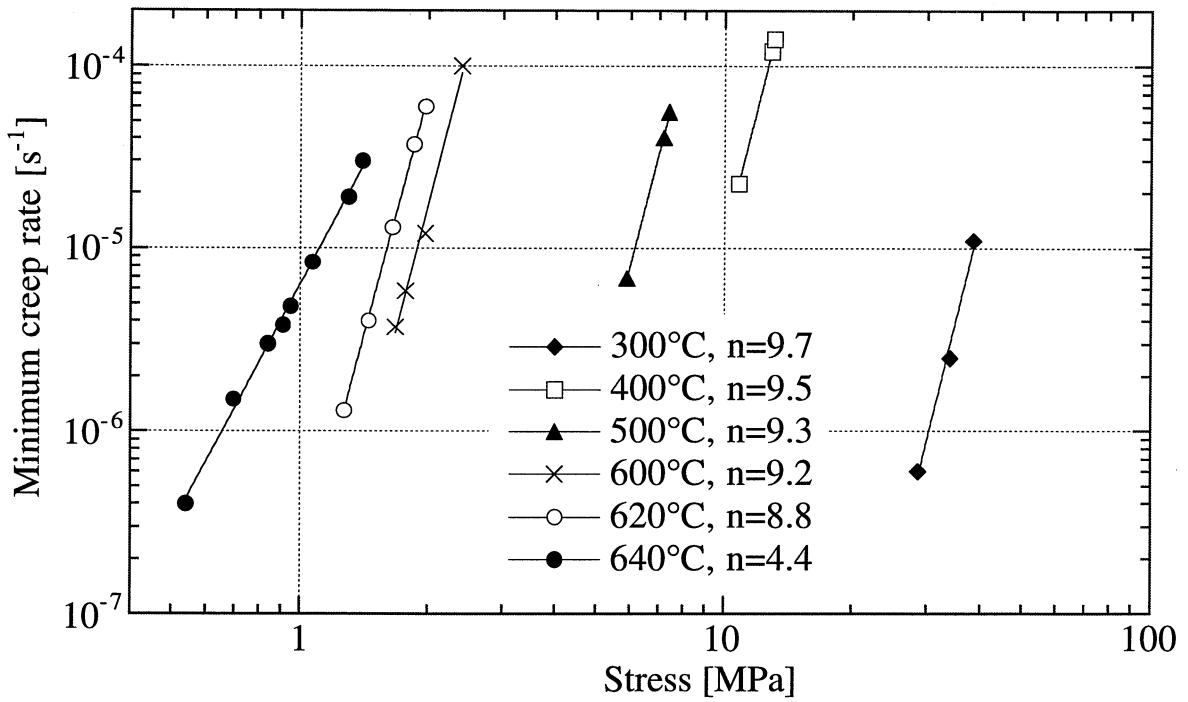


Figure 5.15: minimum creep rate as a function of the stress at different temperatures (logarithmic scale, alloy 1201).

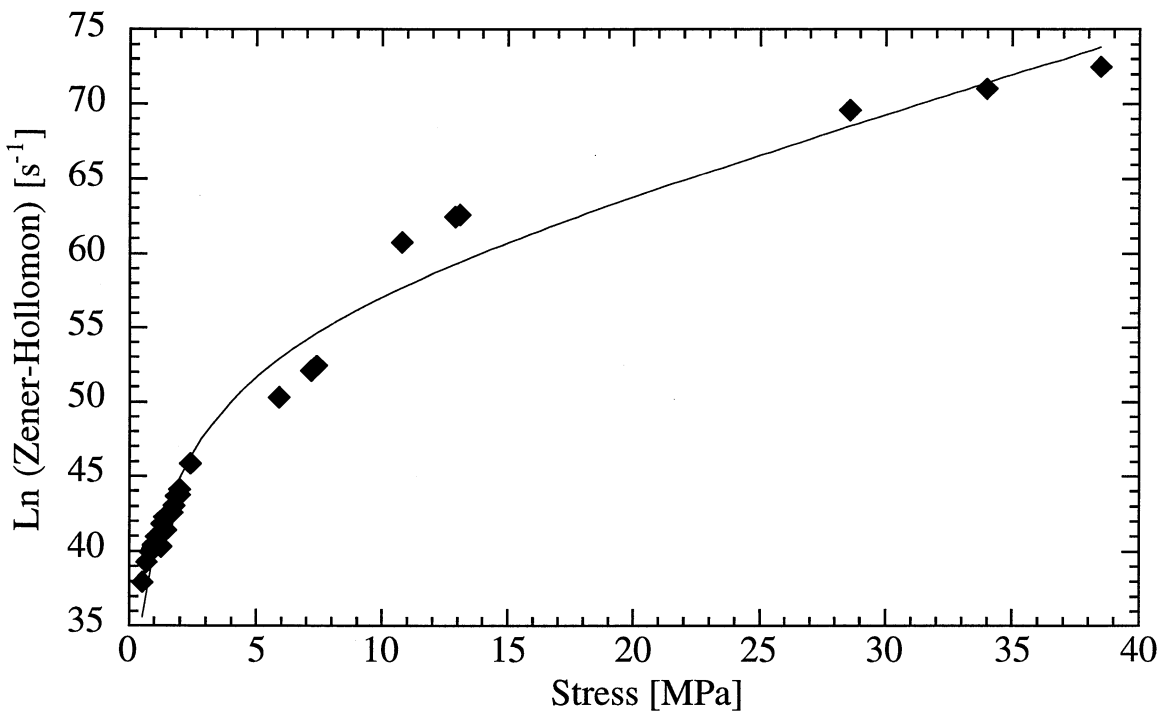


Figure 5.16: fitting of the Zener-Hollomon parameter by a hyperbolic sinus function for the alloy 1201.

where  $A$ ,  $\sigma_0$ , and  $n$  are some alloy-dependent constants,  $Q$  represents the apparent creep activation energy,  $R$  and  $T$  are the universal gas constant and temperature respectively.

After determining the apparent creep activation energy [Drez2], the remaining constants A, n and  $\sigma_0$  were calculated by representing the temperature-compensated Zener-Hollomon parameter,  $\dot{\epsilon}_{vp} \cdot \exp(Q/RT)$ , as a function of stress and by fitting this curve by a hyperbolic sinus function. Figure 5.16 shows the resulting curve fitting and Table 5.2 gives the value of the parameters A, Q,  $\sigma_0$  and n for the alloy 1201. The same results are shown in figure 5.17 and 5.18 for the 3104 alloy. Please note that the points are aligned in the logarithmic scales used to plot the Zener-Hollomon parameter as a function of the stress.

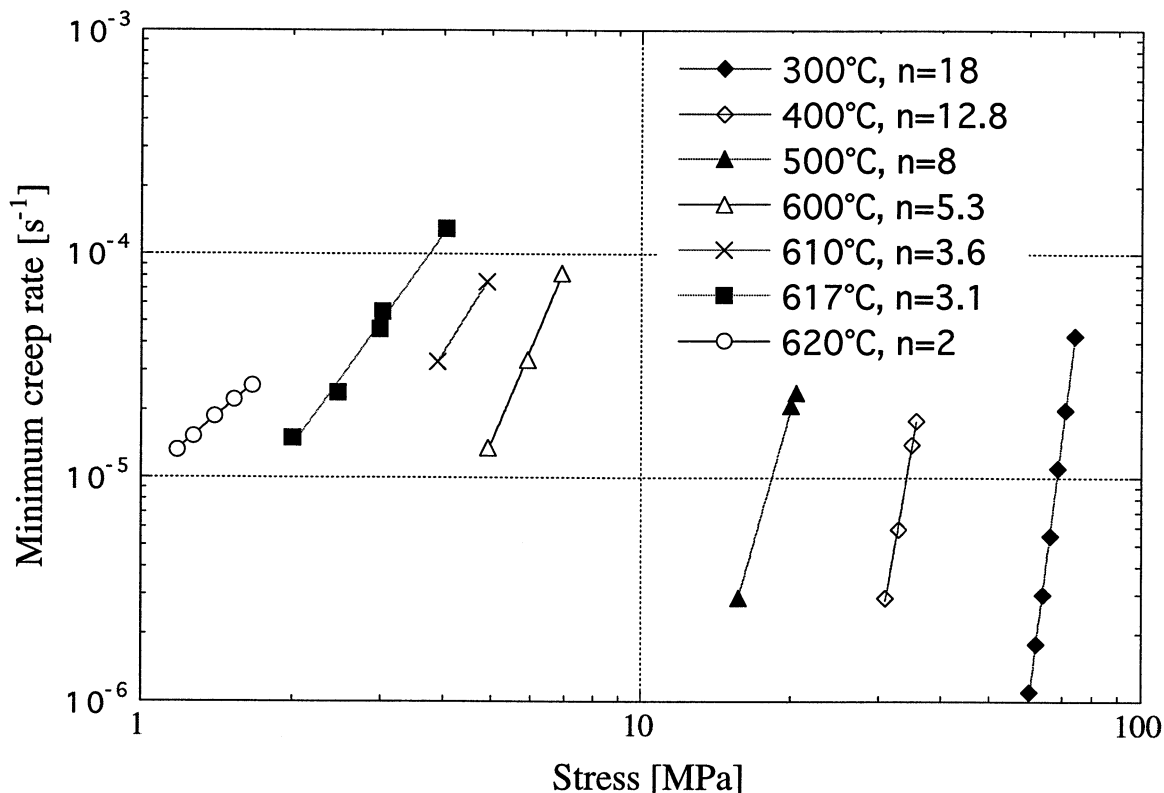


Figure 5.17: minimum creep rate as a function of the stress at different temperatures (logarithmic scale, alloy 3104).

This allows to fit in this case the measured minimum creep rates at different temperatures and loads by an exponential law<sup>1</sup>:

$$\dot{\epsilon}_{\min} = A \cdot \exp\left(\frac{\sigma}{\sigma_0}\right) \cdot \exp\left(-Q/RT\right) \quad (5.3).$$

<sup>1</sup> Note that the exponential law is the limit of the Garafalo law for stresses much higher than  $\sigma_0$ .



Table 5.2 gives the values of the parameters A, Q, and  $\sigma_0$  for the alloy 3104.

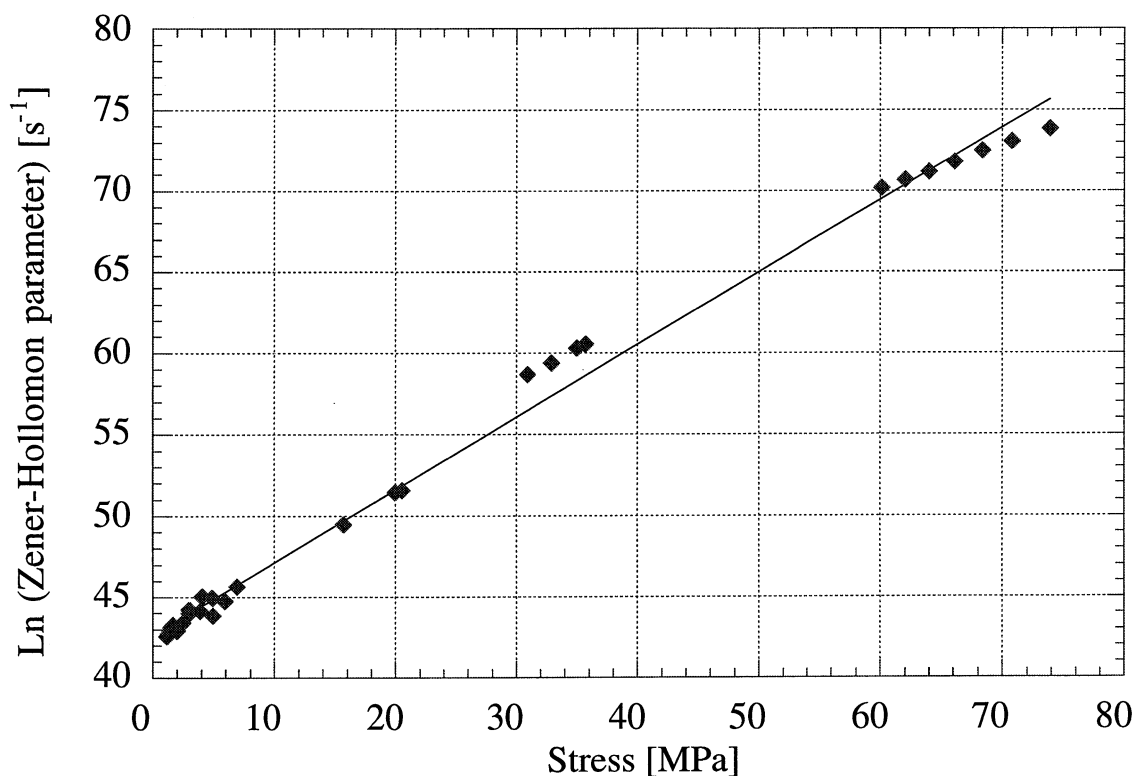


Figure 5.18: best fit of the Zener-Hollomon parameter as a function of stress for the alloy 3104.

	A [ $s^{-1}$ ]	Q [kJ/mole]	n [-]	$\sigma_0$ [MPa]
1201	$2.82 * 10^{25}$	400.	7.13	13.6
3104	$3.44 * 10^{18}$	400.	-	2.24

Table 5.2: parameters for the creep behaviour in the solid state of the 1201 alloy (equation 5.2) and of the 3104 alloy (equation 5.3), as used in the thermomechanical computations.

#### *Viscoplastic behaviour in the mushy state*

The viscoplastic behaviour of the alloys 1201 and 3104 in the semi-solid state was investigated using indentation tests, as described in section 3.2.4. Figure 5.19 shows the force-needle displacement curves for the alloy 1201 tested at 650°C, 652°C and 654°C. At 650 °C, the curves obtained for different needle speed are similar to those calculated by Forge2 (see figures 3.11 and 3.12). On the contrary, at 652°C and 654°C, the force decreases after a short peak or presents many fluctuations and does no longer follow the trend given by

the computed curves. At these temperatures, the three-dimensional network formed by the dendrites is too weak to really oppose a resistance to the needle indentation. Please note that this test is mainly in compression. Consequently, the coherency temperature of the alloy 1201 was set to 650°C. The same procedure was carried out for the 3104 alloy and its coherency temperature was found to be 635°C.

At temperatures lower than the coherency temperature of the alloy but higher than the solidus, the mechanical behaviour of the mush was assumed to follow a viscoplastic Norton-Hoff law:

$$\dot{\epsilon} = k(T) \cdot \left(\frac{\sigma}{\sigma_0}\right)^n \quad (5.4),$$

where  $k$  and  $n$  are alloy- and temperature-dependent parameters ( $\sigma_0$  is set to 1 MPa). These parameters were fitted by comparing the result of the FEM code with the measured force-needle displacement curve.

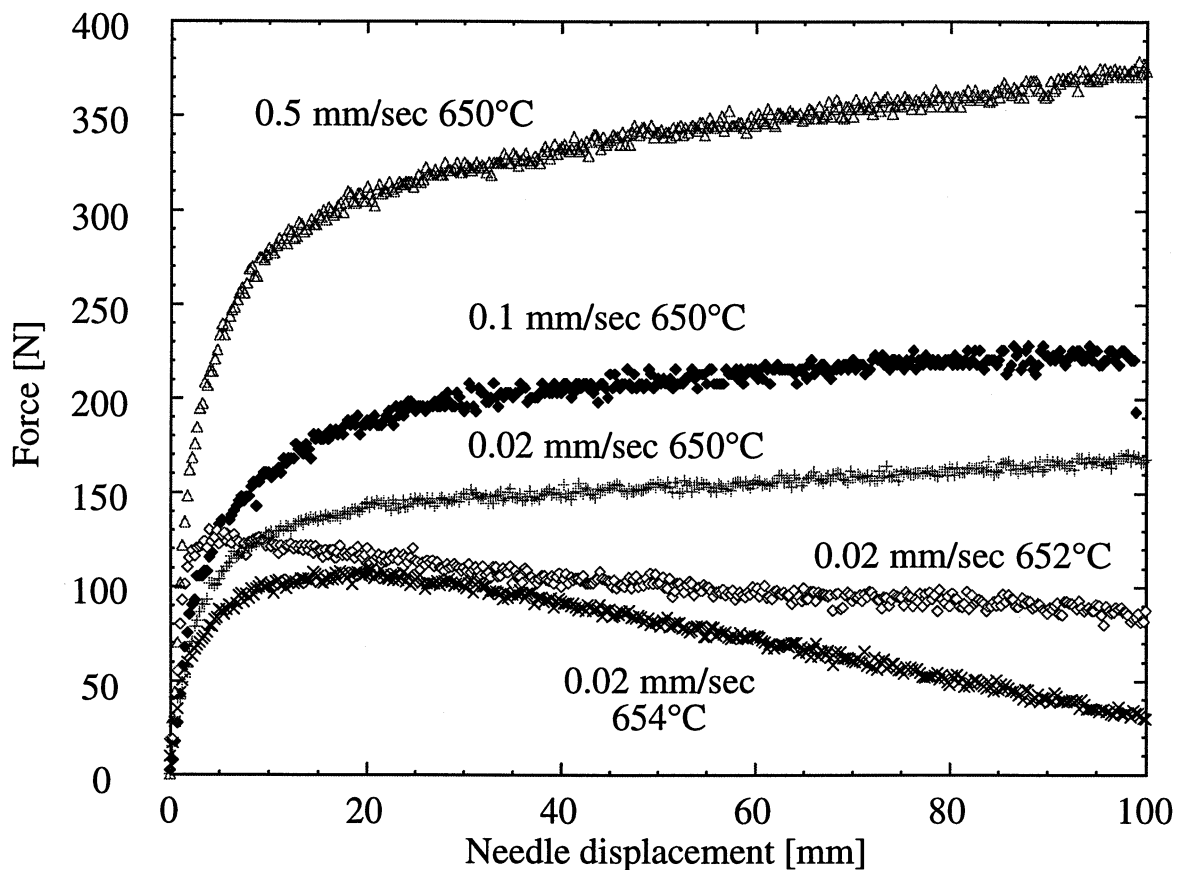


Figure 5.19: determination of the coherency temperature of the alloy 1201.

For the alloys 1201 and 3104, the parameters of the viscoplastic law were determined at four different temperatures and the corresponding parameters are

given in Tables 5.3 and 5.4, respectively. For the numerical computations, the strain rate was interpolated in between the measured values.

Temperature [°C]	k [s <sup>-1</sup> ]	n [-]	σ <sub>0</sub> [MPa]
635.	2.1 x 10 <sup>-6</sup>	4.76	1.
640.	6.9 x 10 <sup>-6</sup>	3.85	1.
645.	1.36 x 10 <sup>-4</sup>	3.5	1.
650.	1.15 x 10 <sup>-3</sup>	3.4	1.

Table 5.3: parameters for the 1201 creep behaviour in the mushy state (as used in the thermomechanical computations).

Temperature [°C]	k [s <sup>-1</sup> ]	n [-]	σ <sub>0</sub> [MPa]
620.	1.1 x 10 <sup>-6</sup>	3.45	1.
625.	8.9 x 10 <sup>-6</sup>	3.13	1.
630.	3.4 x 10 <sup>-5</sup>	3.12	1.
635.	3.8 x 10 <sup>-3</sup>	2.1	1.

Table 5.4: parameters for the 3104 creep behaviour in the mushy state (as used in the thermomechanical computations).

Figure 5.20 shows the measured strain rate as a function of stress using indentation tests at different temperatures for the 1201 alloy. Also plotted on this figure are the results of the creep test at 640°C. It is clearly seen that the two ways of investigating the mechanical behaviour of mushy alloys, creep and indentation tests, give similar results. An apparent creep activation energy of 400 kJ/mole was determined for the two alloys (see Table 5.2), which is larger than the activation energy of aluminium lattice diffusion, 142 kJ/mole, [Frost]. Moreover, the stress exponent is temperature-dependent and larger than typical values found for pure aluminium (see section 2.2). As explained by Frost and Ashby [Frost], discrete obstacles like precipitates, forest dislocations and solute elements, limit the velocity of dislocations: the activation energy of this obstacle-controlled glide is much larger than the self diffusion activation energy. Moreover, the activation energy is stress-dependent (see equation 2.27) and increases to rather large values when approaching melting temperature: Barret et al. [Barr] measured a value of 640 kJ/mole at 630°C for an Al-Fe0.5wt% alloy.

Using the indentation test, Vicente [Vicen] also measured an increase in the apparent activation energy for a Zn-Sn8wt% alloy in its solidification range. This suggests a specificity of the solid skeleton behaviour in the mushy state as compared to the pure solid. An attempt to explain the increase in the apparent creep activation energy for alloys in the mushy state is described in Appendix III. The apparent creep activation energy of 400 kJ/mole determined here is the mean value which gave the best fit (equations 5.2 and 5.3) over the entire temperature range investigated during the present measurements.

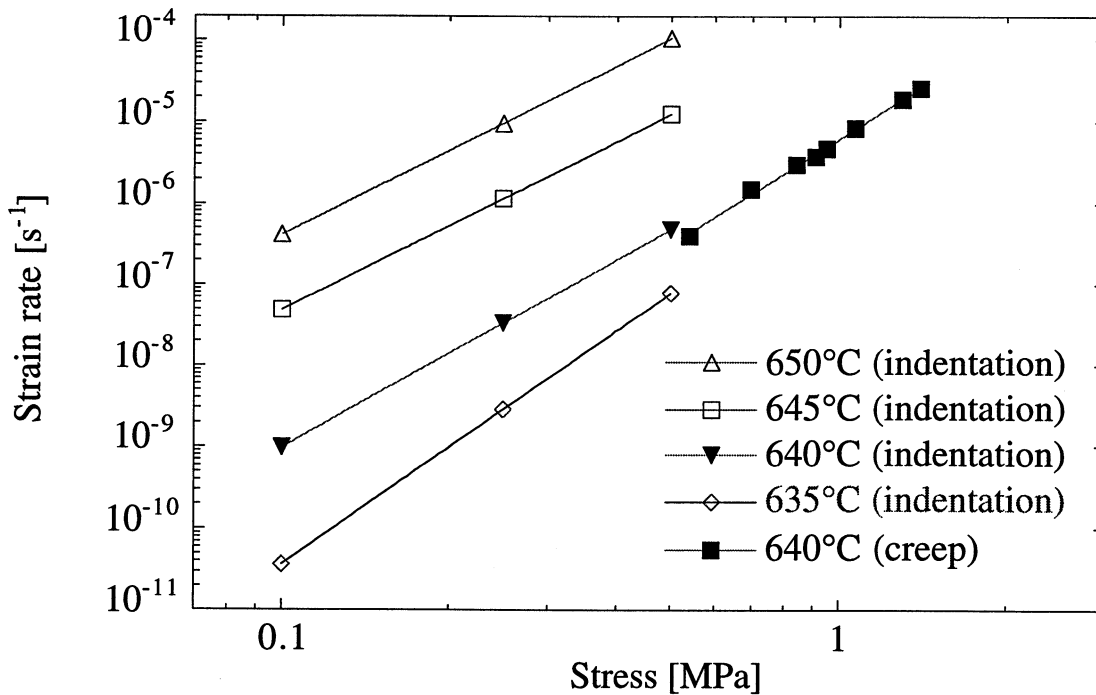


Figure 5.20: measured strain rates as a function of stress using indentation tests. Creep results are also shown for comparison (1201 alloy).

### 5.1.3 Laboratory investigations

After the full-size DC/EM castings, some ingots were cut and samples were machined out to provide as-cast material for further investigations in the laboratory.

#### *1D castings*

In order to determine the temperature-dependent thermal conductivity of the two alloys 1201 and 3104 using inverse modelling, cylindrical castings were solidified under one-dimensional heat flow conditions (see section 3.3.1). Figure 5.21 shows the recorded temperatures as a function of time during the cooling of the alloy 1201. The distance of the thermocouple to the copper chill is also indicated. Unfortunately, three thermocouples broke down during the measurements, likely because of the contraction of the metal.

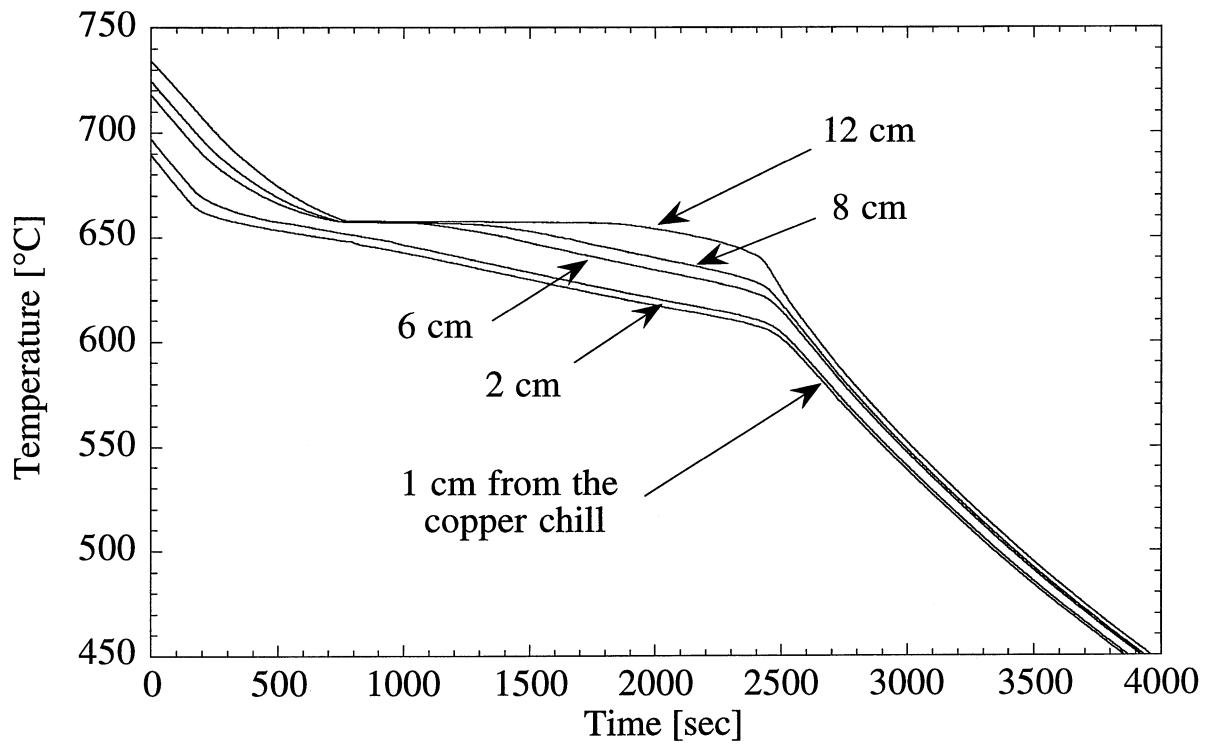


Figure 5.21: recorded temperatures during cooling of the 1201 1D-casting.

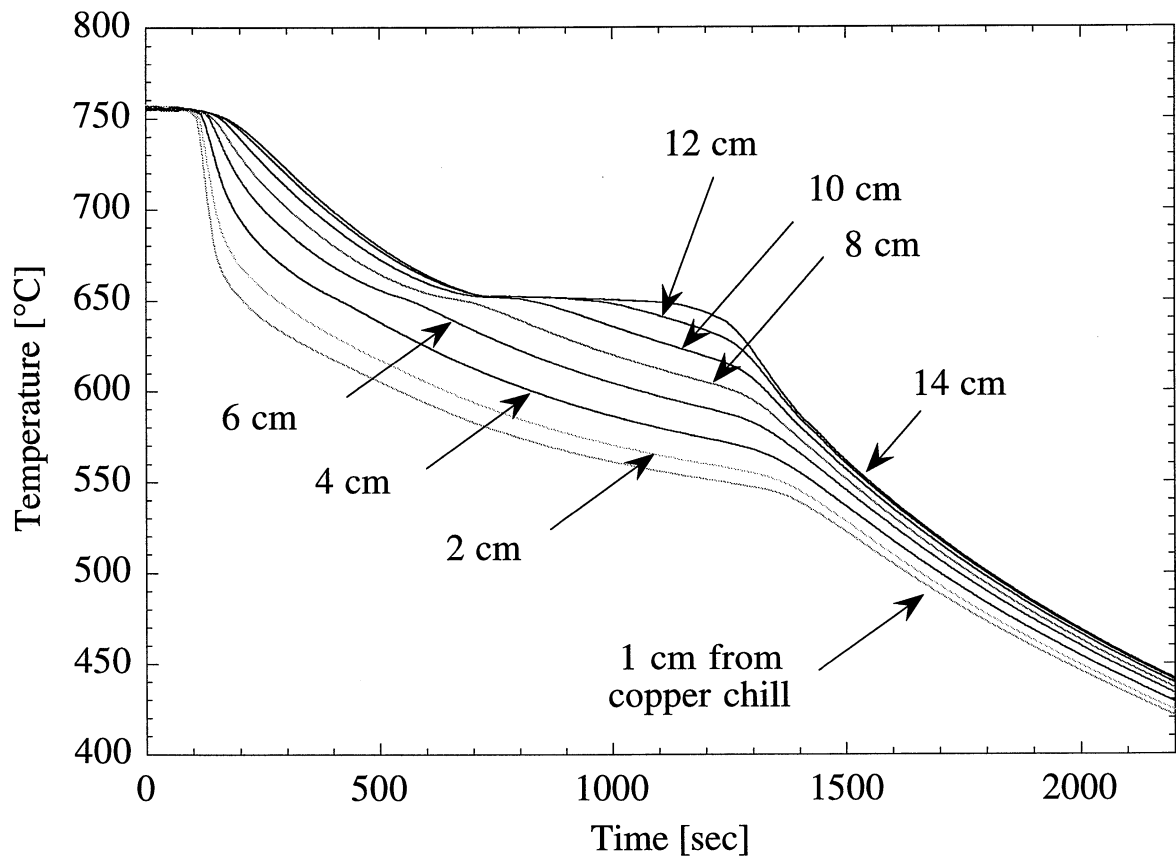


Figure 5.22: recorded temperatures during cooling of the 3104 1D-casting.

Figure 5.22 shows the recorded temperatures as a function of time during the cooling of the alloy 3104 together with the distance of the eight

thermocouples to the copper chill. These thermal histories will be used to compute the thermal conductivity of the two alloys using the inverse method described in section 4.2.

### *Micrographs*

Micrography of as-cast material was carried out for grain inspection (see section 3.3). Figure 5.23 shows a micrograph of the as-cast 1201 alloy. The sample was situated 255 mm from the ingot surface, i.e. on the centreline of the slab, and the plane of polish is perpendicular to the casting direction. This micrograph clearly reveals the equiaxed globular-dendritic microstructure which is typically encountered in the DC/EM casting processes (“cauliflowers-like grains”) [Rap4].

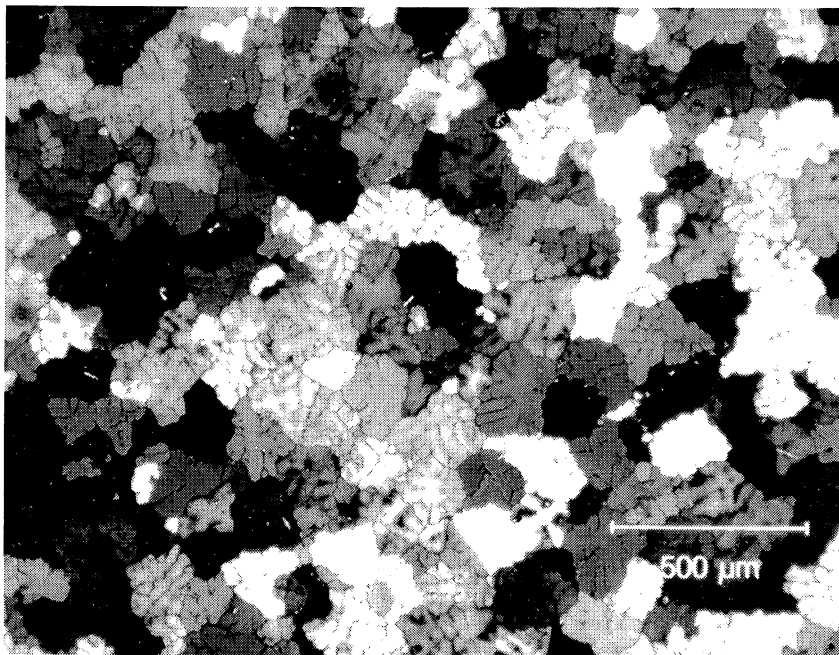


Figure 5.23: micrograph of as-cast 1201 alloy (centreline of the slab).

Using the “test-circle method” described in section 3.3.3, the mean grain diameter can be evaluated for samples situated near the ingot surface, 130 mm from the surface and on the centreline of the slabs. Such results are shown in figure 5.24 for measurements in a plane perpendicular to the casting direction. The inspection of the micrographs in sections parallel to the casting direction revealed that the grains are slightly elongated, the reason being that the growth direction is almost parallel to the direction of the local thermal gradient.

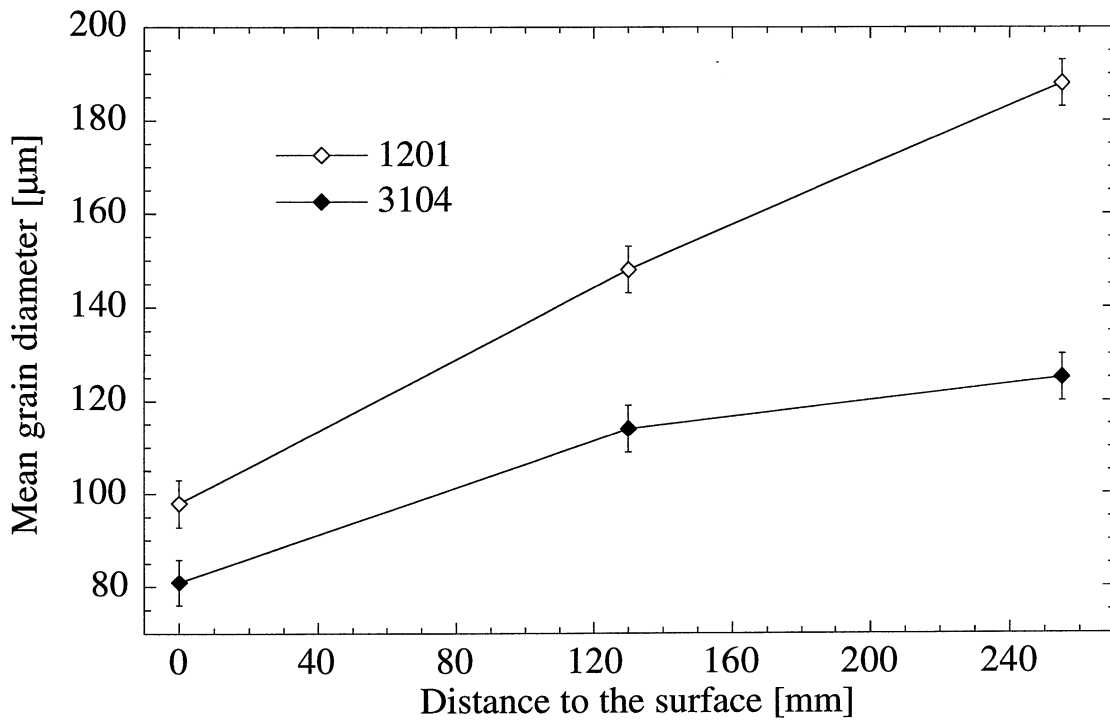


Figure 5.24: mean grain diameter as a function of the distance to the ingot surface.

#### *DTA curves*

The recorded DTA signal during the solidification of the 1201 alloy at the constant rate of  $-1\text{K/min}$  is plotted in figure 5.25. The sample temperature as deduced using equation 3.6 is also shown. The first DTA peak corresponds to the deposition of the primary aluminium phase whereas the second peak traduces the growth along the eutectic valley. The liquidus temperature of the alloy is found to be about  $658^\circ\text{C}$  and the temperature at which the eutectic valley is reached is  $650^\circ\text{C}$ . Note that, contrary to a binary system, the eutectic growth does not occur at a constant temperature as shown in figure 5.25.

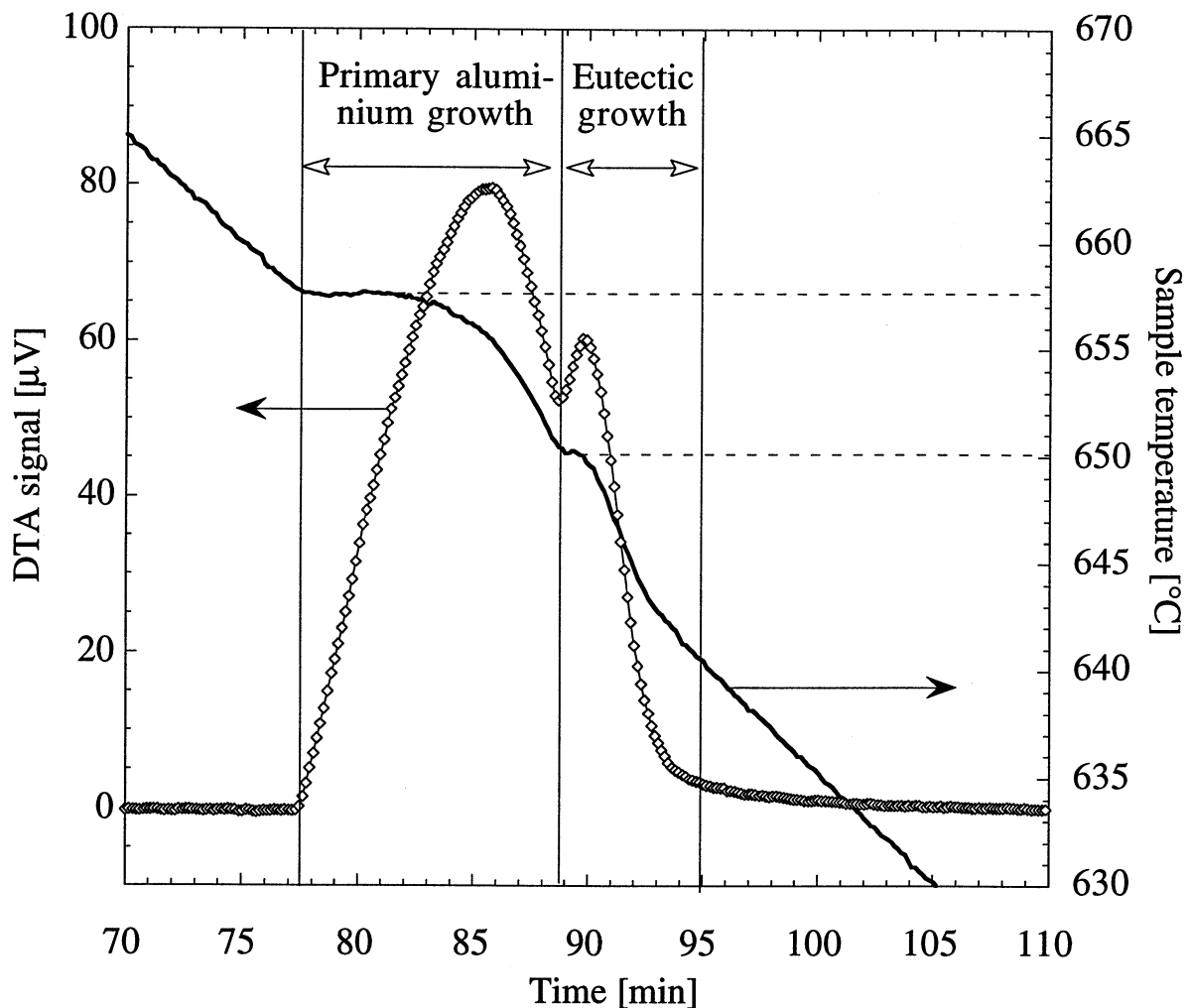


Figure 5.25: DTA signal and sample temperature during the differential thermal analysis of the alloy 1201 at -1K/min.

The end of solidification occurs at approximately 640°C in the present case. Micrography revealed that the resulting microstructure of the DTA specimen is still equiaxed globular-dendritic<sup>1</sup> but with a mean grain diameter of 400 μm. Using the procedure described in section 3.3.2, the solid fraction was calculated. It is represented as a function of the sample temperature in figure 5.26. The solid fraction is about 79% when the eutectic precipitation starts, thus meaning that the total eutectic fraction is 21%. The liquidus temperature of the alloy 1201, 658°C, is in accordance with the measurements performed by Gabathuler [Gaba] and the value provided by Thermo-Calc [The].

<sup>1</sup> The grain refiner is still active.



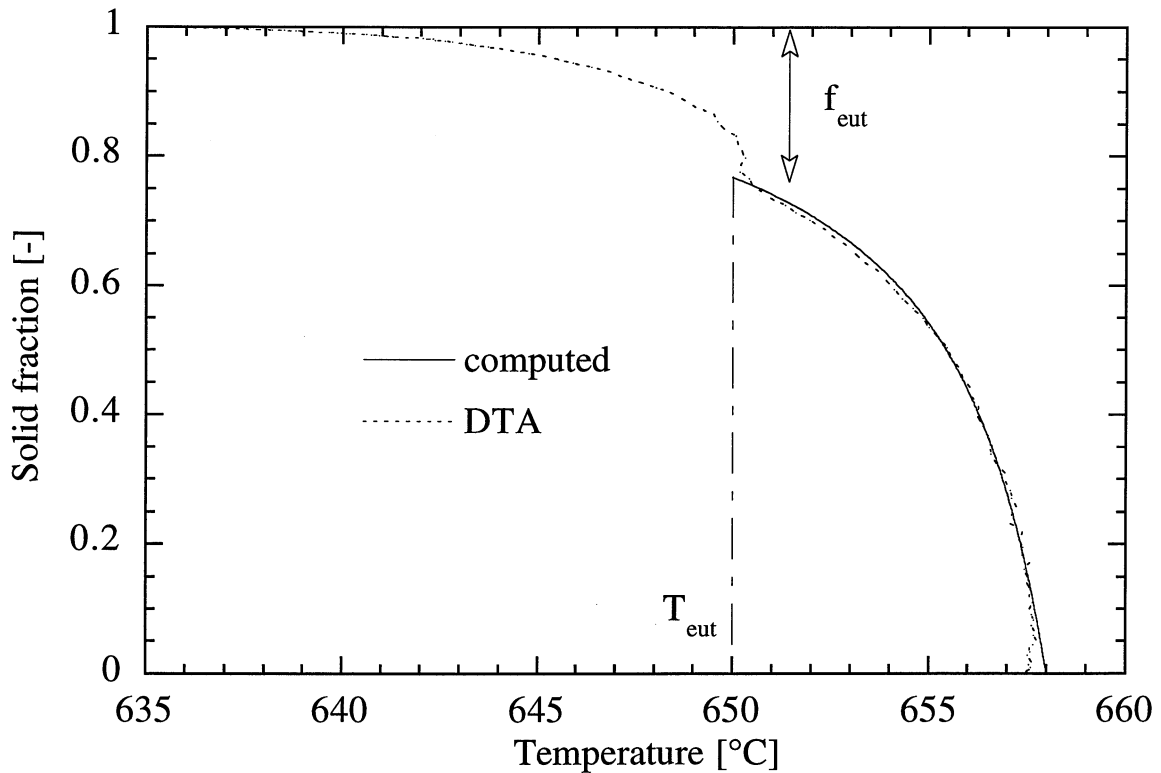


Figure 5.26: computed (see section 5.2.1) and measured  $f_s$ -T curves (1201, -1K/min).

The  $f_s$ -T curve deduced from the DTA measurements will be used for the validation of the microsegregation model presented in the next section.

## 5.2 Modelling results

### 5.2.1 Microsegregation

#### *Solidification of the 1201 alloy*

In this section, the computation of the solidification path of the alloy 1201 is presented. The results obtained for a constant cooling rate of -1K/min are compared with the DTA measurements. Thereafter, the computed solidification paths for cooling rates typically encountered in the DC/EM casting process (-1K/s along the centreline of the strand, -3K/s at mid-distance from the centre and the surface, and -10K/s near the ingot surface), will be presented.

Using the program described in section 4.1, the solidification path of the alloy 1201 was computed at different cooling rates. The composition of this alloy is given in table 3.1. Neglecting the Mg and Mn contents, the industrial alloy 1201 was considered as a ternary Al-Fe-Si alloy. The heat capacity and latent heat of fusion were considered constant, equal to 1080 JKg<sup>-1</sup>K<sup>-1</sup> and 388 kJKg<sup>-1</sup>, respectively. The time step and the number of nodes used for the

computations were 0.1 sec and 100, respectively. The equilibrium phase diagram, as calculated by Thermo-Calc, provides at each time step the values of the liquidus temperature, the liquidus slopes,  $m_i$ , and the partition coefficients,  $k_i$ , associated with silicon and iron. The mean grain radius,  $r_0$ , as measured by metallography (see figure 5.24 and 200  $\mu\text{m}$  for the DTA specimen) was used for the corresponding cooling rate in the computations. The geometric parameter,  $i_{geo}$  (see equation 4.2), was set to 3 (spherical geometry). The heat extraction rate is given by the cooling rate after complete solidification:

$$\frac{dh}{dt} = c_p \cdot \frac{dT}{dt} \quad (5.5)$$

The solid and liquid diffusivities of iron and silicon are temperature-dependent and are assumed to follow an Arrhenius type law:

$$D(T) = D_0 \cdot \exp(-Q/RT) \quad (5.6)$$

The values of the solid and liquid diffusivities are taken from the work of Langsrud [Lan1] and from the Smithells Metals Reference Book [Smit], respectively. The constants,  $Q$  and  $D_0$ , appearing in equations 5.6 are given in table 5.5, together with the value of the diffusivities at 650°C.

When the solidification path reaches the eutectic valley, the computation is stopped: the corresponding temperature is named  $T_{eut}$  and the remaining liquid fraction  $f_{eut}$ , irrespective of the nature of the phase that is subsequently precipitated. Figure 5.27 shows the liquidus map of the Al-Fe-Si equilibrium system as calculated by Thermo-Calc. Also shown on this figure is the solidification path of the 1201 alloy cooled at -1K/min. The solidification of the aluminium solid solution,  $\alpha\text{-Al}$ , starts at the liquidus temperature, 658°C, and ends at 650 °C. In this case, the eutectic fraction,  $f_{eut}$ , is 22% (see figure 5.26) and the eutectic phase that is precipitated is  $\alpha\text{-Al}/\text{Al}_3\text{Fe}$ , i.e. the stable phases. As can be seen in figure 5.26 which shows the comparison between the computed  $f_s$ -T curve and the same curve as deduced from the DTA signal, the solidification of the primary aluminium solid solution is well reproduced. Hence, the assumption of a spherical geometry ( $i_{geo} = 3$ ) to describe and model the growth of an equiaxed globular-dendritic grain, is valid, at least during the primary aluminium solidification. This assumption will be kept for the microsegregation computations at higher cooling rates.

	$D_0$ [m <sup>2</sup> /sec]	Q [kJ/mole]	D(650°C) [m <sup>2</sup> /sec]
Si solid diffusivity	$2.0 \cdot 10^{-4}$	123.5	$2.07 \cdot 10^{-11}$
Fe solid diffusivity	$5.3 \cdot 10^{-3}$	183.4	$2.25 \cdot 10^{-13}$
Si liquid diffusivity	$2.1 \cdot 10^{-7}$	25.7	$7.4 \cdot 10^{-9}$
Fe liquid diffusivity	$2.95 \cdot 10^{-7}$	40.	$1.6 \cdot 10^{-9}$

Table 5.5: parameters defining the Si and Fe solid and liquid diffusivities in aluminium and values at 650°C.

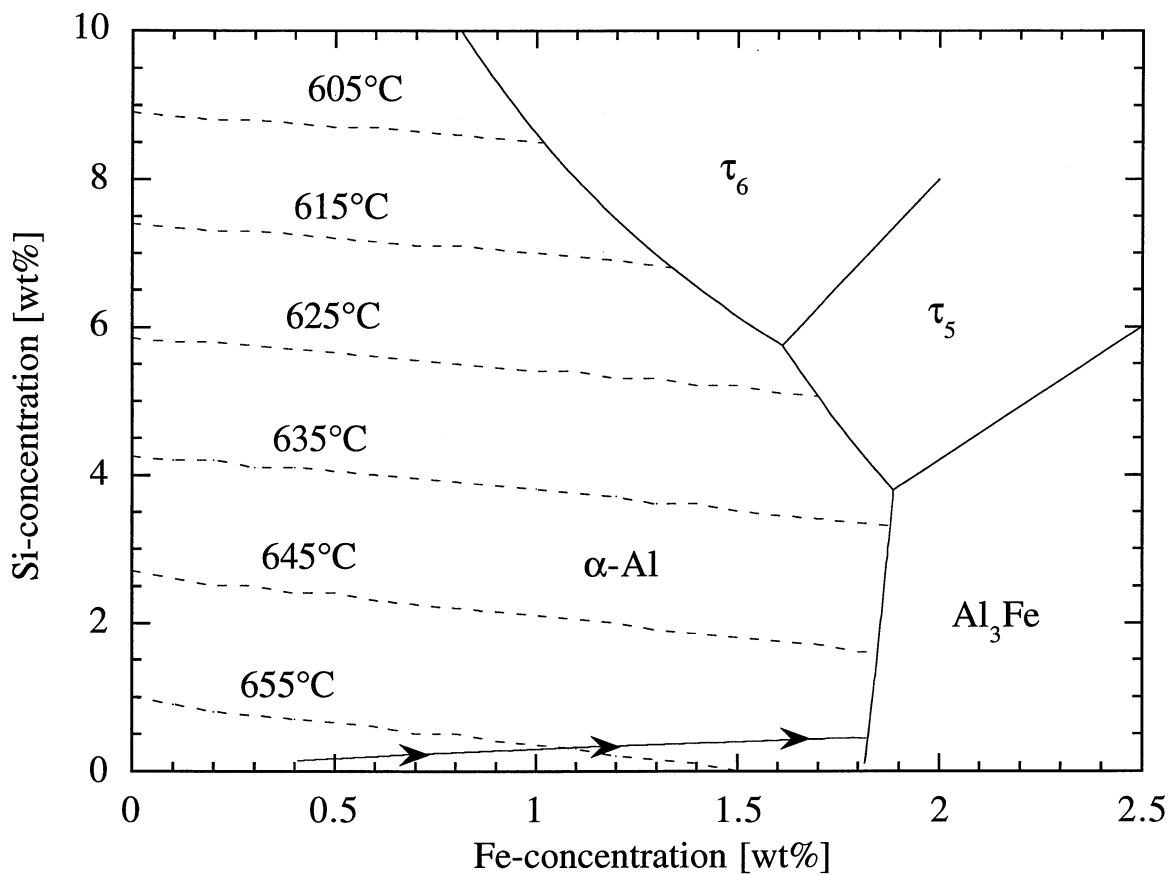


Figure 5.27: liquidus surface as calculated by Thermo-Calc and solidification path of the 1201 alloy solidified at -1K/min.

For cooling rates typical of DC/EM casting, the metastable Al-Fe-Si phase diagram as suggested by Langsrud [Lan1] (see figure 2.7) was used, i.e. the phase boundaries and peritectic/eutectic points were shifted towards higher iron concentrations. The values of the liquidus slopes and partition coefficients were extrapolated from the values provided by Thermo-Calc.

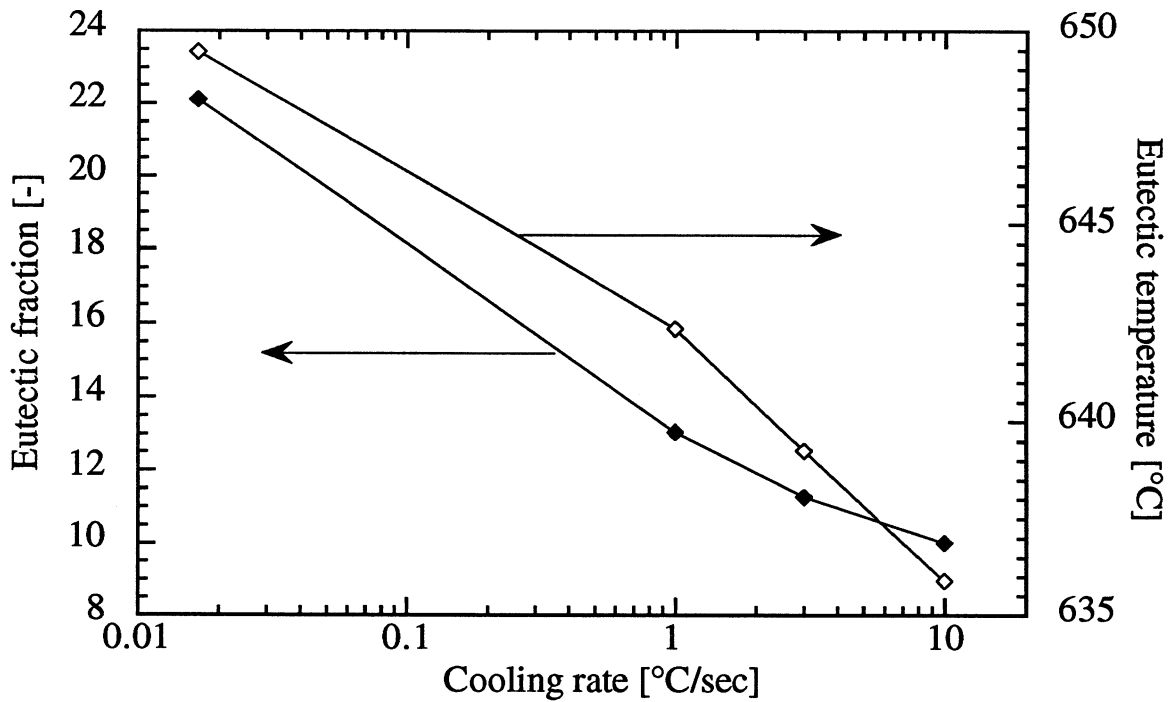


Figure 5.28: computed  $f_{\text{eut}}$  and  $T_{\text{eut}}$  at different cooling rates.

Figure 5.28 shows the values of  $T_{\text{eut}}$  and  $f_{\text{eut}}$  computed for the different cooling rates. Due to the shift of the  $\alpha\text{-Al}/\text{Al}_3\text{Fe}$  phase boundary,  $T_{\text{eut}}$  and  $f_{\text{eut}}$  decrease to  $636^\circ\text{C}$  and 10%, respectively, at  $-10\text{K/s}$ . Note also, that at high cooling rates, the  $\text{Al}_3\text{Fe}$  phase field is replaced by the metastable  $\text{Al}_6\text{Fe}$  and  $\text{Al}_m\text{Fe}$  phase fields [Lan1]. The computed solute profiles are shown in figure 5.29 at three different times. For both solutes, complete liquid mixing is achieved owing to the high liquid diffusivities and the small diffusion distance, the Fourier number in the liquid phase (see equation 2.10) being around 130 and 30 for Si and Fe, respectively. On the other hand, in the solid phase, silicon can diffuse (Fourier number of 0.35) but iron does almost not diffuse<sup>1</sup>. In the present case, iron nearly follows the Scheil's approximation.

---

<sup>1</sup> Note that the solid diffusivity of iron is two orders of magnitude lower than that of silicon, thus giving a Fourier number of  $3.5 \cdot 10^{-3}$ .

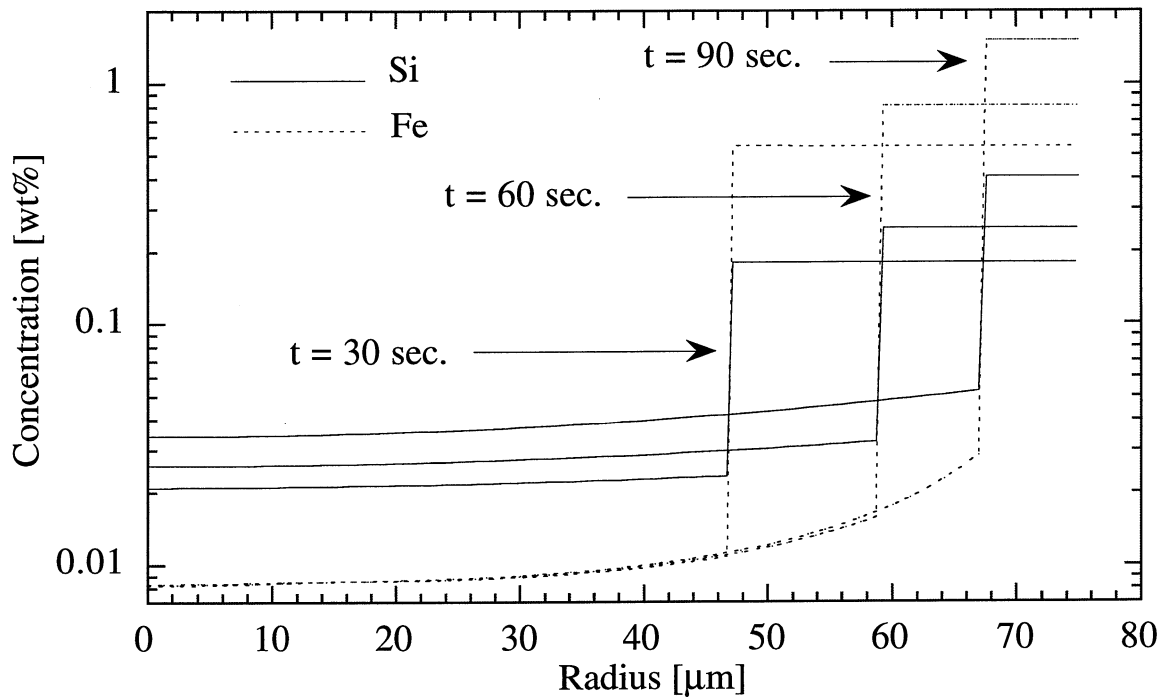


Figure 5.29: computed solute profiles at different times (1201, -3K/s).

The computed solidification paths are reproduced in figure 5.30. The iron concentration when primary solidification is achieved, increases with the cooling rate due to the shift of the phase boundaries [Lan1]. Note that the solidification path slightly varies in shape towards higher silicon content owing to the limited diffusion of the silicon in the solid phase at high cooling rate. Figure 5.31 shows the computed growth rate as a function of the crystal temperature, assuming that one would have perfectly spherical grains ( $igeo = 3$ ). The growth rate rapidly decreases near the liquidus temperature because the grain is small and diffusion is made easier with this geometry. The larger the cooling rate, the higher is the growth rate. In all the computations shown in this section, the solutal balance was preserved within an error lower than 0.5 % for both iron and silicon.

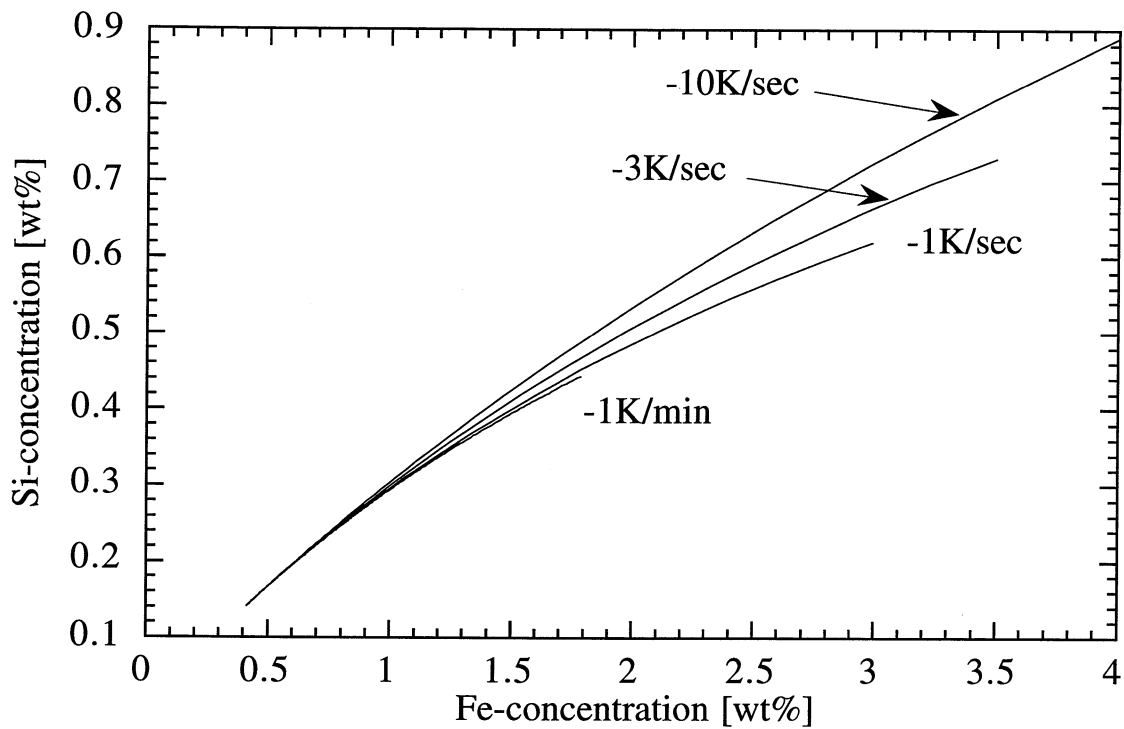


Figure 5.30: computed solidification paths.

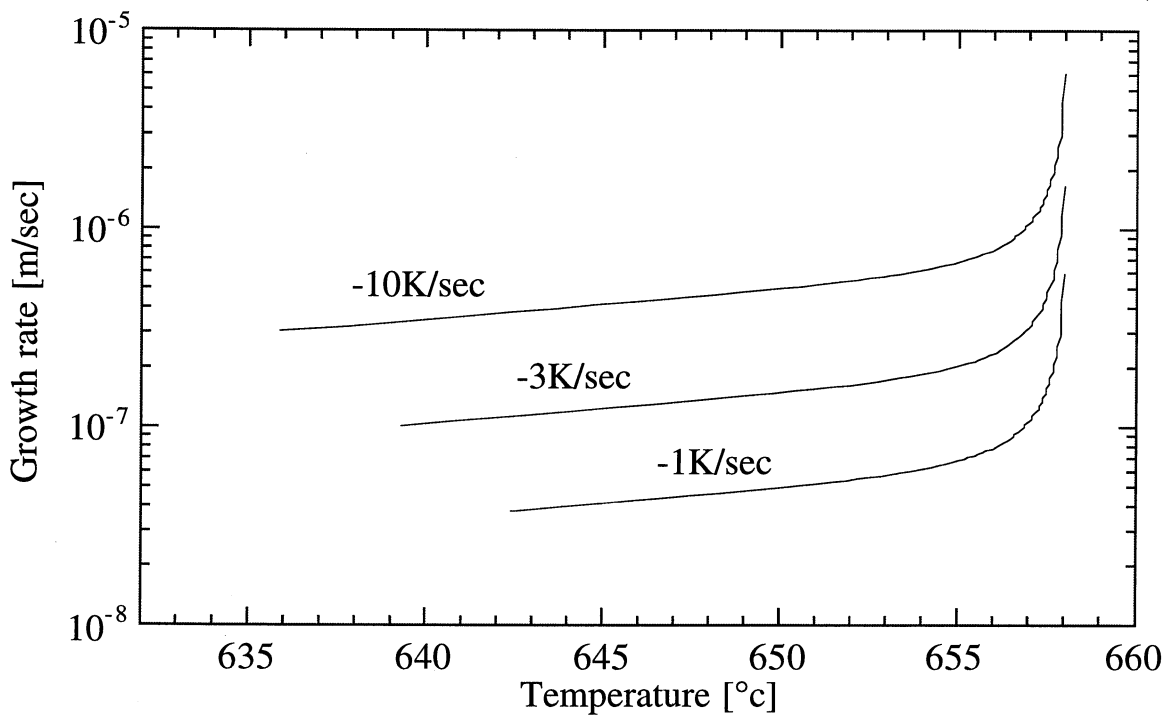


Figure 5.31: growth rate as a function of the temperature for different cooling rates.

The present microsegregation model seems able to correctly reproduce the solidification path of alloys, providing it is linked to the suitable phase diagram, i.e. metastable if required. Future developments would consist in addressing the calculation of the solidification path on the eutectic valley. Finally, the ability of

the present microsegregation model to cope with situations in which partial remelting occurs, is detailed in appendix IV.

### 5.2.2 Inverse modelling

In the present section, the results obtained with inverse modelling are presented. The computed thermal conductivity of the alloys 1201 and 3104 and lateral heat flux along the ingot surface will be then used in the thermomechanical computations.

#### *1D castings: thermal conductivity*

Using inverse modelling, the thermal conductivity of the aluminium alloys 1201 and 3104 were deduced from the temperature measurements within cylindrical castings solidified under one-dimensional (1D) heat flow conditions (see sections 3.3.1 and 4.2.3). The result of such an inverse calculation is shown in figure 5.32 for the alloys 1201 and 3104. The thermal conductivity of pure aluminium as taken from Pehlke [Pehl] is also given for comparison. As can be seen, the inverse modelling calculation gives thermal conductivities which follow the trend of the pure material: they are lowered by about 10 W/mK and 65 W/mK for the alloys 1201 and 3104, respectively. A small oscillation of the thermal conductivity is observed near the phase transition. This is attributed to the way the equivalent specific heat is calculated.

Despite the low thermal conductivity found in the liquid (70-100 W/mK), the value of the thermal conductivity in this phase was increased to a larger value in the numerical computations (300 W/mK) so as to account for liquid convection in the sump. This value was determined by calculating the steady state sump depth in the plane of symmetry (yz) and by comparing the result with the measured value (see section 5.2.2).

Figure 5.33 compares the calculated and measured thermal histories at different locations inside the 3104 1D-casting. The computations were conducted using the thermal conductivity deduced by the inverse method (see figure 5.32). The first thermocouple near the chill was taken as a boundary condition, thus showing a perfect agreement with the measured temperatures.

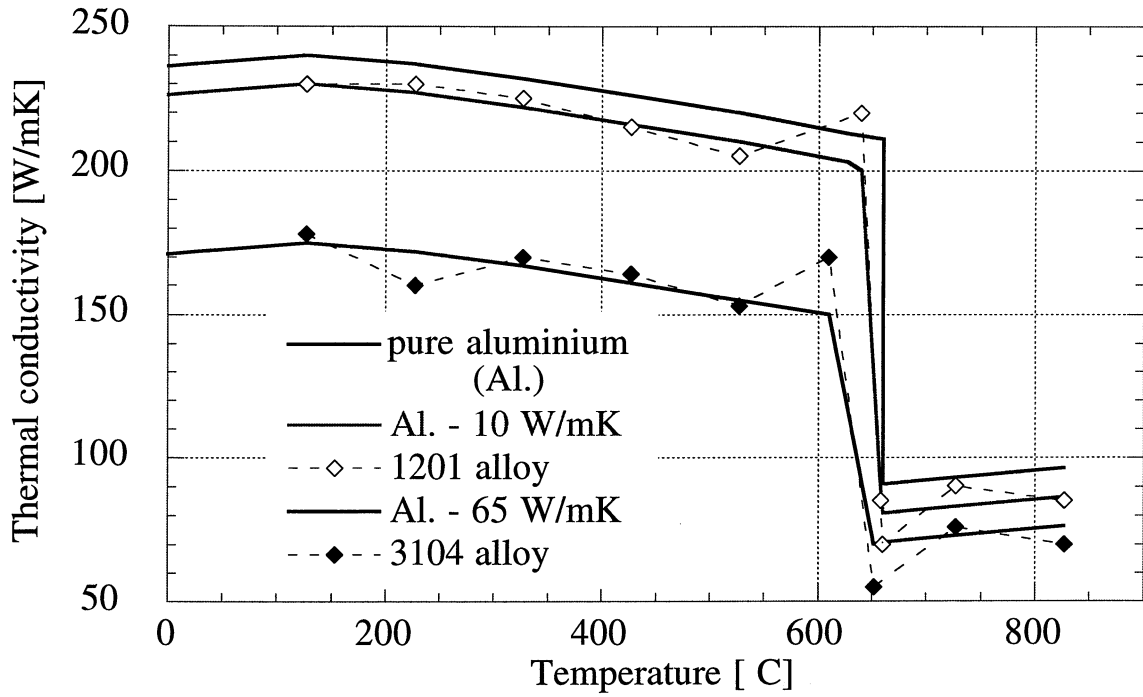


Figure 5.32: temperature-dependent thermal conductivity of the alloys 1201 and 3104 as deduced from inverse modelling and compared with the values for pure aluminium from Pehlke [Pehl].

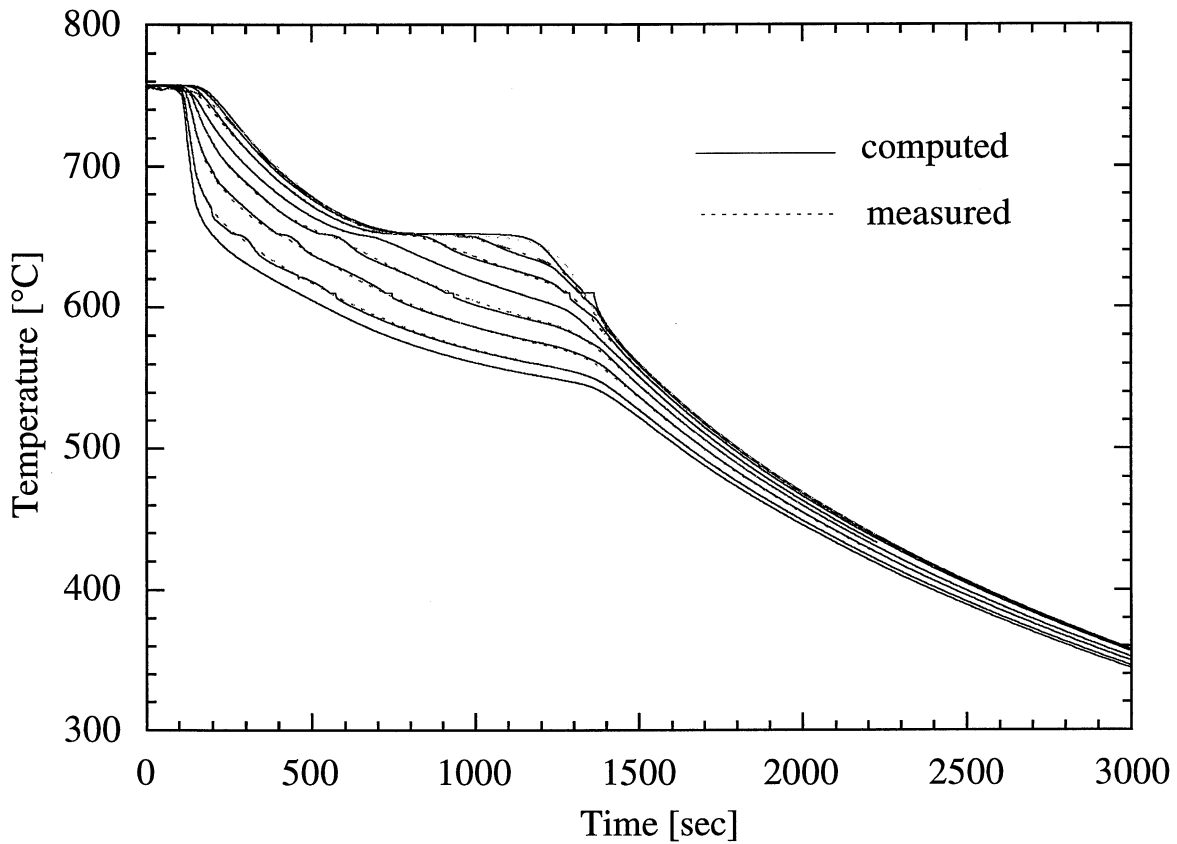


Figure 5.33: measured (dashed lines) and calculated (continuous lines) thermal histories at different locations within the 3104 1D-casting.



### *Boundary condition along the rolling faces*

The boundary conditions along the rolling faces representing the heat extraction in the primary and secondary cooling zones, were also obtained by inverse modelling. Assuming steady state, the temperature profiles presented in figures 5.1 and 5.2, were used to deduce by inverse modelling the height-dependent heat flow extracted at the lateral surface of the ingot by the mould (primary cooling) and by the water spraying system underneath (secondary cooling). The results are shown in figure 5.34 for the alloy 1201 DC-cast at 80 mm/min and for the alloy 3104 DC-cast at 50 mm/min. As can be seen, a heat flow of a few hundreds kW/m<sup>2</sup> is extracted from the ingot during the initial contact with the mould but the heat flow almost vanishes as soon as an air gap forms. At the location of the water spraying impingement, the heat flow is maximum (4 to 4.5 MW/m<sup>2</sup>). It decreases then to lower values as water flows and evaporates along the side of the ingot. A lower casting rate decreases the amplitude of the primary and secondary coolings.

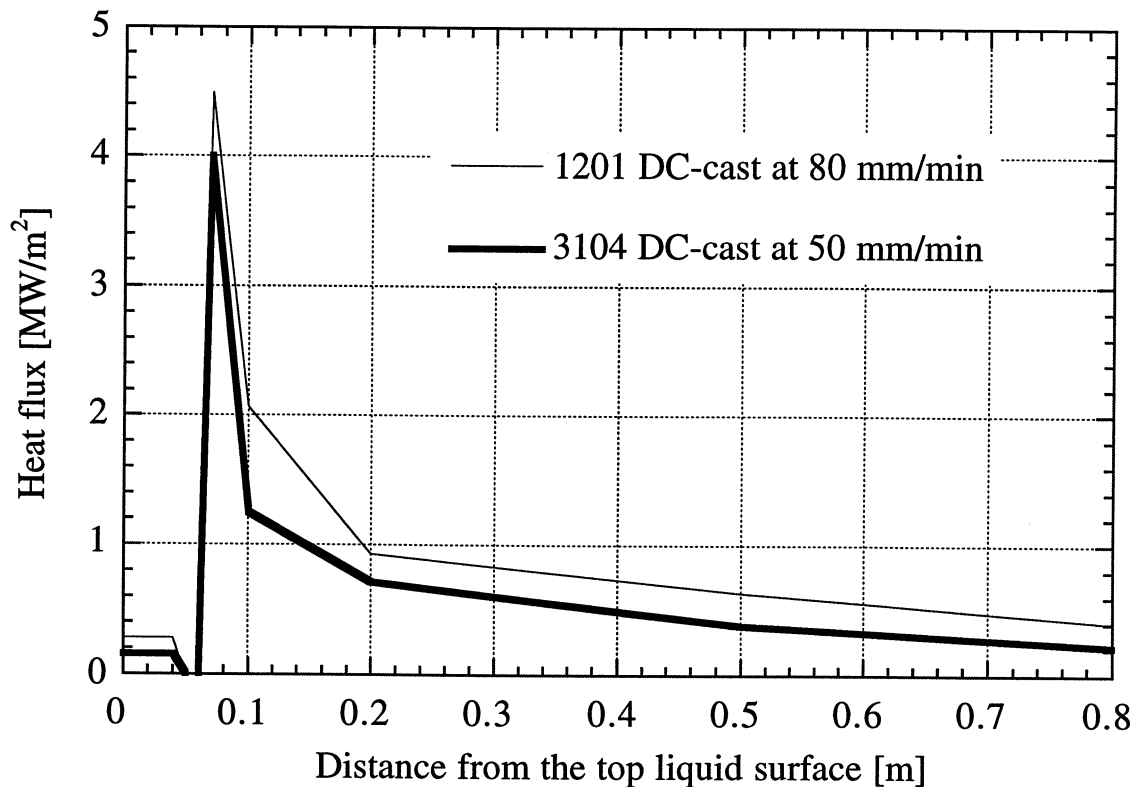


Figure 5.34: height-dependent heat flux along the rolling faces as deduced by inverse modelling.

The temperature profiles calculated with the boundary conditions of figure 5.34 are compared with the measured profiles in figure 5.35 for the 3104 alloy.

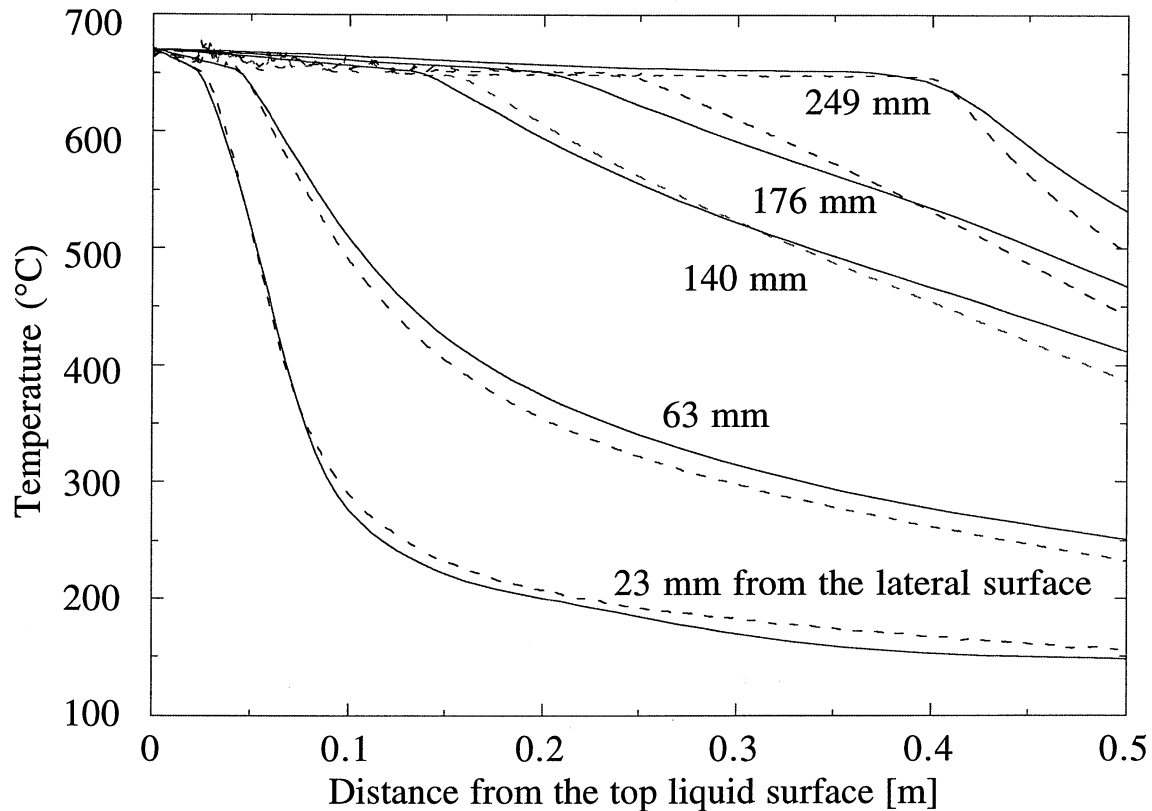


Figure 5.35: measured (dashed lines) and calculated (continuous lines) temperature profiles along five vertical lines (position of the thermocouples) within the 3104 ingot DC-cast at 50 mm/min.

These calculated heat fluxes will be used in the thermomechanical computations when defining the thermal boundary conditions along the rolling faces of the ingot. As will be shown, the thermal boundary conditions applied in the 2D and 3D thermomechanical models play a key role as they dictate the shape and extension of the sump, thus influencing the bending of the solid shell and the resulting ingot cross-section (see next section).

### 5.2.3 Ingot distortions

The results of the temperature, deformation and stress field computation using the 2D and 3D thermomechanical models (see section 4.3) are presented in this section for the alloys 1201 and 3104. The calculated rolling faces pull-in, butt swell, butt curl and non-uniform ingot cross section are compared with the measurements presented in section 5.1. The calculations were performed until a pseudo steady-state was reached, from both a thermal and a mechanical point of view. In order to obtain such conditions, it was found that a cast length of at least 1.5 m had to be modelled. For precaution, the results presented here are for 2.5 meter final length castings.

## *2D model: rolling faces pull-in and butt swell*

The computations of the rolling faces pull-in and butt swell were first carried out in two dimensions (2D) at the mid-plane section (yz) of the 1201 alloy DC-cast at 60 mm/min. Plane strains were assumed in this case, owing to the large width of the ingot compared to its thickness (see figure 4.9). Figure 5.36 shows on its left scale the computed ingot contraction, or pull-in, as a function of the cast length just at the end of casting, i.e., as the metal feeding is stopped, and after complete cooling of the ingot in the casting pit. The ingot surface temperature at the end of casting is also shown on the right scale. The last elements included in the model have a temperature equal to the inlet metal temperature, 670°C. Under the effect of the primary and secondary coolings, the surface temperature rapidly decreases to 100°C and less below the top surface. Most of the contraction of the ingot is induced by the cooling of the solid shell: the last solid to have formed at the end of casting has the size fixed by the mould opening. During cooling, this part of the ingot experiences a 20 mm pull-in. On the other hand, the butt of the ingot is already cold, so the contraction remains the same during the cooling of the ingot. Figure 5.36 clearly demonstrates that a stationary deformation regime had been reached: the transient regime corresponds to the butt-swell and extends to about one meter in cast length. The stationary regime shows a constant contraction which corresponds to the rolling faces pull-in at the plane of symmetry of the ingot.

Figure 5.37 shows the comparison between the measured ingot profile in the plane (yz) (see figure 4.9) and the computed one. Both butt swell and rolling faces pull-in are well reproduced by the 2D model. Also shown on figure 5.37 is the ingot contraction as calculated under the assumption of only thermo-elastic deformation of the metal, i.e.  $\dot{\epsilon}_{vp} = 0$ . (open diamonds). In this case, the ingot pull-in is only 7 mm thus meaning that a thermo-elastic computations would explain only one third of the total rolling faces pull-in in the steady state regime of casting. In order to assess the relative importance of the plastic deformation in the mushy zone, i.e. between the coherency and solidus temperatures, the cumulated plastic strain,  $cps(t)$ , has been computed. This quantity is defined as:

$$cps(t) = \int_0^t \sqrt{\frac{2}{3} d\epsilon_{vp} : d\epsilon_{vp}} \quad (5.7)$$

where  $d\epsilon_{vp}$  is the increment of viscoplastic strain at time  $t$ . This parameter was calculated during the steady state regime of casting at two integration points, one near the vertical axis of the slab and one close to the ingot surface.

The values of this quantity at the coherency, solidus and room temperatures are reported in Table 5.6.

As shown in this table, 15 % of the plastic straining occurs in the mushy zone near the axis of the ingot and only 1% occurs near the surface. The mushy zone is larger along the axis of the slab, thus allowing more time for the metal to relax thermal stresses through creep deformation. On the other hand, the chilling of the ingot surface is so rapid that almost no plastic deformation occurs in the mush.

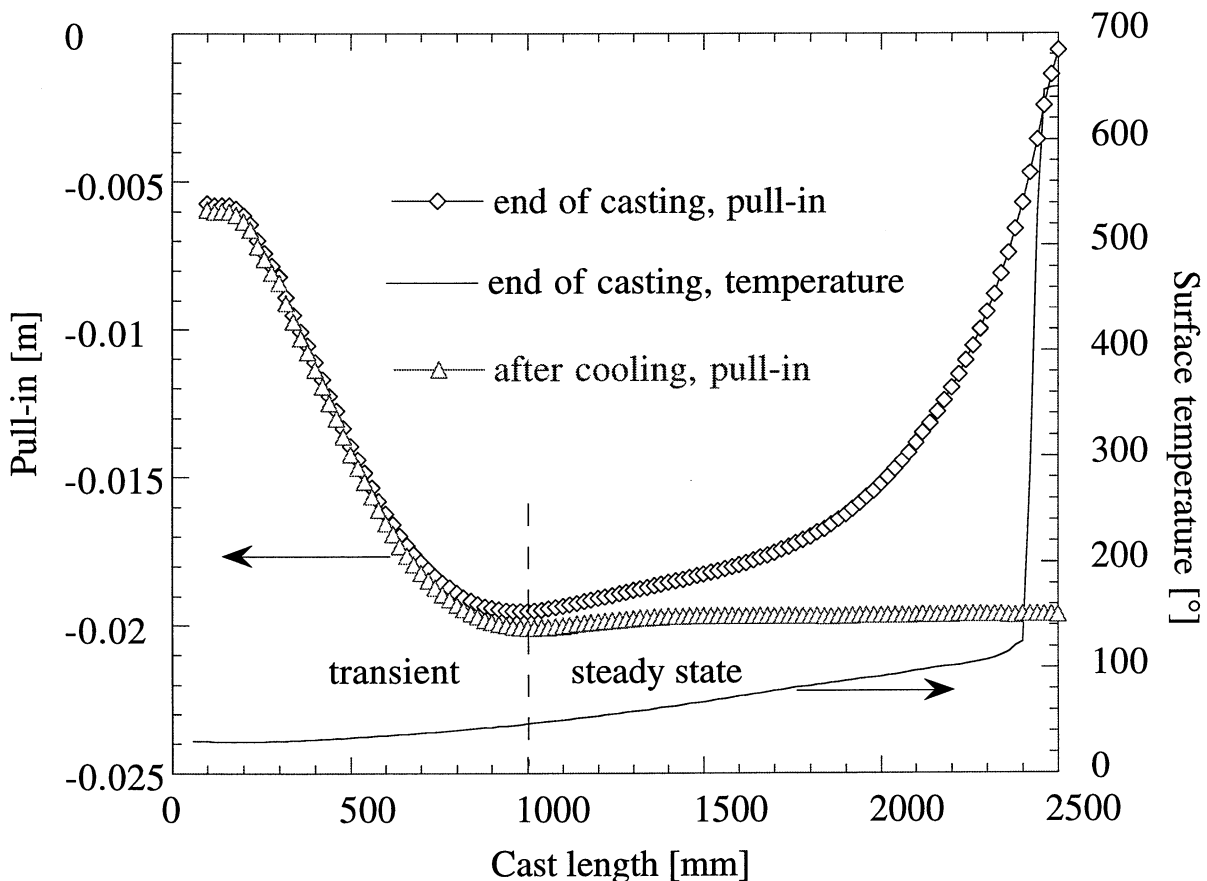


Figure 5.36: computed rolling faces pull-in and ingot surface temperature as a function of the cast length at the end of casting and after complete cooling (1201, 60 mm/min).

The influence of the casting speed on the ingot contraction is reported in figure 5.38 and 5.39. The first figure shows the pull-in profile of a DC-cast 1201 ingot just at the end of casting for three casting speeds, 60 , 70 and 80 mm/min. The butt contraction is not affected by the casting speed whereas the pull-in after a cast length of 50 cm starts to increase significantly with increasing casting rate. This trend is well reproduced on figure 5.39 which shows the computed pull-in after complete cooling for the three casting speeds : the higher the casting speed, the higher the pull-in.

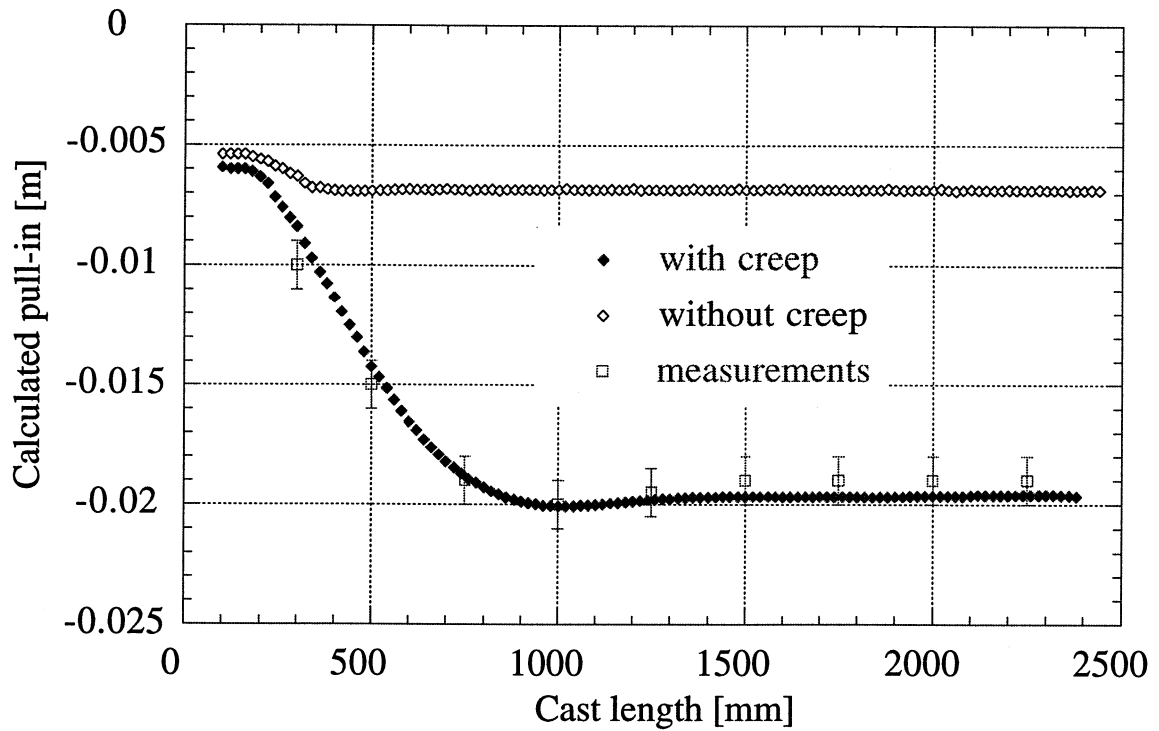


Figure 5.37: computed rolling faces pull-in with and without creep deformation compared with the measurements (1201, 60 mm/min).

Temperature	centre	surface
650 °C (coherence)	0. %	0. %
630 °C (solidus)	0.33 %	0.023 %
20 °C	2.19 %	2.33 %
$\frac{\text{cps}(t_{630}^1)}{\text{cps}(t_{20})}$	15 %	1 %

Table 5.6: value of the cps parameter close to the axis and near the ingot surface at different temperatures.

Figure 5.40 compares the calculated and measured rolling face pull-in as a function of the casting speed for the 1201 alloy. These values correspond to the steady-state pull-in measured after cooling (see figure 5.9). The measured (see table 5.1) and calculated sump depths are also reported in the same diagram. Again, a good agreement is found and the pull-in is clearly correlated with the sump depth.

<sup>1</sup>  $t_{630}^*$  and  $t_{20}^*$  are times for the metal to reach a temperature of 630°C and 20°C respectively.

The influence of the mould opening, and consequently of the ingot thickness, on the steady-state rolling faces pull-in and sump depth is shown in figure 5.41 for the alloy 1201 DC-cast at 70 mm/min. The ingot width (1860 mm) and cooling conditions have been kept constant. When the thickness of the ingot to be cast increases, the sump depth increases and so does the ingot pull-in.

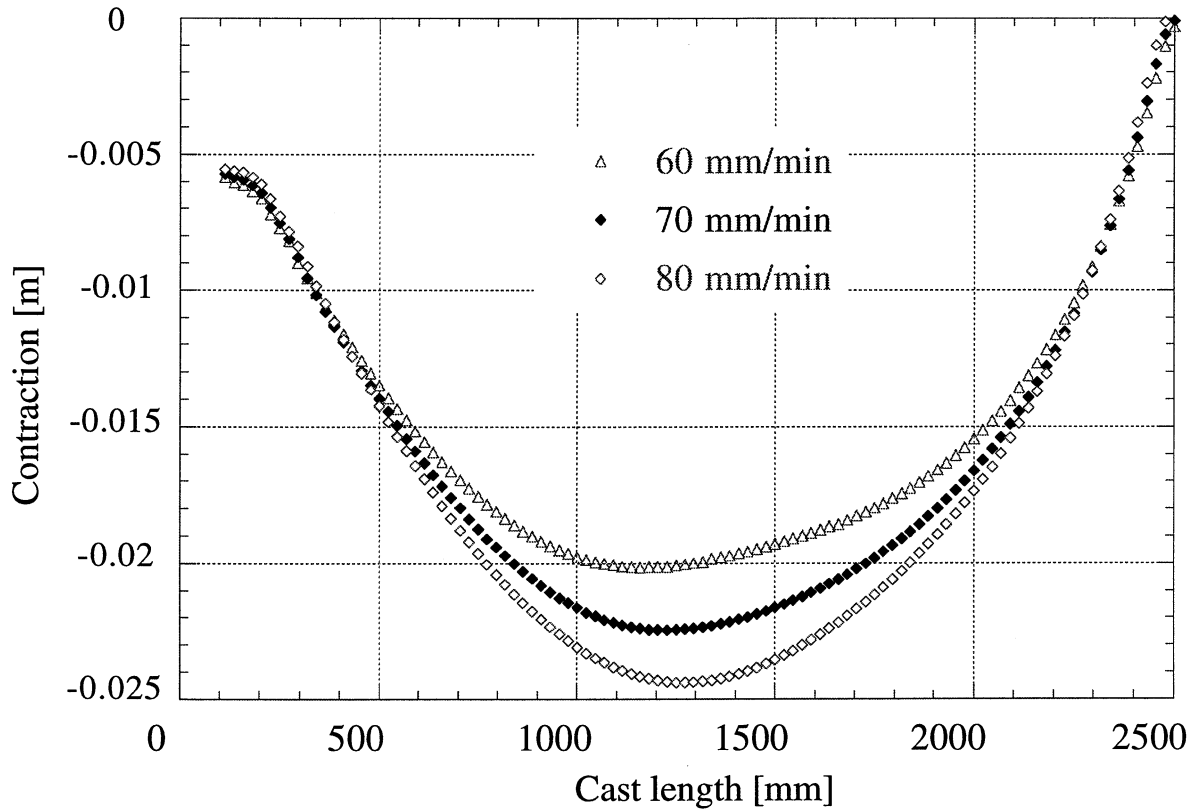


Figure 5.38: effect of the casting speed on the rolling face profile at the end of casting (alloy 1201).

The steady state computed temperature profiles for the alloy 3104 DC-cast and EM-cast at 65 mm/min are reported in figure 5.42 on the left and right, respectively. The distance between the meniscus and the electromagnetic screen was 6 mm. The isotherm corresponding to the coherency temperature of the alloy, 635°C, is shown. Due to the primary cooling, the metal inside the mould is at a lower temperature and therefore experiences contraction and creep flow earlier than that inside the inductor at the same height. Nevertheless, the sump depth remains almost the same in both cases.

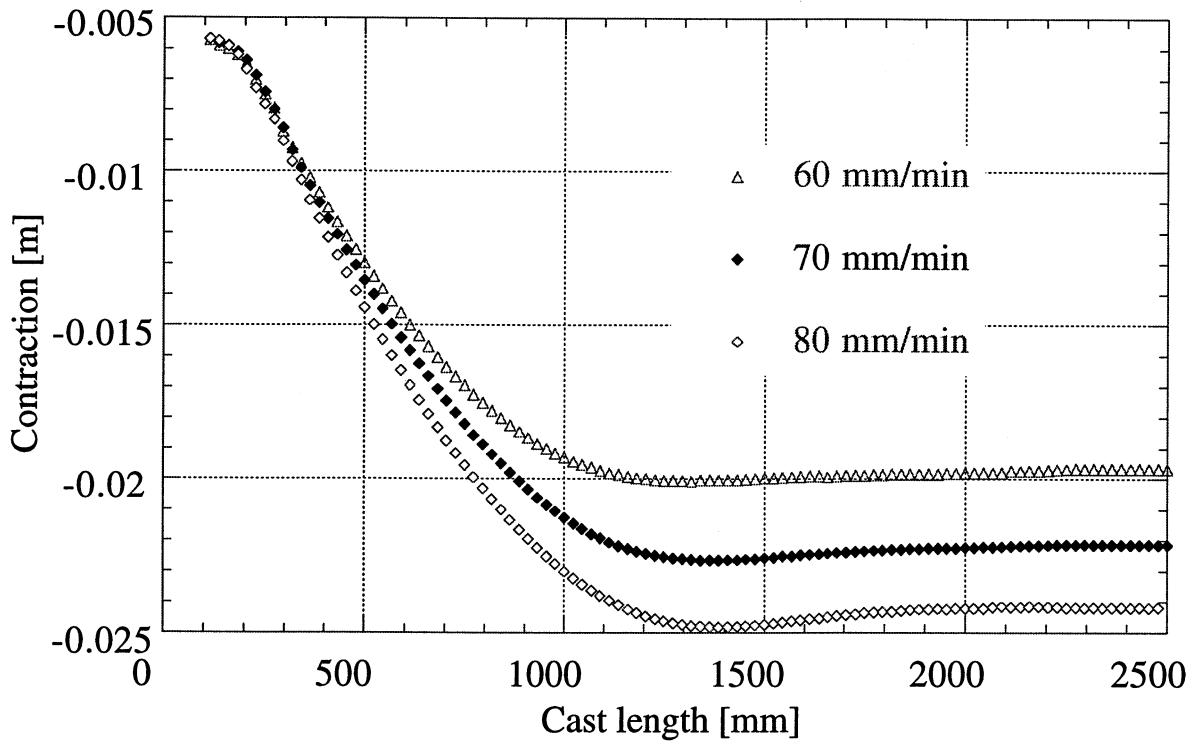


Figure 5.39: computed rolling faces profile after complete cooling (alloy 1201).

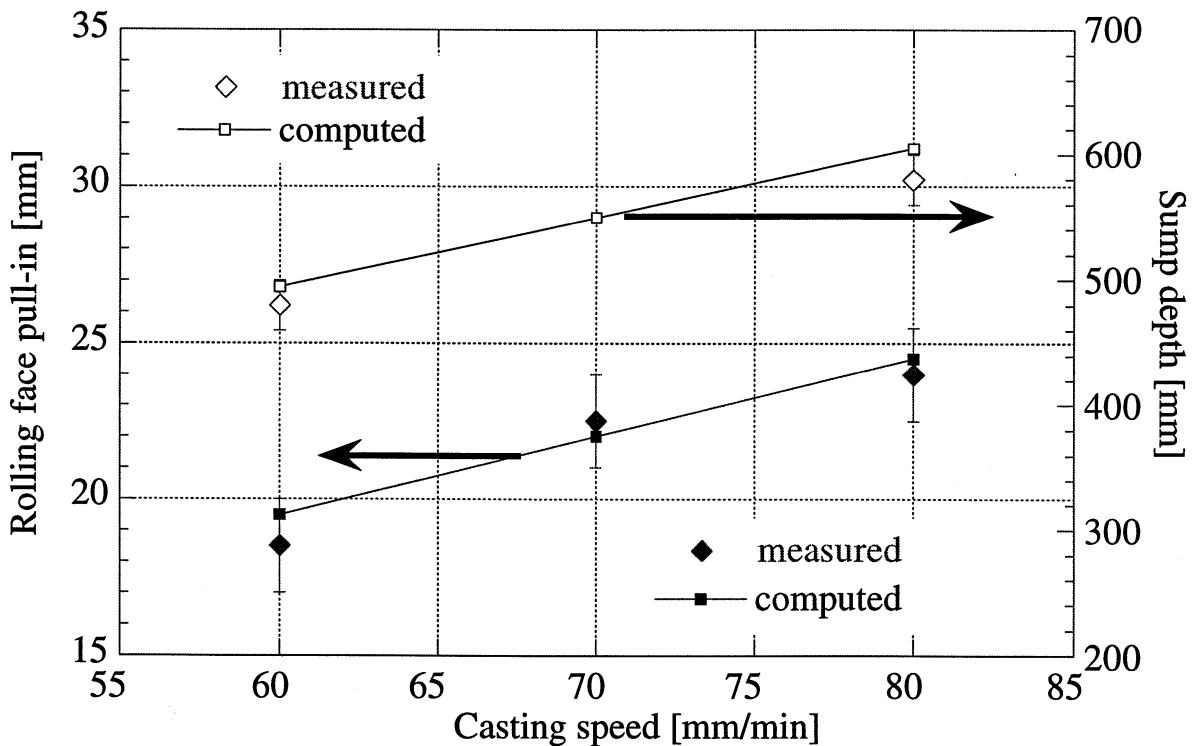


Figure 5.40: comparison between computed and measured rolling faces pull-in (left) and sump depth (right) (1201 alloy).

Figure 5.43 shows the computed ingot profiles for the 3104 alloy DC-cast and EM-cast at 65 mm/min, together with the measurements performed for the EM-cast ingot. Note that for the computations of the EM-casting, the thickness of the enmeshment of the activated layers corresponding to the liquid metal equals the mean position of the meniscus, 266 mm (see figure 5.12), in the (yz)

plane. The computed pull-in is higher for the DC-cast ingot than for the EM-cast one and the butt swell and rolling faces pull-in are well reproduced for the EM-cast ingot.

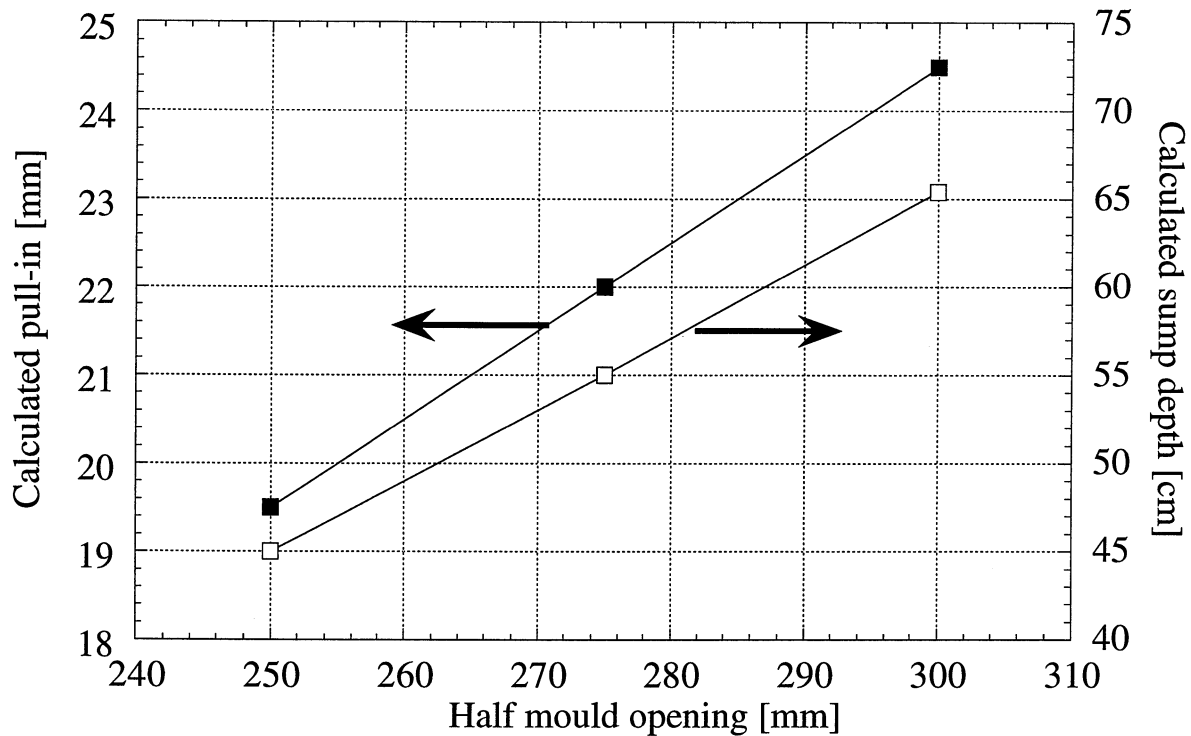


Figure 5.41: calculated rolling faces pull-in and sump depth as a function of the mould opening (1201 alloy DC-cast at 70 mm/min).

Eventually, the residual stresses  $\sigma_{yy}$ ,  $\sigma_{zz}$  and  $\sigma_{yz}$  calculated for the 1201 ingot DC-cast at 60 mm/min after complete cooling are shown in figure 5.44. The ingot surface is in compression ( $\sigma_{yy}$ ,  $\sigma_{zz}$ ) whereas the heart is in tension; this is in accordance with the works of Fjaer and Mo [Fja1] and Dour et al. [Dour]. The shear stress  $\sigma_{yz}$  is almost zero in the centre part of the ingot (in between -6 and +6 MPa) thus proving the important stress relief by viscoplastic flow, especially parallel to the solidification front. Such results can be very useful to optimise first the casting procedure so as to avoid hot tearing and cold cracking and second the temperature and the holding time necessary to relieve the thermal stresses before rolling. The stress build-up during the process is very similar to what can be found in the fields of polymers, especially the so-called skin-core effect [Månson]. Further details can be found in [Drez3].

### Discussion

The agreement between calculated and measured ingot profiles is very satisfactory for both DC (figure 5.37) and EM-casting (figure 5.43). A sensitivity analysis performed with the viscoplastic sinh law reported in table 2.1 gave a steady state ingot contraction of 12.5 mm for aluminium (high and



commercial purity) and of 9 mm for the 5xxx serie alloys (5052 and 5182). These results are far from reality, thus enhancing the need of a correct description of the mechanical behaviour of the alloys and justifying the creep and indentations tests carried out on as-cast samples (see section 3.2).

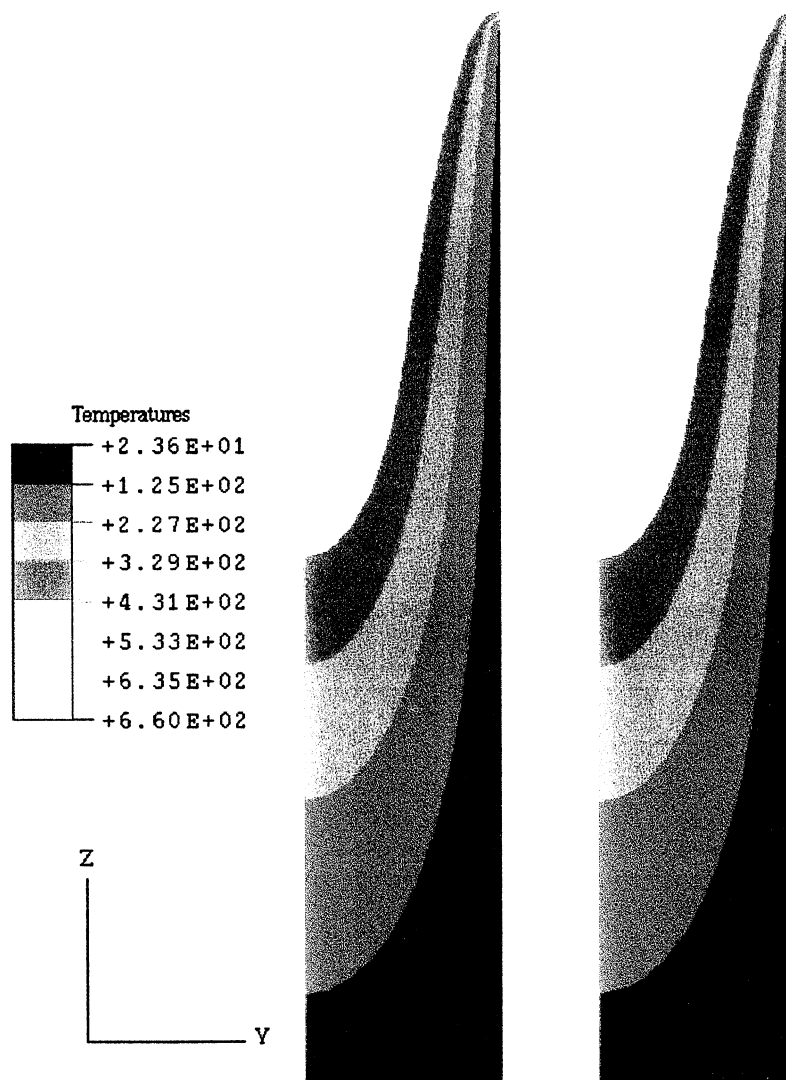


Figure 5.42: computed steady-state temperature profiles during DC-casting (left) and EM-casting (right).

As shown in section 5.1.1, most of the ingot contraction occurs below the mould/inductor as a result of the large thermal gradient induced upon cooling. In DCC, the cooling can be subdivided in two steps, the first one being associated with the contact with the mould and the second one arising when the water jet strikes the surface. Although the measured pull-in clearly reveals these two stages (see figure 5.5), the contraction of the ingot at the exit of the mould only

represents 9 % of the total pull-in after cooling. In EMC, there is only one cooling associated with the water spray and the contraction is continuous.

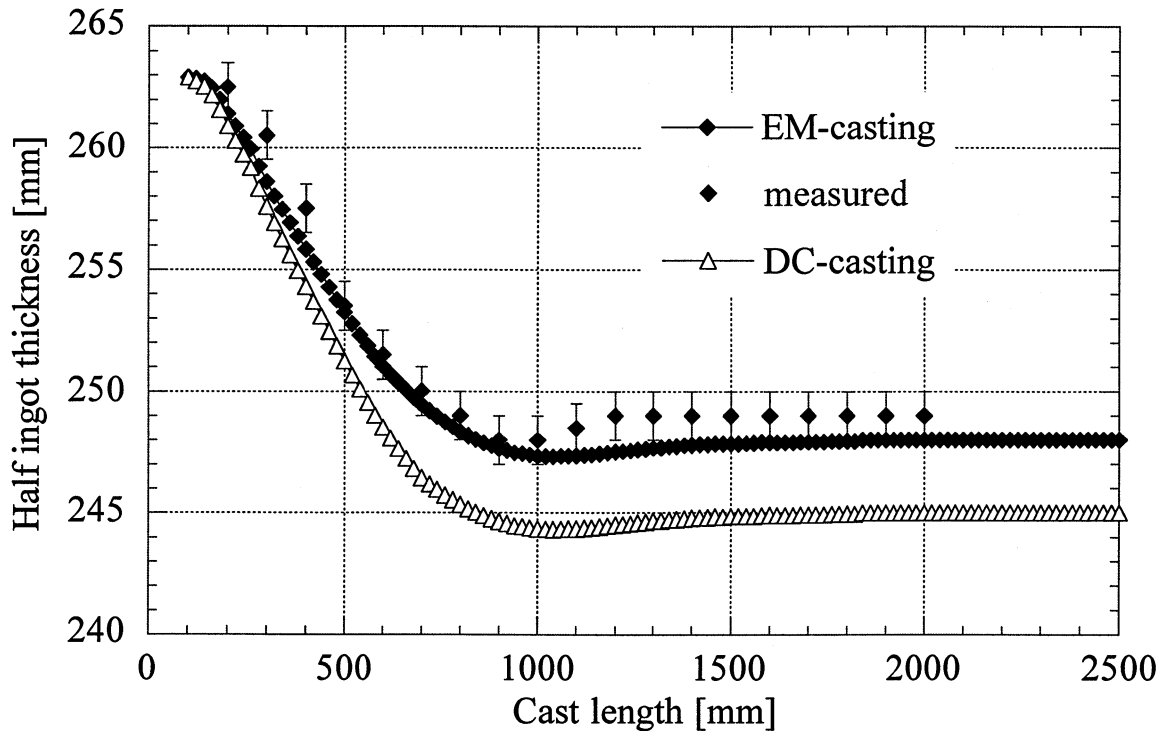


Figure 5.43: computed and measured profile of a 3104 ingot EM-cast at 65 mm/min. The computed 3104 ingot profile DC-cast at the same speed is also shown.

The calculation presented here also shows that most of the contraction is induced by the cooling of the solid ingot. In figure 5.36, it is seen that the last solid to have formed at the end of the casting has about the size fixed by the mould opening (i.e., contraction equal to zero at 2.5 meters when this part has just solidified). After cooling to room temperature, this part of the ingot experiences a 20 mm pull-in, i.e., about 10% contraction. The thermomechanical and thermophysical properties of the alloy being given, it is expected that the pull-in increases with the sump depth. This trend is reflected in figures 5.39 and 5.40. As the casting speed is increased, the liquid pool becomes deeper and the thermal gradient near the cooling water is more horizontal. As a result, the pull-in increases. The same trend is predicted when changing the mould opening: the ingot being thicker, the sump is deeper and the final pull-in is increased (figure 5.41). Please note that the computed ingot contraction (see figures 5.37 and 5.43) remains constant after the transient phase up to the head of the slab: the localised metal contraction at the end of casting is not reproduced by the present thermomechanical model owing to the fact that the solidification shrinkage is set to zero. As can be seen, the final shape of DC and EM-cast ingots is a result of several interplaying phenomena. However, the present computation results have

clearly shown that most of the pull-in is associated with thermal stresses induced upon cooling of the solid and that the contraction at the exit of the mould/inductor is only a minor part of the overall pull-in.

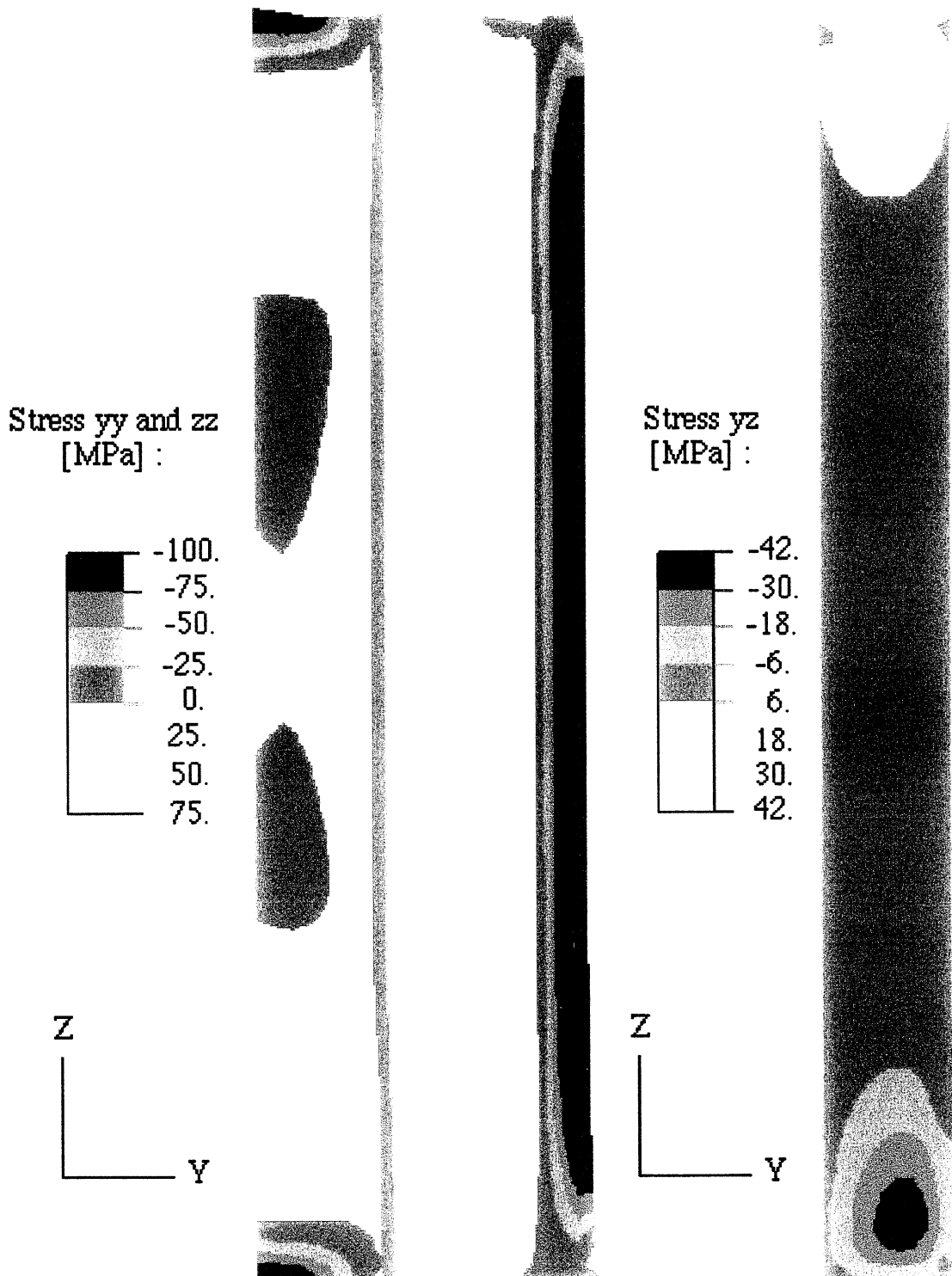


Figure 5.44: computed residual stresses,  $\sigma_{yy}$  and  $\sigma_{zz}$  on the left and  $\sigma_{yz}$  on the right (1201 DC-cast at 60 mm/min).

The horizontal component of the thermal gradient, which is reflected by the liquid pool profile, plays a key role in the deformation of the ingot. The

extension to three dimensions (3D) of the present model is necessary if the resulting ingot cross section is to be computed for a given mould design.

*3D model: butt curl and ingot cross-section*

In this section, the 3D results of the temperature and deformation field computations are presented and compared with the measurements of ingot distortions previously described in section 5.1.1. The computations refer to the DC casting of the alloys 1201 and 3104 at different casting speeds, the nominal ingot cross-section being 1860 x 510 mm. Figure 5.45 shows the computed steady-state temperature profile after a cast-length of 1.5 meter as viewed from the centre.

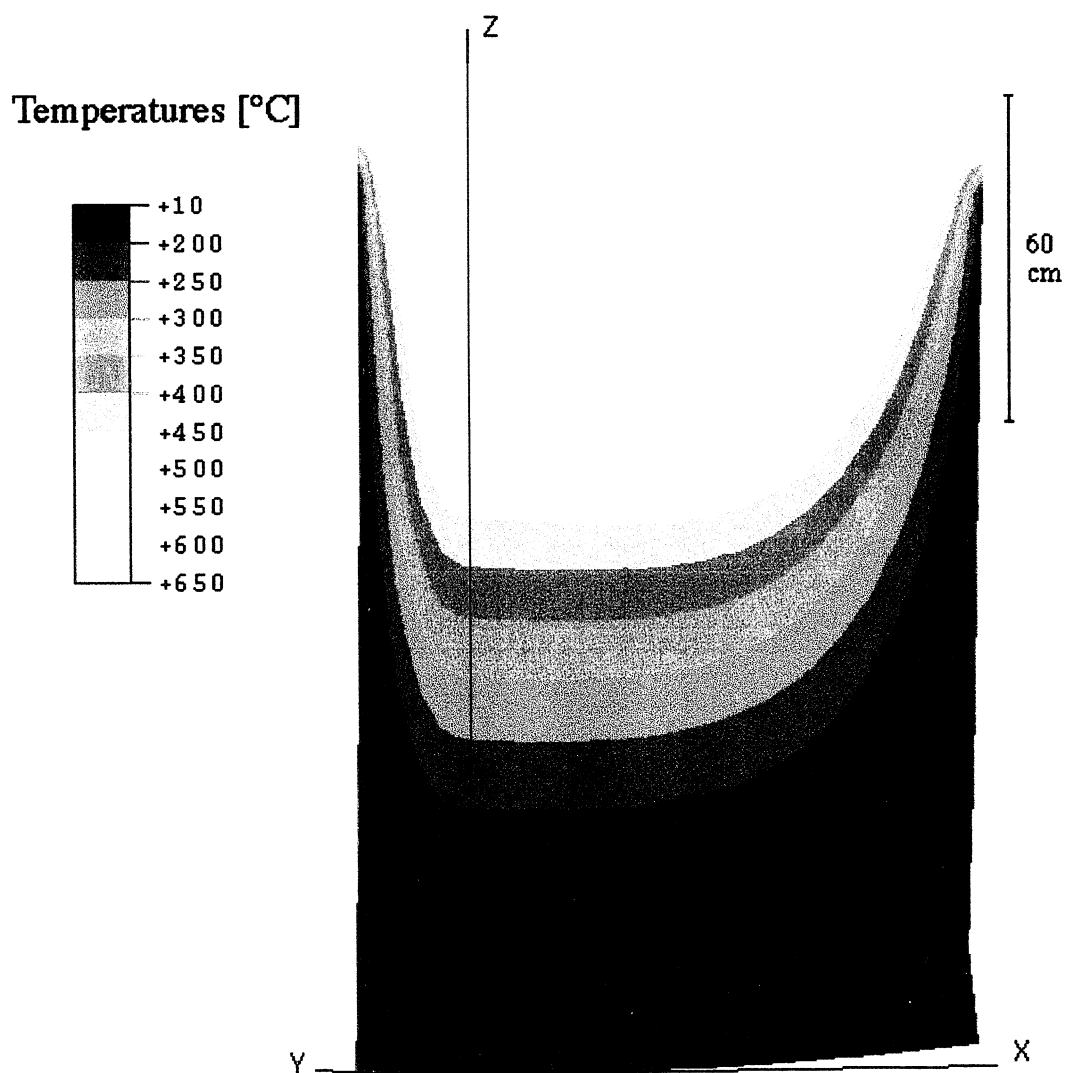


Figure 5.45: computed steady state temperature profile inside the casting as viewed from the centre (1201 DC-cast at 60 mm/min).

Below the exit point of the mould, the temperature at the periphery of the ingot is lower than 200 °C thus giving enough strength to the solid shell to

support the liquid pool. The sump depth is approximately 60 cm, a value which agrees well with the measurements reported in table 5.1. Assuming that the bottom block is totally rigid, the vertical displacement of the metal at the bottom surface represents the width of the air gap that forms between the starting block and the ingot. For the present calculations, the local heat transfer coefficient was a decreasing function of the air gap width: this coefficient decreases from a value of  $2000 \text{ W/m}^2\text{K}$  when the gap, i.e. the vertical displacement of the metal, was lower than 0.1 mm to a value of  $200 \text{ W/m}^2\text{K}$  when the gap was larger than 1 mm. Figure 5.46 presents the calculated vertical displacement of the point at the extreme corner of the lower face of the slab as a function of time. As soon as the cooling water impinges the ingot, the butt rises rapidly, thus generating a large air gap between the metal and the starting block. Consequently, the heat extraction rapidly falls to its low value and provokes a reheating of the butt which can therefore relax the thermal stresses more easily. The ingot butt then falls a few millimetres before rising again after 90 sec. ( figure 5.46).

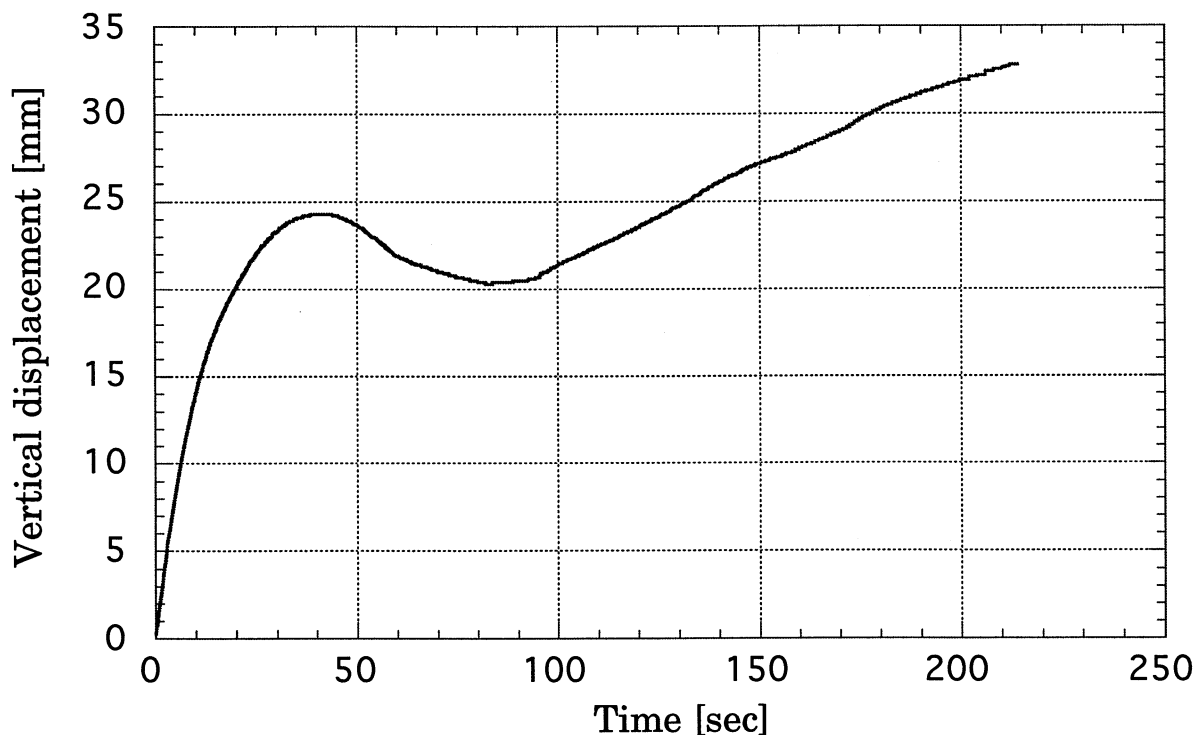


Figure 5.46: computed vertical displacement of the ingot corner as a function of time (the origin of time corresponds to the first chilling by the cooling water on the ingot).

The calculated vertical displacement of the ingot butt plotted in figure 5.46 agrees well with the measurements performed by Carrupt et al. [Carrupt] and Krähenbühl et al. [Kräh]. Although the coupling between thermal and mechanical effects is particularly strong during the start phase of the process, the use of a decreasing heat transfer coefficient leads to a reasonable description of the butt curl phenomenon. The butt curl speed, i.e. the time derivative of the

vertical displacement of the ingot butt, is very high just after the cooling water had impinged the ingot. The model presented here seems suitable and promising in optimising the cooling conditions and also in choosing the appropriate bottom block geometry and casting parameters during the non-stationary starting phase of the DC casting process. Moreover, special attention has to be paid to the stress generation, especially the  $\sigma_{xx}$ -component which may lead to the initiation of longitudinal cracks [Hann, Drez3].

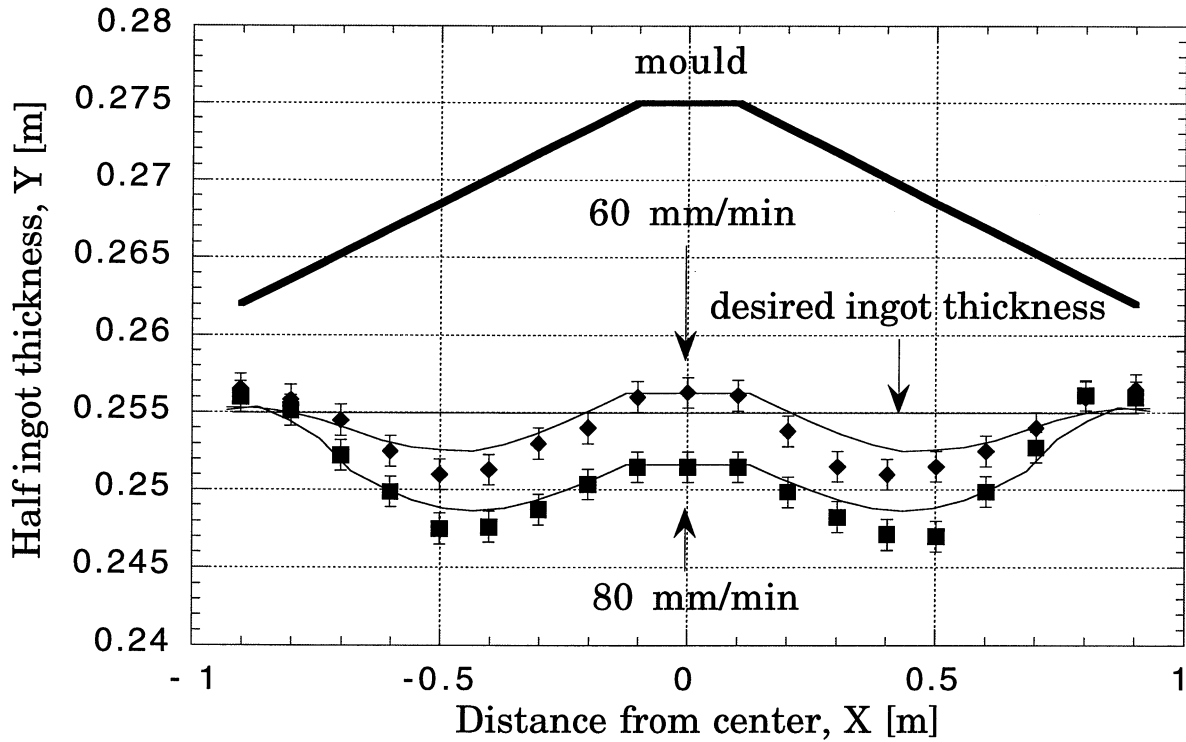


Figure 5.47: computed and measured steady state ingot cross section (1201 DC-cast at 60 and 80 mm/min).

The computed and measured steady-state ingot cross-sections of the 1201 alloy after complete cooling are compared in figure 5.47 for two different casting speeds, 60 mm/min and 80 mm/min (continuous curves and symbols, respectively). Also shown on this figure are the interior mould shape and the desired half ingot thickness which is very close to the final thickness of the short sides. The measured non-uniform contraction and the effect of increased casting speed on the final shape of the ingot are well reproduced by the present model. On figure 5.48, the ingot cross sections at different cast lengths are plotted, thus providing an idea of the butt swell of the ingot. The first section shows an almost constant contraction (6 mm) all around the ingot. This contraction is essentially thermo-elastic in nature and is comparable to the contraction of the short sides. Eventually, figure 5.49 compares the computed and measured ingot cross sections in the steady state regime of casting for the alloy 3104. The agreement is very satisfactory.

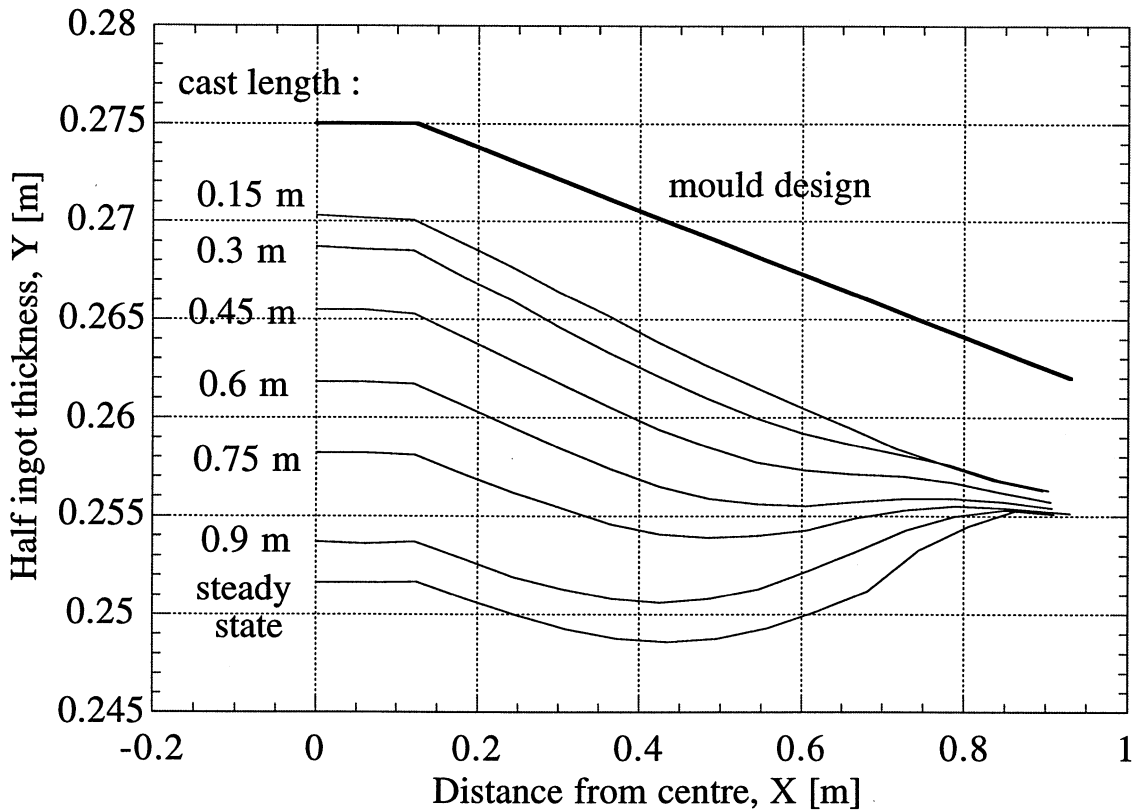


Figure 5.48: computed ingot cross section at different cast length (1201 DC-cast at 80 mm/min).

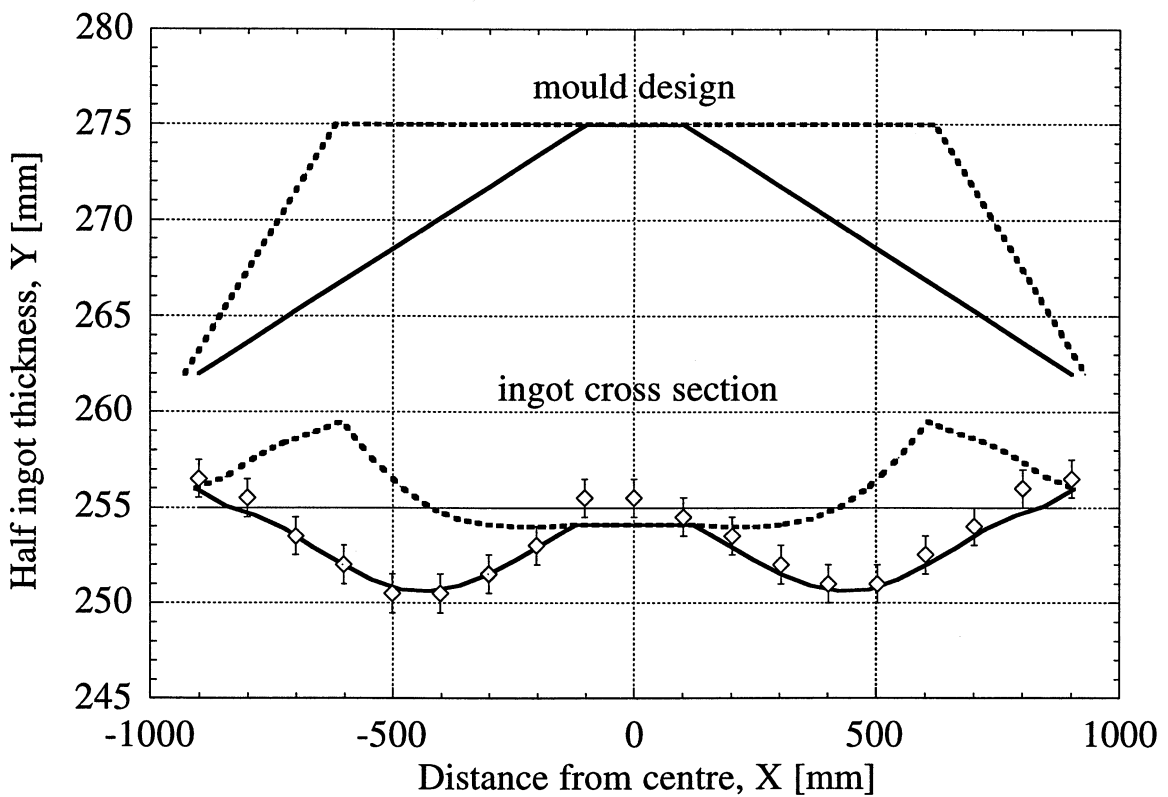


Figure 5.49: computed and measured steady state ingot cross section (3104 DC-cast at 60 mm/min). The resulting ingot cross section for a mould design with a larger central segment is also plotted (dashed lines).

Also shown on this figure is the ingot cross section computed using a mould design with a larger central segment (dashed lines). In this case, the ingot contraction is totally different: the resulting cross section presents the shape of a bone instead of the classical w-type shape.

After this validation of the model, different mould designs were studied: one with no central segment (mould A), one with a small central segment (mould B) and one with a large central segment (mould C). The computed final ingot cross-sections obtained for these three different mould shapes are reported in figure 5.50 together with the corresponding mould designs. The inward pull-in of the centre of the rolling faces and the contraction of the short sides remain constant irrespective of the mould design and correspond to the values calculated by the 2D model.

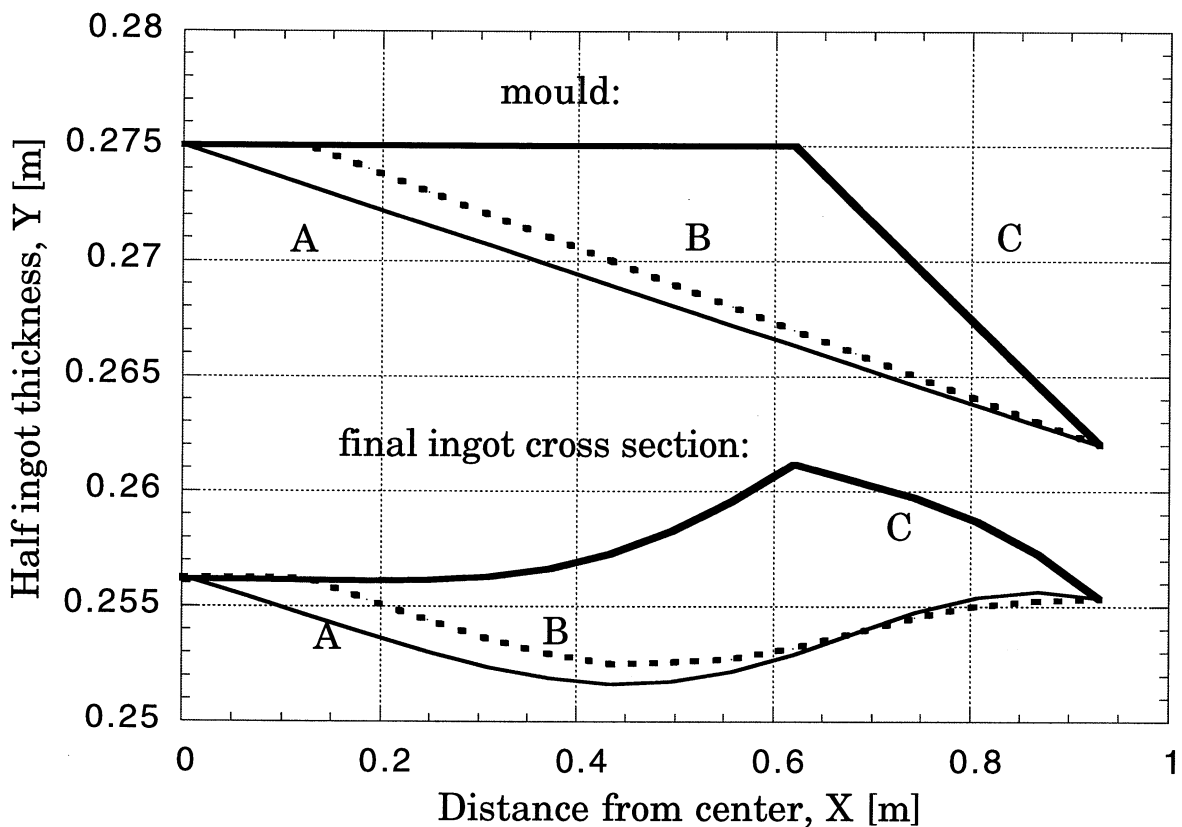


Figure 5.50: computed steady state ingot cross section for three mould designs (1201 DC-cast at 60 mm/min).

The numerical investigation of moulds A and B revealed that the resulting ingot presents a half thickness that is always lower than 256 mm. On the contrary, mould C would produce an ingot with a half thickness larger than 256 mm. This is explained by the contraction along the x direction which is important owing to the dimension of the ingot in that direction and which gives rise to a sort of buckling, either towards the centre of the ingot or outwards. It



clearly appears in figure 5.50 that a central segment in between moulds B and C could produce a flatter rolling sheet ingot.

### *Process optimisation*

Eventually, considerable amount of cast metal could be saved by reducing the scalping thickness of the ingot before rolling. The present 3D thermomechanical model has been validated using ingot cross section measurements carried out in the steady state regime of casting (see figures 5.47 and 5.49). The numerical investigation of moulds A and C revealed that neither of these two moulds are capable of producing flat rolling sheet ingots. The use of straight line segments seems over simplistic for this aim. In the light of these computations, it has been made clear that the three-dimensional extension of the liquid pool in the steady state regime of casting has a great influence in the inward rolling faces pull-in.

In order to calculate the shape of a mould capable of producing nearly flat rolling sheet ingots, an inverse method, similar to that presented in section 4.2, can be used. Let assume that the desired ingot thickness is 510 mm (half ingot thickness of 255 mm) and that the enmeshment is made of  $N$  points along the  $x$  direction (see figure 5.51). In this case, one has to minimise the function:

$$S(\mathbf{B}) = \sqrt{\frac{1}{N} \sum_{i=1}^N [0.255 - U_i^y(\mathbf{B})]^2} \quad (5.8)$$

where  $U_i^y(\mathbf{B})$  is the  $y$ -component of the calculated final position of the point  $i$  of the enmeshment and  $\mathbf{B} = \{\beta_1, \beta_2, \dots, \beta_M\}$  is a vector defining the mould shape. An iterative procedure, similar to the one described in section 4.2.1, is therefore used to find the solution  $\mathbf{B}$  minimising  $S(\mathbf{B})$ . Starting with an initial guess of the parameters  $\beta_i^{v=0}$ , the resulting ingot cross section is computed using the 3D thermomechanical model. Then a perturbation,  $\delta\beta_i$ , on each component  $\beta_i$  is performed to obtain the sensitivity coefficients which allows then to calculate the increments of the coefficients,  $\Delta\beta$ . If these increments are smaller than a certain tolerance, then the solution  $\mathbf{B}$  has been found. If not, then  $\beta^v$  at iteration  $v$  is replaced by  $\beta^{v+\Delta\beta}$  and the procedure is iterated. Within each iteration,  $(M+1)$  direct problems are solved with the direct code, which is very CPU-intensive. As an example, figure 5.51 shows the results obtained with  $M = 3$ . In this case, the vector  $\mathbf{B}$  contains the  $y$  component of the point A, the  $x$  component being zero for symmetry reasons, and the  $x$  and  $y$  components of the point B, these two points defining a two-segmented mould.

The initial guess  $A_0B_0$ , gave a value of  $S$  equal to 3.43 mm (dashed lines), but after the first iteration, the value of  $S$  went down to 0.05 mm. As shown on figure 5.51, the ingot cross section after the first iteration (continuous line) presents a thickness that is much closer to the desired value than that produced by the first mould shape. Nevertheless, the ingot is not totally flat owing to the fact that this procedure was completed with only three “degrees of freedom” to define the mould shape. Inverse modelling applied to the determination of the mould/inductor design required to obtain flat rolling sheet ingot seems promising, but it is still very CPU-intensive<sup>1</sup>. The example presented here clearly demonstrates that the use of three straight segments in designing the mould seems over simplistic. The use of more complex shapes (e.g. more linear segments or parabolic shape) would certainly give better results.

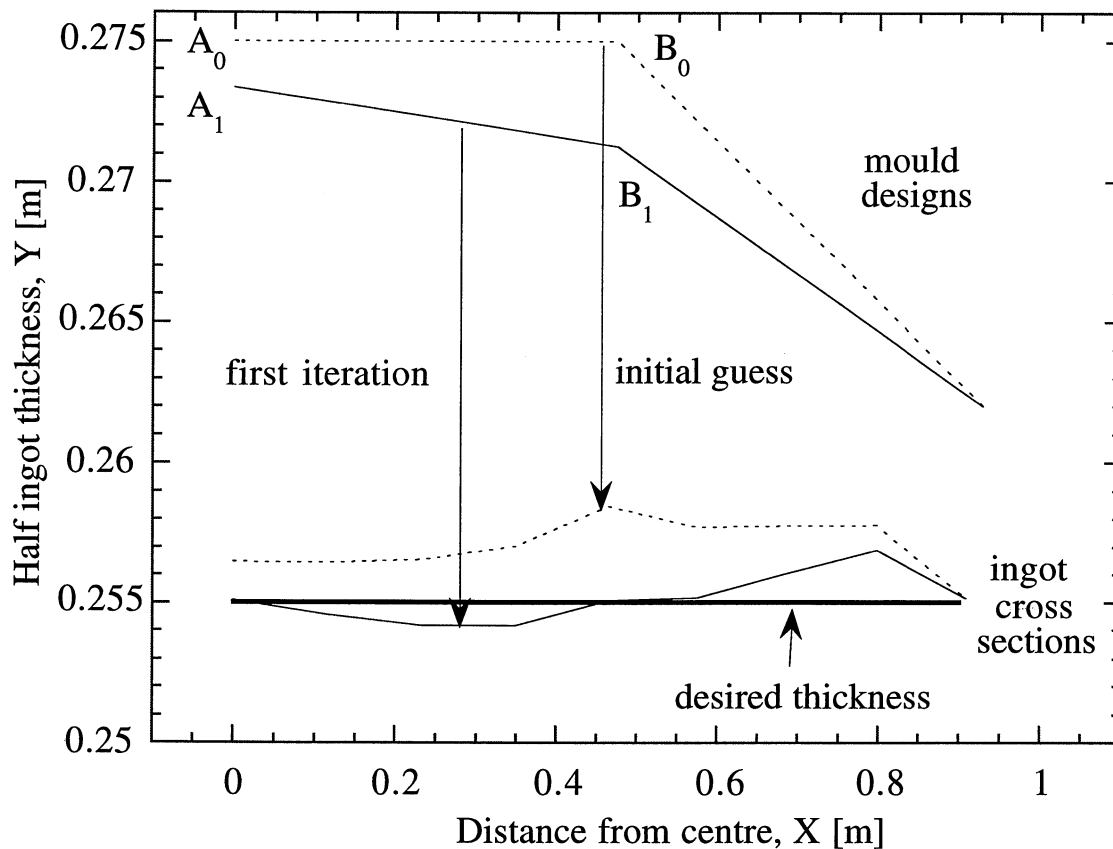


Figure 5.51: optimisation of the mould design using inverse modelling: initial guess  $A_0B_0$  (dashed curve) and results after the first iteration (continuous curve).

<sup>1</sup> For a direct calculation, the computation time was about 5 days on a HP-735 workstation for a domain including 5925 elements and 7200 nodes and representing a cast length of 1.5 m.

## CHAPTER 6

# CONCLUSION

The study of the thermomechanical effects undergone by the ingot and some solidification aspects during the Direct Chill and Electromagnetic Casting of aluminium alloys has been undertaken in the present work. The main outcomes are outlined hereafter.

- The ingot deformation during casting and after cooling has been measured in-situ in order to elucidate the mechanisms responsible for the large and non-uniform contraction of the ingot cross-section. It appears that the air-gap formation in DC casting is only 0.5 % near the centre of the rolling faces at the exit of the mould, whereas the total pull-in after complete cooling of the ingot is about 9 %. This rules out any influence of the solidification shrinkage (about 6% in volume for aluminium) and the friction in the mould is negligible. Thus it is concluded that the pull-in of the faces is mainly due to the thermal stresses which develop upon cooling of the ingot.
- The thermal conductivity and thermomechanical properties (elastic modulus, thermal expansion coefficient and mechanical behaviour in the solid and mushy states) of two aluminium alloys have been measured independently as a function of temperature. The thermal boundary conditions that prevail along the rolling faces of the ingot have been determined using measured cooling curves and an inverse model. These data were used as input data for the thermomechanical models.
- The solidification path of the AA1201 alloy has been computed using a FDM microsegregation model and was validated against DTA measurements. The use of the cooling-rate dependent Al-Fe-Si phase diagram allowed to cope with situations encountered in the DC/EM casting. Moreover, the assumption of a growing sphere to model the equiaxed globular-dendritic growth is valid, at least during the primary phase solidification. Owing to its ability to deal with situations of remelting and open system, this model will be further extended and included in a more general micro-macro-segregation model.
- The two- and three-dimensional thermomechanical models presented in the present work have been validated using the ingot distortion measured after

cooling. These models are able to predict with a good accuracy the butt curl of the ingot during the starting phase and the transient and steady-state rolling faces pull-in as a function of the casting conditions (casting speed, ingot size) and of the alloy composition, for both DC and EM-casting. In particular, it is shown that a nearly steady-state thermomechanical regime is reached after about 1 meter cast length. It has been demonstrated that the horizontal component of the thermal gradient during the stationary casting regime induces an inward bending of the solid shell and is therefore responsible for the large rolling faces pull-in measured at the centre of the ingot. The three dimensional nature of the liquid pool explains why the contraction of the short sides corresponds only to a thermal contraction. Although linear thermal contraction is only 2% for a uniform temperature specimen and would represent 11 mm in the case of a 550 mm width ingot, the *bending* and associated cumulated *deformation* of the solid shells during continuous casting explain the large pull-in in the centre of the rolling faces. It is emphasised that the pull-in is a *relative displacement*, in this case a contraction, and must not be considered as a mechanical deformation.

- The optimisation of the mould/inductor bow and of the casting conditions diminishing butt sawing and cracking initiation during the starting phase and ingot scalping could save development time and cost by avoiding the empirical method of mould design. The use of straight line segments seems over simplistic for this aim. In the light of the computations, it has been made clear that the three dimensional extension of the liquid pool in the steady state regime of casting has a great influence on the inward rolling faces pull-in. The optimisation of the design of a mould capable of producing nearly flat rolling sheet ingots demands three-dimensional calculations which adequately take into account the shape of the sump, the edge reinforcement and the viscoplastic behaviour of the alloy; it is limited at present only by the computing power of the workstations. Nevertheless, a promising inverse method is proposed and will be extended to other geometries within the context of the forthcoming Brite-Euram EMPACT project.

## REFERENCES

- [Abaq] Abaqus theory manual, K. Hibbit and J. Sorensen, Hibbit, Karlson and Sorensen, Inc., Providence, 1995.
- [Ack] Ackermann P. and W. Kurz in *Materials science and engineering*, 75, 1975, p. 79.
- [Alu] *Aluisuisse Casthouse Seminar*, 1994. Aluisuisse-Lonza Services Ltd., Chippis, Switzerland.
- [Ampu] Ampuero J., A. F. A. Hoadley and M. Rappaz in *Modeling of Casting, Welding and Advanced Solidification Processes 5*, edited by M. Rappaz, M. R. Ozgu and K. W. Mahin, TMS, 1991, p.449.
- [Ana] Anand L. in *J. of Eng. and Tech.*, 104 (1982), p.12.
- [And] Andrade E. N. in *Proc. Roy. Soc. London*, 90A (1914), p.329.
- [Arnb] Arnberg L., G. Ghai and L. Backerud in *Materials Science and Engineering*, A173, 1993, p.101.
- [Bäck] Backerud, Krol and Tamminen: *Solidification Characteristics of Aluminium Alloys*, volume 1: Wrought Alloys, Universitet-forlaget AS, 1986.
- [Bak] Bakken J. A. and Bergström T. in *Light Metals*, TMS, 1986, pp. 883-896.
- [Barr] Barrett C. R., Muehleisen E. C. and Nix W. D. in *Mat. Sci. and Eng.*, 10 (1972), p. 33.
- [Batt] Battle T. P. in *Inter. Mat. Rev.*, 37-6 (1992), p. 249.
- [Bellet] Bellet M., Chenot J. L., Fourment L., Massoni E. and Montmitonnet P.: *Séminaire de Plasticité, éléments finis et mise en forme de métaux*, Sophia-Antipolis, Ecole des Mines de Paris, Cemef, 1994.
- [Bod] Bodner S. R. and Partom Y. in *J. of Appl. Mech.*, June 1975, p. 385.
- [Bohn] Bohner Marc: *Simulation de la microségrégation du silicium dans la solidification équiaxe de la fonte grise*, Semester work, EPFL, LMPH, 1988.
- [Brans] Branswyck O., J. Collot, P. Vicente-Hernandez, A.-M. Chaze and C. Levailant in *Euromat 1991*, Ed. J. W. Clyne (Inst. Metals, London 1992), p. 124-130.
- [Bro1] Brody H. D. and Flemings M. C. in *Trans. AIME*, 236 (1966), p.615.
- [Bro2] Brody H. D., P. Wisniewski, A. Gokhale and J. Mathew in *Modeling of Casting, Welding and Advanced Solidification Processes 4*, edited by A.F. Giamei and G.J. Abbaschian, TMS, 1988, p.351.
- [Brow] Brown S. B., Kim K. H. and L. Anand in *Inter. J. of Plast.*, 5 (1989), p.95.
- [Camp] John Campbell: *Castings*, Butterworth-Heinemann, 1991.
- [Carrupt] Carrupt B. and C. Moulin in *8<sup>th</sup> International Sheet and Plate Conference*, Louisville, Kentucky, 5-8 Oct. 1993.
- [Clax] Claxton R. J. in *Journal of metals*, Feb. 1975, p.14.
- [Cly] Clyne T.W. and Kurz W. in *Met. Trans.*, 12A (1981), p.615.

- [Comb] Combeau H., Drezet J.-M, Mo. A. and Rappaz M., Modelling of microsegregation in macrosegregation computations, accepted for publication in *Met. Trans.*, 1996.
- [Crank] Crank J. in *Quarterly Journal of Mechanics and Applied Mathematics*, 10, 1957, p.220.
- [Cutt] T. Cuttard, *Caractérisation ultrasonore à haute température et sous contrainte de traction de composites céramique-céramique*, PhD thesis, Université de Limoges, 1993.
- [Dahle] A. K. Dahle and L. Arnberg in *Journal of Metals*, March 1996, p. 34.
- [Dean] Dean N. F., Mortensen A. and M. C. Flemings in *Met. Trans*, 25A (1994), p. 2295.
- [Decul] Decultieux F., P. Vicente, C. Levaillant in *Modeling of Casting, Welding and Advanced Solidification Processes VI*, edited by T.S. Piwonka, V. Voller and L. Katgerman, TMS, 1993, p.617.
- [Diet] Dieter G. E.: *Mechanical metallurgy*, McGraw-Hill book, London, 1988.
- [Dour] Dour G., Durand F. and Brechet Y in *Modeling of Casting, Welding and Advanced Solidification Processes VII*, edited by M. Cross and J. Campbell, TMS, 1995, p.295.
- [Drez1] J.-M. Drezet, M. Rappaz, B. Carrupt and M. Plata in *Met. Trans.*, vol 26B, 1995, p. 821-829.
- [Drez2] J.-M. Drezet and G. Eggeler in *Scripta Met. et Mater.*, vol. 31, Sept. 1994, p. 757.
- [Drez3] J.-M. Drezet and M. Rappaz in *Proceedings of the Fourth European Conference on Residual Stresses*, Cluny, June 96, France.
- [Droste] Droste W. and W. Schneider in *Light Metals*, 1991, p.945.
- [Emley] E.F. Emley in *International Metals Reviews*, June 1976, pp. 75-115.
- [Evans] J. W. Evans in *Journal of Metals*, 47-5, May 1995.
- [Fja1] Fjaer H.G. and A. Mo in *Met. Trans.*, vol. 21B, 1990, p. 1049.
- [Fja2] Fjaer H.G. and E. K. Jensen in *Light Metals*, 1995, p. 951.
- [Flem1] Flemings M. C.: *Solidification Processing*, McGraw-Hill, 1974.
- [Flem2] Flemings M. C. in *Met. trans.*, vol 22A, 1991, p.957.
- [Frost] Frost H. J. and M. F. Ashby: *Deformation-mechanism maps: the plasticity and creep of metals and ceramics*; Pergamon press 1982.
- [Gaba] J.P. Gabathuler : *Thermoanalyse*, Alusuisse internal technical report, June 1985.
- [Gan] Ganesan S. and Poirier D. R. in *J. of Crystal Growth*, 97 (1989), p.851.
- [Gar1] Garafalo F. in *Trans. Met. Soc. AIME* , 227 (1963) p. 351.
- [Gar2] Garafalo F. in *ASTM Spec. Tech. Publ.*, 283 (1960), p. 82.
- [Git] Gittus J. H. in *ASME J. Eng. Mater. Tech.*, vol. 98 (1976), p.52.
- [Giov] Giovanola B. and Kurz W. in *Met. Trans*, 21A (1990), p. 260.
- [Gril] Grill A. and K. Schwerdtfeger in *Ironmaking and steelmaking*, vol. 3, 1979, p. 131.
- [Grün1] G. U. Grün and W. Schneider in *Light Metals*, TMS, 1996.
- [Grün2] G. U. Grün, I. Eick and D. Vogelsang in *Light Metals*, TMS, 1994, p.863.

- [Gul] Gulliver G. H. in *J. inst. metals*, 9, 1913, p.120.
- [Hatch] *Aluminium: Properties and Physical Metallurgy*, ed. by John E. Hatch, ASM, Metals Park, Ohio, 1983.
- [Halder] Halder E., Roosz A., Exner H. E. and Fischmeister H. F. in *Materials Science Forum*, 13 (1987), p.547.
- [Hann] Hannart B., F. Cialti, R. V. Schalkwijk in *Light Metals*, 1994, p. 879.
- [Harp] Harper J. and Dorn J. E. in *Acta Met.*, 5 (1957), p. 654.
- [Hein] Heinlein M., S. Mukherjee and O. Richmond in *Acta Mechanica*, vol. 59, 1986, p. 59.
- [Her] Herring C. in *J. Appl. Phys.*, 21 (1950), p. 437.
- [Ho] Ho K. and R. Pehlke in *Met. Trans*, vol. 16B, 1985, p.585.
- [Hosf] Hosford W. F. and M. Caddell: *Metals forming mechanics and metallurgy*, Prentice-Hall, 1983.
- [Hu] Yu H. in *Light metals*, 1980, p.613.
- [Incro] F. P. Incropera and D. P. de Witt, *Fundamentals of heat and mass Transfer*, J. Wiley & Sons, New York, 1985.
- [Ivan] Ivantsov G. P. in *Doklady Akademii Nauk SSSR*, 58 (1947), p. 567.
- [Jan] Janin B. in *E-MRS meeting*, Strasbourg, 1986, p. 305.
- [Jen] Jensen E. K. and W. Schneider in *Light Metals*, 1990, p. 937.
- [Jon] Jonas J., Sellers C.M. and Tegart W. J. in *Met. Rev.*,14 (1969), p.1.
- [Kat] Katgerman L. and S.C. Flood in *Production, Refining, Fabrication and Recycling of Light Metals*, edited by M. Bouchard and P. Tremblay, vol. 19, 1990, p.97.
- [Kir] Kirkwood D. H.: *Microsegregation in Mat. Sci. and Eng.*, 65 (1984), p.101.
- [Kob] Kobayashi S. in *Trans. of the Iron and Steel Inst. of Japan*, 26 (1985).
- [Koz] Kozlowski P. F., Thomas B. G., J. A. Azzi and H. Wang in *Met. Trans.*, 23 A, p.903, 1992.
- [Kräh] Krähenbühl Y., R. Von Kaenel, B. Carrupt, J.C. Weber in *Light Metals*, 1990, p. 893.
- [Kris] Kristiansson J. O. in *J. of Thermal Stresses*, vol. 5, 1982, p.315.
- [Kurz] Kurz W. and Fisher D. J.: *Fundamentals of solidification*, Trans. Tech., 1989.
- [Lac] Lacaze J. in *Post-graduate Course in Solidification*, Calcom, (1993), chapter 3.
- [Lall] Lalli L. A. and De Ardo A. J. in *Met. Trans.*, 21A (1990), p. 3101.
- [Lan1] Langsrud Y. in *Key Engineering Materials*, 44 (1990), p. 95.
- [Lan2] Langsrud Y., Dons A. L., Jensen E. K. and Brusethaug S. in the 3rd *Inter. Conf. on Al. Alloys*, vol. I, Trondheim, Norway.
- [Land] Landau H. G. in *Quarterly of Applied Mathematics*, 8, 1955, p.81.
- [Lang] *Hot deformation of aluminium alloys*, ed. by Langdon, Merchant, Morris and Zaidi, TMS, 1990.
- [Law] Lawrence R. R. in *TMS, AIME*, 1976, p.457.
- [Lynn] Lynnworth L. C. in *J. of testing and evaluation*, vol 1(2), 1973, p.119.

- [Mag] Magnin B., L. Katgerman and B. Hannart in Modeling of Casting, Welding and Advanced Solidification Processes VII , edited by M. Cross and J. Campbell, TMS, 1995, p. 303.
- [Magn] P. Magnin: PhD thesis no. 560, EPFL, Lausanne (1985).
- [Månson] J.-A. Månson and J. C. Seferis, in Journal of Composite Materials, vol. 26, No. 3, 1992.
- [Mar] Mariaux S., M. Rappaz, Y. Krähenbühl, M. Plata in Light Metals, TMS, 1992, p. 175.
- [Matsu] Matsumiya T., Kajioka H., Mizoguchi S., Ueshima Y. and Esaka H. in Trans. ISIJ 24 (1984), p. 873.
- [Matu] K.H. Matucha: *Materials Science and Technology*, edited by R.W. Cahn, P. Haasen and E. J. Kramer, vol. 8: Structure and Properties of non-ferrous Alloys, VCH, 1996.
- [Math] Mathew J. and H.D. Brody in Nuclear Metallurgy, vol. 20(2), 1976, p. 978.
- [Meta] Metals Handbook, vol. 8: *Metallography*, Structures and Phase Diagrams, ASM, Metals Park, 1973.
- [Mill] *Unified constitutive equations*, ed. by A. K. Miller, Elsevier applied science, 1987.
- [Moha] Mohanty P. S., Samuel F. H., Gruzleski J. E. and Kosto T. J. in Light Metals, TMS, 1994, p. 1039.
- [Mo1] Mo A., T. E. Johnsen, B. R. Henriksen, E. K. Jensen and O. R. Myhr in Light Metals, ed. by U. Mannweiler, TMS, 1994.
- [Mo2] Mo A. and E.J. Holm in J. Thermal Stresses, vol. 14, 1991, p. 571.
- [Mond] Mondolfo L.F.: *Aluminum alloys: structure and properties*, Boston: Butterworths, 1976.
- [Mori] Moriceau J. in Light Metals, 1975, p. 119.
- [Moto] Motomura M., S. Shimamura and T. Nishimura in Journal of Japanese Institute of Light Metals, 1976, p.432.
- [Nab] Nabaro F. R. N. in Phys. Soc., London (1948), p. 75.
- [Ned] *Thermal stresses and Hot tearing during the DC casting of AlMgSi billets*, PhD thesis, Sintef, Oslo, 1991.
- [Nish] Nishida Y., W. Droste, S. Engler in Met. Trans, vol. 17B, 1986, p.833.
- [Nguy] Nguyen T. G., D. Favier and M. Suéry in Int. J. of Plasticity, vol. 10, No 6, 1994.
- [Oro] Orowan E. in Proc. Phys. Soc., 52 (1940) p.8.
- [Papa] Papadakis E. P., Fowler K.A. and Lynnworth L. C. in J. of Applied Physics, vol. 45(6), 1974, p.2409.
- [Pehl] Pehlke R. D., Jeyrajan A. and Wada H.: *Summary of thermophysical properties for casting alloys and mold materials*, Univ. Michigan report (1982).
- [Peria] P. Peria, Aluminium is hundred, in Matériaux et techniques, p.149, May 1986.
- [Petzow] Petzow G. and Effenberg G.: *Ternary Alloys*, vol. 5, p. 394.
- [Pola] Polakovic A., L. Taborsky and H. Hydross in Kovove Materialy, 1, XII, Bratislava, 1974.
- [Rap1] Rappaz M. and Thévoz P. in Acta Met., 35-12 (1987), p. 2929.



- [Rap2] Rappaz M., J.L. Desbiolles, J.-M. Drezet, Ch.-A. Gandin, A. Jacot and P. Thevoz in *Modeling of Casting, Welding and Advanced Solidification Processes*, TMS, 1995, p. 449.
- [Rap3] Rappaz M, Charbon Ch. and Sasikumar R. in *Acta Met. et Mater.*, 42(7),1994, 2365.
- [Rap4] Rappaz M. in *Proceedings of the Fifth International Conference on Aluminium Alloys*, Grenoble, July 96, France.
- [Ret] Rettenmayr M. in *Mat. Rev. Soc. Symp. Proc.*, 278 (1992), p. 325.
- [Rich1] Richmond O. in *Modeling of Casting, Welding and Advanced Solidification Processes*, edited by H.D. Brody and D. Apelian, TMS, 1981, p.215.
- [Rich2] Richmond O. and R.H. Tien in *J. Mech. Phys. Solids*, 1971, vol. 19, p. 273.
- [Roosz] Roosz A. and Exner H. E. in *Acta Met. et Mater.*, 38-10 (1990), p. 2003.
- [Ross] Rosset A.: *Constitutive viscoplastic equations and their use for the prediction of residual stresses and strains in solidification processes*, Cost 504, round III, project CH2, final report, November 1955.
- [Sam1] Sample V. M. and L.A. Lalli in *Mat. Sci. Tech.*,vol. 3, 1987, p. 28.
- [Sam2] Sample V. M., Lalli L. A. and Richmond O. in the 3rd Inter. Conf. on Al. Alloys, Trondheim, Norway.
- [Scheil] Scheil E. in *Zeitschrift für Metalkunde*, 34 (1942), p.70.
- [Secon] Secondé J. F. and M. Suéry in *J. of Mat. Science*, vol.19, 1984, p. 3995.
- [Sell1] Sellars C. M. in the 3rd Inter. Conf. on Al. Alloys, vol. II, p.89, Trondheim, Norway.
- [Sell2] Sellars C. M. and W. J. Teggart in *Mémoires scientifiques rev. mét.*, LXIII, 9, 1966.
- [Shep] Sheppard T. and D. S. Wright in *Metals technology*, June 1979, p.215.
- [Smel] Smelser R. E. and O. Richmond in *Modeling of Casting, Welding and Advanced Solidification Processes 4*, edited by A.F. Giamei and G.J. Abbaschian, TMS, 1988, p.313.
- [Smit] *Smithells Metals Reference Book*, sixth edition, edited by E. A. Brandes, 1983.
- [Spea] Spear R. E. and H. Yu in *Aluminum*, 1984, p.440.
- [Straub] S. Straub and W. Blum in *Scripta Met. et Mater.*,24 (1990), p.1837.
- [The] Thermo-calc, a Databank for Calculation of Phase Equilibria and Phase Diagrams, Sundman B., Jansson B. and Andersson J. O., Division of Physical Metallurgy, Royal Institute of Technology, Stockholm, Sweden.
- [Thé1] Thévoz P. and Rappaz M. in *E-MRS Strasbourg* (1986), p. 247.
- [Thé2] Thévoz P., Desbiolles J. L. and Rappaz M. in *Met. Trans*, 20A (1989), p. 311.
- [Thé3] Thévoz P., Rappaz M. and Desbiolles J. L. in *Light Metals*, TMS, 1990, p. 975.

- [Thé4] Thévoz P. and Rappaz M. in Modeling of Casting, Welding and Advanced Solidification Processes V, ed. by Rappaz, Ozgu and Mahin, TMS, 1991, p. 387.
- [Thom1] Thomas B. G. in Modeling of Casting, Welding and Advanced Solidification Processes 6, edited by T.S. Piwonka, V. Voller and L. Katgerman, TMS, 1993, p.519.
- [Thom2] Thomas B. G., I.V. Samarasekera and J.K. Brimacombe in Met. Trans., vol. 18B, 1987, p.119.
- [Tim] Timoshenko S.P. and Goodier J.N.: *Theory of elasticity*, McGraw-Hill, Kogakusha Ltd, third edition.
- [Tro] Tromborg E., Dons A. L., Orsund R., Jensen E. K. and Arnberg L. in Modeling of Casting, Welding and Advanced Solidification Processes VI, ed. by Piwonka, Voller and Katgerman, TMS, 1993, p. 103.
- [Vicen] Vicente P.: *Vers une approche thermomécanique du procédé de fonderie: caractérisation rhéologique et microstructurale d'alliages métalliques a l' état semi-solide*, PhD thesis, 1994, Ecole Nationale Supérieure des Mines de Paris.
- [Voce] Voce E. in J. Inst. Metals, 74 (1948), p.537.
- [Wea1] Weaver C.H. in TMS, AIME, 1976, p. 441.
- [Wea2] Weaver C.H. in Light Metals, 1991, p. 953.
- [Weck] Weckman D. C. and P. Niessen in Canadian Metallurgical Quarterly, vol.23, 1984, p. 209.
- [Weer] Weertman J. in Trans. AIME, vol. 227 (1963) , p. 1475.
- [Wein] Weiner J. H. and Boley B. A. in J. Meac. Phys. Solids, vol. 11 (1963), p.145.
- [Well] Wells M. R., Bolingbroke R., Samarasekera I. V., Hawbolt E. B. and Brimacombe J. K. in Light Metals Processing and Applications, proceedings (1993), p.483.
- [Wire] Wire G. L., Ellis F. V. and Che-Yu Li in Acta Met., vol. 24, p.677, 1976.
- [Wiskel] J.B. Wiskel and S.L. Cockcroft in Met. Trans., vol. 27B, pp. 119-137.
- [Wisn] Wisniewski P. and H. D. Brody in Modeling of Casting, Welding and Advanced Solidification Processes V, edited by M. Rappaz, M. R. Ozgu and K. W. Mahin, TMS, 1991, p. 273.
- [Wong] Wong W. A. and J. J. Jonas in Trans. of the Met. Soc. of AIME, vol. 242, Nov. 1968, p.2271.
- [Yu] Yu H. in Light metals, 1980, p.613.
- [Zab] Zabaras N. and V.R. Voller in Modeling of Casting, Welding and Advanced Solidification Processes 4, edited by A.F. Giamei and G.J. Abbaschian, TMS, 1988, p.683
- [Zen] Zener C. and Holloman H. H. in J. of Appl. Phys., 15 (1944), p.22.

## APPENDIX I : LANDAU TRANSFORMATION FOR THE SOLUTE DIFFUSION

The diffusion equation which has to be solved in the solid phase and for a given solute element  $i$  (the indice  $i$  is omitted in the following) is :

$$D^s \left[ \frac{\partial^2 w}{\partial r^2} + \frac{\text{igeo} - 1}{r} \frac{\partial w}{\partial r} \right] = \frac{\partial w}{\partial t} \quad (\text{I-1})$$

The variable domain  $r \in [0, r^*(t)]$  is transformed into a fixed domain  $\varepsilon \in [0, 1]$  using the following relation :

$$\varepsilon = \frac{r}{r^*(t)} \quad (\text{I-2})$$

The concentration field,  $w(r, t)$ , is transformed into  $w(r(\varepsilon, t), t)$  and the new partial derivatives can be written as :

$$\left[ \frac{\partial w}{\partial r} \right]_t = \left[ \frac{\partial w}{\partial \varepsilon} \right]_t \cdot \left[ \frac{\partial \varepsilon}{\partial r} \right]_t = \frac{1}{r^*(t)} \cdot \left[ \frac{\partial w}{\partial \varepsilon} \right]_t \quad (\text{I-3a})$$

By derivating equation I-3a, one obtains:

$$\left[ \frac{\partial^2 w}{\partial r^2} \right]_t = \frac{1}{r^*(t)^2} \cdot \left[ \frac{\partial^2 w}{\partial \varepsilon^2} \right]_t \quad (\text{I-3b})$$

The time derivative is found as follows:

$$\begin{aligned} \left[ \frac{\partial w}{\partial t} \right]_\varepsilon &= \left[ \frac{\partial w}{\partial t} \right]_r + \left[ \frac{\partial w}{\partial r} \right]_t \cdot \left[ \frac{\partial r}{\partial t} \right]_\varepsilon = \\ &= \left[ \frac{\partial w}{\partial t} \right]_r + \frac{\varepsilon \cdot v}{r^*(t)} \cdot \left[ \frac{\partial w}{\partial \varepsilon} \right]_t \end{aligned} \quad (\text{I-3c})$$

where  $v$  is the velocity of the interface (i.e.,  $v = dr^*/dt$ ). It is to be noted that this procedure automatically introduces the normalized velocity of the node,  $v_\varepsilon$ , given by a linear interpolation :

$$v_\varepsilon = \left[ \frac{\partial \varepsilon}{\partial t} \right]_r = - \frac{r}{[r^*(t)]^2} \cdot \frac{dr^*}{dt} = - \frac{\varepsilon}{r^*(t)} \cdot v \quad (\text{I-4})$$

Combining Eqs. I-1 to I-3 finally gives for the solid phase :

$$D^s \cdot \frac{1}{[r^*]^2} \cdot \frac{\partial^2 w}{\partial \varepsilon^2} - \frac{\partial w}{\partial t} + \frac{\partial w}{\partial \varepsilon} \cdot \left[ \frac{\varepsilon v}{r^*} + \frac{D^s (\text{igeo} - 1)}{\varepsilon r^{*2}} \right] = 0 \quad (\text{I-5})$$

In the liquid phase and for each solute element  $i$ , the variable domain  $r \in [r^*(t), r_0]$  is transformed similarly into a fixed domain  $\eta \in [0,1]$  using the following relation :

$$\eta = \frac{r - r^*(t)}{r_0 - r^*(t)} \quad (\text{I-6})$$

Using the same procedure as above, the concentration field,  $w(r,t)$ , is transformed into  $w(r(\eta,t),t)$  thus giving:

$$D^l \cdot \frac{1}{[r_0 - r^*(t)]^2} \cdot \frac{\partial^2 w}{\partial \eta^2} - \frac{\partial w}{\partial t} + \frac{\partial w}{\partial \eta} \cdot \left[ \frac{1}{r_0 - r^*(t)} \cdot \frac{D^l (\text{igeo} - 1)}{r^*(t) + \eta (r_0 - r^*(t))} + v \cdot \frac{1 - \eta}{r_0 - r^*(t)} \right] = 0 \quad (\text{I-7})$$

For each solute element  $i$ , equations (I-5) and (I-7) are solved together using FDM, a fully implicit scheme and no upwinding owing to the fact that the advection term is small compared to diffusion. A regular mesh of  $N_s$  nodes in the solid and  $N_l$  nodes in the liquid is used. The boundary conditions that is applied at  $\varepsilon = 0$  is that of a closed system :

$$\frac{\partial w}{\partial \varepsilon} = 0 \quad \text{for} \quad \varepsilon = 0 \quad (\text{I-8})$$

The conditions at the interface, local thermodynamic equilibrium and solute flux conservation (see equations 3.4 and 3.8) are introduced in the FDM equation system using a first order approximation of the solute interfacial gradients. The boundary conditions that is applied at the external boundary of the domain (equation 3.10) transforms into :

$$\frac{\partial w}{\partial \eta} = (r_0 - r^*(t)) \frac{\partial w}{\partial r} = \frac{r_0 (r_0 - r^*(t))}{D^l \text{igeo}} \cdot \frac{d\bar{w}}{dt} \quad \text{for} \quad \eta = 1 \quad (\text{I-9})$$

This condition resumes to that of a closed system when  $\bar{w}$  is constant in the volume element. Knowing the solid-liquid interface velocity,  $v$ , and for a given period of time,  $dt$ , the resulting equations system is solved using the TDMA (Tri-Diagonal Matrix Algorithm) routine: the new concentration profiles,  $w_s(\varepsilon)$  and  $w_l(\eta)$ , are then calculated for each solute element.

## APPENDIX II : THERMAL LINEAR CONTRACTION COEFFICIENT

The aim of this appendix is to show how the mean coefficient of thermal linear contraction has been derived for the computations with Abaqus. It is assumed that the alloy contracts during solidification as soon as it reaches its coherency temperature,  $T_c$ .

The differential thermal linear dilatation coefficient,  $\alpha_d(T)$ , as found in [Hatch] has been fitted by a third degree polynomial (see figure II.1):

$$\alpha_d(T) = A + BT + CT^2 + DT^3 \quad (\text{II-1})$$

The change in length  $l$  with respect to the length  $l_0$  at the reference temperature ( $T_0 = 0^\circ\text{C}$ ) is therefore given by the thermal dilatation :

$$\varepsilon_d = \frac{\Delta l}{l_0} = \int_{T_0}^T \alpha_d(\theta) d\theta = AT + \frac{BT^2}{2} + \frac{CT^3}{3} + \frac{DT^4}{4} \quad (\text{II-2})$$

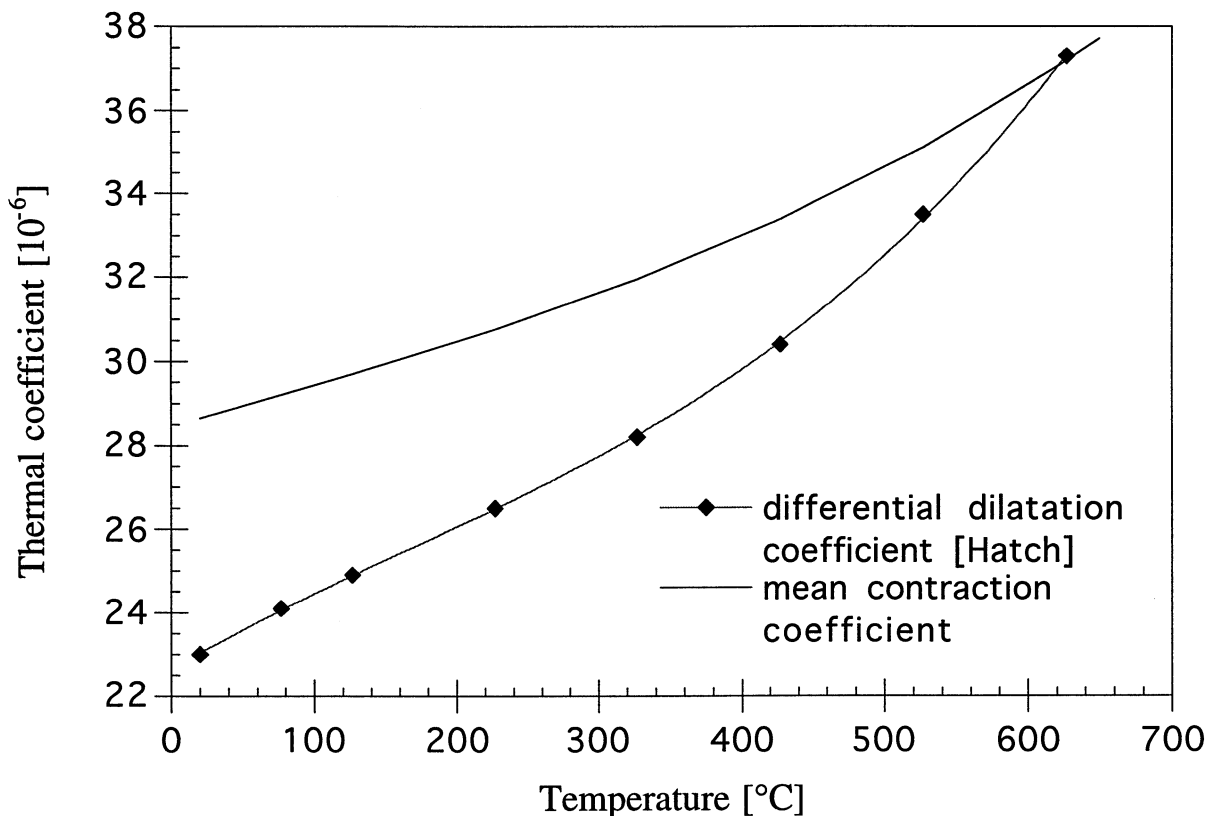


Figure II.1: differential dilatation coefficient from [Hatch] and mean contraction coefficient as used in the computations with Abaqus ( $T_c = 650^\circ\text{C}$ ).

With the help of figure II.2, one can derive now the thermal contraction using as a reference temperature  $T_c$  :

$$\varepsilon_c = \frac{\Delta l'}{l_0'} = \frac{\Delta l - \Delta L}{l_0'} = \frac{\varepsilon_d \cdot l_0 - \varepsilon_d(T_c) \cdot l_0}{l_0 + \varepsilon_d(T_c) \cdot l_0} = \frac{\varepsilon_d - \varepsilon_d(T_c)}{1 + \varepsilon_d(T_c)} \quad (\text{II-3})$$

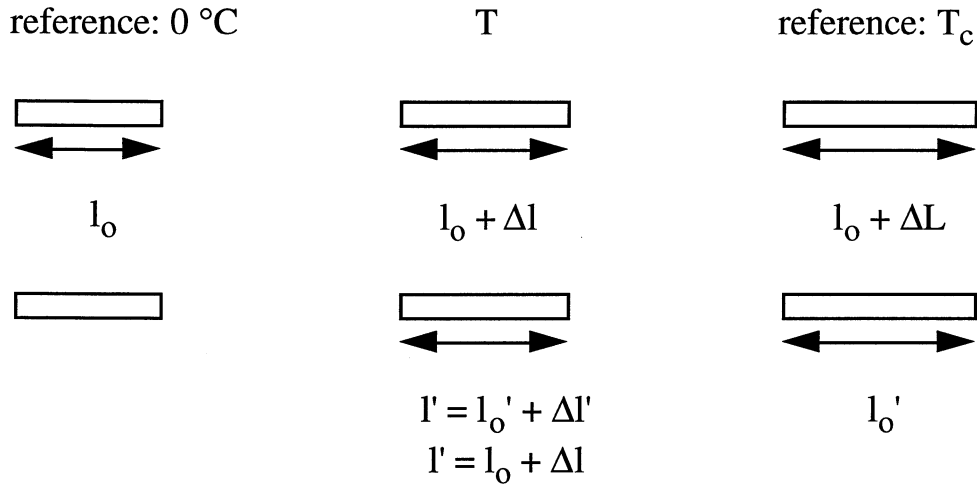


Figure II.2: derivation of the thermal contraction from the reference temperature  $T_c$ .

To compute the thermal deformation, Abaqus uses the mean thermal contraction coefficient,  $\alpha_c^m$ , defined with the reference temperature  $T_c$  :

$$\alpha_c^m = \frac{\varepsilon_c}{T - T_c} = \frac{1}{1 + \varepsilon_d(T_c)} \cdot \frac{\varepsilon_d - \varepsilon_d(T_c)}{T - T_c} \quad (\text{II-4})$$

Using the fact that  $T_c$  is a root of the polynomial  $\varepsilon_d - \varepsilon_d(T_c)$ ,  $\alpha_c^m$  is written as:

$$\alpha_c^m = \frac{1}{1 + \varepsilon_d(T_c)} \cdot [A' + B'T + C'T^2 + D'T^3] \quad \text{with:}$$

$$A' = A + \frac{BT_c}{2} + \frac{CT_c^2}{3} + \frac{DT_c^3}{4}, \quad B' = \frac{B}{2} + \frac{CT_c}{3} + \frac{DT_c^2}{4}, \quad C' = \frac{C}{3} + \frac{DT_c}{4}$$

$$\text{and } D' = \frac{D}{4} \quad (\text{II-5}).$$

$\alpha_c^m$  is represented as a function of the temperature in figure II.1, using  $T_c = 650^\circ\text{C}$ . Note that for temperatures higher than  $T_c$ ,  $\alpha_c^m$  is set to zero in the 2D and 3D thermomechanical models.

### APPENDIX III : HIGH APPARENT CREEP ACTIVATION ENERGIES IN MUSHY ZONE MICROSTRUCTURES

In this appendix, a simple model is proposed to explain the increase in the apparent creep activation energy, as measured by creep and indentation tests in aluminium alloys in the mushy state, i.e. at temperatures greater than the solidus temperature. Further details can be found in [Drez2]. Creep data are generally presented using the well established equation for the minimum creep rate:

$$\dot{\epsilon}_{\min} = A \cdot \exp\left(\frac{-Q}{RT}\right) \cdot \sigma^n \quad (\text{III.1}),$$

where  $A$  is a constant,  $\dot{\epsilon}_{\min}$  is the minimum creep rate,  $Q$  represents the apparent creep activation energy and  $R$  and  $T$  are universal gas constant and temperature, respectively. Figure III.1 shows the strain recorded during the creep test of the alloy 1201 under 1 MPa and at 640°C, i.e. 8°C above the solidus temperature of the alloy (632°C). The calculation of the strain rate allows the determination of  $\dot{\epsilon}_{\min}$ ,  $5 \cdot 10^{-6} \text{ s}^{-1}$  in the present case.

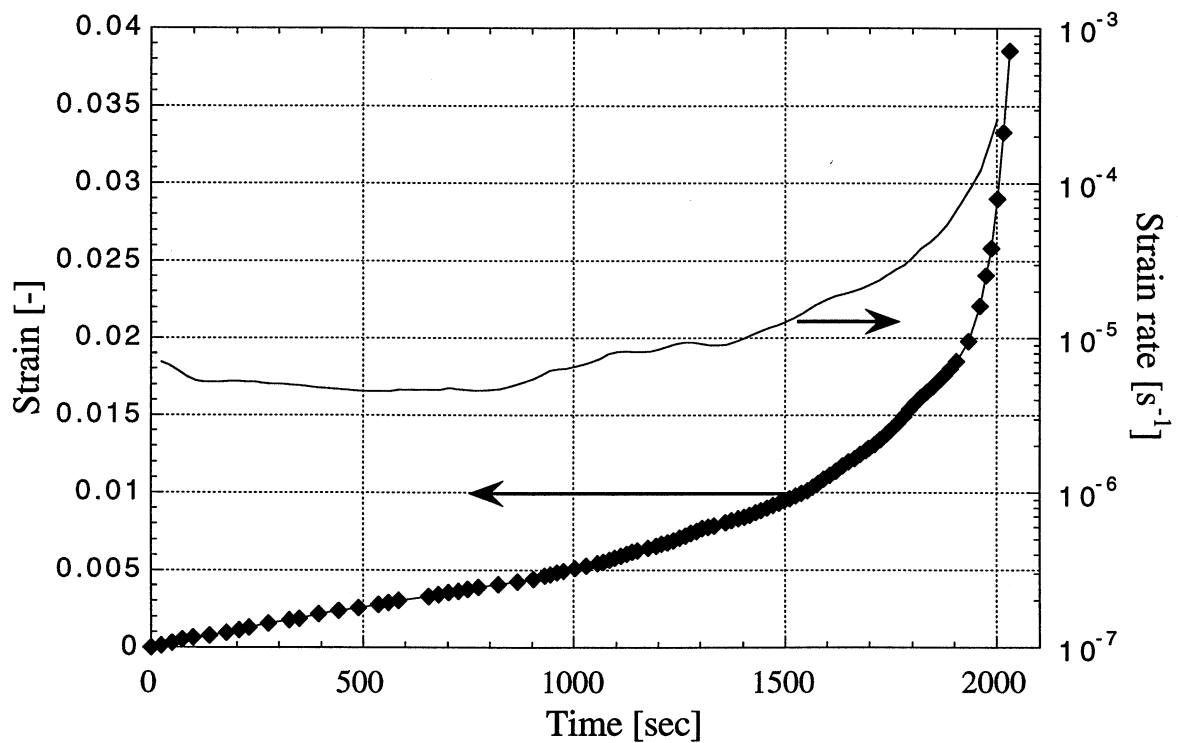


Figure III.1: creep strain and strain rate as a function of time for alloy 1201 (640°C, 1 MPa).

On the other hand, concerning the indentation tests, the viscoplastic behaviour of the mush was assumed to be described by the Norton-Hoff law (see section 5.1.2):

$$\dot{\epsilon} = k(T) \cdot \sigma^n \quad (\text{III.2}),$$

where the consistency  $k(T)$  was measured at different temperatures. One can also assume that  $k(T)$  follows an Arrhenius-type law:

$$k(T) = k_0 \cdot \exp\left(\frac{-Q}{RT}\right) \quad (\text{III.3}).$$

To determine the value of  $Q$  present in equations III.1 and III.3, the measured strain rates are represented as a function of  $1/T$  on a logarithmic scale at a given stress,  $\sigma$ , the slope of this curve being therefore the apparent creep activation energy. This procedure is shown in figure III.2 using creep and indentation measurements at 0.5 MPa.

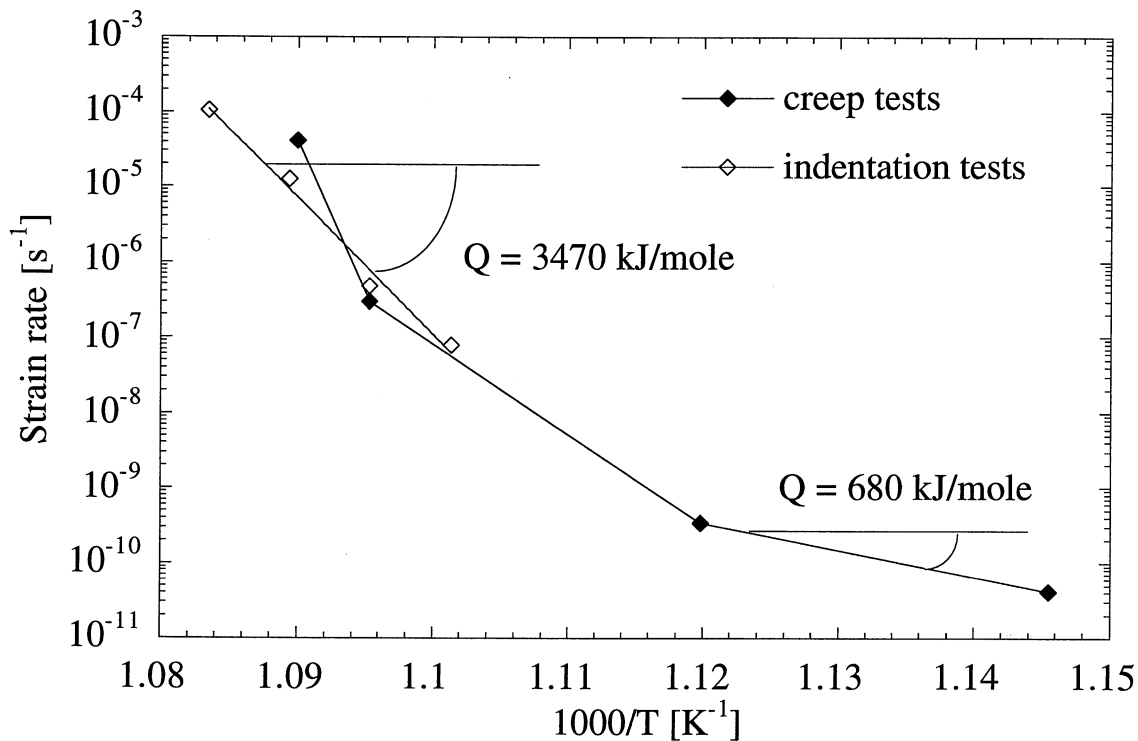


Figure III.2: estimation of the creep apparent energy using creep and indentation measurements, at a given stress of 0.5 MPa.

The indentation strain rates are well aligned and provide a value of  $Q$  of 3470 kJ/mole. On the other hand, the apparent activation energy determined using creep data, increases with increasing temperature from 686 kJ/mole at temperatures lower than 620°C to about the value determined by indentation tests. Nevertheless, Straub and Blum [Straub] did not observe such high values of apparent creep activation energies in single phase high purity aluminium tested in the same temperature range. On the other hand, using indentation tests, Vicente [Vicen] measured an apparent activation energy of 721 kJ/mole for a Zn-Sn8wt% alloy. This value is very high compared to the value at low



temperatures, 60 kJ/mole. Eventually, Barrett et al. [Barr] measured a value of 640 kJ/mole for an Al-Fe0.5wt% at 630°C. These values are much higher than activation energy values (142 kJ/mole for aluminium) which can be rationalised on the basis of diffusion assisted climb processes which control creep of pure metals and single phase alloys [Frost].

Figure III.3 shows the microstructure of the alloy 1201 after creep testing at 640°C and water-quenching. The former liquid phase transforms into a fine eutectic microstructure which appears between the primary phase dendrites. Note that the globular-dendritic microstructure, which looks like “cauliflowers”, have coarsened during the heating and testing periods.

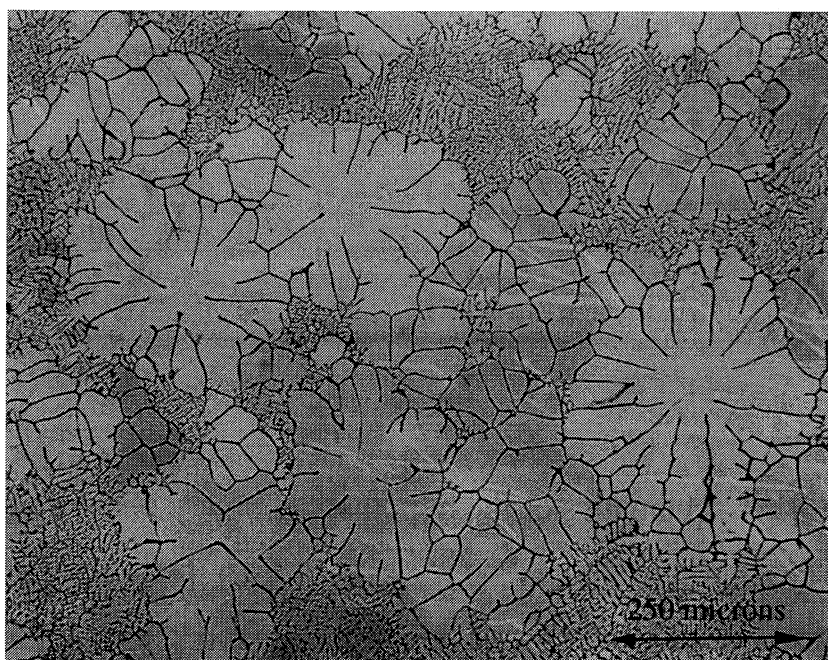


Figure III.3: two-phase microstructure of the 1201 alloy after quenching from 640°C.

#### *Rationalisation of high apparent creep activation energies*

In order to explain these high apparent creep activation energies, let us consider a simple binary eutectic system which is schematically shown in figure III.4. A constant partition coefficient,  $k=0.27$ , was chosen. In this phase diagram, we consider three values of concentration:  $c_a$  (2.4%) which is far from the eutectic concentration,  $c_c$  (11.5%) which is near the eutectic concentration and  $c_b$  (8.5%). These three concentrations will allow us to consider the influence of the alloy composition on creep behaviour with special emphasis placed on the role of the part of the microstructure which is eutectic.

Under typical casting conditions, the volume fraction of solid,  $f_s(T)$ , is better described by the Scheil's equation (equation 2.6) than by the lever rule.

The Scheil's model predicts some  $\alpha/\beta$ -eutectic formation even for alloy concentrations lower than the maximum solubility of B in A, i.e. 4wt% in the present case. When heating such an alloy above  $T_{eut}$  for testing (indentation or creep), the eutectic regions will melt first and some back-diffusion will bring the system closer to the lever rule.

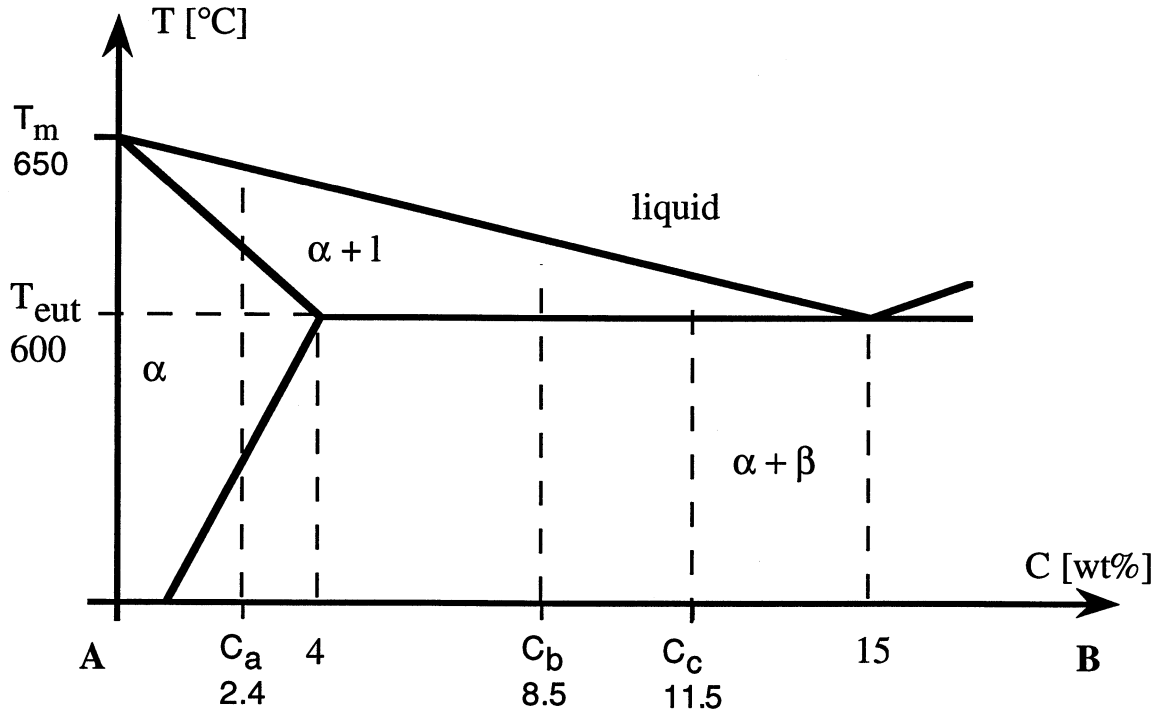


Figure III.4: schematics of the hypothetical binary phase diagram.

Let us now introduce a simple *solid-liquid model* of the mushy zone microstructure for low volume fractions of liquid. In this model, the liquid part of the mushy zone remains as isolated pockets and fully unloads the stresses which are transferred to the remaining solid. The load carrying cross section perpendicular to the direction of the applied stress is given by  $S_0 \cdot f_s(T)$ , where  $S_0$  is the cross section of the sample. The load carrying cross section decreases as the amount of liquid in the two phase region increases. It is now assumed that solid state creep does not depend on concentration, i.e. at temperatures below  $T_{eut}$ , the three alloy compositions,  $c_a$ ,  $c_b$  and  $c_c$ , show the same creep behaviour, represented by the following equation:

$$\dot{\epsilon} = A \cdot \exp\left(\frac{-Q}{RT}\right) \cdot \sigma^4 \quad (\text{III.4}),$$

with  $A = 2.3 \cdot 10^{33}$  and  $Q = 700000$  J/mole.  $\sigma$  is the stress in MPa,  $T$  the temperature in Kelvin and  $\dot{\epsilon}$  the strain rate in  $s^{-1}$ . During viscoplastic flow above the eutectic temperature, the mushy zone microstructure forms and the solid cross section decreases. The effective stress acting over the solid is given by:

$$\sigma = \frac{\sigma_0}{f_s(T)} \quad (\text{III.5}),$$

where  $\sigma_0$  is the applied stress which was chosen as 0.5 MPa in the calculations. Hence, the flow rate becomes:

$$\dot{\epsilon} = A \cdot \exp\left(\frac{-Q}{RT}\right) \cdot \left(\frac{\sigma_0}{f_s(T)}\right)^n \quad (\text{III.6}),$$

The apparent creep activation energy  $Q'$ , as determined above using creep and indentation tests measurements, is defined as:

$$Q' = -R \cdot \frac{d \ln \dot{\epsilon}}{d(1/T)} \quad (\text{III.7}),$$

Assuming that the exponent  $n$  is temperature-independent, this gives:

$$Q' = Q - nRT^2 \cdot \frac{d \ln(f_s)}{dT} \quad (\text{III.8}).$$

At temperatures lower than  $T_{eut}$ ,  $f_s = 1$  and  $Q' = Q$ . At temperatures greater than  $T_{eut}$ , the temperature derivative of  $f_s$  (equation 2.7) allows to calculate  $Q'$ . According to the Scheil's model, the temperature derivative of the  $f_s$ - $T$  relation presents a discontinuity at  $T_{eut}$  and therefore leads to a discontinuity in the apparent creep activation energy at the eutectic temperature. Figure III.5 shows the flow rates as calculated from equation III.6 for temperatures slightly higher than  $T_{eut}$ . It can be clearly seen that the apparent creep activation energy for the mushy zone microstructure can become much higher than the creep activation energy in the solid state. This apparent activation energy increases with temperature and its value is strongly dependent on the alloy composition. The alloy of composition  $c_a$  contains a small fraction of eutectic phase that melts at  $T_{eut}$ . Thus, the solid fraction is less than one at temperatures just above  $T_{eut}$  and the apparent creep energy is higher (782 kJ/mole in this case against 700 kJ/mole for the solid). For alloy compositions  $c_b$  and  $c_c$ , significantly higher apparent creep activation energies are obtained at temperatures just above  $T_{eut}$ ; this is simply due to the fact that parts of the alloys are now liquid and do not carry any load.

The results presented in figure III.5 clearly show that mechanical data for mushy zone microstructures with a low volume fraction of liquid phase cannot be obtained by simply extrapolating lower temperature solid state data. Based on a simple solid-liquid model of the mushy zone microstructure, unusually high values of apparent creep activation energies can be obtained. Activation energy

values depend on the phase diagram, the temperature, and the composition of the alloy. The results obtained using the simplified model outlined above are in good qualitative agreement with the experimental data, figure III.2.

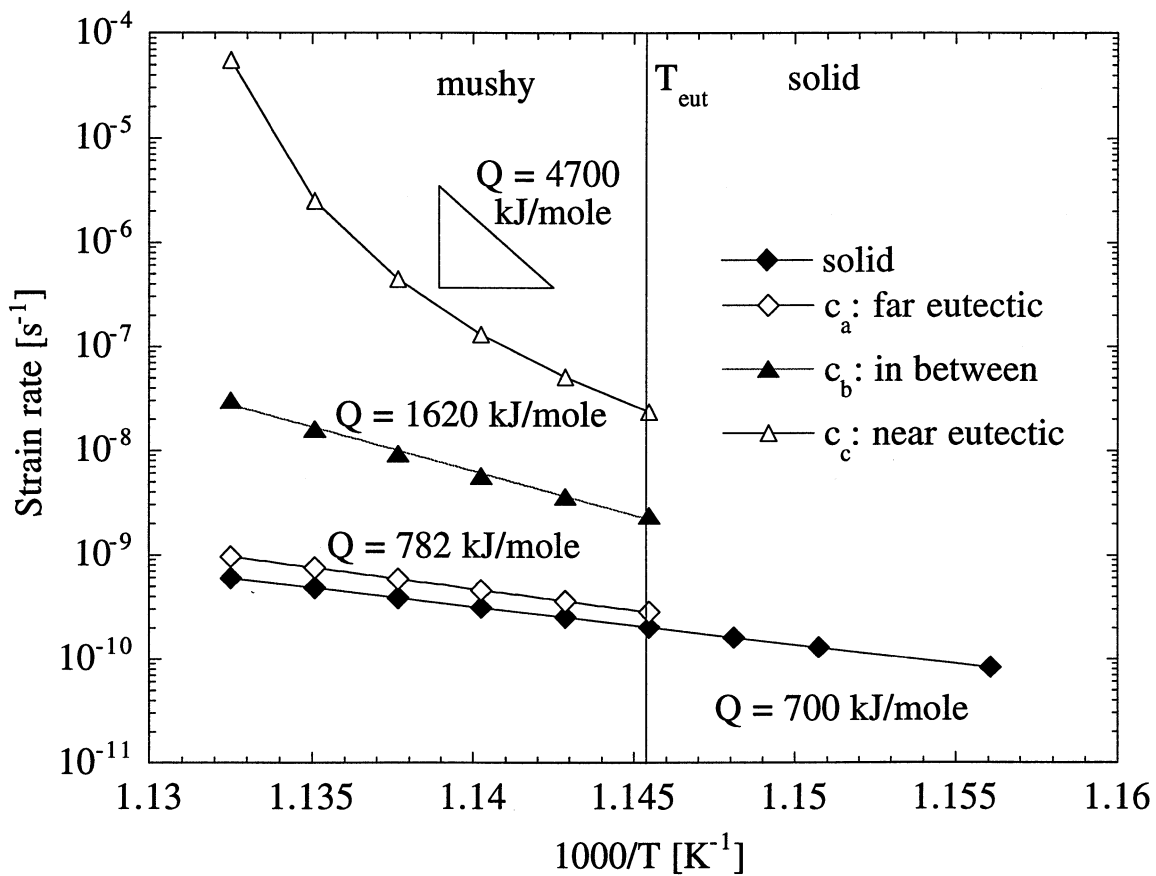


Figure III.5: temperature dependence of the strain rate as calculated for the three selected alloy compositions and for the solid.

The present simple model can help to explain the extremely high values of apparent creep activation energies in mushy zone microstructures. Reality is probably more complex. First, the stress exponent varies with temperature, especially near the melting temperatures. Second, it must be expected that, even before significant parts of the solid melt, the rate of grain boundary sliding will have increased greatly, possibly due to the formation of a liquid grain boundary phase. Enhanced creep rates in the solid-liquid region can be explained by the fact that the liquid may act as a lubricant allowing the grains of the materials to slide over each other more easily, or, that the liquid may provide a high diffusivity path, allowing diffusional transport away from load-bearing points or surfaces, very much as grain-boundary diffusion does during Coble creep [Frost].

## APPENDIX IV: SOLIDIFICATION/REMELTING IN A CLOSED OR OPEN SYSTEM

During the DC casting process, remelting occurs on the ingot surface when an air gap forms in between the metal and the mould, as shown in figure 5.5. In order to assess the accuracy of the microsegregation model to simulate remelting, the enthalpy variation displayed in figure IV.1 was considered for a closed system (constant concentration of 5 wt% for both solute elements of a ternary system). During the first 150 seconds, the alloy solidifies. It then remelts during the next 100 seconds before being re-solidified. The material parameters defining the ternary system considered here are the same as those given in table 4.1, except for those redefined in table IV.1.

	$D_s$ [m <sup>2</sup> /sec]	$D_l$ [m <sup>2</sup> /sec]	$m$ [-]	$k$ [-]	$c_0$ [wt]
element 1	$10^{-11}$	$9 \cdot 10^{-9}$	-60	0.25	0.05
element 2	$10^{-12}$	$9 \cdot 10^{-9}$	-60	0.1	0.05

Table IV.1: parameters defining the ternary system considered in the present computations.

The computed growth rate that is plotted in figure IV.1 (right scale) becomes negative when the enthalpy starts to increase after the first 150 s meaning that remelting occurs. The solidification path corresponding to the variation of enthalpy shown in figure IV.1 is displayed in figure IV.2 together with the Scheil and lever rule limits. The model predicts a loop during the remelting period. The temperature during the remelting becomes higher than the value predicted by the lever rule. Please note that the Scheil and lever rule limits do not show a loop owing to the fact that the solidification path in these two cases is totally reversible for a closed system [Comb]. The computed solute profiles are plotted in figure IV.3 at the beginning ( $t=150s$ ), at the middle ( $t=200s$ ) and at the end ( $t=240s$ ) of the remelting period. As already found for a binary system [Comb], the shape of the solid solute profile changes from a concave form at  $t=150s$  to a convex form near the interface during remelting ( $t=200$  and  $240s$ ). Moreover, the point of maximum solute concentration does no longer correspond to the interface position but is gradually displaced towards the centre of the remelting grain. This complex behaviour of the solute profile at the onset of remelting (or more generally at any change of the interface movement direction) is in accordance with the results published for a binary system [Comb].

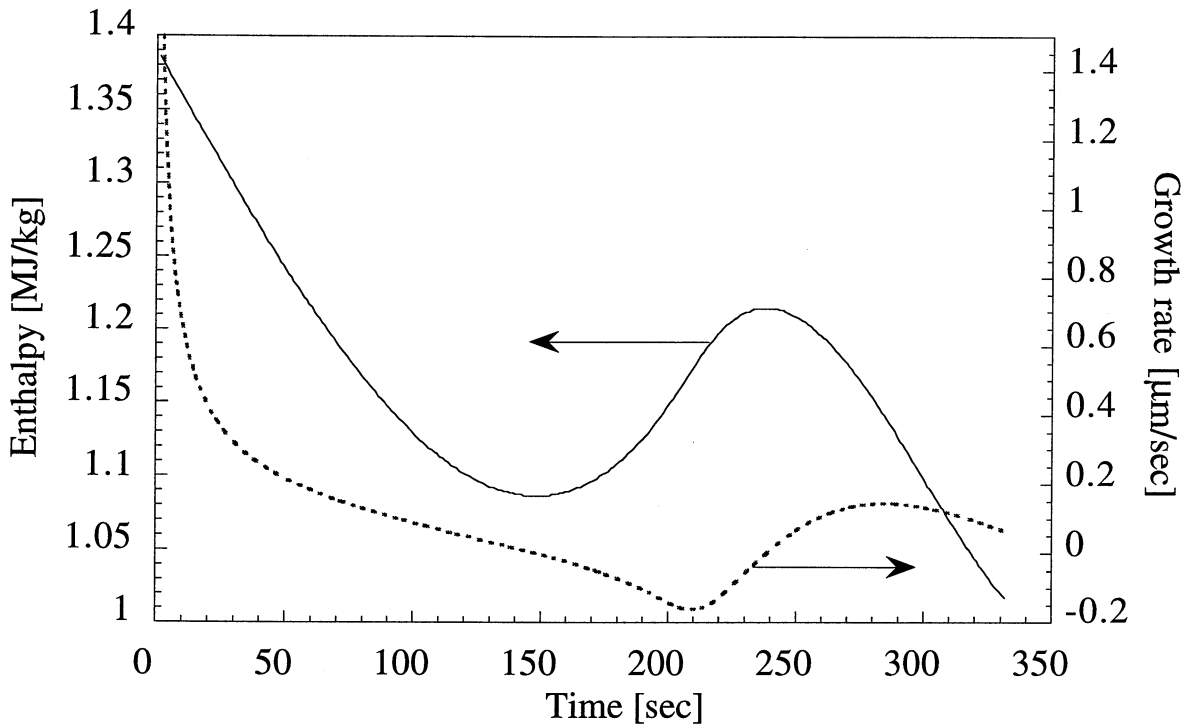


Figure IV.1: imposed enthalpy versus time and computed corresponding growth rate.

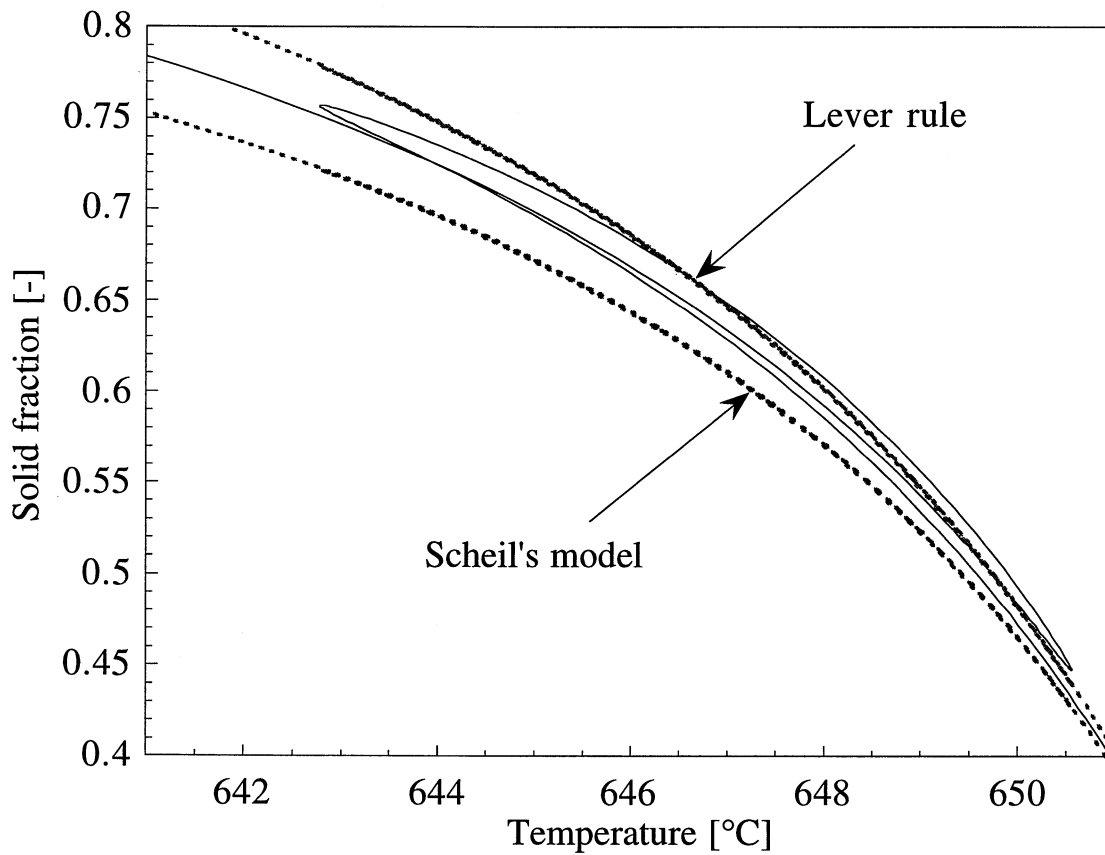


Figure IV.2:  $f_s$ - $T$  curves as computed for the 1201 alloy. The lever rule and Scheil's limits are also plotted.

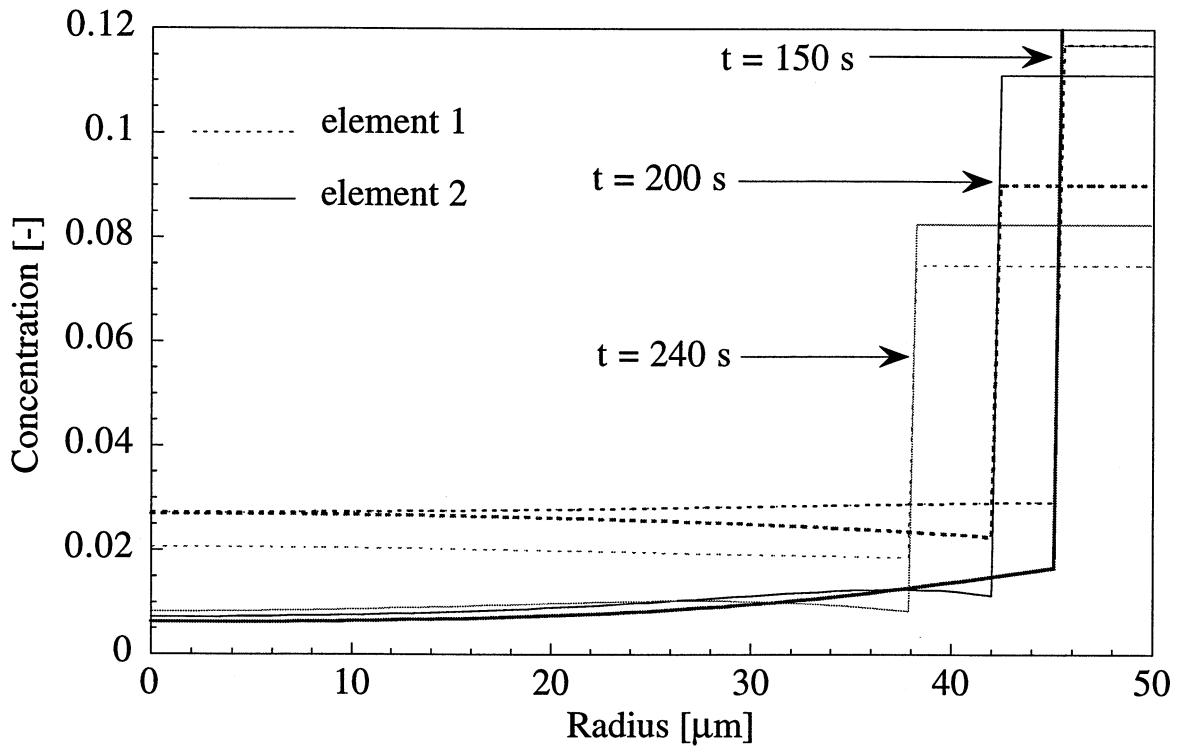


Figure IV.3: solute profiles during remelting,  $t = 150$  s and  $t = 240$  s correspond respectively to the begin and the end of the remelting period.

As pointed out in section 2.1, macrosegregation is associated with variations in the average solute concentrations at the scale of the process mainly induced by convection: they can range up to  $\pm 100\%$  of the nominal alloy element concentrations [Comb]. Under such conditions, the small volume element associated with the growing spherical grain is no longer a closed system. In order to test the present microsegregation model for such an open system, variations of the average solute concentration of element 2,  $w_2$ , have been imposed as indicated in figure IV.4<sup>1</sup>. As can be seen in this figure, the average solute concentration of element 2 is kept constant and equal to 5 wt% while the enthalpy,  $h$ , decreases during the first 25 s, The enthalpy is then kept constant, and the average concentration is first lowered to 1 wt% between 25 s and 45 s (negative segregation) and then increased to 9 wt% between 45 s and 65 s (positive segregation). Both the enthalpy and the solute concentration are kept constant at times larger than 65 s. The cooling curve,  $T(t)$ , and evolution of the solid fraction,  $f_s(t)$ , associated with the enthalpy and solute curves shown in figure IV.4 are displayed in figure IV.5. Note that the variations of  $f_s(t)$  when  $h$  is constant are closely associated with the variations of  $T(t)$  since the heat balance has to be satisfied (see equation 4.1).

<sup>1</sup> The average solute concentration of element 1 is kept constant equal to 5 wt%.

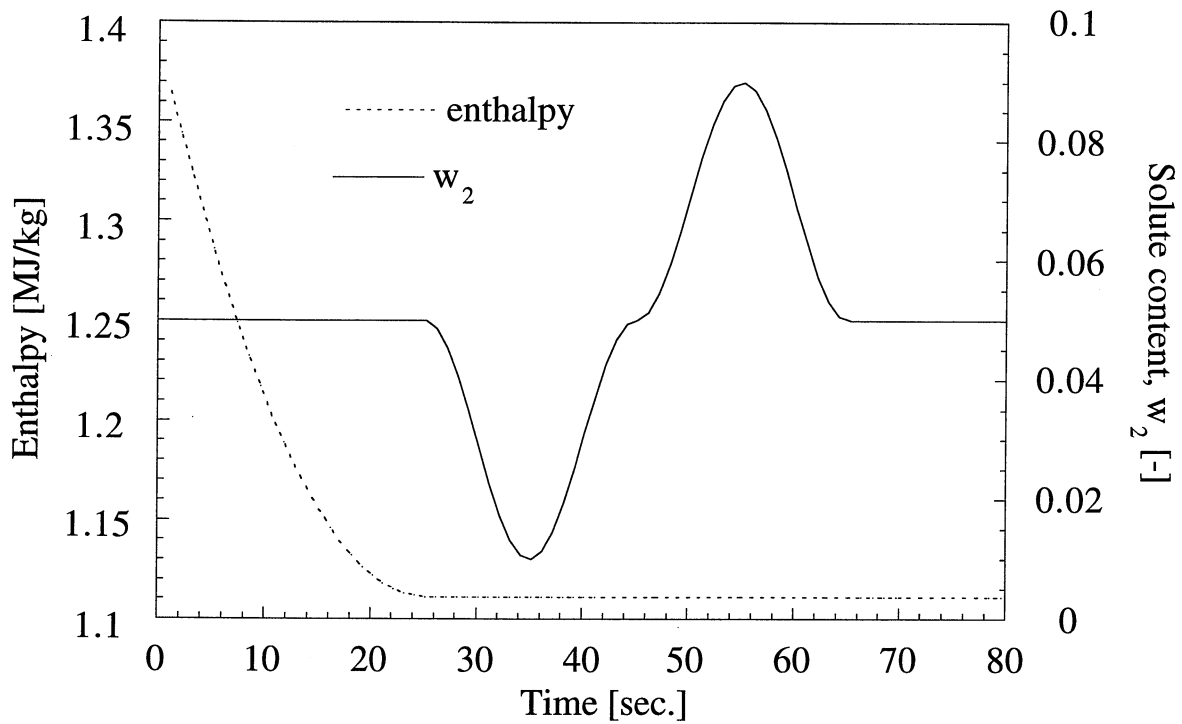


Figure IV.4: imposed enthalpy and total solute content of element 2 as a function of time.

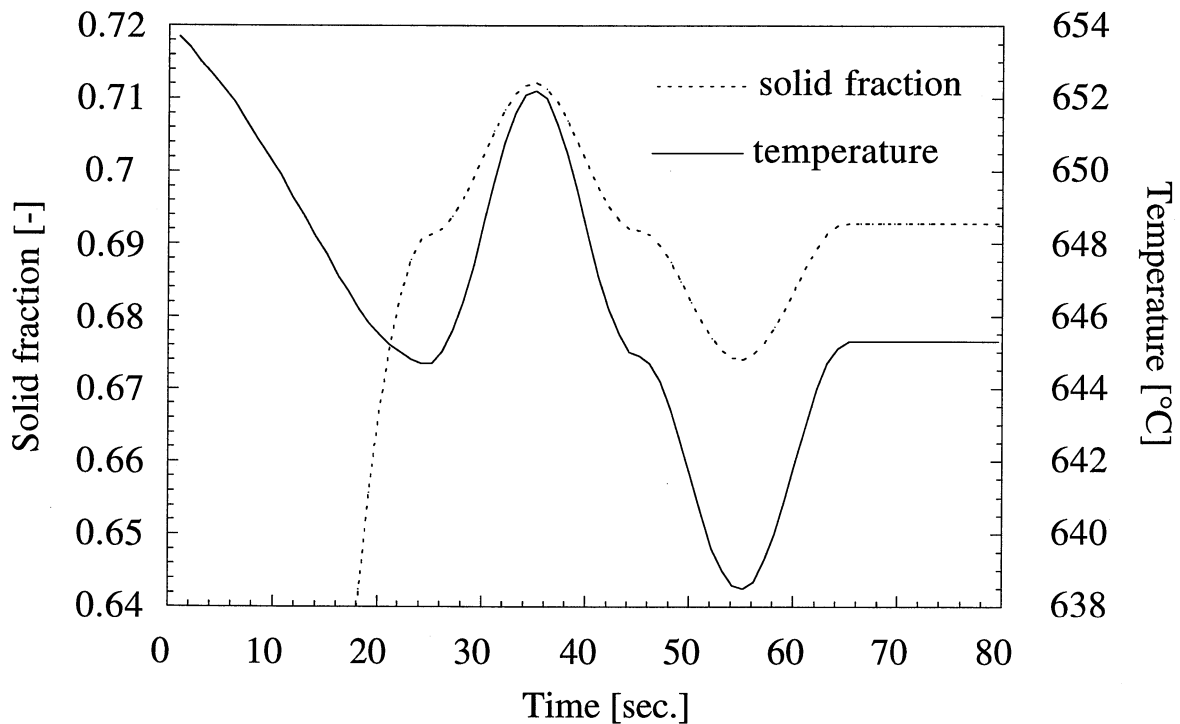


Figure IV.5: computed solid fraction,  $f_s(t)$ , and temperature,  $T(t)$ .

As can be seen in figure IV.5, the system can still solidify or remelt under adiabatic conditions ( $h$  constant) due to variations of the overall solute content. Remelting (solidification) could even occur for a decreasing (increasing) enthalpy if the increase (decrease) of the average concentration is sufficiently large.



# CURRICULUM VITAE

## **Jean-Marie DREZET**

born in Pontarlier (France) on January 15th, 1968

French nationality

## **FORMATION**

1986 : French baccalauréat série C (Maths and Physics), Lycée V. Hugo, Besançon, France.

1987-1988 : Classes préparatoires aux grandes écoles, Lycée V. Hugo, Besançon, France.

1989-1990 : Ecole Nationale Supérieure de Physique de Grenoble (INPG), Grenoble, France.

1990-1991 : School year at the Département des Matériaux, Ecole Polytechnique Fédérale de Lausanne, Switzerland.

1991 : Degree of physicist engineer (Ecole Nationale Supérieure de Physique de Grenoble, INPG)

1991-1992 : National service as assistant in physics at Ecoles Militaires de Saint-Cyr, France.

1992-1996 : Assistant, PhD-student in Laboratoire de Métallurgie Physique (LMPH), Ecole Polytechnique Fédérale de Lausanne, Switzerland.

## **ADDRESS**

Laboratoire de Métallurgie Physique / EPFL

MX-G Ecublens

CH-1015 Lausanne, Switzerland

# LIST OF PUBLICATIONS

## Articles

J.-M. Drezet, M. Rappaz, B. Carrupt and M. Plata: "Experimental investigation of thermo-mechanical effects during direct chill and electromagnetic casting of aluminum alloys" in *Met. Trans.* **26B**, August 1995, pp. 821-829.

J.-M. Drezet and G. Eggeler: "High apparent creep activation energies in mushy zone microstructures" in *Scripta Met.* **31-6**, 1995, pp. 757-762.

H. Combeau, J.-M. Drezet, M. Rappaz and A. Mo: "Modeling of Microsegregation in Macroseggregation Computations", accepted for publication in *Met. Trans. A*.

J.-M. Drezet and M. Rappaz : "Modeling of Ingot Distortions during Direct Chill Casting of Aluminium Alloys ", accepted for publication in *Met. Trans. A*.

## Conference proceedings

J.-M. Drezet and M. Plata: "Thermomechanical effects during direct chill and electromagnetic casting of aluminum alloys, Part I: experimental investigation" in *Light Metals 1995*, Ed. J.-W. Evans, (TMS Publ., Warrendale, USA, 1995), pp. 931-940.

J.-M. Drezet, M. Rappaz and Y. Krähenbühl: "Thermomechanical effects during direct chill and electromagnetic casting of aluminum alloys, Part II: numerical simulation", *Light Metals 1995*, Ed. J.-W. Evans, (TMS Publ., Warrendale, USA, 1995), pp.941-950.

J.-M. Drezet, M. Rappaz and Y. Krähenbühl: "Numerical and experimental study of rolling faces pull-in during direct chill casting of aluminium alloys" in *Modeling of Casting, Welding and Advanced Solidification*

Processes, Eds: M. Cross et J. Campbell (TMS Publ., Warrendale, USA, 1995), pp. 197-204.

M. Rappaz, J.-L. Desbiolles, J.-M. Drezet, Ch.-A. Gandin, A. Jacot and Ph. Thévoz: "Application of inverse methods to the estimation of boundary conditions and properties" in Modeling of Casting, Welding and Advanced Solidification Processes, Eds: M. Cross et J. Campbell (TMS Publ., Warrendale, USA, 1995), pp. 449-457.

J.-M. Drezet, M. Rappaz and Y. Krähenbühl: "Modeling of Thermomechanical Effects during Direct Chill Casting of AA1201 Aluminium Alloy" in Proceedings of the 5th International Conference on Aluminium Alloys, their Physical and Mechanical Properties, ICAA 1996, Grenoble, France.

J.-M. Drezet, M. Rappaz and Y. Krähenbühl: "Ingot Distortions and Residual Stresses in Direct Chill Casting of Aluminium Alloys" in Proceedings of the 4th European Conference on Residual Stresses, ECRS 1996, Cluny, France.

### **Miscellaneous**

Y. von Kaenel, J.-Ch. Giachetto, J. Stiegler, J.-M. Drezet and E. Blank: "A new interpretation of bulge test measurements using numerical simulation", to appear in Diamond and Related Materials, 1996.

S. Finnie, W. Cheng, I. Finnie, J.-M. Drezet and M. Gremaud: "The computation and Measurements of Residual Stresses in Laser Deposited Layers", in Proceedings of the 4th European Conference on Residual Stresses, ECRS 1996, Cluny.



Sinon l'enfance, qu'y avait-il alors qu'il n'y a plus ?

Plaines ! Pentes ! Il y avait plus d'ordre !

Et tout n'était que règnes et confins de lueurs.

Et l'ombre et la lumière étaient plus près d'être une même chose ...

Pour fêter une enfance

King Light's settlements

Saint John Perse.